Universität Zürich
Physik-Institut

www.physik.uzh.ch

Wissenschaftlicher Jahresbericht

April 2009 - März 2010

Winterthurerstrasse 190, CH-8057 Zürich/Schweiz

Universität Zürich
Physik-Institut
www.physik.uzh.ch

Wissenschaftlicher Jahresbericht

April 2009 - März 2010

Winterthurerstrasse 190, CH-8057 Zürich/Schweiz

The picture on the front shows Laura Baudis in her Zurich laboratory. On the back, the top part of the Xurich detector is shown. This small liquid xenon time projection chamber is used for r&d for the XENON project presented in Sec. 4.

Sekretariat	044 635 5721	secret@physik.uzh.ch
Prof. C. Amsler	044 635 5784 022 767 2914	amsler@cern.ch
Prof. L. Baudis	044 635 5777	lbaudis@physik.uzh.ch
Prof. H.-W. Fink	044 635 5801	hwfink@physik.uzh.ch
Prof. H. Keller	044 635 5748	keller@physik.uzh.ch
Prof. J. Osterwalder	044 635 5827	osterwal@physik.uzh.ch
Prof. A. Schilling	044 635 5791	schilling@physik.uzh.ch
Prof. U.D. Straumann	044 635 5768	strauman@physik.uzh.ch

The annual reports are available on the internet: http://www.physik.uzh.ch/reports.html.

Begleitwort

Die experimentelle Forschung am Physik-Institut umfasst mit seinen neun Forschungsgruppen ein breites Spektrum verschiedener aktueller Forschungsthemen der modernen Physik: von der Untersuchung biologischer Systeme über die Oberflächenphysik und die Physik magnetischer und supraleitender Materialien bis hin zu fundamentalen Wechselwirkungen und Systemen in der Elementarteilchen- und Astroteilchenphysik. Alle Forschungsgruppen verfolgen Projekte in enger Zusammenarbeit mit nationalen und internationalen Forschungsstätten, wie beispielsweise dem Paul Scherrer Institut, dem IBM Forschungslaboratorium Rüschlikon, dem CERN in Genf, dem DESY in Hamburg, sowie mit in- und ausländischen Universtäten. Die Forschungsgruppen wurden im Berichtsjahr neben der Universität Zürich auch vom Schweizerischen Nationalfonds, mit Drittmittelbeiträgen von nationalen und internationalen Forschungsinstituten, im Rahmen von EU-Projekten, sowie von in- und ausländischen Stiftungen unterstützt.

Ende 2009 konnte der weltgrösste Teilchenbeschleuniger LHC (Large Hadron Collider) am CERN nach einer Verzögerung wegen einer technischen Panne in Betrieb genommen werden. Im März 2010 konnten erstmals Protonen mit einer Schwerpunktsenergie von sieben Tera-Elektronenvolt (TeV) erfolgreich zur Kollision gebracht werden. Damit hat die eigentliche Forschungsarbeit mit dem LHC begonnen, von der wir neue Erkenntnisse über grundlegende Fragen der Physik erwarten. Das Physik-Institut ist am LHC massgeblich an zwei Experimenten im Rahmen von internationalen Kollaborationen beteiligt. Im LHCb-Experiment wird die Symmetrie zwischen Materie und Antimaterie untersucht und allfällige indirekte Effekte neuer Physik studiert (Gruppe Prof. U. Straumann). Das CMS-Experiment verfolgt unter anderem die Ziele nach dem Higgs-Boson zu suchen und neue Physik jenseits des Standard-Modells zu finden (Gruppe Prof. C. Amsler). Im April 2009 hat Prof. V. Chiochia seine Tätigkeit im Rahmen einer vom SNF finanzierten Förderungsprofessur am Physik-Institut aufgenommen. Auch seine Gruppe ist am CMS-Experiment beteiligt, insbesondere beschäftigt sie sich mit dem Betrieb des Silizium-Pixeldetektors und der Datenanalyse.

Dieser Jahresbericht dokumentiert die zwischen April 2009 und März 2010 erzielten Fortschritte der Forschungsgruppen des Physik-Instituts. Er ist relativ kurz gefasst und es werden nur die *Highlights* der Forschungsarbeiten der einzelnen Gruppen erwähnt. Die detaillierte Publikationsliste am Ende des Berichtes widerspiegelt alle Forschungsaktivitäten im Berichtsjahr.

An dieser Stelle möchte ich dem technischen und administrativen Personal des Physik-Instituts herzlich danken, das mit grossem Engagement wesentlich mitgeholfen hat, die Forschungsarbeiten zum Erfolg zu bringen. Besonderen Dank möchte ich den forschungsfördernden Institutionen aussprechen, mit deren finanzieller Unterstützung eine Realisierung dieser Forschungsprojekte erst möglich wurde.

Zürich, im Mai
Prof. Dr. Hugo Keller

Der vollständige Jahresbericht wie auch die Jahresberichte früherer Jahre können auf der Website des Physik-Instituts (http://www.physik.uzh.ch/reports.html) eingesehen werden.
Die Forschungsprojekte des Physik-Instituts findet man auf den Websites der Forschungsdatenbank der Universität Zürich (http://www.research-projects.uzh.ch/math/unit71600/index.htm).

Mitarbeiter

Wissenschaftliches Personal

Dr. Christof	Aegerter	Phys. Systembiologie
Dr. Ernest	Aguiló	CMS
Meral	Aksak	Oberflächenphysik
Dr. Enver	Alagöz	CMS
Prof. Claude	Amsler	ArDM, DIRAC, CMS
Dr. Jonathan	Anderson	LHCb
Sebastian	Arrenberg	CDMS
Ali	Askin	XENON
Daniel	Assmann	Phys. Systembiologie
Holger	Bartolf	PTM
Prof. Laura	Baudis	CDMS, GERDA, XENON
Annika	Behrens	XENON
Markus	Bendele	Supraleitung & Magnetismus
Dr. Roland	Bernet	LHCb
Vittorio	Boccone	ArDM
Saskia	Bosma	Supraleitung & Magnetismus
Olaf	Bossen	PTM
Tobias	Bruch	CDMS, GERDA, XENON
Dr. Thomas	Brugger	Oberflächenphysik
Angela	Büchler	LHCb
Albert	Bursche	LHCb
Nicola	Chiapolini	LHCb
Prof. Vincenzo	Chiochia	CMS
William	Creus	ArDM
Huanyao	Cun	Oberflächenphysik
Michel	De Cian	LHCb
Dr. Simon Marie	de Visscher	CMS
Dr. Jan-Hugo	Dil	Oberflächenphysik
Dr. Andreas	Engel	PTM
Dr. Conrad	Escher	Bio-Physik
Carlotta	Favaro	CMS
Dr. Alfredo	Ferella	GERDA, XENON
Prof. Hans-Werner	Fink	Bio-Physik
Francis	Froborg	GERDA
Arno	Gadola	CTA
Giulia	Ghielmetti	Phys. Systembiologie
Prof. Thomas	Greber	Oberflächenphysik
Dr. Heinz	Gross	Bio-Physik
Dr. Dominik	Grögler	Bio-Physik
Henrik	Grundmann	PTM
Zurab	Guguchia	Supraleitung & Magnetismus
Marijke	Haffke	XENON

Wissenschaftliches Personal (cont)

Viktor	Hangartner	LHCb
Dr. Matthias	Hengsberger	Oberflächenphysik
Ben	Huber	CTA
Kevin	Inderbitzin	PTM
Andreas	Jaeger	CMS
Prof. Hugo	Keller	Supraleitung & Magnetismus
Alexander	Kish	XENON
Dr. Tatiana	Latychevskaia	Bio-Physik
Dominik	Leuenberger	Oberflächenphysik
Dr. Jean-Nicolas	Longchamp	Bio-Physik
Dr. Haifeng	Ma	Oberflächenphysik
Dr. Aaron	Manalaysay	CTA, XENON
Dr. Teresa	Marrodan-Undagoitia	XENON
Fabian	Meier	Oberflächenphysik
Barbara	Millan Mejias	CMS
Martin	Morscher	Oberflächenphysik
Dr. Katharina	Müller	H1, LHCb
Dr. Ferenc	Muranyi	Supraleitung & Magnetismus
Ulrike	Nienhaus	Phys. Systembiologie
Dr. Krzysztof	Nowak	H1
Prof. Jürg	Osterwalder	Oberflächenphysik
Dr. Polina	Otyugova	ArDM,CMS
Praveen	Prem	Supraleitung & Magnetismus
Dr. Christian	Regenfus	CMS, ArDM, DIRAC
Mark	Reibelt	PTM
Mirena Ivova	Rikova	CMS
Dr. Peter	Robmann	CMS, H1, $\pi \to e\nu$
Tanja	Rommerskirchen	CMS
Dr. Josef	Roos	Supraleitung & Magnetismus
Silvan	Roth	Oberflächenphysik
Christophe	Salzmann	LHCb
Dr. Roberto	Santorelli	GERDA, XENON
Prof. Andreas	Schilling	PTM
Thomas	Schluck	Phys. Systembiologie
Dr. Alexander	Schmidt	CMS
Dr. Marc	Schumann	XENON
Dr. Luca	Scotto Lavina	ArDM
Bartosz	Slomski	Oberflächenphysik
Dr. Hella	Snoek	CMS
Dr. Olaf	Steinkamp	LHCb, CTA
Elvira	Steinwand	Bio-Physik
Dr. Simon	Strässle	Supraleitung & Magnetismus
Prof. Ulrich	Straumann	H1, LHCb, $\pi \to e\nu$, CTA
Michal	Tarka	CDMS, GERDA
Dr. Mark	Tobin	LHCb

Wissenschaftliches Personal (cont)

Dr. Andries	van der Schaaf	$\pi \to e\nu$
Dr. Jeroen	van Tilburg	LHCb
Dr. Ivo	Vellekoop	Phys. Systembiologie
Dr. Achim	Vollhardt	Elektronik, LHCb, CTA
Dr. Stephen	Weyeneth	Supraleitung & Magnetismus
Dr. Lotte	Wilke	CMS
Bastian M.	Wojek	Supraleitung & Magnetismus
Dr. Hirofumi	Yanagisawa	Oberflächenphysik

Technisches und administratives Personal

Eva	Baby	Sekretariat
Kurt	Bösiger	Werkstatt
Tiziano	Crudeli	Zeichnen
Denis	Dürst	Werkstatt
Walter	Fässler	Dokumentation, Elektronik
Omid	Fardin	Werkstatt
Daniel	Florin	Elektronik
Ruth	Halter	Sekretariat
Martin	Klöckner	Oberflächenphysik
Bruno	Lussi	Werkstatt
Reto	Maier	Werkstatt
Hanspeter	Meyer	Elektronik, CMS
Tizian	Naterop	Werkstatt
Lucien	Pauli	Vorlesungsbetrieb
Jacky	Rochet	CMS, ArDM, DIRAC
Monika	Röllin	Sekretariat
Dr. Jean-Pierre	Ruder	CHIPP
Marcel	Schaffner	Werkstatt
Jacqueline	Schenk	Sekretariat
Silvio	Scherr	Werkstatt
Stefan	Siegrist	PTM
Peter	Soland	Elektronik
Stefan	Steiner	CAD, CMS, LHCb, CTA
Michael	Weber	Vorlesungsbetrieb

Contents

Physics of Fundamental Interactions and Particles 1

1 Towards a dark matter experiment 1

2 Search for Cold Dark Matter with CDMS-II 8

3 Search for the Neutrinoless Double Beta Decay with GERDA 11

4 Search for Cold Dark Matter Particles with XENON 14

5 A Cherenkov Telescope Array for Very High Energy Astronomy (CTA) 17

5.1 Active Mirror Control 18

5.2 Light Concentrators 19

5.3 FlashCam 20

6 Testing lepton universality, the $\pi \rightarrow e\overline{\nu}$/ $\pi \rightarrow \mu\overline{\nu}$ branching ratio 22

6.1 The new mini-TPC beam tracker 23

6.2 Target waveform analysis 23

6.3 $\pi \rightarrow e\nu$ positron energy response 24

6.4 Outlook 24

7 Study of Coulomb-bound πK-pairs 25

8 Particle Physics at DESY/HERA (H1) 30

8.1 Measurement of the longitudinal structure function F_L 31

8.2 Multiple interactions in photoproduction 33

8.3 Photon analysis 34

9 High-precision CP-violation Physics at LHCb 36

9.1 The LHCb Experiment 36

9.2 The Zürich Group in LHCb 37

9.3 Tracker Turicensis 37
9.4 Track reconstruction and alignment 38
9.5 Physics studies 39
9.6 Outreach activities 41
9.7 Summary and Outlook 42

10 Particle physics with CMS **43**
10.1 Commissioning of CMS silicon pixel detector with first collision data 44
10.2 Spatial alignment of the silicon pixel and strip tracker 46
10.3 Improvements to the pixel hit reconstruction 47
10.4 Improvements to b-quark tagging techniques 47
10.5 Studies of $B_s \to (J/\psi)\phi$ and B_c-decays 48
10.6 Modeling of Higgs and jet production at the LHC 50
10.7 Search for Supersymmetry (SUSY) in multi-jet final states 51
10.8 Upgrades of the computing infrastructure 51
10.9 Preparation for future upgrades of the CMS pixel detector 52

Condensed Matter Physics 53

11 Superconductivity and Magnetism **53**
11.1 Field dependent superfluid density in optimally doped $SmFeAsO_{1-x}F_y$ 53
11.2 Pressure induced static magnetic order in superconducting $FeSe_{1-x}$ 55
11.3 NMR investigations of orbital currents in YBCO compounds 57
11.4 Oxygen isotope effects within the phase diagram of cuprates 58

12 Phase transitions and superconducting photon detectors **60**
12.1 Physics of superconducting thin-film nanostructures 60
12.2 Unveiling the peak effect in resistivity data of Nb_3Sn using vortex shaking 61
12.3 Construction of an ac-calorimetry experiment for vortex-shaking experiments 63
12.4 Structural phase transition in magnetic insulators 64

13 Surface Physics **66**

13.1 Switching surface texture by hydrogen intercalation 68

13.2 Unconventional Fermi surface spin textures in surface alloys 69

13.3 Optical control of field-emission sites by femtosecond laser pulses 71

14 Physics of Biological Systems **73**

14.1 Non-destructive imaging of individual bio-molecules 74

14.2 Low-aberration micrometer-sized electron lenses 78

15 Physical Systems Biology and non-equilibrium Soft Matter **87**

15.1 Imaging through turbid media 87

15.2 The influence of mechanical stress on growth in the wing imaginal disc of Drosophila 90

Infrastructure and Publications **93**

16 Mechanical Workshop **93**

17 Electronics Workshop **97**

18 Publications **99**

18.1 Elementary particles and their interactions 99

18.2 Condensed matter 111

1 Towards a dark matter experiment

C. Amsler, V. Boccone, W. Creus, L. Scotto Lavina, P. Otyugova, C. Regenfus, and J. Rochet

(ArDM and DARWIN Collaborations)

We are constructing at CERN a 1 ton liquid argon detector (ArDM) to detect both charge and luminescence produced by recoil nuclei, following a WIMP interaction. WIMPs (Weak Interacting Massive Particles) are prime candidates for the dark matter in the universe.

Charged particles lead to ionization and excitation of argon atoms, forming excimers with the lowest singlet and the triplet excited states decaying by VUV photon emission in a narrow band around 128 nm. The singlet and the triplet states have different decay times, respectively $\tau_1 \simeq 5$ ns and $\tau_2 \simeq 1.6$ μs in liquid (1). However, impurities such as water, air and CO_2, can absorb the VUV light and reduce τ_2 (2). The population ratio singlet/triplet depends on ionization density. For minimum ionizing projectiles, such as electrons and photons, the ratio is $\approx$0.3, while for alpha particles and nuclear recoils one finds a ratio of $\approx$4 (1). Hence nuclear recoils from WIMPs populate mostly the fast decaying singlet state. In addition, the ionization yield is much lower for nuclear than for minimum ionizing particles. This is due to quick recombination which decreases the charge and enhances the luminescence. The higher ratio of light to charge production for nuclear recoils and the higher population of the fast decaying state can both be used to reduce background in WIMP searches.

The ArDM experiment consists of a 1 t liquid argon (LAr) detector to search for WIMPs interacting elastically with argon nuclei. A sketch illustrating the measurement principle is shown in Figures 1.1 and 1.2. The apparatus collects signals from scintillation and ionization independently. The ionization charges drift towards the gas phase in an electric field of

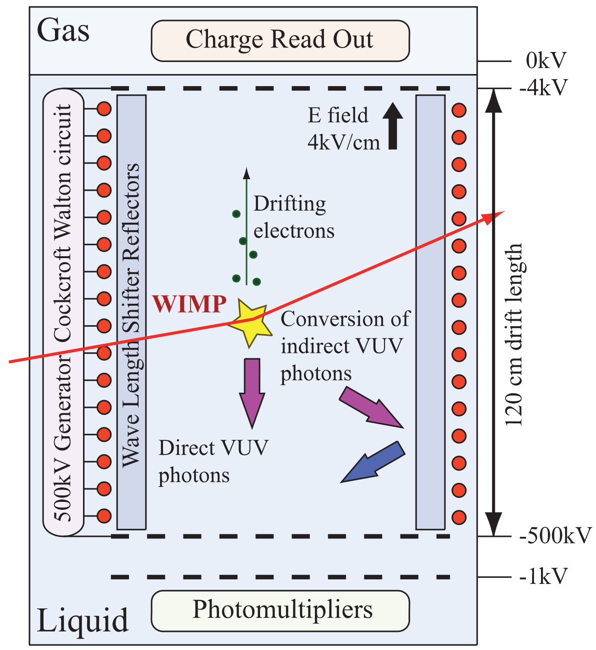

Figure 1.1:
Conceptual layout of the ArDM experiment.

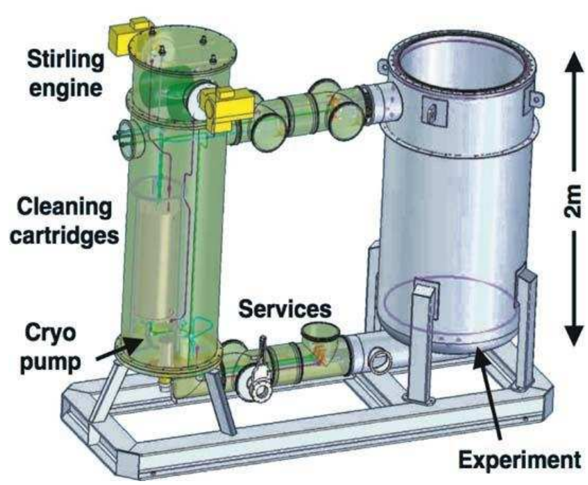

Figure 1.2:
3D sketch of the ArDM cryogenic setup with LAr cleaning circuit and main dewar.

4 kV/cm supplied by a Greinacher (Cockroft-Walton) chain with 210 stages. The charge is extracted from the liquid into the gas phase by a high electric field between two extraction grids (below and above the liquid surface). A large area electron multiplier (LEM) is used to amplify the charge. The field shaping rings are covered on their inner sides with reflectors to shift the 128 nm fluorescence light into the visible range and to increase the light collection efficiency (3). Fourteen photomultipliers (PMT) are located below the HV cathode (–500 kV). The fiducial mass of the detector is estimated to be about 850 kg. The LAr recirculation and purification system (based on a CuO cartridge), provides the purity for drift distances of up to 120 cm. A 3D sketch of the detector is shown in Fig. 1.2.

The detector is currently installed on the surface in building 182 at CERN and our group has developed the light

readout system. The ArDM detector was filled for the first time with 1 ton of LAr in May 2009 (4). Several important parameters such as cryogenic operation at high LAr purity over weeks, stable and flawless operation of the light readout system, high scintillation light yield, and detection of events down to energies of the order of tens of keV could be verified.

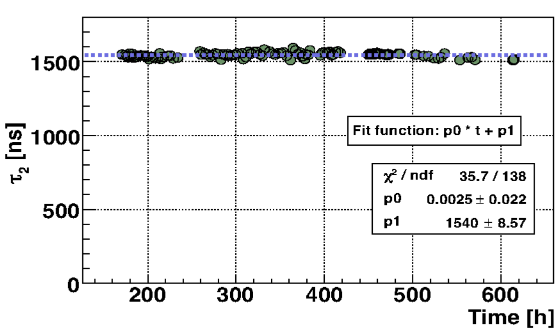

Figure 1.3: Monitoring of the LAr purity in ArDM from the slow luminescence component τ_2 during 600h of operation.

The test was performed with a partial light readout assembly consisting of 7 (instead of 14) Hamamatsu R5912-MOD PMTs with Pt-underlays, no electric field and no charge readout. The PMT glass was coated with a thin layer of a transparent TPB-paraloid compound to increase the collection efficiency for VUV light. The side reflectors were made of 15 Tetratex foils (120×25 cm^2), coated with Tetraphenyl butadiene (TPB) wavelength shifters (WLS) of optimum thickness (5), using a custom made evaporator. The apparatus was filled with LAr with the side reflectors fully immersed and kept full for about 3 weeks, while various measurements with radioactive sources were performed.

The monitoring of the LAr purity was performed by measuring the decay time of the slow component of the light signal (τ_2) (2). The purity was found to be constant (Fig. 1.3), around $\tau_2 \simeq 1.5\ \mu$s, in agreement with expectations (1). Figure 1.4 shows the fluctuations of the PMT calibration constants as a function of time.

To study the detector response to photons we used a ^{22}Na source (E$_\gamma$=511 keV and 1274 keV) and a ^{137}Cs source (E$_\gamma$=661 keV). For ^{137}Cs the data were obtained with the LAr detector in self-trigger mode, while for ^{22}Na the detector was in coincidence with an external NaI scintillator. The response spectra in

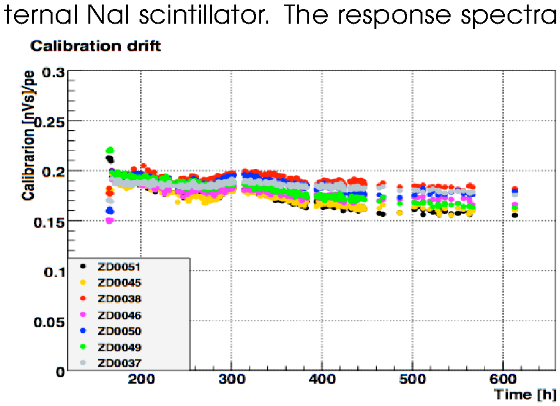

Figure 1.4: Fluctuation of the PMT calibration constants as a function of time.

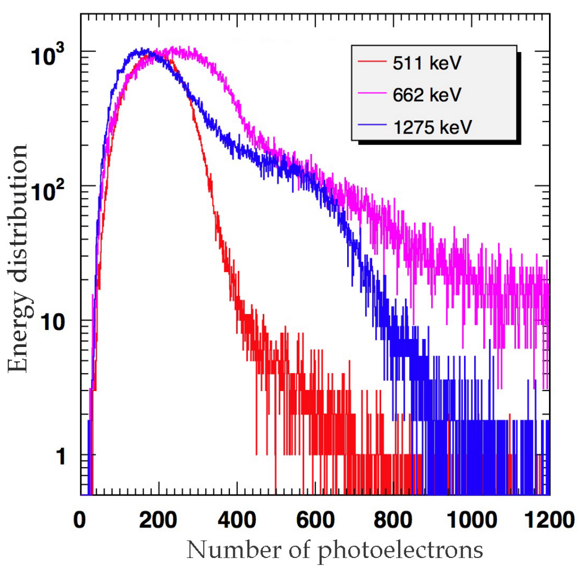

Figure 1.5: Energy spectra for ^{137}Cs and ^{22}Na.

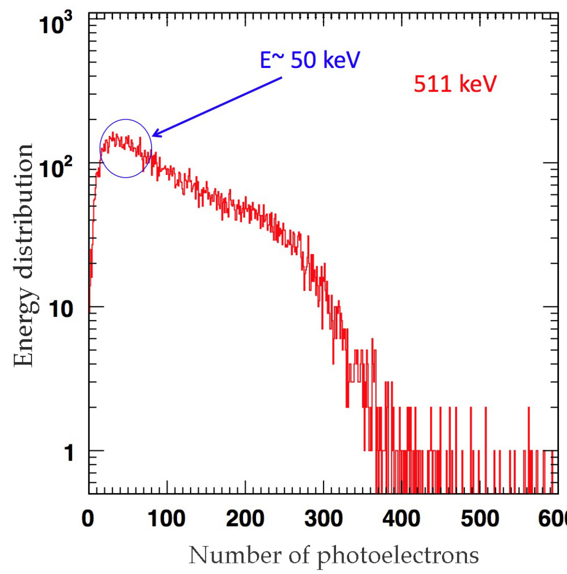

Figure 1.6: Energy distribution for 511 keV γs.

Fig. 1.5. The shapes of the distributions can be reproduced and fitted assuming multiple Compton scattering in the detector (7). The light yield is estimated to be ~0.5 photoelectrons/keV for electrons with the 7 PMTs assembly. Furthermore, by triggering on the total energy deposited by two of the three γs (511 and 1275 keV) we could select the signal from the second 511 keV γ in LAr. Figure 1.6 shows that a lower threshold of 50 keV for electrons can be reached already with 7 PMTs.

Even small neutron fluxes around 1 MeV are potentially dangerous, since the neutron-argon cross section is some 18 orders of magnitude larger than for WIMPs. It is therefore essential to investigate the response of the dark matter detector to neutrons as a function of recoil energy. We first studied the detector response to neutrons from an Am-Be source producing 3×10^4 1/s neutrons in the 1 – 10 MeV range. Data were taken for different positions of the source. Figure 1.7 shows the ratio CR between the integrated pulse height of the prompt light (< 50 ns) and that of the total light, as a function of integrated pulse height. These data were taken with the source located on the upper flange of the detector. As expected, neutrons leading to the nuclear recoil band (N.R.) mainly populate the fast decaying singlet state. Figure ?? (left) also shows the contributions from γs leading to Compton electrons (E.R. band). The corresponding decay time distributions for the two bands are shown in Fig. 1.8, fitted with exponentials convoluted with Gaussians.

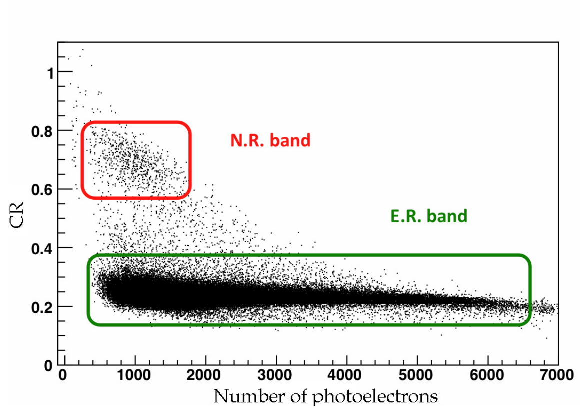

Figure 1.7:
Ratio CR of fast to total amplitude for the Am-Be-source on the top flange of the ArDM detector. The upper box shows nuclear recoils (N.R.), the lower box electron recoils (E.R.).

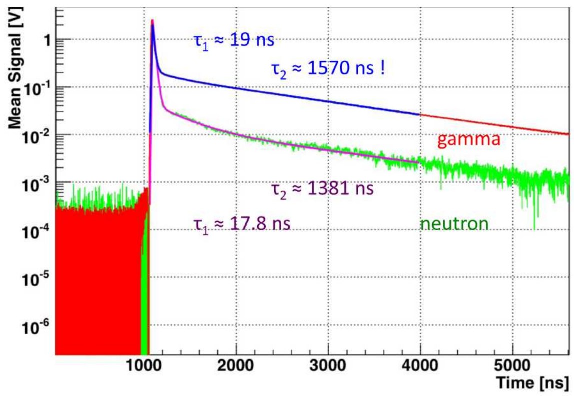

Figure 1.8: Decay time distributions corresponding to the two regions indicated in Fig. 1.7 with the fast and the slow components.

The ArDM detector was upgraded in summer 2009 to the final 14 PMTs. The deposition of WLS on the PMT windows was performed using a fast evaporation technique at the thin film laboratory of CERN. A photograph of the array under UV illumination before installation in the ArDM detector is shown in Figs. 1.9.

In autumn 2009 measurements were started in gaseous argon (GAr, Ar60 at room temperature and 1.1 bar pressure) using a movable ^{241}Am source (5.5 MeV αs) to obtain an estimate for the light yield with the fully equipped light readout. We collected data immediately after GAr filling to evaluate the maximum purity reached with the new turbopump system, then gathered more data as a function of time to observe the purity degradation. The best vacuum level reached before filling was 10^{-5} mbar, for which the measured slow component of the excimer-state decay τ_2 was found to be 3.04$\pm$0.04 μs, in accord with known values in gas at atmospheric pressure (2). Figure 1.10 shows for each PMT with a measurement of the mean life τ_2 of the slow component, the degradation of argon purity as a function of time.

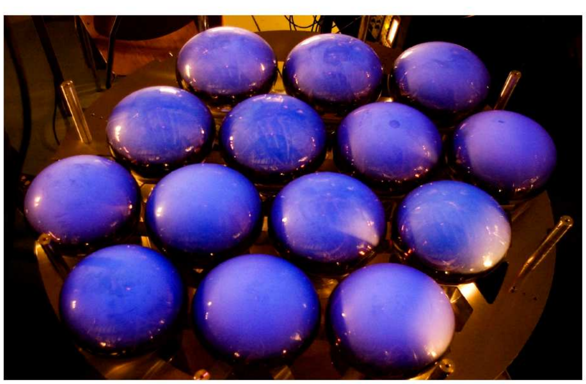

Figure 1.9: The 14 cryogenic PMTs coated with WLS, ready to be installed at the bottom of the ArDM apparatus, illuminated with UV light.

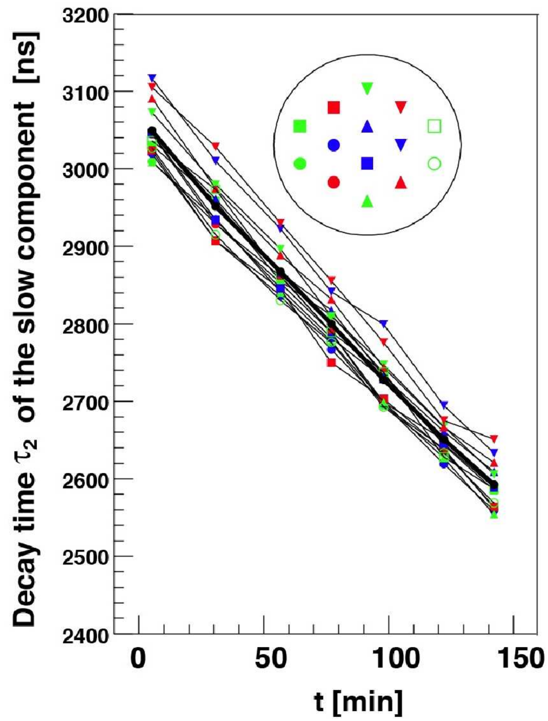

Figure 1.10: Measurement of the slow component of the luminescence in gaseous argon as a function of time (see text), for various source positions in the detector and for different PMTs (inset).

We have also contributed to the online data acquisition system and to the offline software. We developed, starting from the previous existing software, and a new analysis framework to satisfy basic needs, namely easy and fast access to the data, a modular package to include the forthcoming charge readout, which can also incorporate Monte Carlo data. The package was used to analyze the late 2009 data. For example, the signal offset was previously evaluated for each event by assessing the average value of the pedestal (before event trigger time), and by rejecting events for which the width of the pedestal distribution was exceeding a preset value. In the new approach a peak finding algorithm is applied instead to the pedestal trace, searching for anomalies such as PMT dark counts, background photons, and pile-up events. Also, PMTs near the detector edges collect less light due to geometrical inefficiencies. This makes the selection of e.g. αs less inefficient from single PMTs and more prone to background. Instead, the new framework applies all cuts on the total light collected from the 14 PMTs.

As already mentioned, neutrons with energies around 1 MeV or less will contribute to the background in WIMP searches. On the other hand, radioactive neutron sources can be used to study the luminescence yield from nuclear recoils in noble liquids (Fig. ?? above). Heavily ionizing particles such as recoiling nuclei generate significantly less light than electrons (for equal energy deposits). The quenching factor and its dependence on energy are poorly known for LAr and LXe, but lies in the range 0.15– 0.30 (8). We intend to measure the quenching factor as a function of recoil energy down to 10 keV by studying neutron-argon and neutron-xenon scattering with monoenergetic neutrons. Furthermore, the probability for multiple neutron interactions is large (while WIMPs interact only once). This can be studied with monoenergetic neutrons in a large cell (and in ArDM). This R&D work will benefit to both ArDM and the design of a next-generation noble liquid dark matter facility in Europe (DARWIN), which was recently funded by ASPERA, and to which we participate (together with the group of Prof. L. Baudis).

We have therefore purchased a neutron source from NSD-Fusion GmbH. The source delivers monoenergetic 2.45 MeV neutrons (up to 10^7 s^{-1}) from the reaction dd $\rightarrow$He^{3}n. The fusion generator, designed and optimised in collaboration with the maufacturer, was delivered at the end of 2009. The generator is based on a high voltage plasma discharge (30 - 120 kV, 1 - 15 mA). The gas pressure is controlled by heating getter disks which store the deuterium on their surfaces. Due to the excellent efficiency of the shielding the radiation dose remains far below the limit of 2.5 μSv/h at maximum fluence, and we are authorized to operate the generator at CERN without further shielding, but within a closed fence with safety and radiation interlock against X-rays, γs and neutrons (Figs. 1.11 and 1.12).

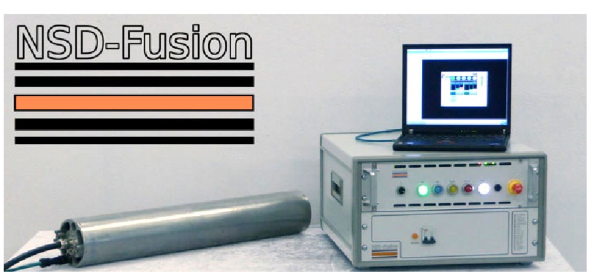

Figure 1.11: Components of the neutron generator (fusion chamber, HV power supply and controller).

Figure 1.12: Installation in the laboratory showing the 1600 kg cylindrical shielding (grey) made of water extended polyester (WEP) mixed with a boron absorber (Colemanite, $CaB_3O_4(OH)_3 \cdot H_2O$).

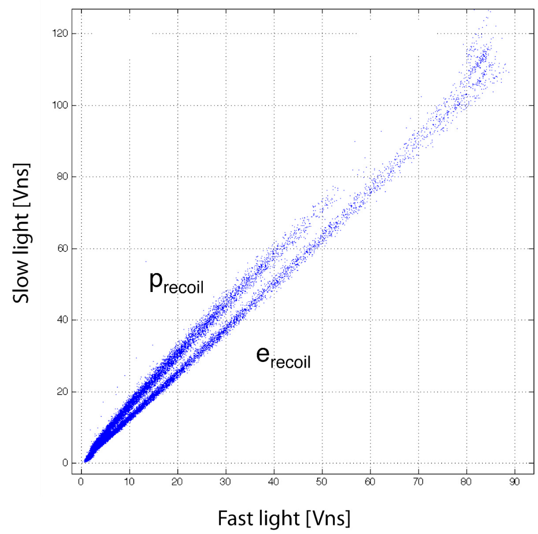

Figure 1.13: Proton and electron separation in liquid scintillator from the Am-Be source. Plotted is the distribution of integrated pulse height vs. integrated pulse height within the first 15 ns.

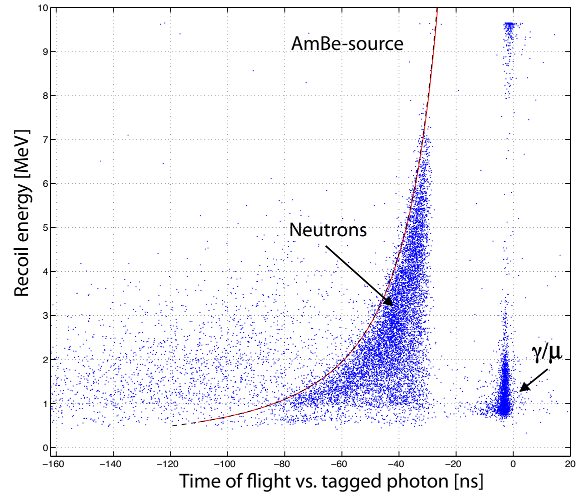

Figure 1.14: Recoil proton energy vs. time-of-flight. The red line shows the expected boundary. The accumulation on the far right is due to γs and cosmic muons.

The generator is routinely running in our laboratory and we are currently completing the system with a collimator, mechanical parts to hold the test chamber, and neutron detector components for the scattering experiment.

Three liquid EJ301 scintillator cells (diameters 2, 3 and 5″) were purchased from SCIONIX. They are suitable for fast neutrons ($>$ 50 keV) and give information on the neutron energy, the recoiling proton being absorbed in the cell. However, calibration is required due to the non-linearity of light output vs. proton energy. Typically half of the 2.45 MeV neutrons scatter on the carbon component and are not detected. Protons and electrons lead to different pulse shapes in the scintillator (Fig. 1.13). A precise timing ($<$ 1ns) can be achieved to select neutron energies by time-of-flight. We have performed measurements on the 3″ detector with a 370 MBq Am-Be source located at a distance of about 1m. The source produced $3{\cdot}10^4$ n/s from the αBe reaction in the energy range 1 – 10 MeV. The neutron energy could be measured by time-of-flight by triggering on a 4.4 MeV γ (from ^{13}C* decays) emitted in coincidence, and compared with the measured proton recoil energy (Fig. 1.14).

In the setup sketched in Fig. 1.15 neutrons from the dd-source are scattered in the 3″ scintillation counter and detected under the angle θ by the 5″ counter. Figure 1.16 shows the proton recoil spectra for neutrons in the 3″ target counter which would be uniform (due to the isotropic scattering in the c.m.s.) in the absence of multiple scattering, scattering on carbon and for infinite energy resolution. Figure 1.17 shows the sum of energy deposits in both counters (for θ = 45°) which should ide-

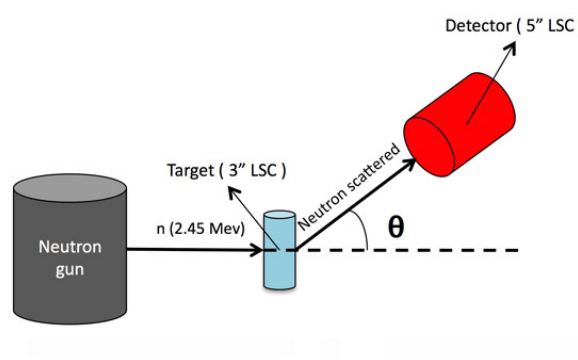

Figure 1.15: Sketch of the scattering experiment.

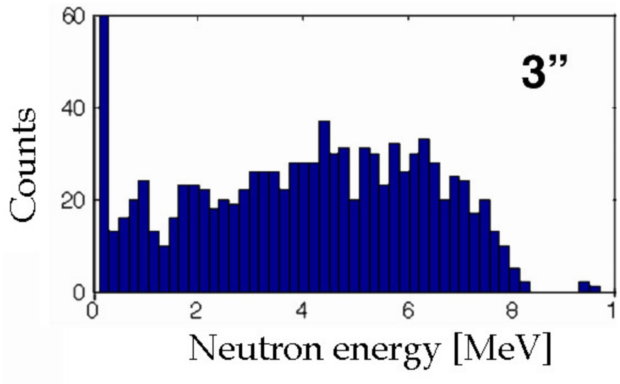

Figure 1.16: Proton recoil energy distribution in the 3″ target counter.

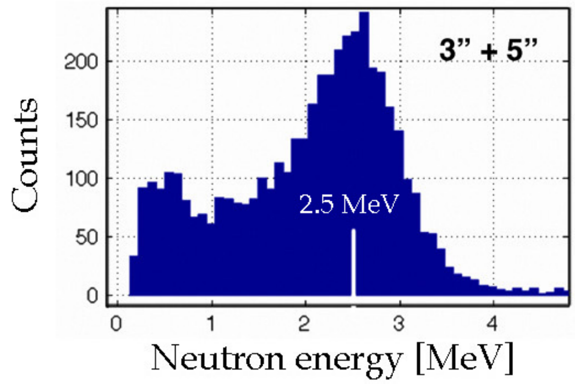

Figure 1.17: Sum of the energy deposits in the 3″ and 5″ counters.

ally be equal to the initial neutron energy. Indeed the distribution peaks around the expected incident energy of 2.5 MeV. The low energy enhancement is due to energy losses in the collimator.

R&D work for subdetector components is now being finalized and the results for the light readout efficiency are quite encouraging. The next run of the LAr detector equipped with 14 PMTs and a simple anode plane for the charge readout is planned for July 2010. This run should bring the experiment close to the point when physics operation could start. Pending are the construction and installation of the LEMs for the charge readout, and the implementation of a cryocooler and improved liquid recirculation system (H_2O filter). These items are in the hands of the ETHZ group. Upon completion, the detector will be moved to an underground location, probably the Canfranc underground laboratory in the Pyrenees.

[1] A. Hitachi *et al.*, Phys. Rev. **B27** (1983) 5279

[2] C. Amsler *et al.*, Journal of Instrumentation **3** (2008) P02001

[3] V. Boccone *et al.*, Journal of Instrumentation **4** (2009) P06001

[4] C. Amsler, Proc. 2009 Conf on HEP, Krakow (2009), PoS(EPS-HEP 2009)110;
P. Otyugova, Proc. 5th Patras Workshop on Axions, WIMPs and WISPs (2009);
C. Regenfus, Proc. TAUP 09 Conf., Rome, prep. arXiv:0912.2962v1 [phys.ins-det] (2009)

[5] H. Cabrera, Master Thesis, Universität Zürich (2007)

[6] C. Amsler *et al.*, Journal of Instrumentation **3** (2008) P02001

[7] V. Boccone, PhD thesis, Universität Zürich, in preparation

[8] D. M. Mei *et al.* Astropart. Phys. **30** (2008) 12

2 Search for Cold Dark Matter with CDMS-II

S. Arrenberg, L. Baudis, T. Bruch

in collaboration with: Department of Physics, Brown University, Department of Physics, California Institute of Technology, Department of Physics, Case Western Reserve University, Fermi National Accelerator Laboratory, Lawrence Berkeley National Laboratory, Massachusetts Institute of Technology, Department of Physics, Queen's University, Department of Physics, Santa Clara University, Department of Physics, Stanford University, Department of Physics, Syracuse University, Department of Physics, University of California, Berkeley, Department of Physics, University of California, Santa Barbara, Departments of Physics & Elec. Engr., University of Colorado Denver, Department of Physics, University of Florida, Gainesville, School of Physics & Astronomy, University of Minnesota, Minneapolis.

(CDMS-II Collaboration)

The Cryogenic Dark Matter Search (CDMS II) experiment seeks to detect recoiling atomic nuclei (nuclear recoils) from WIMP scattering events using high-purity Ge (230 g) and Si (100 g) detectors kept at cryogenic temperature (<50 mK). Each detector is ~10 mm thick disc with 76 mm in diameter, which is photolitographically patterned with sensors to detect the phonons and ionization generated by incident particles. These detectors can distinguish between nuclear and electronic recoils, since nuclear recoils generate less ionization than electronic recoils of the same deposited energy, allowing event-by-event rejection of background with a misidentification rate of less than one in 10^4.

CDMS II operated an array of 30 such detectors (19 Ge and 11 Si) in a low-radioactivity installation at the Soudan Underground Laboratory (713 m below the surface). While the depth of the experimental facility greatly reduces the rate of background events from particle showers induced by cosmic rays, the environmental radioactivity is shielded to negligible levels with concentric layers of lead and polyethylene. Data taken during four period of stable operation between July 2007 and September 2008 were analyzed, leading to the world's best upper limits on the WIMP-nucleon spin-independent cross section for WIMP masses above 42 GeV/c^2. These results have been recently published in Science (6).

The main contribution of our group is in the data analysis effort, with focus on basic data analysis, on understanding the various background sources and on the physics analysis with respect to standard dark matter candidates, inelastic dark matter models, dark matter interacting with electrons (2) and solar axion searches (3). In the following we present some of the highlights of our contributions, namely the results for standard WIMPs and for inelastic dark matter.

Due to their greater sensitivity to spin-independent WIMP scattering, only Ge detectors were used for the WIMP search. A total exposure of 612 kg-days was considered for the analysis. After detector calibration, a series of criteria to identify candidate WIMP-scattering events were defined. WIMP candidates were required to deposit 10-100 keV of energy in a single detector, have ionization and phonon characteristics of nuclear recoils and have no identifiable energy deposition in the scintillator shield that surrounds the passive shield layers. To avoid unconscious bias, a "blind analysis", in which the exact selection criteria were defined without prior knowledge of the content of the signal region or its vicinity was performed. The fraction of nuclear recoil events accepted by these selection criteria was measured using a calibration sample of nuclear recoil events induced by a ^{252}Cf source. The expected rate of background events from misidentified electronic recoils that happen within a few μm of the detector's surfaces is 0.8±0.1(stat)±0.2 (syst). Neutrons from cosmic rays and radioactivity of the detector materials are expected to generate an average of ~0.1 nuclear recoils which would be indistinguishable from WIMP scatters.

After finalizing all event selection criteria, the signal region was "unblinded" and two candidate events at recoil energies of 12.3 keV and 15.5 keV were observed (Fig. 2.1 and Fig. 2.2). These events occurred during periods of nearly ideal experimental performance, were separated in time by several months, and took place in different detectors (T1Z5 and T3Z4). Although these candidate events thus match the expectations for WIMP scattering events, the probability to have observed two or more background events in this exposure is 23%. Hence, the results can not be interpreted as evidence for WIMP interactions, nor can either event be rejected as a WIMP scatter. These data constrain

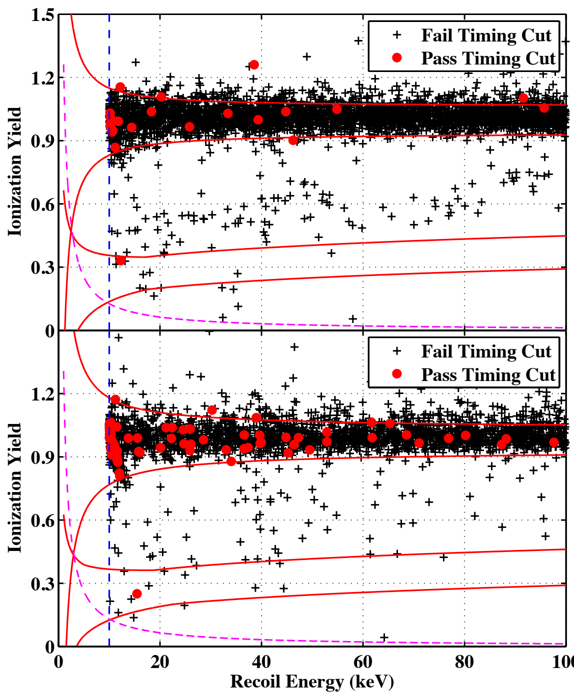

Figure 2.1: Ionization yield versus recoil energy for events passing all cuts, excluding yield and timing. The top (bottom) plot shows events for detector T1Z5(T3Z4). The solid red lines indicate the 2σ electron and nuclear recoil bands. The vertical dashed line represents the recoil energy threshold and the sloping magenta dashed line is the ionization threshold. Events that pass the timing cut are shown with round markers. The candidate events are the round markers inside the nuclear-recoil bands.

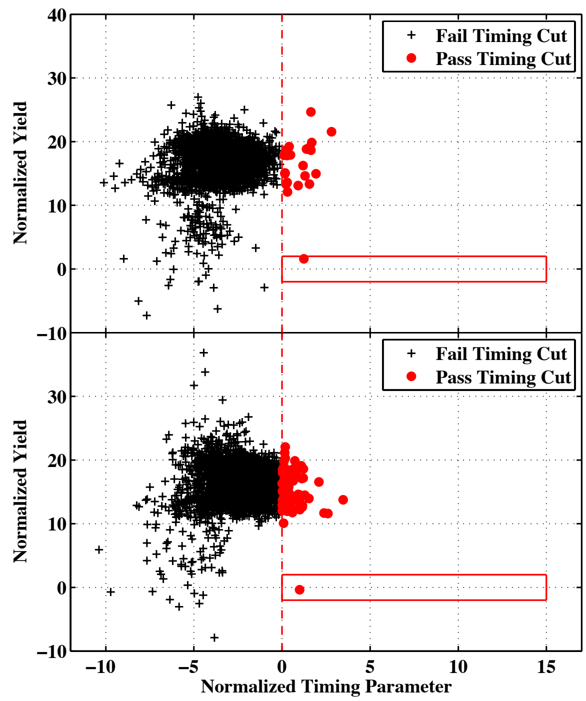

Figure 2.2: Normalized ionization yield (number of standard deviations from mean of nuclear recoil band) versus normalized timing parameter (timing relative to acceptance region) for events passing all cuts, excluding yield and timing. The top (bottom) plot shows events for detector T1Z5(T3Z4). Events that pass the phonon timing cut are shown with round markers. The solid red box indicates the signal region for that detector. The candidate events are the round markers inside the signal regions.

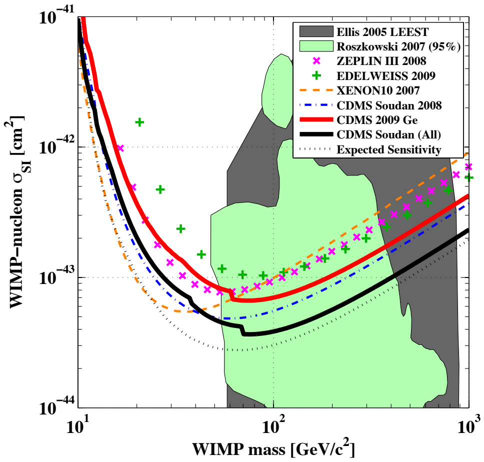

Figure 2.3: 90% C.L. upper limits on the WIMP-nucleon spin-independent cross section as a function of WIMP mass. The red (upper) solid line shows the limit obtained from the latest CDMS-II exposure analyzed. The solid black line shows the combined limit for the full data set recorded at Soudan. The dotted line indicates the expected sensitivity for this exposure based on our estimated background combined with the observed sensitivity of past Soudan data. Prior results from CDMS [4] and other experiments (see legend) are shown for comparison. The shaded regions indicate allowed parameter space calculated from certain Minimal Supersymmetric Models.

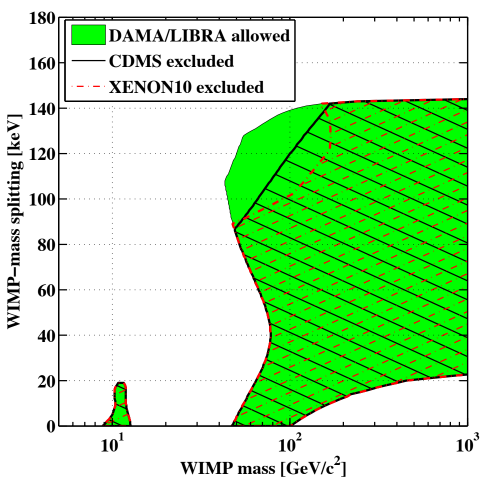

Figure 2.4: The shaded green region represents WIMP masses and mass splittings for which there exists a cross section compatible with the DAMA/LIBRA [7] modulation spectrum at 90% C. L. under the inelastic dark matter interpretation [5]. The excluded regions for CDMS II (solid-black hatched) and XENON10 [8] (red-dashed hatched) are shown.

the spin-independent WIMP-nucleon scattering cross section to be less than 7.0×10^{-44}cm^2 (3.8×10^{-44}cm^2 when combined with previous CDMS II results (4)) for a WIMP mass of 70 GeV/c^2 (Fig. 2.3).

The CDMS-II data were also analyzed under the hypothesis of WIMP inelastic scattering (5). In this model, which has been invoked to reconcile the annual modulation observed by DAMA/LIBRA (7) with null observations from other experiments, the WIMP-nucleon scattering occurs only via inelastic scattering with the dark matter particle transiting into an excited state. Thus, only WIMPs with sufficient energy to up-scatter into the excited state can scatter off nuclei in the detector. The mass splitting between the WIMP and its excited state is considered to be a free parameter; in order to explain the DAMA/LIBRA results, the splitting needs to be around 120 keV (6). Our analysis shows that CDMS II data disfavor all but a narrow region of the parameter space allowed by DAMA/LIBRA that resides at a WIMP mass of 100 GeV/c^1 and mass splittings of 90-140 keV (Fig. 2.4).

[6] Z. Ahmed et al. (CDMS Collaboration), Science **1186112** (2010).

[2] Z. Ahmed et al. (CDMS Collaboration), Phys. Rev. **D81**, 042002 (2010).

[3] Z. Ahmed et al., Phys. Rev. Lett. **103**, 141802 (2009).

[4] Z. Ahmed et al., Phys. Rev. Lett. **102**, 011301 (2009).

[5] D. Tucker-Smith, N. Weiner, Phys. Rev. **D64**, 043502 (2001).

[6] S. Chang, G.D. Kribs, D. Tucker-Smith and N. Weiner, Phys. Rev. **D79**, 043513 (2009).

[7] R. Bernabei et al., Eur. Phys. J. **C56**, 333 (2008).

[8] J. Angle et al., Phys. Rev. **D80**, 115005 (2009).

3 Search for the Neutrinoless Double Beta Decay with GERDA

L. Baudis, T. Bruch, A. Ferella, F. Froborg, R. Santorelli, M. Tarka

in collaboration with:
INFN Laboratori Nazionali del Gran Sasso LNGS, Institute of Physics, Jagellonian University,Cracow, Institut für Kern- und Teilchenphysik, Technische Universität Dresden, Joint Institute for Nuclear Research, Dubna, Institute for Reference Materials and Measurements, Geel, Max Planck Institut für Kernphysik, Heidelberg, Università di Milano Bicocca e INFN Milano, Milano, Institute for Nuclear Research of the Russian Academy of Sciences, Institute for Theoretical and Experimental Physics, Moscow, Russian Research Center Kurchatov Institute, Max-Planck-Institut für Physik, München, Dipartimento di Fisica dell`Università di Padova e INFN, Physikalisches Institut, Eberhard Karls Universität, Tübingen

(GERDA Collaboration)

GERDA is an experiment to search for the $0\nu\beta\beta$ decay in enriched ^{76}Ge detectors in Hall A of LNGS. The aim of GERDA Phase I and II is to reach a sensitivity of 270 meV and 110 meV for the effective Majorana neutrino mass, respectively. This is achieved by operating bare HPGe crystals in a large volume (70 m^3) of liquid argon (LAr), which serves as a passive shield (in Phase I) against the external radioactivity. The liquid argon is surrounded by a water shield instrumented with PMTs.

The construction phase of GERDA at LNGS is finished. At the end of 2009, the cryostat was cooled down, filled with liquid argon and, using an active cooling system, a stable temperature of 88 K was reached. The cryostat is thus ready for detector deployment. Several water drainage tests were performed with a partially filled water tank. These tests also provided an opportunity to test the PMTs and read out the veto detector with its final DAQ system. The detector commissioning lock has been installed in the clean room on top of the water tank in March 2010. The lock system will be ready for first detector deployment by the end of April. The first detectors to be deployed will be three non-enriched HPGe detector. These have been mounted in their low-mass holders and tested in liquid argon in the LNGS GERDA test facility. All three are showing excellent energy resolution and stable leakage currents at a few tens of pA, and are thus ready for deployment in the GERDA cryostat. After the planned tests with non-enriched detectors, the deployment of the enriched phase I detectors can start. Concomitantly, the R&D for the phase II detectors is proceeding.

Our group is responsible for the GERDA calibration system as well as for R&D on phase II detectors (in our case, on broad energy germanium detectors). Here we will present some highlights of our contributions to the calibration system during the past year.

Our Monte Carlo efforts were focused on simulating the gamma and neutron induced background from the calibration sources in their parking position for the final Phase I configuration. The geometry of the simulated Phase I detector array with the three calibration sources and their absorbers is shown schematically in Fig. 3.1. For three ^{228}Th calibration sources, with an activity of 20 kBq each, we obtain a conservative background rate of 3×10^{-5} events/kg·yr·keV and 2.4×10^{-5} events/kg·yr·keV in the region of interest for the neutrinoless double beta decay from the gammas and neutrons emitted by these sources, respectively. We have also studied

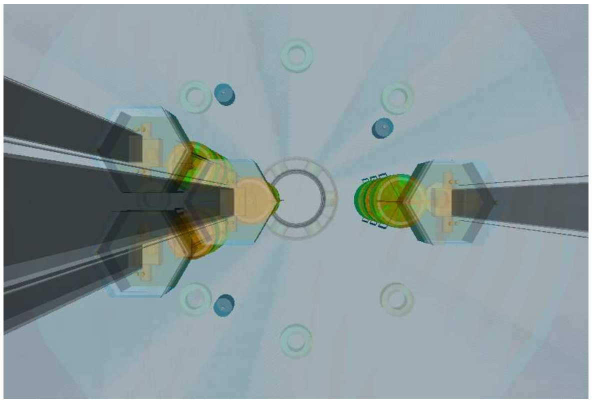

Figure 3.1: Top view of the Phase I detector array (four detector strings a three crystals each) with the three calibration sources along with their tantalum absorbers.

the background coming from neutron capture in detector and surrounding materials while the sources are in calibration and in parking position. Of all the produced isotopes, only ^{77}Ge is potentially dangerous. It decays with a $T_{1/2}$ = 11.3 h, a Q-value for the β-decay of 2.7 MeV, emitting several gammas with energies up to about 2.35 MeV. The decay of this isotope in the Ge crystals has been simulated, with a rate of 0.045 decays/kg·yr (given the short half-life, the production and the decay rates are in equilibrium). Assuming the measured neutron flux of 9×10^{-4} n/s·kBq and a total activity of 60 kBq, we obtain a background rate of 7.4×10^{-6} events/kg·yr·keV in the signal region.

The three tantalum rings for the sources and absorbers in their parking positions were mounted on the inside of the calibration source flange in January 2010. Subsequently, the lowering system for one of the calibration sources including absorber was successfully tested on site. Several lowering cycles down to 10 m ensured that there are no oscillations of the system even with relatively high moving speeds and that no problems occur during the insertion of the absorber into the tantalum ring. An upgrade of the manual lowering system to a motorized one is on its way.

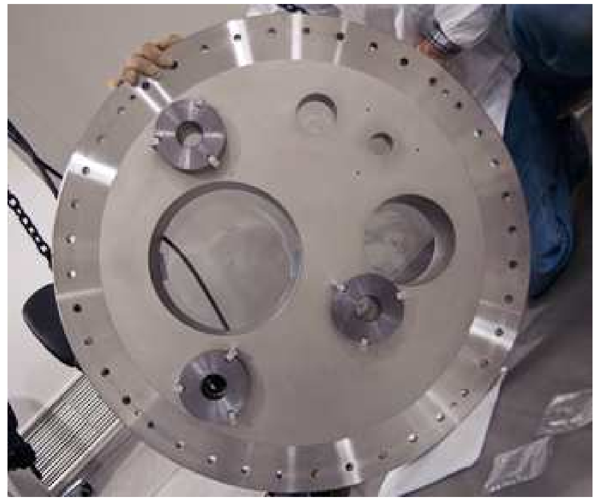

Figure 3.2: Calibration source flange with three tantalum rings mounted. The rings provide additional shielding against the gammas from the ^{228}Th sources in their parking positions.

The custom made ^{228}Th source (in collaboration with PSI) has been sent for a precise calibration to IRMM in Geel, along with a new, 25.5 kBq commercial source purchased from Eckert&Ziegler. Two new ^{228}Th custom sources have been produced: one of ~30 kBq source at PSI, and one of ~40 kBq source at Mainz. These sources have been sent for encapsulation to Eckert&Ziegler Braunschweig and will arrive at IRMM for a precise calibration by the end of April 2010. After the calibration procedure, the sources will be sent to LNGS where the neutron fluxes will be measured. To speed up this process, we are acquiring a LiI(Eu) neutron detector, to be installed at LNGS in a few weeks from now. ^{6}Li has a large cross section for neutron capture (940 barns for thermal neutrons), the relevant reaction being n + ^{6}Li $\rightarrow \alpha$ + ^{3}H + 4.8 MeV. The alpha and the tritium are stopped even in a thin layer of a LiI crystal and their full energy is detected. We are studying the optimal moderator thickness and shield configuration via MC simulations based on the Geant4 toolkit.

We have remeasured the n-flux of the first custom source, and in addition we have measured the flux of a commercial source from

Eckert&Ziegler, as well as the background with a ^{3}He counter at LNGS. The detector was inserted in a 6 cm diameter and 6 cm height polyethylene cylinder, which was wrapped in Cd foil and placed in a boron doped paraffin shield.

The neutron rates for the custom and commercial source were measured to be $(2.7\pm0.5)\times10^{-2}$ n/s and $(1.4\pm0.2)\times10^{-1}$ n/s, respectively. Considering that the sources had activities of 15 kBq and 43 kBq, we find a factor of about 1.7 difference in the n-rates. The ^{3}He counter was calibrated with an AmBe neutron source, with a flux of about (10 ± 1) n/s, giving a neutron rate of about 0.72 n/s; hence above numbers assumed an efficiency of about 0.07 for both the AmBe and ^{228}Th sources. A Monte Carlo simulation of the actual geometry and the AmBe n-spectrum, as well as the ThO_2 n-spectrum yielded overall efficiencies of 0.095 and 0.152, respectively. Using these efficiencies, the neutron rate for the custom source goes down to about 0.013 n/s, or, using the activity of 15 kBq, to 9×10^{-4} n/s·kBq. These results will be cross checked by using the LiI(Eu) detector to be installed at LNGS. The relative gamma activities of the two sources have been determined with the Gator HPGe detector, by placing them on a thin stainless steel tube 10 cm above the detector's endcap.

We have cross checked our predictions of the neutron fluxes from the commercial and custom sources, and estimated the systematic uncertainties coming from the $(\alpha$,n) cross sections. We have used the cross sections given in SOURCES, calculated the cross sections using EMPIRE, and also took measured cross sections from the EXFOR database. Since we find that there is quite some variation in the cross sections from these sources, in order to be conservative we have considered the upper and lower envelopes as a function of energy. We thus obtained following intervals for the neutron rates: $(4.5$–$7.3)\times10^{-4}$ n/s·kBq for a $^{228}ThO_2$ source, $(3.1$–$7.3)\times10^{-2}$ n/s·kBq for a ^{228}Th source embedded in $NaAlSiO_2$ and $(2.1$–$4.2)\times10^{-2}$ n/s·kBq for a ^{228}Th source in Al_2O_3. We are also investigating potential contaminations in the custom $^{228}ThO_2$ source and their contributions to the measured neutron flux.

We have started to work on the analysis scheme of the calibration data. The raw calibration data will go through the same analysis pipeline as all other GERDA data. The basic event information (waveforms etc, called Tier-1) will be written out as Majorana-Gerda-Data (MGD) objects. Subsequently, parameters such as energy, pulse rise-time, baseline noise, saturation etc (called Tier-2) will be extracted from the waveforms, using different reconstruction and noise-filtering algorithms. These algorithms, as well as the entire calibration analysis pipeline will be first tested on regular calibration data taken with a commercial ^{228}Th source and a natural HPGe detector in our lab at the Physik Institut. The goal of the calibration analysis pipeline is to calculate the position and energy resolution of the full energy peaks, as well as the number of events under each peak and to look at the stability of the calibration parameters with time. The calibration parameters for each detector and calibration run will be stored as MGD objects, providing a direct interface with the GERDA analysis software. A web interface will also be provided, that will be used for the visual inspection of the individual detector spectra and parameters, and the evolution of these parameters in time.

4 Search for Cold Dark Matter Particles with XENON

A. Askin, L. Baudis, A. Behrens, T. Bruch, A. Ferella, M. Haffke, A. Kish, A. Manalaysay, T. Marrodan-Undagoitia, R. Santorelli, M. Schumann

in collaboration with:
Columbia, INFN, University of Coimbra, University of Münster, MPIK Heidelberg, Rice, Subatech, Bologna, STJU, Nikhef

(XENON Collaboration)

The goal of the XENON (1) program is to detect Weakly Interactive Massive Particles (WIMPs), which may be responsible for the dark matter in our galaxy, via their collision with Xe nuclei. The current phase, XENON100, is a 161 kg liquid xenon time projection chamber (TPC) operated in the interferometer tunnel at LNGS in an improved XENON10 shield (2). It uses two arrays of low-radioactivity, UV-sensitive photomultipliers (Hamamatsu R8520-06-Al 1" square PMTs) to detect simultaneously the prompt (S1) and proportional (S2) light signals induced by particles interacting in the sensitive xenon volume, containing 62 kg of ultra pure liquid xenon (LXe). The remaining 99 kg of LXe are used as an active veto shield against background events; the LXe scintillation in the veto region is detected by additional PMTs of the same type. While the fiducial mass of XENON100 was increased by a factor of 10 with respect to the XENON10 experiment, the background has been demonstrated to be lower by a factor of 100 (Fig. 4.1). This was achieved through careful selection of ultra-low background materials, by placing the cryogenic system and high-voltage feedthroughs outside of the shield, by using the self-shielding power of xenon as well as the active LXe shield, by purifying the LXe for the radioactive ^{85}Kr with a dedicated column at LNGS, and by an improved passive shield.

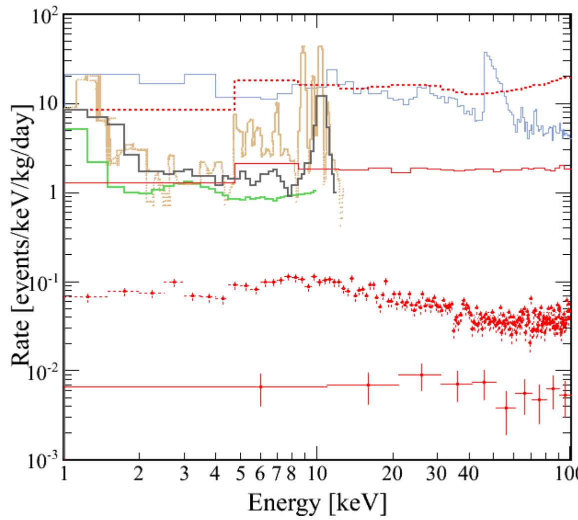

Figure 4.1: Raw event rate in the XENON100 experiment before (62 kg of LXe) and after (40 kg of LXe) a fiducial volume cut (lowest two red curves). This background rate is compared to the ones of XENON10 (before, and after a fiducial volume cut, upper two red curves), CRESST (blue), CoGeNT (brown), CDMS (grey) and DAMA (green).

The aim of XENON100 is to probe WIMP-nucleon cross sections down to $\sim 2\times10^{-45}$ cm^2 at a 100 GeV WIMP mass, after a life-exposure of 6000 kg days (200 days with 30 kg fiducial mass, taking into account the detector's acceptance). The dark matter search run started in January 2010, and the current raw exposure (with the data in the signal region being masked) is about 5000 kg days. The optimization of data analysis tools necessary to unveil this large data set is ongoing. The XENON100 experiment will continue running throughout 2010 and will either detect WIMPs, or set strong constrains on theoretical WIMP models. In either case, a larger scale experiment is needed and we have proposed the XENON1T detector (2.4 t of LXe in total, 1.1 t in the fiducial volume) (3) with the construction and the dark matter search phases to start by mid 2011 and 2014, respectively.

The current activities of our group focus on calibrations and stability monitoring of the XENON100 PMTs, position reconstruction algorithms based on neural networks, material screening with the Gator HPGe detector, Monte Carlo simulations of backgrounds and light-collection efficiencies, energy calibrations with various sources, as well as operations, data processing and analysis (along with Columbia, we are leading the analysis effort). We are also involved in R&D activities for XENON1T (3) and are leading the DARWIN (4) project. In the following, we can only highlight a small subset of our XENON related activities during the past year.

We have performed a first dark matter analysis on 11.2 live days of background data, taken during the commissioning of the detector in the period of October-November 2009. For this analysis, we have chosen a nuclear recoil energy interval between 9.7 – 31.6 keV (corresponding to 4 – 20 photoelectrons in S1, as determined in extensive detector calibration measurements) and a fiducial mass of 40 kg. We have applied simple data selection criteria, which were developed and tested on low-energy nuclear and electronics recoils from ^{241}AmBe and ^{60}Co sources, respectively. In particular, we require a two-fold PMT coincidence in a 20 ns window for the S1 signal and discard events which contain more than a single S1-pulse. For the S2 signal, we set a lower threshold of 300 photoelectrons, corresponding to about 15 ionization electrons, and require that events contain only one S2 pulse above this threshold, as WIMPs are expected to interact only once. We also discard events with energy deposits in the veto volume of the TPC and require that the width of the S2 pulse be consistent with what is expected from the inferred drift time due to the diffusion of the electron cloud (5).

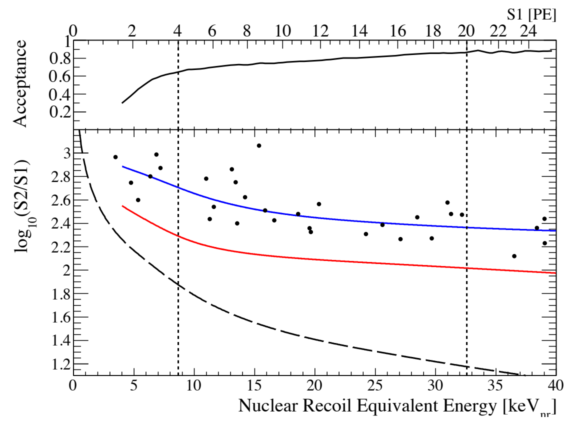

Figure 4.2: $\log_{10}$(S2/S1) (bottom) and cut acceptance (top) as functions of nuclear recoil energy. A total of 22 events are observed in the electron recoil band (the median is shown as the blue curve) in the energy region between 9.7 – 31.6 keV (inside the two vertical dotted lines) and no events are observed in the pre-defined signal acceptance region below the nuclear recoil median (red line) and above the S2 threshold (dashed line).

The distribution of events in $\log_{10}$(S2/S1) versus nuclear recoils energy is shown in Fig. 4.2. While a total of 22 electronic recoil events are observed, no WIMP candidates are seen in the pre-defined signal region.

Based on this null observation of signal candidate events and on standard dark matter halo assumptions, we derive an upper limit on the WIMP-nucleon elastic scattering cross section, taking into account the S1 resolution dominated by Poisson fluctuation. The resulting 90% confidence upper limit is shown in Fig. 4.3. This limit has a minimum at a cross section of 3.4×10^{-44}cm^2 for a WIMP mass of 55 GeV/c^2 for a spectrum-averaged exposure 170 kg·days. It excludes all parameter space for the interpretation of the CoGeNT and DAMA signals as being due to light mass WIMPs at 90% confidence (12). This initial results of XENON100, which uses only a short exposure, demonstrates the potential of this de

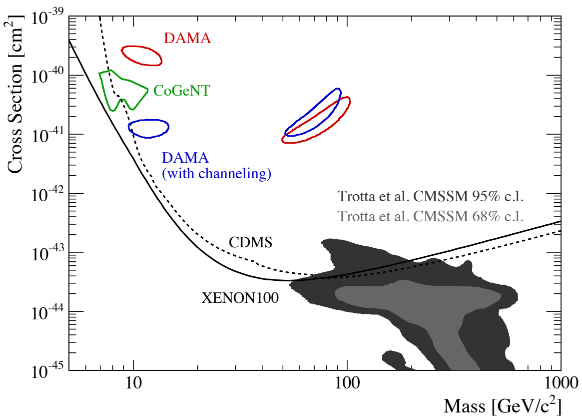

Figure 4.3:
90% confidence limit on the spin-independent elastic WIMP-nucleon cross section (solid line), together with the best limit to date from CDMS (dashed) [6], expectations from a theoretical model [7], and the areas favored by CoGeNT (green) [8] and DAMA (blue/red) (3σ, 90%) [9].

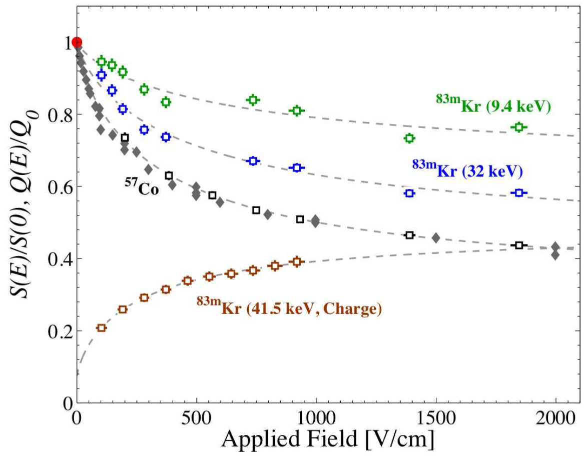

Figure 4.4: Field quenching of the scintillation light of ^{57}Co (black) and the two lines of ^{83m}Kr (9.4 keV and 32.1 keV, in green and blue, respectively). The bronw line shows the charge quenching for the sum of both ^{83m}Kr lines. The data from the literature [11] is shown as grey points.

tector to discover Galactic WIMP dark matter.

Using our small liquid xenon time projection chamber (Xürich) located in the Physik Institut, we have tested a new method for calibrating liquid xenon detectors based on a short-lived ($T_{1/2}$ = 1.8 h) ^{83m}Kr source. The ^{83m}Kr source has transitions at 9.4 keV and 32.1 keV, and, being a noble gas like xenon, it disperses uniformly in all regions of the detector. Even for low source activities, the existence of the two transitions separated by 154 ns provides a method of identifying the decays that is free of background. We found that at decreasing energies, the LXe light yield increases, while the amount of electric field quenching is diminished. Figure 4.4 shows the light yield as a function of the applied field, normalized to the zero field value, of the two ^{83m}Kr transitions and of the ^{57}Co 122 keV line.

We plan to use this method for a uniform calibration of the XENON100 detector at low energies at the end of the dark matter run. For the near future, we plan to use the Xürich prototype to measure the light and ionization yields of nuclear recoils at low energies.

[1] E. Aprile et al.(XENON Collaboration), New Astr. Rev. **49**, 289 (2005).

[2] E. Aprile, L. Baudis, PoS(idm2008) 018, arXiv:0902.4253 (2009).

[3] E. Aprile et al. (XENON Collaboration), XENON1T at LNGS proposal, April 2010.

[4] http://darwin.physik.uzh.ch/

[5] T. Doke, Nucl. Instrum. Methods **196**, 87 (1982).

[6] Z. Ahmed et al. (CDMS Collaboration), Science **1186112** (2010).

[7] R. Trotta et al., J. High Energy Phys. **12**, 024 (2008).

[8] C. E. Aalseth et al. (CoGeNT) (2010), 1002.4703.324

[9] C. Savage, G. Gelmini, P. Gondolo, and K. Freese, JCAP **3200904**, 010 (2009), C. Savage, K. Freese, P. Gondolo, and D. Spolyar, JCAP **0909**, 036 (2009).

[10] A. Manalaysay et al., arXiv:0908.0616 [astro-ph.IM], to appear in Rev. Sci. Instr. (2010).

[11] E. Aprile et al., Phys. Rev. Lett. **97**, 081302 (2006)

[12] E. Aprile et al.(XENON Collaboration), submitted to Phys. Rev. Lett. (2010).

5 A Cherenkov Telescope Array for Very High Energy Astronomy (CTA)

D. Florin, A. Gadola, R. Gredig, B. Huber, A. Manalaysay, S. Steiner, O. Steinkamp, U. Straumann, A. Vollhardt

in collaboration with: University of Geneva, EPFL Lausanne, ETH Zürich, Jagiellonian University Cracow, MPI für Kernphysik Heidelberg, University of Leeds, Universität Tübingen.

The full CTA collaboration consists of 115 institutes from 23 countries.

(CTA)

For electromagnetic radiation starting with the ultraviolet, the Earth's atmosphere becomes increasingly more opaque with increasing photon energy. As a result, astronomical observations in these regimes must be made from very high elevation, or from space. Telescopes such as FERMI (1) and Chandra (2) are thus deployed as satellites. However, as the photon energy increases further, through the tens of GeV range, telescopes are unable to contain the particles produced by the photon's impact with absorber materials, and direct observations are again not possible. Because of this, the energy range of several tens of GeV and above, Very High Energy (VHE) gamma radiation, is sometimes referred to as the "last electromagnetic window".

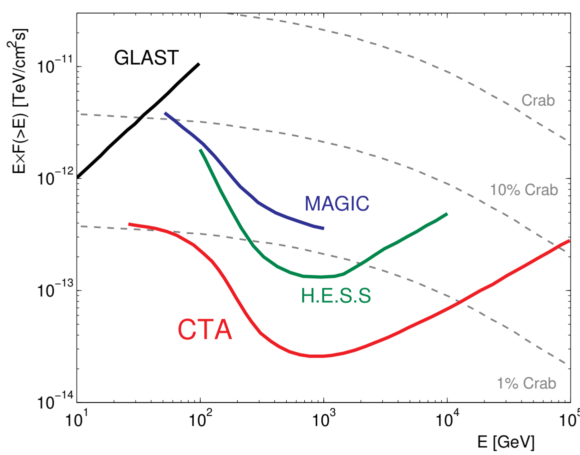

Figure 5.1: The sensitivity of several gamma ray observatories as a function of energy. The flux from the Crab nebula is shown as a reference.

Where atmospheric attenuation of photons generally hinders ground-based telescopes, this effect is actually employed in order to observe the VHE window. A VHE gamma ray will enter the atmosphere and produce an electron-positron pair. This pair, together sharing the energy of the initial gamma ray, will induce an electromagnetic shower in the upper atmosphere of many highly energetic, charged particles. Though these charged components of the shower may not reach the ground, they produce a cone of Cherenkov light that does reach the ground, and typically covers a circular area of roughly 250 m in diameter. The currently running MAGIC (3), H.E.S.S. (4), and VERITAS (5) observatories, which are Imaging Atmospheric Cherenkov Telescopes, operate by detecting this Cherenkov light and are able to reconstruct the energy and direction of the initial gamma ray. Figure 5.1 shows the sensitivities of MAGIC, H.E.S.S., and FERMI. The next generation of VHE telescopes, the Cherenkov Telescope Array (CTA), will improve upon these works by using optimized optical designs, improved light readout and electronics, and deploying a large array of such IACTs.

5.1 Active Mirror Control

CTA will consist of three complementary arrays of IACTs, differing in mirror size and number and distribution of telescopes. The Large Size Telescope (LST) array will use 20-30 m primary mirrors, the Medium Size Telescope (MST) array 10-12 m primary mirrors, and the Small Size Telescope (SST) array 5-8 m primary mirrors. Constructing single mirrors to precision shape and uniformity becomes increasingly difficult as the size of the mirror increases. Instead, the primary mirrors will be constructed from a collection of "mirror segments", which are smaller mirrors of 1-2 m^2 area, placed together to form a larger mirror. With such a segmented primary mirror, each segment can be individually oriented, correcting for any irregularities on large scales. The segmented nature of the MAGIC primary mirror can be seen in Fig. 5.2. H.E.S.S. and VERITAS likewise use segmented primary mirrors.

Throughout the lifetime of the telescope, it can become necessary to readjust the orientation of the mirror segments. This can occur because of varying weather conditions, or because the telescope frame flexes and bends when placed in different zenith positions. In order to accomplish this task in a systematic way, the CTA group at UZH is developing an Active Mirror Control (AMC) system. In

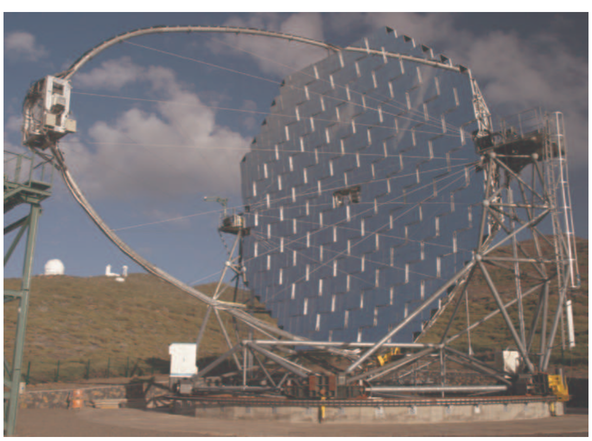

Figure 5.2: The MAGIC telescope.

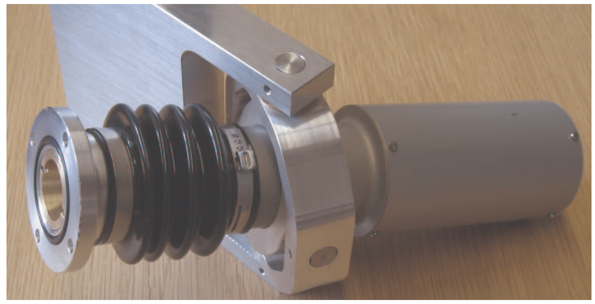

Figure 5.3: The AMC actuator.

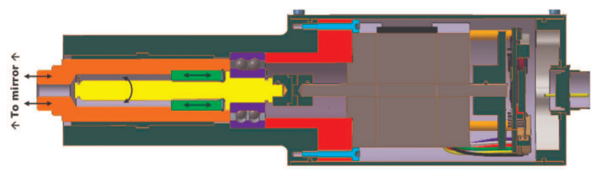

Figure 5.4: A cross sectional schematic diagram of the actuator, exposing the inner components.

this system, each mirror segment is attached to the main telescope frame at three positions. One attachment is a fixed point, while the other two attachments are movable actuators.

The two attachments that provide the motion, seen in Figs. 5.3 and 5.4, contain a step motor drive in the rear section, connected to a M8$\times$1 spindle (1 turn = 1 mm later motion), with a maximum range of 36 mm. The connection between the step motor and the spindle is such that it is able to make accurate changes in elevation as small as 15 μm.

The actuators provide a moving force of 400 N. The maximum applied forces, in case of hurricane-force winds, would not exceed 6000-7000 N, and the devices shown here have been tested and confirmed to hold more than 9000 N of extended applied force. The lifetime of CTA could be decades, exposing the hardware to varying weather conditions including rain, snow, wind, extremes of temperature, and extended use. The long term durability of these devices is therefore paramount.

An outdoor test stand has been constructed to test this long term durability of the AMC actuators. The test stand supports a "dummy mirror" of similar size and shape as a mirror segment, supported in three positions by a fixed point and two actuators. Figure 5.5 shows this test, with both actuators visible.

The actuators have been continuously cycled over 3 mm over the course of more than one year. This process has completed over 1.2 million cycles, an equivalent of roughly 30 years of telescope usage. Control of the actuators is performed wirelessly, over a ZigBee industry standard wireless protocol. Soon, the actuators will be removed from the test stand, disassembled, and inspected for mechanical wear.

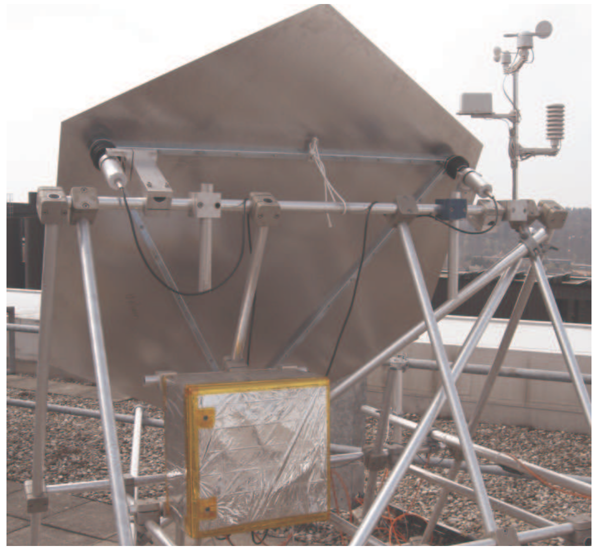

Figure 5.5: The test stand of the AMC actuators. The actuators have been cycled over 1.2 million times, equivalent to roughly 30 years of use.

5.2 Light Concentrators

The light that reflects from the telescope's primary mirror will be concentrated at the mirror's focal point, and is therefore the location of the camera. In order to allow for a field of view of 5°, the camera must cover an area 1-2 m in diameter. Obtaining 100% coverage of such an area with photodetectors alone is costly and impractical. Instead, the effective coverage of each single photodetector is enhanced by a Light Concentrator (LC), which focuses the flux of photons incident upon a large area onto a smaller area. Typical LC designs consist of a set of mirrors arranged in a hollow cone shape. The shape of the cone can be parabolic, or they can take the shape of a tilted parabola, often called a Winston Cone. In addition to a hollow cone, a solid LC can be constructed which relies on total internal reflection to accomplish the concentration, seen in Fig. 5.6. A solid LC has the advantage that, due to refraction at the entrance, larger entrance area to exit area ratios are allowed than for a hollow cone of similar size.

Figure 5.6: A collection of solid, refracting light concentrators constructed at UZH.

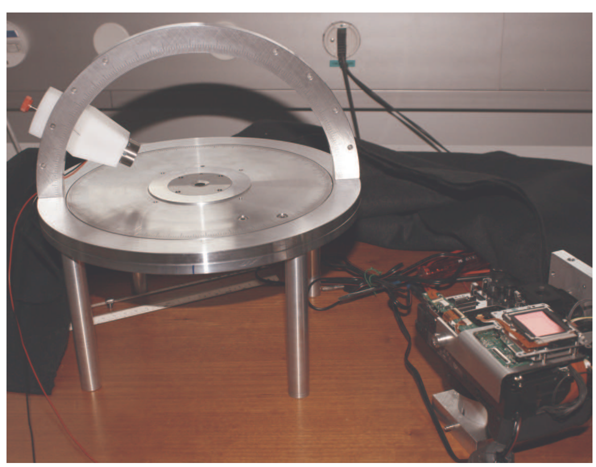

Figure 5.7: The test station for measuring the transmission properties of the LC array.

A test station has been constructed at UZH to measure the performance of various LC

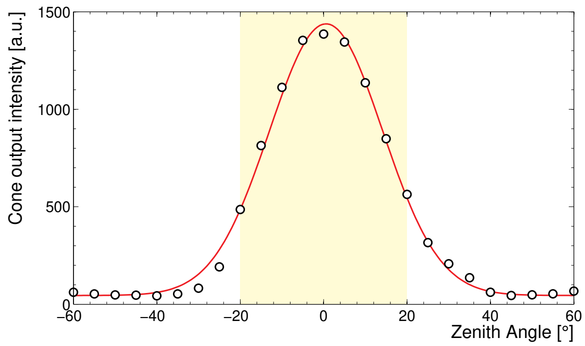

Figure 5.8: The response of the parabolic light concentrators as a function of zenith angle of the light source, relative to the intensity at 0°. The angle subtended by the primary mirror, ±20°, is indicated by the shaded yellow region.

designs, seen in Fig. 5.7. The test stand holds an array of five LCs, the entrance of one cone is exposed to light, while the entrances of the remaining four LCs are blocked. This is done to study possible cross-talk effects between neighboring LCs. The exit faces of all five cones are optically coupled to a Complementary Metal-Oxide-Semiconductor (CMOS) photo sensor. This sensor is most commonly used in digital cameras. The test stand has a mounting device for a light source that can be adjusted to illuminate the LC from any direction within the hemisphere that lies above the entrance face of the LC.

The ability of the LCs to collect and concentrate the light that crosses the cone entrance is an important feature, but also the behavior of this feature as a function of the incoming angle of the light. Two competing effects demand attention to this behavior. First, the LC will collect light from all segments of the primary mirror, which subtends $\pm\sim 20°$ at the position of the camera. The LC must allow light from all mirror segments or else the field of view is compromised. Second, extraneous light not coming from the primary mirror might also be incident on the LC. Naturally, this light is of no scientific importance and presents only background. This feature demands a high attenuation of light at zenith angles larger than ±20°. Figure 5.8 shows the light acceptance as a function of the zenith angle of our prototypes measured with the test setup described above.

5.3 FlashCam

The CTA group at UZH also contributes to the development of a fully digital photon sensor readout called FlashCam, together with the University of Geneva, EPFL Lausanne, ETH Zürich, Jagiellonian University Cracow, MPI für Kernphysik Heidelberg, University of Leeds, and University of Tübingen. A fast ADC will allow the storage of data continuously in a digital ring buffer, replacing the classical analog ring buffer electronics. Such a digital camera will make it possible to use all information of the full precision data for triggering purposes. The implementation in Field-Programmable Gate Array (FPGA) devices will allow for reliable and flexible calibration and other online calculations.

Each analog channel is sampled by two ADCs. A 250 MS/s high gain channel is used to determine accurate timing and low threshold trigger information, while a 80 MS/s low gain channel allows for accurate measurement of large signal amplitudes. Monte Carlo (MC) simulation studies, together with an ADC hardware evaluation, have shown that with such a system the full VHE gamma ray shower information can be determined, while the prices for the ADCs are still affordable, assuming a total of about 100'000 readout channels to be equipped in the final CTA MST system.

This requires a sampling clock with a very good phase stability over the whole CTA system. The clock generation and distribution possibilities are studied presently by the electronics workshop.

One of the critical items of the telescope simulation consists of the electronic coupling from the photon sensor to the ADC. Therefore a laboratory system has been set up to record a photomultiplier signal from a fast pulsed laser diode with a selection of different anti-aliasing filters, different sampling frequencies, and realistic cabling. A preamplifier, which fits to the signal specifications and allows for gain adjustment has been developed by the electronics workshop. The measured data was compared to the simulation and found to be in good agreement.

The group is also looking into trigger options and their implementations in an FPGA. Standard triggering ideas for such telescopes use the summed amplitude of all pixels to form the trigger. At high gamma ray energies, this technique is adequate, but signals from low gamma ray energies are inundated with ambient light hitting the camera, called Night Sky Background (NSB). In order to deal with this, triggering schemes involving clustering algorithms that are able to distinguish a valid Cherenkov pulse (which is highly clustered) from NSB (which is uniformly distributed) are being studied and characterized. Such triggering algorithms are feasible only in the context of a fully digital system.

[1] A. Neronov and I. Vovk, Science **328**, 73 (2010).
[2] N. S Brickhouse et al., Astrophys. J. **710**, 1835 (2010).
[3] J. A. Coarasa et al., MAGIC Collaboration, J. Phys. Soc. Jap. Suppl, **77B**, 49 (2008).
[4] B. Opitz et al., HESS Collaboration, AIP Conf. Proc. **1223**, 140 (2010).
[5] D. Hanna et al., VERITAS Collaboration, J. Phys. Conf. Ser. **203**, 012118 (2010).

6 Testing lepton universality, the $\pi \to e\overline{\nu}/\, \pi \to \mu\overline{\nu}$ branching ratio

P. Robmann, A. van der Schaaf, U. Straumann, P. Truöl and A. Palladino (guest from PSI/Virginia)

in collaboration with: University of Virginia, Charlottesville, USA; Institute for Nuclear Studies, Swierk, Poland; JINR, Dubna, Russia; Paul Scherrer Institut, Villigen, Switzerland and Rudjer Bošković Intitute, Zagreb, Croatia

(PEN Collaboration)

Fundamental fermions (quarks and leptons) are replicated in three families which appear to have a universal coupling strength g to the gauge bosons mediating the electroweak interaction.

Lepton universality is constrained best by the observed value (1) of the branching ratio

$$R^{\rm exp}_{e/\mu} \equiv \Gamma_{\pi\to e\overline{\nu}(\gamma)}/\Gamma_{\pi\to\mu\overline{\nu}(\gamma)} = 1.230(4)\times 10^{-4}\,. \tag{6.1}$$

The PEN experiment (2) aims at reducing the uncertainty in 6.1 by an order of magnitude which would bring it into the region of the accuracy of the Standard Model prediction. The main component of PEN is a pure-CsI crystal ball shown in Fig. 6.1. Further details on the theoretical motivation and a description of the PEN detection system can be found in the Annual Reports 2006/7.

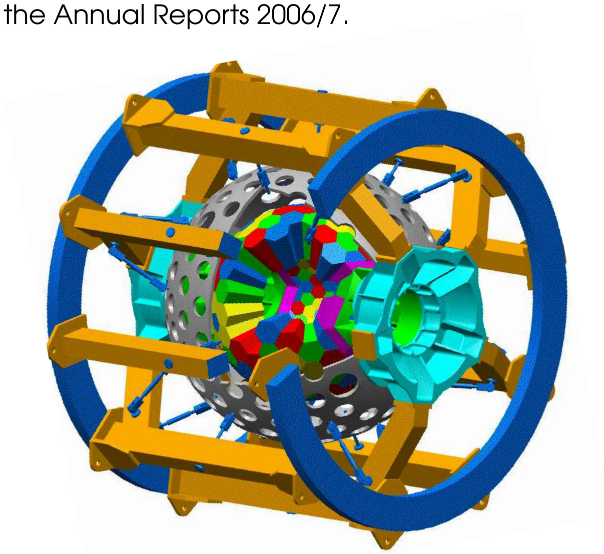

Figure 6.1: The 220 element $\sim 3\pi$ Sr pure CsI spherical electromagnetic calorimeter (see also Fig.6.2).

Whereas $\sim$ 98% of the $\pi \to e\overline{\nu}(\gamma)$ decays are unambiguously identified by their positron energy, in the remaining $\sim$ 2% the observed energy leaks into the region below $m_\mu c^2/2$ dominated by $\pi \to \mu\overline{\nu}(\gamma)$ followed by $\mu \to e\nu\overline{\nu}(\gamma)$. For this reason it is crucial to know (measure and/or simulate) the full $\pi \to e\overline{\nu}(\gamma)$ energy distribution. For this purpose $\pi \to \mu\overline{\nu}$ events have to be suppressed by many orders of magnitude and the remaining contribution has to be estimated by an analysis of the $\pi \to e$ time distribution. The suppression is based on the observation of the intermediate 4.1 MeV muon. In order to find the muon for very short pion or muon decay-times and for events in which particles decay before stopping a very precise analysis of the signal waveform from the active pion stopping target has been developed (see last years Annual Report).

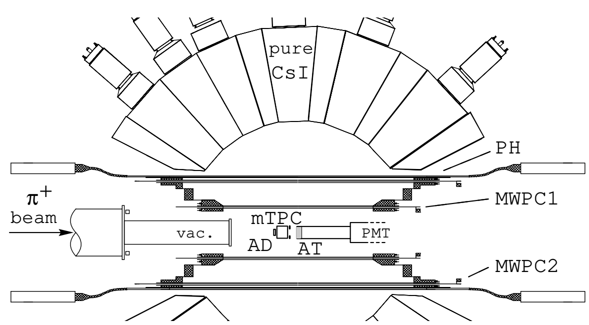

Figure 6.2: PEN setup in the configuration of 2009. CsI: electromagnetic calorimeter (see also Fig. 6.1), PH: plastic scintillator hodoscope, MWPC1/2: cylindrical multi-wire proportional chambers for e^+ tracking, AD: active degrader, mTPC: mini time-projection chamber for π^+ tracking, AT: active target.

6.1 The new mini-TPC beam tracker

PEN has been taking data during 2008 and 2009 and a final measuring period has been scheduled for the year 2010. During these years, improvements were made, particularly to the beam tracking detector. Figure 6.2 illustrates the setup used in 2009. The signals of all beam detectors are recorded with waveform digitizers. For 2010 the mini-TPC has been replaced by a thin-walled version which will allow us to move the detector closer to the target.

The mini-TPC gives four space points with a resolution of 0.3 mm in vertical (drift) direction and 1 mm in horizontal direction using charge division (see also Fig. 6.3).

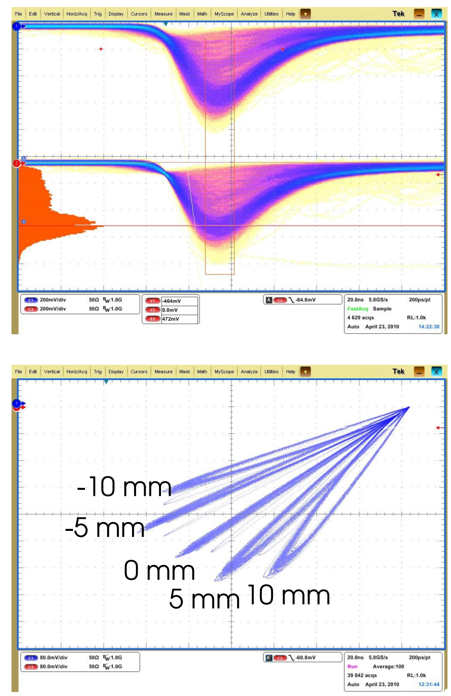

Figure 6.3: Oscilloscope pictures of the signals observed at both ends of a resistive wire of the mini-TPC. The detector was irradiated with a collimated ^{55}Fe source. Both the individual signals (top) and their correlation (bottom) are shown.
In the bottom view the source position along the wire was varied in steps of 5 mm. Signals follow a loop starting and ending at the origin. Central hits result in identical signals which thus populate the diagonal. For off-center hits the relative amplitude deviates most from unity during the rise time. For later times the position dependence fades away so the loops return to the diagonal. For this reason the off-line position algorithm only uses the first ~30 ns of the recorded wave forms.

6.2 Target waveform analysis

As discussed in great detail in the previous report the target waveform is fit with two different hypotheses. A 2-peak fit assumes a $\pi \to e\nu$ decay and a 3-peak fit assumes $\pi \to \mu\nu$ followed by $\mu \to e\nu\overline{\nu}$. In both fits constraints are made on the signal amplitudes (deposited energies) which allows a clean separation even when signals appear simultaneously.

Figures 6.4 and 6.5 demonstrate the superb separation obtained with the 2008 data.

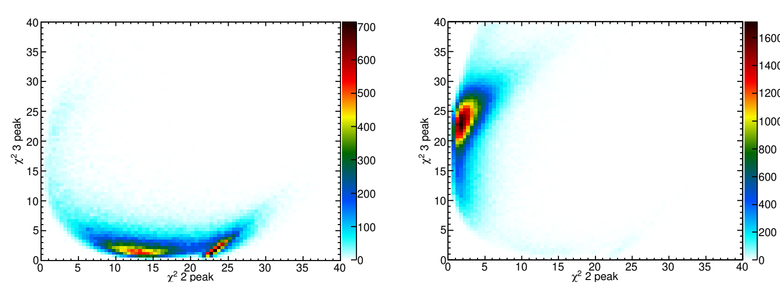

Figure 6.4: Distributions of χ^2 values from 2-peak and 3-peak fits to the target wave form for two regions of positron energy. Left: below 60 MeV selects an almost pure sample of $\pi \to \mu \to e$ events.
Right: above 60 MeV selects a pure sample of $\pi \to e\nu$ events.

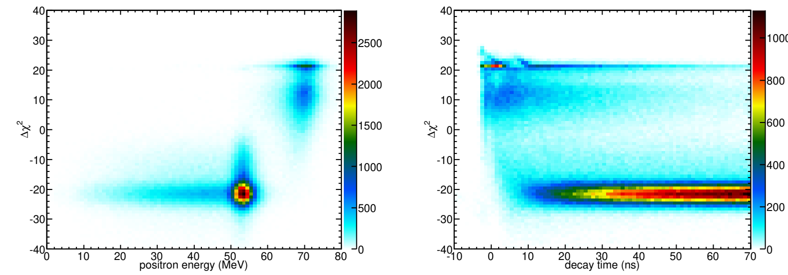

Figure 6.5: The difference in χ^2 of the two fits versus positron energy (left) and decay time (right). The energy region below 50 MeV was pre-scaled by 1:64 in the trigger for data readout.

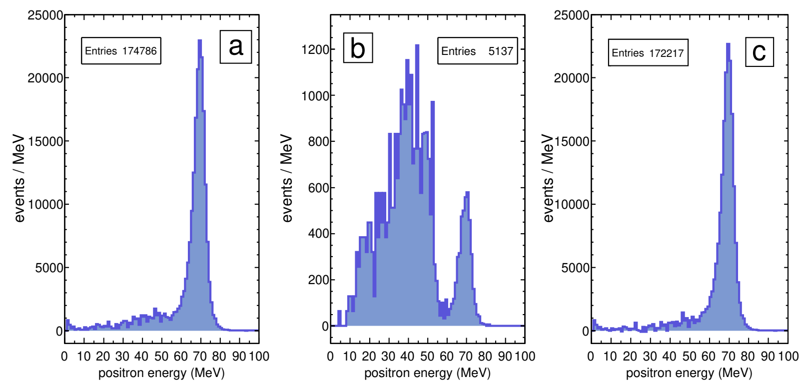

Figure 6.6: The $\pi \to e\nu$ positron energy response function from 2008 data. Events are selected with good 2-peak fit. Panel a: events with decay times below 30 ns, panel b: events with decay times 140 - 200 ns, and panel c: the $\pi \to e\nu$ component in (a) obtained by subtracting muon background extrapolated from (b). A small prompt background remains at very low energy.

6.3 $\pi \to e\nu$ positron energy response

As mentioned in the introduction, the major source of systematic errors resides in the knowledge of the $\pi \to e\nu$ energy distribution in the overlap region below 52 MeV. Even when selecting pion decays within 50 ns and even when $\pi \to \mu\nu$ can be suppressed by four orders of magnitude with the help of the target waveform analysis the overlap region contains similar contributions from the two decay modes and an analysis of the time distribution is required to disentangle them. The analysis is complicated by the contributions from $\pi \to \mu\nu$ decays just before the pion would have stopped. Figure 6.6 shows the actual state of the art.

6.4 Outlook

Off-line calibration procedures have been finalized and a sophisticated likelihood analysis based on multi-dimensional probability density functions is being developed. In addition to the two main signal processes, a series of other event types have to be included: radiative decays, in-flight decays, various types of accidental coincidences and pion reactions have been identified so far. It is our aim to determine all probability density functions as much as possible from the measurement but simulations will have to reproduce these results and extrapolate them where necessary.

Whereas data taking will be finished in August 2010 we forsee at least one more year before the result from a blind analysis will become available.

[1] G. Czapek et al., Phys. Rev. Lett. **70** (1993) 17; D. I. Britton et al., Phys. Rev. Lett. **68** (1992) 3000.

[2] PEN Collaboration, PSI experiment R-05-01, D. Pocanic and A. van der Schaaf, spokespersons.

7 Study of Coulomb-bound πK-pairs

C. Amsler, A. Benelli[1], C. Regenfus, and J. Rochet

in collaboration with:
CERN, Czech Technical University, Institute of Physics and Nuclear Physics Institute ASCR (Czech Republic), Laboratori Nazionali di Frascati, Messina University, Trieste University, KEK, Kyoto Sangyo University, Tokyo Metropolitan University, IFIN-HH (Bucharest), JINR (Dubna), Skobeltsin Institute for Nuclear Physics (Moscow), IHEP (Protvino), Santiago de Compostela University, Bern University.

(DIRAC-II Collaboration)

The goal of the DIRAC experiment at CERN (PS212) is to measure the lifetime of electromagnetically bound $\pi^+\pi^-$ or $K^\pm\pi^\mp$ pairs (the so-called $\pi\pi$- and πK- "atoms"). Their mean lives are directly related to the isospin 0 and 2 s-wave scattering lengths (a_0 and a_2) for $\pi\pi$, and to the corresponding isospin 1/2 and 3/2 scattering lengths ($a_{1/2}$ and $a_{3/2}$) for πK. More precisely, the mean life is related to the absolute value of the difference between the two scattering lengths (1), a quantity that was calculated within the framework of Chiral Perturbation Theory (ChPT) with high precision, 1.5% for $|a_0 - a_2|$ (2), and 5.5% from Roy-Steiner dispersion-relations for $|a_{1/2} - a_{3/2}|$ (3). Thus a measurement of the mean life from DIRAC provides a valuable test of low-energy QCD concepts involving the u- and d-quarks for $\pi\pi$, and extending to the s-quark for πK. The expected mean life of πK-atoms is about 3.7 fs (1), with rather large uncertainties.

Results for $\pi\pi$-atoms have been published earlier by the DIRAC-I collaboration (4). A mean life of $2.91^{+0.49}_{-0.62}$ fs was measured, in good agreement with predictions from ChPT. We shall focus here on πK-atoms (DIRAC-II) in which we are mainly involved.

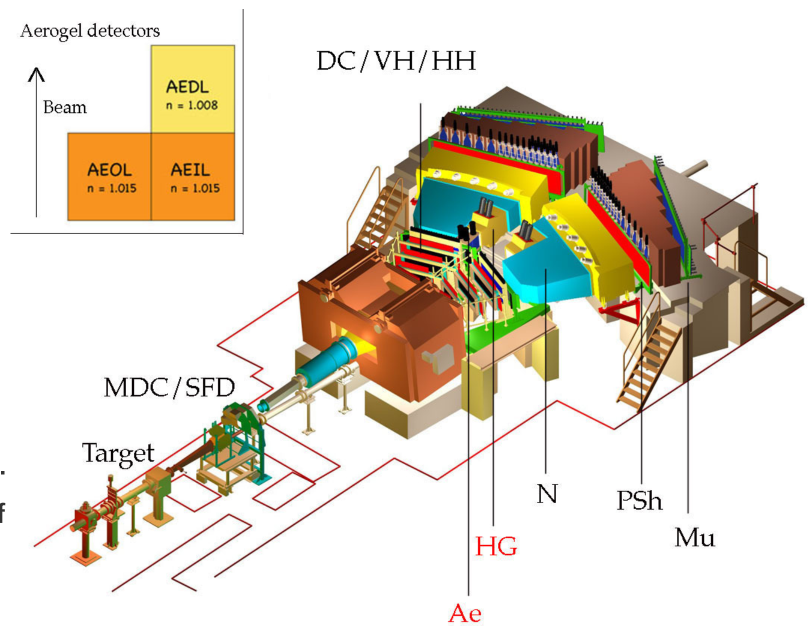

Figure 7.1: DIRAC-II spectrometer:

MDC	**microdrift chambers,**
SFD	**scintillator fibre detector,**
DC	**drift chambers,**
VH, HH	**vertical and horizontal scintillation hodoscopes,**
PSh	**preshower,**
Mu	**muon counters,**
Ae	**aerogel,**
HG	**heavy gas and**
N	**nitrogen Čerenkov counters.**

The inset shows the arrangement of the three aerogel modules.

[1] Visitor from JINR, Dubna

A sketch of the DIRAC-II spectrometer is shown in Fig. 7.1. The 24 GeV/c proton beam from the PS impinges on a thin Pt- (or Ni-) target. The secondary particles emerging from the target in the forward direction are analyzed in a double-arm magnetic spectrometer. Positive particles are deflected into the left arm, negative ones into the right arm. Electrons and positrons are vetoed by N_2-Čerenkov detectors and muons by their signals in scintillation counters behind the steel absorbers. Particle identification is performed by the heavy gas (C_4F_{10}) and aerogel Čerenkov counters. The former detects pions (but not kaons), while the latter also detects kaons (but not protons).

Our group has developed and built a large volume (37ℓ) aerogel Čerenkov counter in the left arm (positive charges) for kaon detection and proton suppression (5), and the heavy gas system (6). The aerogel detector consists of three independent modules (inset of Fig. 7.1). Two of them (AEIL close to the proton beam and AEOL at larger angles) have refractive index $n = 1.015$ and are used for kaons between 4 and 5.5 GeV/c. At small angles the momenta increase up to 8 GeV/c and hence AEDL, with the lower index $n = 1.008$, is used to suppress fast protons that also fire AEIL.

The measurement of the mean life is as follows: Atoms produced in the forward direction are ionized while crossing the target, leading to "atomic" $\pi^{\pm}K^{\mp}$-pairs with very small relative momenta between the kaons and the pions (typically $<$ 3 MeV/c in the c.m.s system). Since ionization competes with annihilation into $K^0\pi^0$ (or $\overline{K}^0\pi^0$), the number of atomic pairs grows with increasing lifetime. Unbound πK-pairs ("Coulomb-pairs") which interact electromagnetically are also produced. The number of produced atoms is related to the number of Coulomb-pairs (7), For relative momenta below 3 MeV/c the ratio of the number of produced atoms to that

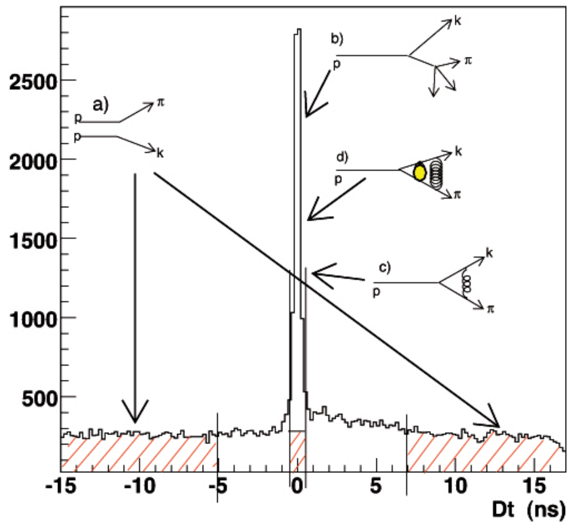

Figure 7.2: Distribution of the $\pi - K$ time difference for (a) accidentals, (b) non-Coulomb pairs, (c) Coulomb-pairs, and (d) πK-atoms.

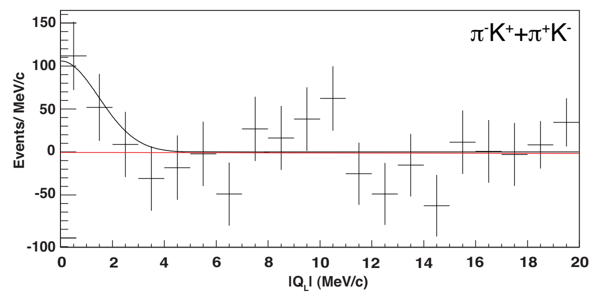

Figure 7.3: Residuals between data and the fitted background for π^-K^+ and π^+K^- from the 2007 data. A Gaussian fit has been applied (solid line) to illustrate the distribution of atomic-pairs.

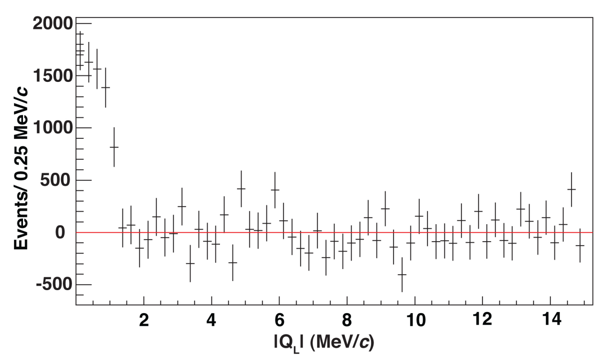

Figure 7.4: Residuals between data and the fitted background for $\pi^+\pi^-$ (from ref. [9]).

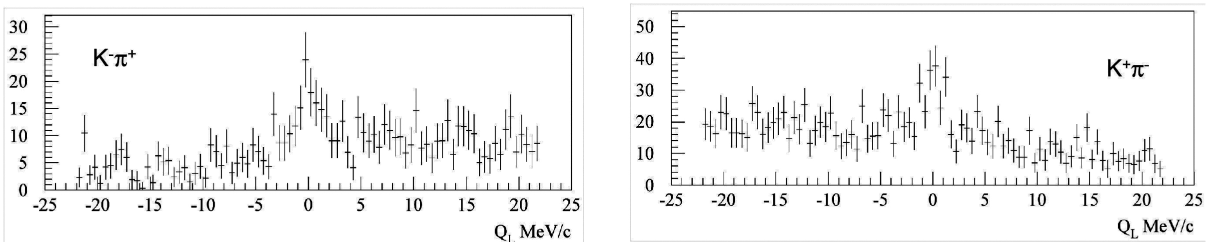

Figure 7.5: Q_L distribution for selected π^+K^- and π^-K^+ events. The peak at small $|Q_L|$ is due to Coulomb- and atomic pairs (see text).

of Coulomb-pairs is around 60%. Detection efficiencies are taken into account by Monte Carlo simulation. The background stems from non-Coulomb pairs due to K and π mesons from long-lived resonances (and therefore do not interact), and from accidentals (pairs produced by two different proton interactions). Figure 7.2 shows a distribution of the time difference between particles in the two arms of the spectrometer.

The DIRAC collaboration observed πK-atoms for the first time with the data collected in 2007 (Figs. 7.3 and 7.4). For comparison we also show the results for $\pi^+\pi^-$-atoms from the same data runs. We have detected 173 $\pm$ 54 πK atomic pairs (8), thus with a statistical significance of 3.2σ. However, the evidence for πK-atoms was strengthened by the simultaneous observation of Coulomb-pairs from which the fraction of expected $bound$ pairs could be calculated (7). The latter was in excellent agreement with the number of observed atoms. This result led to a lower limit for the mean life of πK-atoms of 0.8 fs in the 1s-state, at a confidence level of 90%, which could be translated into an upper limit of $|a_{1/2} - a_{3/2}| <$ 0.58 m_π^{-1}. Details can be found in ref. (8; 9; 10).

For the 2007 results we had used only the detectors downstream of the magnet. The kaon selection is described in detail in ref. (8; 9). Two planes of scintillator fibers (SFD, see Fig. 7.1) and 16 planes of micro drift chambers (MDC) are now available to determine the interaction point in the target with better precision. We can thus select events with relative transverse momentum smaller than 4 MeV/c, thus reducing the background by typically a factor of 4.

Figure 7.5 shows the distribution of the relative longitudinal momentum Q_L for πK-pairs for a sample of the data, using the SFD planes. The enhancement at low $|Q_L|$ is due to Coulomb- (and atomic) pairs. The background for larger $|Q_L|$ is substantially lower than for data without SFD information (8).

In the 2007 runs ADCs for the aerogel detectors were not available. ADC and TDC information from the three aerogel modules is now recorded. To determine the light yield and detection efficiency for kaons we first selected a pure pion beam in the left arm by applying time-of-flight cuts, and also requiring a signal in the heavy gas counter. The ADC/TDC response was then analyzed as a function of pion momentum and used to estimate the response to protons. The prediction was compared to data from a pure proton beam in the left arm, applying a time-of-flight cut, requiring no signal in the heavy gas counter, and a $\pi^- p$ invariant mass consistent with the decay of a Λ-hyperon. Prediction and measurements were found to be in very good agreement. Hence the detection efficiency for kaons with the aerogel and the contamination from protons could be estimated reliably.

Figure 7.6 shows the light yield for kaons and protons from the "heavy" aerogel (AEOL) in the relevant momentum range between 4.0 and 5.5 GeV/c. For example, kaons can be identified with an efficiency of 0.95 by requiring at least 2 photoelectrons, while the contamination from protons is 0.05. The results for the AEIL are similar (Fig. 7.7). Above 5.5 GeV/c we also used the information from the "light" aerogel (AEDL) for which we obtained an average kaon efficiency of 0.95 above 5 GeV/c, while the proton contamination rose from 0.15 at 5 GeV/c to a worrying $\simeq$ 100% above 7 GeV/c, due to the low light yield of this detector. However, a computer simulation shows that even a proton contamination at this level is not problematic. Figure 7.8 shows the $|Q_L|$ distribution for simulated $\pi^- p$ events, assuming in the reconstruction that the proton is in fact a kaon. No enhancement is observed around $Q_L = 0$, and therefore the proton contamination is automatically taken into account when subtracting the background.

We collected more data in 2009. The Zurich group is currently analyzing the 2008 data sample using the new SFD detectors (provided by our Japanese collaborators), and is also implementing the corresponding Monte Carlo simulation. The SFD should improve the transverse momentum resolution from 3 MeV/c to 1 MeV/c. Data taking for DIRAC-II has been approved at least until the end of 2010 by the CERN committees, at which time we should achieve a significance of 5 – 6 standard deviations on the evidence for πK-atoms and, correspondingly, an accuracy of 40% on the lifetime (or 20% on the scattering lengths). This is a significant improvement on current knowledge, but somewhat more modest than expected, mainly due to a one year beam magnet breakdown, and the low proton beam flux that was finally delivered.

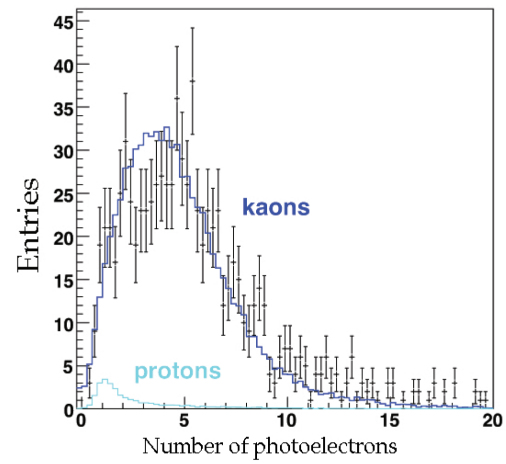

Figure 7.6:
Light yield in photoelectrons from the aerogel Čerenkov counters AEOL for kaons and protons.

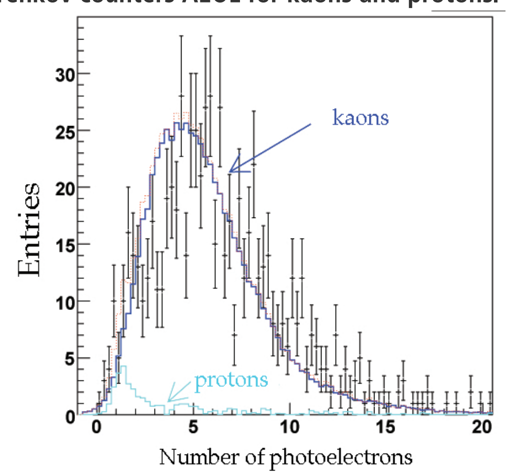

Figure 7.7: As in Fig. 7.6 for the AEIL counters

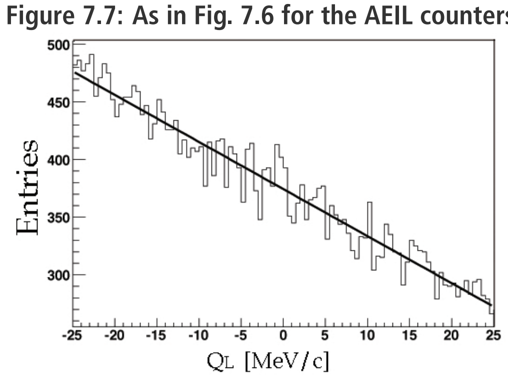

Figure 7.8:
Distribution of the longitudinal momentum difference Q_L for $p\pi^-$ events assumed to be $K^+\pi^-$.

[1] J. Schweizer, Phys. Lett. **B587** (2004) 33

[2] G. Colangelo *et al.* Nucl. Phys. **B603** (2001) 125

[3] P. Büttiker, S. Descotes-Genon, B. Moussallam,
Eur. Phys. J. **C33** (2004) 409

[4] B. Adeva *et al.* (DIRAC Collaboration),
Phys. Lett. **B619** (2005) 50

[5] Y. Allkofer *et al.*,
Nucl. Instr. Meth. in Phys. Res. **A582** (2007) 497;
Y. Allkofer *et al.*,
Nucl. Instr. Meth. in Phys. Res. **A595** (2008) 84

[6] S. Horikawa *et al.*,
Nucl. Instr. Meth. in Phys. Res. **A595** (2008) 212

[7] L. L. Nemenov, Sov. J. Nucl. Phys. **41** (1985) 629;
L. Afanasyev and O. Voskresenskaya,
Phys. Lett. **B453** (1999) 302

[8] B. Adeva *et al.* (DIRAC Collaboration),
Phys. Lett. **B674** (2009) 11

[9] Y. Allkofer, PhD Thesis, University of Zurich (2008)

[10] C. Amsler, Proc. of Science PoS EPS-HEP (2009) 078

8 Particle Physics at DESY/HERA (H1)

K. Müller, K. Nowak, P. Robmann, U. Straumann, and P. Truöl

in collaboration with:
C. Grab and T. Zimmermann, Institut für Teilchenphysik der ETH, Zürich, S. Egli, M. Hildebrandt, and R. Horisberger, Paul Scherrer Institut, Villigen, and 38 institutes outside Switzerland

(H1 - Collaboration)

The analysis of the data taken by the H1 experiment during 15 years of running is still ongoing. Many analyses were completed using the full data set with an integrated luminosity of 183 pb^{-1} for collisions with electrons and 291 pb^{-1} for collisions with positrons. In addition, first analyses are published which combine the measurements of H1 and ZEUS (1; 2). The deep insight into the structure of the proton at very small distances which result from the precise measurements of H1 and ZEUS has a major impact on the LHC experiments. The final months of HERA operation were devoted to collisions at lower proton energies: 6.2 pb^{-1} and 12.4 pb^{-1} were collected with 27.4 GeV positrons colliding with 575 or 460 GeV protons, respectively. This data has been used for a first direct measurement of the longitudinal structure function F_L, an analysis which was presented for an extended kinematical range at last years conferences.

Fourteen publications (1-14) and several contributions to the 2009 Europhysics Conference on High Energy Physics in Krakow (15,16,18-23) resulted from the continuing effort in the analysis of the H1 data. New results, partly preliminary (24), concern the following topics:

- Direct measurement of the longitudinal structure function F_L in an extended range of Q^2 (19) and for diffractive events (21).
- Precise determination of the neutral electroweak current cross sections over a large range of Q^2 as well as the extraction of the parton density functions (PDF) (1; 12; 14) and the extraction of the charm and beauty contribution to the proton structure function (3; 7).
- Determination of the running coupling constant α_s in jet production (11; 15).
- Production of ρ, K^{*0} and ϕ-mesons (16) and prompt photons (4) at very low Q^2 (photoproduction).
- Final combined analysis of multi-lepton production (6) and production of isolated leptons with large missing momentum (2).
- Search for states and interactions outside the Standard Model (SM), such as single top production (9), excited quarks (10) or squarks (18).
- Measurement of the cross sections and hadronic final state of diffractive events (16; 20; 21; 22)

In the past years our analysis effort concentrated on events with isolated photons produced in either photoproduction ($Q^2 \approx 0$) (25),(26), shortly discussed below (Sec. 8.3), or deep inelastic scattering (DIS, $Q^2 > 4$ GeV^2) (27),(28). Both analyses are finished and have been published. They have been presented in detail in previous annual reports (29). Our involvement in the analysis of prompt photons will continue though with emphasis on less isolated photons (Katharina Müller). One of us (Peter Truöl) continues to serve as referee in the heavy flavour working group.

8.1 Measurement of the longitudinal structure function F_L

The inclusive neutral current DIS cross section at low Q^2 can be written in its reduced form as

$$\begin{aligned} \sigma_r &= \frac{d^2\sigma}{dxdQ^2} \times \frac{Q^4 x}{2\pi\alpha(1+(1-y)^2)} \\ &= F_2(x,Q^2) - \frac{y^2}{1+(1-y)^2} F_L(x,Q^2) \end{aligned} \quad (8.2)$$

Here, y is the inelasticity of the scattering process. The cross section is determined by two independent structure functions F_L and F_2 which are related to the $\gamma^* p$ absorption cross sections of longitudinally and transversely polarised photons, σ_L and σ_T, according to $F_2 \propto (\sigma_L + \sigma_T)$ and $F_2 \propto \sigma_L$. In the Quark Parton Model the value of F_L is zero since longitudinally polarised photons do not couple to spin 1/2 quarks. In Quantum Chromodynamics (QCD) F_L differs from zero due to the presence of gluons in the proton. In the so called DGLAP approximation of perturbative QCD at lowest order F_L is given by

$$F_L = \frac{\alpha_s}{4\pi} x^2 \int_x^1 \frac{dz}{z} [\frac{16}{3} F_2(z) + 8\Sigma e_q^2 (1 - \frac{x}{z}) z g(z)].$$

At low x, F_L directly determines the gluon density in the proton, which is only constrained indirectly by the Q^2 evolution of $F_2(x,Q^2)$. As it is evident from 8.2, the structure functions F_L and F_2 can be extracted by fitting a straight line to σ_r as a function of $y^2/(1+(1-y^2))$. A measurement of DIS cross sections at fixed x and Q^2 but different inelasticities y was achieved at HERA by varying the proton beam energy from nominal 920 GeV to 575 and 460 GeV, while keeping the positron beam energy constant. In these low energy runs a dedicated trigger was used to efficiently trigger the energy depositions with a threshold of 2 GeV. At small energies the trigger was complemented by the CIP2k (31) trigger, developed at our institute. A first direct measurement of the longitudinal structure function F_L was published in 2008 (32). New analyses, presented below, extend the kinematic range probed by the published measurement in four-momentum transfer squared $5 < Q^2 < 800$ GeV and Bjorken x (19) and extract F_L in diffractive events (21).

The sensitivity to F_L is largest at high y as its contribution is proportional to y^2. The kinematic variables x,y and Q^2 are determined from the energy E'_e and polar angle Θ_e of the scattered positron. At low Q^2, high y values correspond to low values of the scattered positron energy. At low energies also hadronic final state particles may mimic an positron signal leading to high background, mainly by photoproduction (γp) processes at $Q^2 \simeq 0$ GeV^2. Removal of the γp background contribution is the major challenge of the measurement of F_L. Part of the γp events are uniquely identified by detecting the scattered positron in tagging calorimeters close to the beampipe downstream of the positron beam. This measurement can be used to tune the simulation of the background. A further method uses the charge symmetry of the background. The charge of the positron candidate is determined from the curvature of the track associated to the positron. Besides small corrections, energy deposits from γp processes are charge symmetric. The wrong charge signal is then used to statistically subtract the background.

Figure 8.1 shows the longitudinal cross sections at low Q^2 as a function of Q^2 at their average x value, it significantly extends the kinematic range of the published measurement (32) ($12 < Q^2 < 90$ GeV^2). The measurement clearly differs from zero and is described by the NLO predictions based on the parton density functions from the H1 fit. For $Q^2 > 10$ GeV^2, the measurement is well described by the NLO H1 fit (30), whereas at low Q^2 the perturbative QCD calculation underestimates the measurement. Dipole models (33; 34) are found to describe the data well. For the entire Q^2 range the measurement is consistent with a value of $R \simeq F_L/(F_L + F_2) = 0.25$.

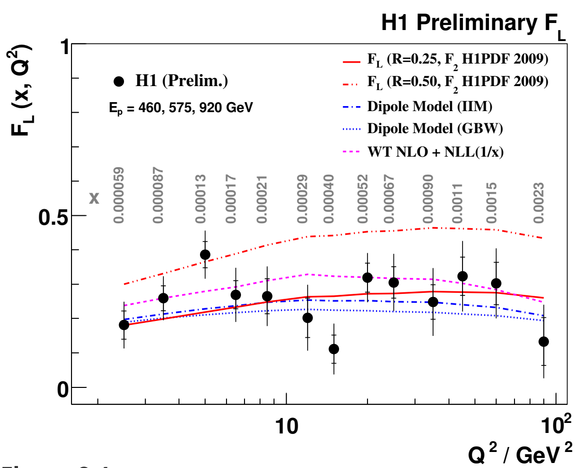

Figure 8.1:
Longitudinal cross section F_L at low Q^2 as a function of Q^2 at their average x value. The curves represent the predictions of a perturbative a QCD calculation at next-to-leading order (NLO) using the H1 PDF 2009 [30] as well as a dipole model [33; 34].

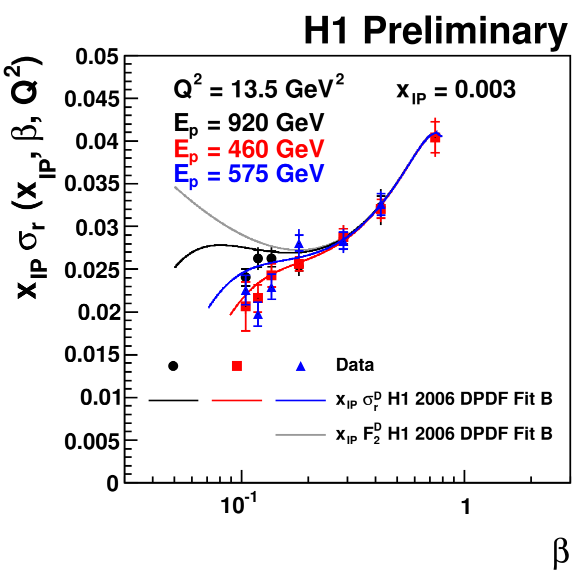

Figure 8.2: Reduced diffractive cross section at E_p= 460, 575 and 920 GeV, the inner error bars are statistical, the outer error bars show the statistical and systematic errors added in quadrature. The cross sections are normalised at 0.28< β <0.42 where the effect of F_L^D is negligible.

For the first measurement of the longitudinal diffractive structure function F_L^D a similar strategy as for the F_L analysis is adopted. In diffraction, the hadronic state system is separated from the scattered proton by a gap that can be observed by the lack of response in the forward parts of the H1 detector (rapidity gap method). The accuracy of this method depends strongly on the understanding of the noise level of the detectors involved.

The data are analysed in the kinematic region $Q^2 > 7$ GeV^2 and $y < 0.9$. Figure 8.2 shows the differential cross section for all three proton beam energies at $7 < Q^2 < 32$ GeV^2 and $0.001 < x_{IP} < 0.01$ as a function of β. Here, $\beta = Q^2/(Q^2+M_X^2)$ and $x_{IP} = (Q^2+M_X^2)/(Q^2+W^2)$, where M_X is the mass of the diffractive system and W the invariant mass of the gamma-proton system. The figure shows also the analytical prediction for σ_r^D to illustrate the effect of the longitudinal structure function. The reduced cross section drops at low β depending on the factor $y^2/(1+(1-y)^2)$ which differs for the three beam energies. The resulting F_L^D measurement is shown in figure 8.3 for four different values of β. The result is compatible with the H1 2006 fit of the diffractive parton density functions (35). Hence, the measurement fully supports the concept of QCD factorisation in diffraction and is an important test of the understanding of the nature of diffractive processes.

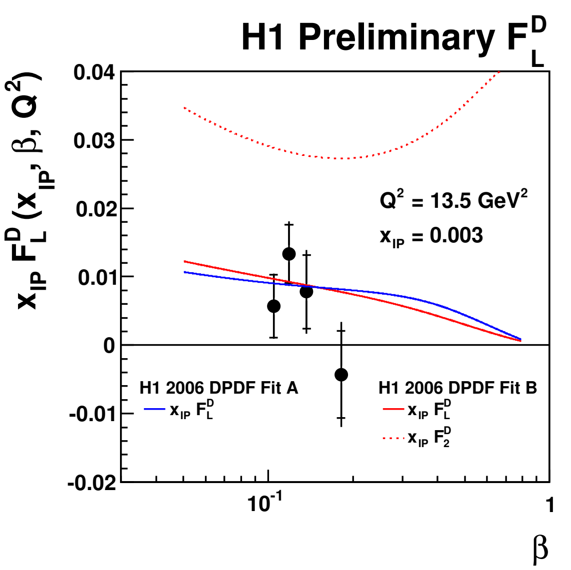

Figure 8.3: Longitudinal diffractive cross section F_L^D compared to the H1 2006 DPDF fits.

8.2 Multiple interactions in photoproduction

Multiple parton interactions (MIA), also referred to as underlying event, play an important role both in electron proton scattering at HERA and even more in high energy proton proton collisions at the TeVatron or the LHC. There,the underlying event is an important element of the hadronic environment within which all physics at the LHC, from Higgs searches to physics beyond the standard model, will take place. In order to tune the Monte Carlo models it is important to measure as many aspects of multiple interactions as possible.

In quasi-real photoproduction ($Q^2 \simeq 0$) the photon has a point-like as well as a hadronic (resolved) component. The transition from a point-like photon to a hadronic object can be studied at HERA as a function of x_γ, the momentum fraction of the parton from the photon which takes part in the hard interaction. Multiple or multi-parton interactions are expected for resolved photons ($x_\gamma < 1$) but not for point-like photons ($x_\gamma \simeq 1$). In photoproduction at HERA the underlying event is studied in di-jet events. The underlying event is defined as everything except the lowest order process (two jets). Besides contributions from higher order QCD radiation and hadronisation it receives also contributions from multi-parton interactions.

Figure 8.4 shows the charged particle multiplicity as a function of the azimuth, where the leading jet is by definition at $\Phi = 180°$, for a resolved photon enriched ($x_\gamma < 0.7$) sample. The data are compared to predictions from PYTHIA. The inclusion of multiple interactions clearly improves the description in the region transverse to the jet ($60° < \Delta\Phi < 120°$ and $240° < \Delta\Phi < 300°$). as well as in the toward ($120° < \Delta\Phi < 240°$) and away ($300° < \Delta\Phi < 60°$) regions, where it contributes as a pedestal to the track multiplicity.

Figure 8.5 shows the average charge multiplicity in the region of the jet P_T^{Jet1} with the highest transverse momentum for $x_\gamma < 0.7$. The track multiplicity rises with P_T^{Jet1}. While the distribution for $x_\gamma > 0.7$ (not shown here), which contains only one hard interaction, is reasonably well described by the simulation, this is clearly not enough to describe the distribution in the resolved enriched sample, especially at lower values of P_T^{Jet1}. Including multi-parton interactions brings the prediction

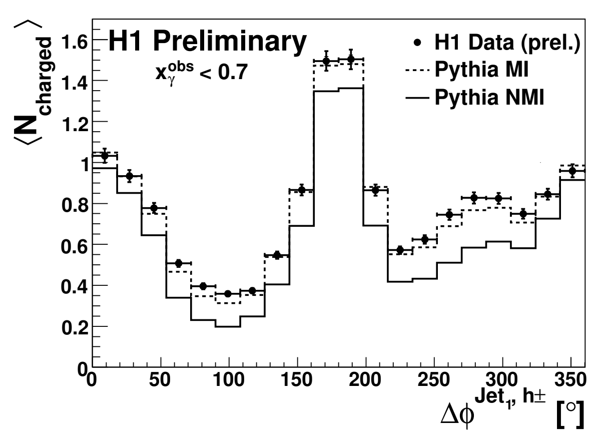

Figure 8.4: Charged particle multiplicity for $x_\gamma < 0.7$. The leading jet axis is by definition at $\Phi = 180°$. The data is compared to PYTHIA with and without multiple interactions.

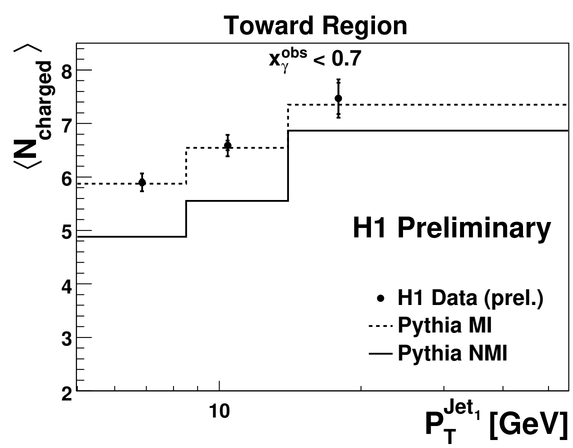

Figure 8.5:
Charged particle multiplicity for $x_\gamma < 0.7$ in the region close to the leading jet. The data is compared to PYTHIA with and without multiple interactions.

in good agreement with the measurement. In the region transverse to the leading jet the average charged particle multiplicity ranges between 0.5 to 2.5 particles, almost independent of P_T^{Jet1}. Again, the region of $x_\gamma > 0.7$ is reasonably well described without including MIA, whereas the region of $x_\gamma < 0.7$ requires multiple interactions to be included. In regions where the photon develops a hadronic structure this measurement fully supports the picture of multi-parton interactions as observed at the TeVatron (36).

8.3 Photon analysis

Isolated photons have been in the focus of our group for the past few years, the effort resulted in two publications (25; 27) and two completed PHD thesis (26; 28). The analysis of isolated photon emerging from the hard subprocess $ep \rightarrow e\gamma X$ - so called prompt photons - in photoproduction (PhD thesis of Krzysztof Nowak) was finished during last year. The analysis is based on events at very low Q^2 with the scattered electron escaping detection through the beam pipe and an isolated photon. The data collected during 2004-2007 correspond to a total integrated luminosity of 340 pb^{-1}, three times the value of the previous measurement. Isolated photons with transverse energy $6 < E_T^\gamma < 15$ GeV and pseudo-rapidity $-1.0 < \eta^\gamma < 2.4$ are selected in events with inelasticity $0.1 < y < 0.7$. To ensure isolation of the photon, the energy fraction z of the photon-jet carried by the photon candidate has to be larger than 90% ($z \equiv E^\gamma / E^{photon-jet} > 0.9$). The isolation rejects a large part from the background from decay photons of neutral hadrons in dijet photoproduction events. The photon signal is extracted by combining different shower shape variables into a discriminator. A novel method, based on a regularised unfolding procedure (37; 38), was developed for this analysis to simultaneously unfold the cross section and determine the fraction of signal and background. Final results of the analysis have been shown in last years report. Overall it was shown that QCD calculations based on the collinear factorisation in NLO (39; 40) or the k_T factorisation approach (41) underestimate the cross section at low transverse momenta of the photon (E_T^γ) and that they are not able to fully describe the transverse correlations between the photon and the jet. The transverse correlations are particularly sensitive to the fraction of resolved events in the sample and to higher order effects. It was therefore studied whether the description of the data by the models could be improved by increasing the intrinsic transverse momentum $< k_T >$ of the partons in the proton which could mimic higher order gluon radiation. Figure 8.6 shows the cross section as a function of the transverse correlation between the jet and the photon for the sample in which direct interactions are enhanced ($x_\gamma > 0.8$). Two variables are defined: $p_\perp$, the transverse momentum of the photon perpendicular to the jet direction and $\Delta\Phi$ the azimuthal difference. The measurement is compared to a NLO prediction (39; 40) which has no intrinsic $< k_T >$ and clearly under-

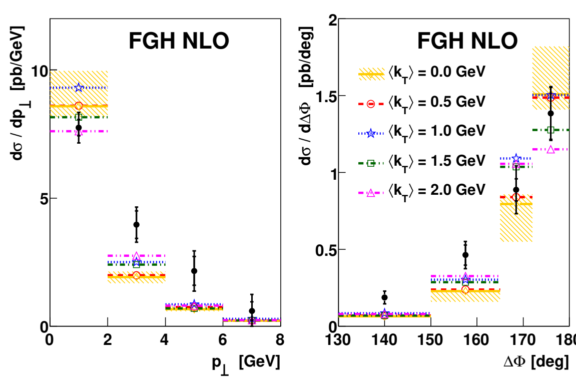

Figure 8.6:
Cross sections for prompt photons in photoproduction with $x_\gamma > 0.7$ as a function of $p_\perp$, the transverse momentum of the photon perpendicular to the jet direction and $\Delta\Phi$ the azimuthal difference. The measurement is compared to a NLO prediction [39; 40] with different assumptions on the intrinsic transverse momentum of the partons in the proton.

estimates the tails. With increasing $< k_T >$ the description of the tails improves, though the last bin in $\Delta\Phi$ remains low. Our studies in this field will continue by analysing less isolated photons which may be used to extract the quark to photon fragmentation function.

[1] F. D. Aaron *et al.* [H1/ZEUS], JHEP **1001** (2010) 109.

[2] F. D. Aaron *et al.* [H1/ZEUS], JHEP **1003** (2010) 035.

[3] F. D. Aaron *et al.* [H1], Phys. Lett. **B 686** (2010) 91.

[4] F. D. Aaron *et al.* [H1], Eur. Phys. J. C **66** (2010) 17.

[5] F. D. Aaron *et al.* [H1], Phys. Lett. B **681** (2009) 391.

[6] F. D. Aaron *et al.* [H1/ZEUS], JHEP **0910** (2009) 013.

[7] F. D. Aaron *et al.* [H1], Eur. Phys. J. C **65** (2010) 89.

[8] F. D. Aaron *et al.* [H1], Phys. Lett. B **681** (2009) 125.

[9] F. D. Aaron *et al.* [H1], Phys. Lett. B **678** (2009) 450.

[10] F. D. Aaron *et al.* [H1], Phys. Lett. B **678** (2009) 335.

[11] F. D. Aaron *et al.* [H1], Eur. Phys. J. C **65** (2010) 363.

[12] F. D. Aaron *et al.* [H1], Eur. Phys. J. C **64** (2009) 561.

[13] F. D. Aaron *et al.* [H1], Phys. Lett. B **673** (2009) 119.

[14] F. D. Aaron *et al.* [H1], Eur. Phys. J. C **63** (2009) 625.

[15] F. D. Aaron *et al.* [H1], Eur. Phys. J. C **67** (2010) 1.

[16] F. D. Aaron *et al.* [H1], JHEP **1005** (2010) 032.

[17] Contributed papers by the H1-Coll. to EPS2009, the 2009 Europhysics Conference on High Energy Physics, Krakow, 16-22 July, 2009; only papers are listed, which are not yet submitted to journals.

[18] **Search for Squark Production in R-Parity Violating Supersymmetry at HERA** [17].

[19] **Measurement of the Longitudinal Structure Function F_L of the Proton at Low x in an extended Q^2 range** [17].

[20] **Diffractive photoproduction of jets with the H1 detector** [17].

[21] **Measurement of the diffractive longitudinal structure function F_L^D at HERA II** [17].

[22] **Measurement of diffractive deep-inelastic scattering with a leading proton at HERA-2** [17].

[23] **A Measurement of the Pomeron Trajectory based on Elastic Rho Photoproduction** [17].

[24] Preliminary H1 results to be presented at the 2010 Workshop on Deep Inelastic Scattering (DIS 2010), Florence, April 19-23, 2010, *http://www-h1.desy.de/publications/H1preliminary.short_list.html*.

[25] F. D. Aaron *et al.* [H1], Eur. Phys. J. C **66** (2010) 17.

[26] **Prompt photon production in photoproducion at HERA**, Krzysztof Nowak, PhD Thesis, University of Zürich (2009) http://www-h1.desy.de/publications/theses_list.html.

[27] F. D. Aaron *et al.* [H1], Eur. Phys. J. C **54** (2008) 371.

[28] **Isolated photon production in deep-inelastic scattering at HERA**, Carsten Schmitz, PhD Thesis, University of Zürich (2007) http://www-h1.desy.de/publications/theses_list.html.

[29] Physik-Institut, University of Zürich, Annual Reports 1996/7 ff.; available at *http://www.physik.unizh.ch/reports.html*.

[30] C. Adloff *et al.* [H1], Eur. Phys. J. C **30** (2003) 1.

[31] J. Becker *et al.*, Nucl. Instrum. Meth. A **586** (2008) 190.

[32] F. D. Aaron *et al.* [H1], Phys. Lett. **B 665** (2008) 138.

[33] K. Golec-Biernat and M. Wüsthoff, Phys. Rev. D **59** (1999) 014017.

[34] E. Iancu, K. Itakura and S. Munier, Phys. Lett. **B 590** (2004) 199.

[35] A. Aktas *et al.* [H1], Eur. Phys. J. C **48** (2006) 715.

[36] A. A. Affolder *et al.* [CDF], Phys. Rev. D **65** (2002) 092002.

[37] V. Blobel, "An unfolding method for high energy physics experiments," Proc. Advanced Statistical Techniques in Particle Physics, Durham (2002).

[38] R. Brun and F. Rademakers, Nucl. Instrum. Meth. A **389** (1997) 81, Version 5.22 was used.

[39] M. Fontannaz, J. P. Guillet and G. Heinrich, Eur. Phys. J. C **21** (2001) 303.

[40] M. Fontannaz and G. Heinrich, Eur. Phys. J. C **34** (2004) 191.

[41] A.V. Lipatov and N.P. Zotov, Phys. Rev. D **72** (2005) 054002.

9 High-precision CP-violation Physics at LHCb

J. Anderson, R. Bernet, A. Büchler, A. Bursche, N. Chiapolini, M. De Cian, C. Elsasser, K. Müller, C. Salzmann, S. Steiner, O. Steinkamp, U. Straumann, J. van Tilburg, M. Tobin, A. Vollhardt

in collaboration with: The silicon tracking group of LHCb: University of Lausanne; Max Planck Institute, Heidelberg, Germany; University of Santiago de Compostela, Spain; and Ukrainian Academy of Sciences, Kiev, Ukraine.

The full LHCb collaboration consists of 54 institutes from Brazil, China, France, Germany, Ireland, Italy, The Netherlands, Poland, Romania, Russia, Spain, Switzerland, Ukraine, the United Kingdom, and the United States of America.

(LHCb)

9.1 The LHCb Experiment

LHCb (1) is a dedicated b-physics experiment at the Large Hadron Collider (LHC) at CERN. The LHC delivered its first high energy proton-proton collisions at 2.2 TeV centre-of-mass energy in autumn 2009 and has been operating at 7 TeV centre-of-mass energy since the end of March 2010. The LHCb experiment has been operated routinely from the first day of collisions and the recorded data are being used to complete the commissioning of the detectors, tune reconstruction algorithms and validate the expected performance. For example, K_s, Λ and J/ψ invariant-mass signals have been reconstructed showing close-to-nominal masses and mass resolutions. A first B-decay candidate event was recorded in April 2010. The LHC is going to operate at 7 TeV centre-of-mass energy until the end of 2011. The instantaneous luminosity will gradually increase and an integrated luminosity of about 1 fb^{-1} should have been delivered to each of the experiments by the end of 2011. This data set should permit LHCb to confirm its physics potential and to improve on existing measurements in key physics channels. The LHC will then be shut down for about one year for further consolidation work, before increasing the centre-of-mass energy to the nominal 14 TeV.

The main goal of LHCb is to perform precision measurements of CP violating processes in the B meson systems and to search for rare B decays. Unique triggering and particle-identification capabilities will permit to measure CP asymmetries in many different decay modes and to perform consistency checks of the Standard Model. CP-violating asymmetries are generated by processes involving internal loops of virtual particles and are therefore sensitive to contributions from heavy new particles that are predicted in most extentions of the Standard Model. Similarly, the branching fractions of rare decays can be significantly enhanced by virtual contributions from new particles. The measurement of such processes provides a powerful tool to search for "new physics" beyond the Standard Model, complementary to direct searches at the high energy frontier that will be performed by other experiments at the LHC.

Fig. 9.1 shows a vertical cross section through the LHCb detector. LHCb is laid out as a single-arm forward spectrometer. One of the crucial tasks in LHCb is the efficient and precise reconstruction of the trajectories and momenta of the charged particles that are generated in the decays of the B mesons. The tracking system consists of a silicon-microstrip vertex detector (VELO) and four planar tracking stations: the TT (Tracker Turicensis) up-

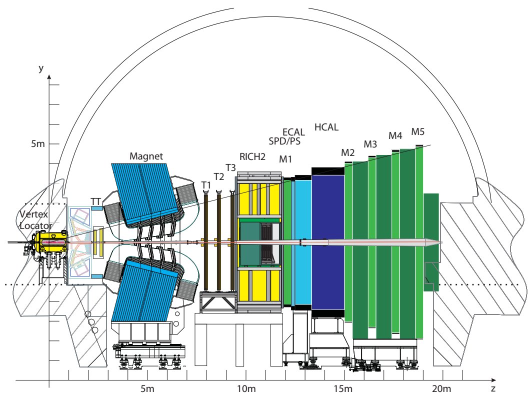

Figure 9.1:
Vertical cross section through the LHCb detector.

stream of the LHCb dipole magnet and T1-T3 downstream of the 4 Tm dipole magnet. The TT has an active area that is 160 cm wide and 130 cm high and is covered by four layers of silicon micro-strip detectors. In the much larger stations T1-T3, two detector technologies are employed: A 120 cm wide and 40 cm high region in the centre of these stations is covered with silicon micro-strip detectors (Inner Tracker, IT), the outer part of these stations is covered by straw drift-tube detectors. Other components of the LHCb detector are two ring-imaging Cherenkov detectors (RICH1 and RICH2), calorimeters (SPD,PS,ECAL,HCAL) and muon chambers (M1-M5).

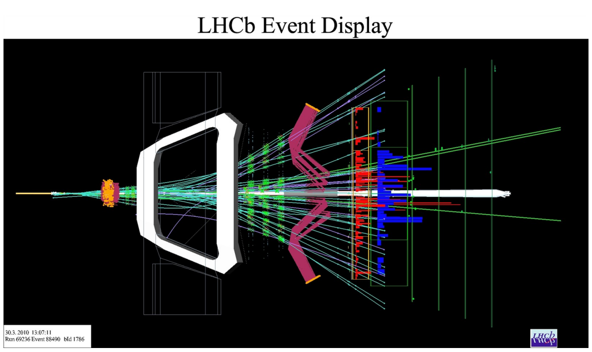

Figure 9.2:
Event display of an event registered during the first LHC proton-proton collisions at 7 TeV centre-of-mass energy.

9.2 The Zürich Group in LHCb

Our group has played a leading rôle in the development and construction of the LHCb Silicon Tracker (ST), which comprises the TT and the IT. The TT was conceived, designed and made in Zürich, and the optical digital readout links for both the TT and the IT were developed and assembled at our institute. We are now responsible for the commissioning, operation and maintenance of the TT and its readout in LHCb. We are also responsible for the software alignment of the TT and contribute to the track reconstruction software.

The preparation of physics analyses takes up an increasing fraction of our effort. This comprises the use of simulated data sets to develop reconstruction strategies and establish the physics reach of the experiment, as well as the analysis of the first data from LHC collisions to test reconstruction algorithms and validate the expected performance of the detector.

9.3 Tracker Turicensis

The installation of the TT in LHCb was completed in 2008 and the detector has been operated routinely since then. In 2009, a large fraction of our efforts went into getting the detector and its readout into the best possible shape for the first LHC collisions. By the time the LHC turned on in October 2009, more than 99% of the 144’000 detector channels were fully operational. Algorithms for automatic monitoring and archiving of operation parameters were developed and deployed. The automatic configuration of operation parameters for different operating conditions, using finite-state-machines, has been implemented and commissioned.

The first LHC collision data have then been used to tune operation parameters such as bias voltage and signal readout timing. Tools and histograms that allow an efficient online

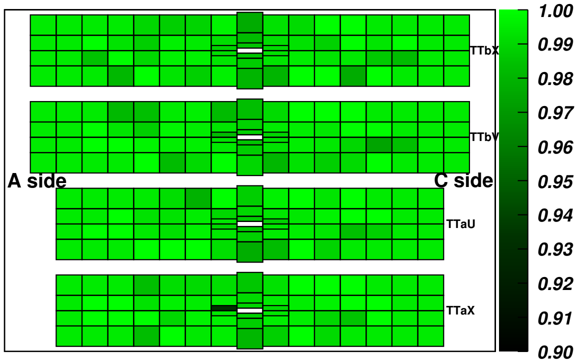

Figure 9.3:
Efficiency map of the TT detector. Each rectangle represents one readout sector and the colour encodes the measured hit efficiency in this sector.

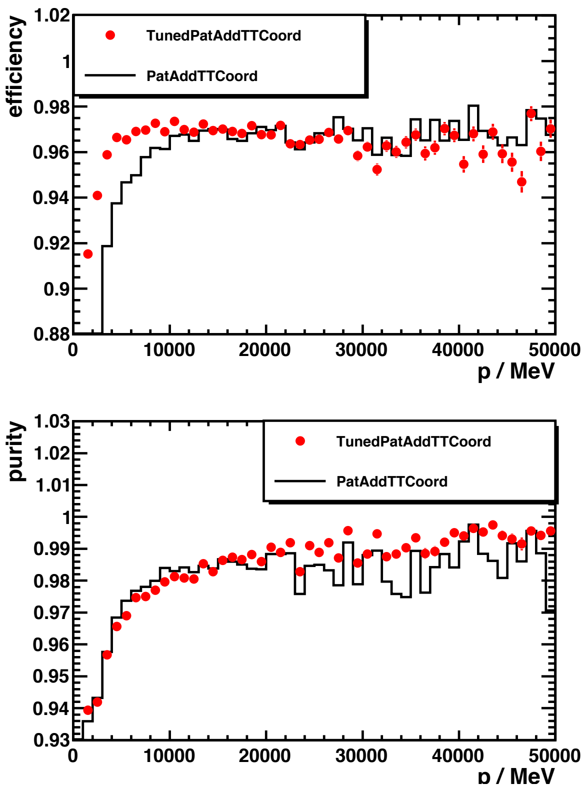

Figure 9.4:
TT hit assignment efficiency (top) and purity (bottom) as a function of the reconstructed particle momentum. The black line shows the performance for the existing algorithm, the red dots show the performance after improvements.

monitoring of the detector performance have been developed and implemented. An example of a monitoring plot showing the hit efficiency for each readout sector of the TT is shown in Fig. 9.3. The average hit-detection efficiency of the detector exceeds 99%.

In charge of these efforts and responsible for the operation of the TT is J. van Tilburg, who is permanently stationed at CERN. He receives major support from J. Anderson and M. Tobin, who are based in Zürich but spend significant fractions of their time at CERN taking shifts as detector operators. In addition, J. Anderson looks into the offline study of the TT performance and its impact on track reconstruction, and M. Tobin is responsible for the online monitoring of the detector performance.

These efforts will continue to require a significant amount of manpower for the coming year. In addition to the continual effort required to maintain smooth operation and high efficiency, the detector performance will have to be monitored carefully as the LHC luminosity increases and operation parameters might have to be re-adjusted.

9.4 Track reconstruction and alignment

The reconstruction of the trajectories and momenta of charged particles in LHCb relies on the Vertex Locator, the tracking stations T1-T3 downstream of the magnet and the TT just in front of the magnet. Simulation studies have demonstrated that adding TT measurements to a track significantly improves the momentum resolution. Using existing pattern recognition algorithms, the efficiency for adding TT measurements to a track is of the order of 97% for particle momenta above 10 GeV but decreases sharply for momenta below 10 GeV. M. De Cian has developed improvements to the pattern recognition algorithm that improve its efficiency for particles with low momenta while keeping the purity constant (see Fig. 9.4).

The TT is assembled from 896 individual silicon micro-strip sensors. In order to fully exploit the detector information and to avoid biases in the momentum reconstruction, the position of each of these detector elements should be known to significantly better than the intrinsic hit resolution of 50 μm. For a detector of the size of the TT, such a positioning precision is impossible to achieve in hardware. The position of each detector element must therefore be reconstructed from the data. C. Salzmann is working on this as part of his PhD thesis. He will be joined by N. Chiapolini and A. Bursche, who have recently started their PhD theses in our group. The TT is a single tracking station with only four detection layers and its alignment relies on tracks reconstructed in the other parts of the tracking system. The alignment of the TT is therefore sensitive to residual misalignments of these other detectors, making it an excellent tool for monitoring problems in the overall detector alignment. An example of this is shown in Figs. 9.5 and 9.6. Figure 9.5 shows a distribution of the residual misalignments of the detector elements with respect to external tracks. The width of this distribution shows that the TT elements are aligned to a precision of about 20 μm with respect to the remainder of the tracking system. Figure 9.6 shows by how much each of the detector elements has to be shifted from its nominal position in order to achieve this agreement in the alignment procedure. A clear "scaling" is observed in two of the detection layers: The shift increases linearly with the position of the detector element. This correlation points to a remaining problem with the LHCb alignment procedure and is currently under investigation.

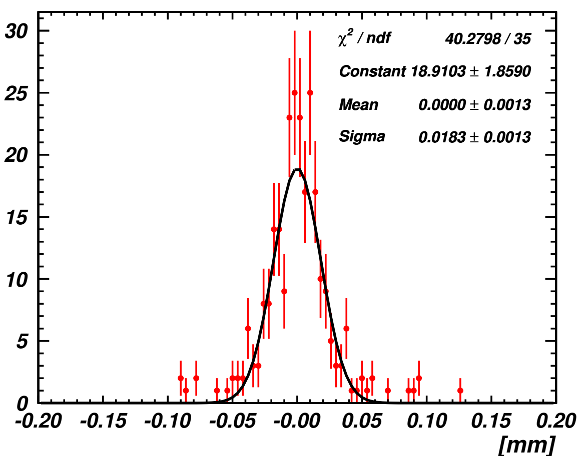

Figure 9.5:
Distribution of residual misalignments of detector elements in the TT, after software alignment.

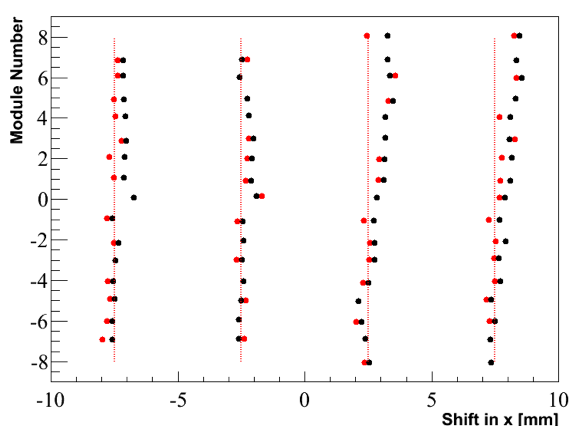

Figure 9.6:
Horizontal shift of each detector element with respect to its nominal position. The dotted vertical lines indicate the nominal positions for each of the four detection layers of the TT, the red and black points show the positions of individual detector elements after the software alignment.

9.5 Physics studies

We have chosen four physics topics that we will pursue in our group: the measurement of the branching ratio of the rare decay $B_s^0 \to \mu^+\mu^-$; the measurement of the CP-violating phase β_s of $B_s^0\overline{B}_s^0$ mixing; the measurement of the forward-backward asymmetry and other observables in $b \to s\ell^+\ell^-$ decays; and the measurement of parton distribution functions in decays $\gamma^\star/Z \to \mu^+\mu^-$. Each of these topics builds upon previous experience of members of our group, from earlier simulation studies in LHCb or from analyses performed in other experiments (e.g. search for $B_s^0 \to \mu^+\mu^-$ at D0 (2), search for $B \to K^\star\mu^+\mu^-$ at D0 (3), measurement of proton parton distribution functions at H1 (4)).

The measurement of the branching fraction of the decay $B_s^0 \to \mu^+\mu^-$ is one of the early key measurements for LHCb. The branching fraction for this decay is predicted to be of the order of 3×10^{-9} in the Standard Model but can be significantly enhanced within extensions of the Standard Model. Currently, the best measured upper limit has been reported by the CDF experiment at the Tevatron. Using 3.7 fb^{-1} of data, they set an upper limit of 3.6×10^{-8} at 90% confidence level (5). Simulation studies show that LHCb should be able to reach this limit with only 50 pb^{-1} of proton-proton collisions at 7 TeV centre-of-mass energy. The analysis strategy is described in detail in the recently published LHCb road map document (6). One of the crucial steps for the extraction of a possible signal will be a precise modeling of the B_s^0 mass resolution from data, using control channels such as $B_s^0 \to K^+K^-$ and $B_s^0 \to \pi^+\pi^-$. A. Büchler is working on this aspect of the analysis as part of her PhD thesis, supervised by J. van Tilburg and O. Steinkamp. Using the first collision data, she is currently looking at $K_s \to \pi^+\pi^-$, $\Lambda \to p\pi^-$ and other decays to develop appropriate tools and study possible biases from particle identification cuts. An example of a K_s signal is shown in Fig. 9.7. C. Elsasser is about to join this effort for his Master thesis.

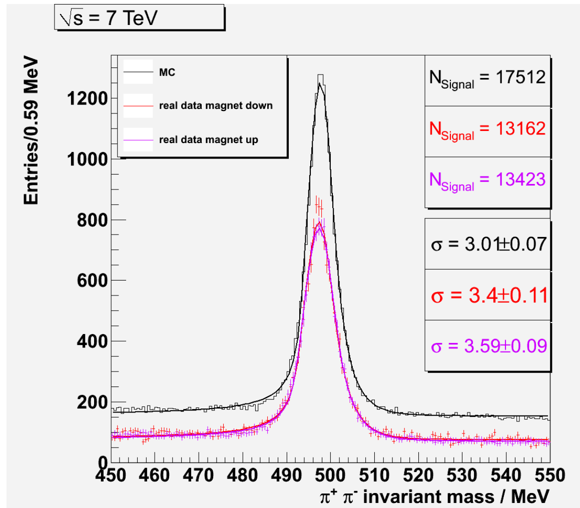

Figure 9.7: $\pi^+\pi^-$ invariant-mass distributions showing a K_s^0 peak. Here, the mass resolution in collision data is slightly worse than in simulated data and the event yield is significantly lower. This is attributed to a not yet perfect alignment of the tracking detectors.

The CP-violating phase β_s is very small in the Standard Model (7) but can be significantly enhanced in new-physics models. The most promising approach to measuring this phase in LHCb is via the time-dependent CP asymmetry in the decay $B_s^0 \to J/\psi\phi$. A simulation study of an alternative approach, using the decay $B_s^0 \to J/\psi\eta'$, was performed in our group earlier (8). As a first step towards an analysis using LHC collision data, C. Salzmann is looking into the calibration channel $B_d^0 \to J/\psi K^\star$ which has a similar topology as $B_s^0 \to J/\psi\phi$ but a much higher branching fraction. In particular, he is studying the effect of residual detector misalignments on the invariant-mass resolution of the J/ψ and B_s^0 signals. He is supervised in this work by J. van Tilburg.

Decays $b \to s\ell^+\ell^-$ proceed through suppressed loops in the Standard Model and are therefore sensitive to possible contributions from new physics. One of the interesting observables is the forward-backward asymmetry, A_{FB}, which is defined through the angle between the ℓ^+ and the direction of flight of the B meson in the di-lepton rest frame. This asymmetry as a function of the di-lepton invariant mass can be predicted with small theoretical uncertainties. An LHCb simulation study of the decay channel $B_d^0 \to K^\star\ell^+\ell^-$ has shown that the zero-crossing of the asymmetry can be measured with a precision of 0.46 GeV^2 using 2 fb^{-1} of data at 14 TeV centre-of-mass energy. Again, $B_d^0 \to J/\psi K^\star$ serves as a calibration channel and $J/\psi \to \mu^+\mu^-$ decays are used to determine muon identification efficiencies from collision data. M. De Cian works on this analysis as part of his PhD thesis work under the supervision of J. Anderson. A $J/\psi \to \mu^+\mu^-$ invariant-mass signal is shown in Fig. 9.8.

Previous measurements of the proton's parton distribution functions (PDFs) have been performed at fixed target experiments, at HERA and at the Tevatron. At LHCb, the proton's PDF can be probed through a measurement of the differential cross-section for di-muon production via the Drell-Yan process. The cross-section for this process at LHC energies has been calculated at NNLO (9). The dominant theoretical uncertainties, due to the knowledge of the PDFs, are largest at higher production rapidities and lower di-muon invariant masses. LHCb will be able to explore these regions due to its high rapidity coverage and low momentum trigger thresholds. By measuring the differential Drell-Yan cross-section as a function of di-muon mass and rapidity, LHCb will therefore probe a large, partially unknown kinematic domain, providing constraints on the PDFs down to Bjorken-x values of 10^{-6}. Preparations for a measurement of the Drell-Yan cross-section at LHCb are well advanced. As part of his PhD thesis work at UC Dublin before joining our group, J. Anderson investigated a cross-section measurement at the Z mass. He showed that systematic uncertainties are expected to be 1% and that with an integrated luminosity of 50 pb^{-1} a total cross-section measurement will already be systematics limited (10). Since joining our group he has extended this analysis to the low-mass region (11). Again it is expected that cross-section measurements in this region will rapidly become systematics limited. A. Bursche and N. Chiapolini have recently started their PhD theses on this topic. Under the supervision of J. Anderson and K. Müller they commenced investigations of the systematic uncertainties associated with the trigger, tracking and muon identification efficiencies for these events using the first collision data collected by LHCb.

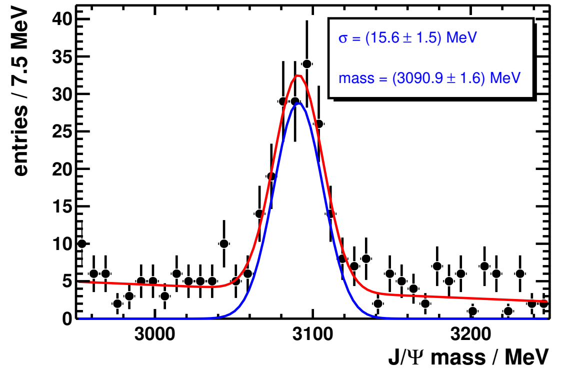

Figure 9.8: $\mu^+\mu^-$ invariant-mass distribution from collision data, showing a clear J/ψ signal.

Figure 9.9: Celebrating the first 7 TeV collisions in LHCb. This page was shown on information screens throughout Universität Zürich.

9.6 Outreach activities

The successful startup of the LHC has spawned great interest in the public and in public media. We have engaged in a number of outreach activities trying to meet this interest. We have prepared a German-language brochure explaining the LHCb experiment and its goals in laymen's terms (12), we participated with a stall at the "Nacht der Forschung" that took place in downtown Zürich in September 2009. A. Büchler participated as a guide for journalists on the media day organized by CERN on the occasion of the first collisions at 7 TeV centre-of-mass energy. A page celebrating the first collisions in LHCb was shown on information screens throughout Universität Zürich (see Fig. 9.9).

9.7 Summary and Outlook

The LHCb experiment was ready and in good shape to collect the first high-energy proton-proton collisions from the LHC and has been collecting data routinely from the first day of LHC operation. Invariant-mass signals of K_s, Λ and J/ψ have been reconstructed and permit detailed studies of the detector performance. A first B-decay candidate has been recorded. Our group will continue to play an important rôle in the operation of the detector. More work is needed to study the detector performance in detail and to fine-tune operation parameters as the instantaneous luminosity of the LHC increases. Reconstruction algorithms that have been developed on simulated datasets can now be exercised on the first collision data. The LHC is foreseen to run continuously until the end of 2011, delivering an integrated luminosity of about 1 fb^{-1} at a centre-of-mass energy of 7 TeV. The data collected during this time will permit LHCb to verify its physics potential and to improve on existing measurements in key analyses. We are engaged in a number of physics analyses, to which we expect to make significant contributions, building on existing expertise in the group. We are looking forward to exciting results for the coming years.

[1] The LHCb detector at the LHC, 2008 JINST 3 S08005.

[2] R. P. Bernhard, *Search for rare decays of the B_s^0 meson with the D0 experiment*, PhD thesis, Universität Zürich (2006).

[3] A. Wenger, *Search for the Rare Decays $B^\pm \to K^\pm\mu^+\mu^-$ and $B^0 \to K^\star\mu^+\mu^-$ with the D0 experiment*, PhD thesis, Universität Zürich (2008).

[4] for example: F. D. Aaron et al. [H1 Collaboration and ZEUS Collaboration], *Combined Measurement and QCD Analysis of the Inclusive ep Scattering Cross Sections at HERA*, JHEP 1001 (2010) 109 [arXiv:0911.0884 [hep-ex]].

[5] CDF collaboration, *Search for $B_s \to \mu^+\mu^-$ and $B_d \to \mu^+\mu^-$ decays in 3.7 fb^{-1} of $\overline{p}p$ collisions with CDF-II*, CDF public note 9892.

[6] The LHCb Collaboration, *Roadmap for selected key measurements of LHCb*, LHCb-PUB-2009-029, arxiv/0912.4179 (2010).

[7] CKMfitter 2008, see webpage.

[8] D. Volyanskyy, *The Trigger Tracker and a Monte Carlo Study of the $B_s \to J/\psi\eta'$ Decay in the LHCb Experiment*, PhD thesis, Universität Zürich (2007).

[9] C. Anastasiou, L.J. Dixon, K. Melnikov and F. Petriello, Phys. Rev. Lett. 91 (2003).

[10] J. Anderson, *Testing the electroweak sector and determining the absolute luminosity at LHCb using dimuon final states*, PhD thesis, University College Dublin (2007); J. Anderson and R. McNulty, *Measuring $\sigma_Z \cdot Br(Z \to \mu^+\mu^-)$ at LHCb*, LHCb note 2007-114 (2007).

[11] J. Anderson, *Probing low-x with Drell-Yan events at LHCb*, Proc. XVII International Workshop On Deep-inelastic Scattering And Related Subjects, Prog. High Energy Phys. 3 (2009).

[12] available for download at http://lhcb-public.web.cern.ch/lhcb-public/en/LHCb-outreach/documentation/LHCb_German_mod_zh2.pdf

10 Particle physics with CMS

E. Aguiló, E. Alagöz[2], C. Amsler, S. de Visscher, M. Ivova, B. Millán Mejías, P. Otyugova, C. Regenfus, P. Robmann, J. Rochet, T. Rommerskirchen, A. Schmidt, S. Steiner, D. Tsirigkas[3], and L. Wilke[4]

V. Chiochia, C. Favaro, A. Jaeger, and H. Snoek

In collaboration with: Paul Scherrer Institut (PSI) and the CMS Collaboration

The silicon pixel detector is the innermost component of the CMS experiment (1) at the LHC. It allows a precise reconstruction of the directions of charged particles and the identification of displaced vertices from long-lived particle decays. The 53 cm long barrel pixel section, counting about 48 million channels, consists of three cylindrical layers at radii between 4.4 cm and 10.2 cm. Two endcap disks at each side of the barrel provide coverage up to large rapidities.

We were involved since 1995 in the design, construction and commissioning of the barrel pixel detector (1). We have led prototype tests with CERN beams, measuring sensor performances before and after irradiation, such as position resolution, detection efficiency, charge sharing and Lorentz deflection. In addition, we have contributed to the development and commissioning of the readout chip. We have designed and built in the Institute workshop the mechanical and cooling structure and the two service tubes which provide coolant and power, and transfer the signals to and from the pixel detector. Details can be found in earlier reports and in various publications such as refs. (2; 3; 4).

After a commissioning phase with cosmic rays CMS started recording proton collisions in December 2009 at the center-of-mass energy of 900 GeV (Fig. 10.1). During the run a world

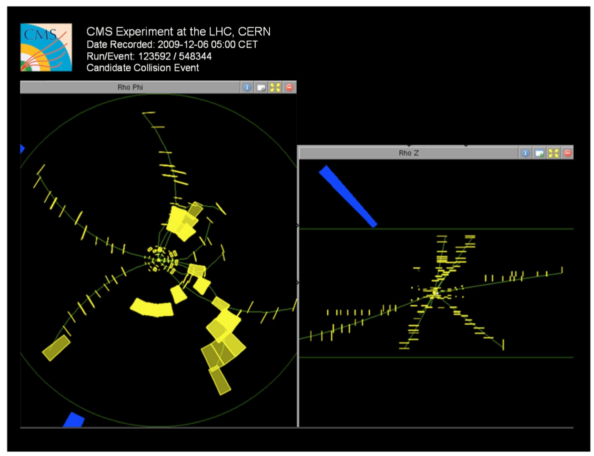

Figure 10.1: Event displays of the first pp-collisions registered by CMS at 900 GeV in December 2009.

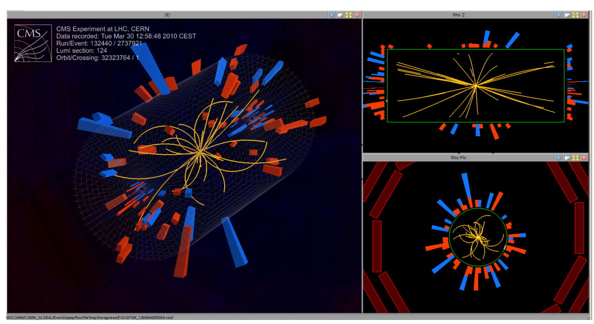

Figure 10.2: Event displays of pp-collisions at 7 TeV registered in March 2010.

record center-of-mass energy of 2.36 TeV was achieved with the LHC. A first physics publication on multiplicity distributions has already appeared (5). A run at 7 TeV has started in March 2010 (Fig. 10.2) which is expected to last until autumn 2011, with the goal to reach an integrated luminosity of 1 fb^{-1}.

[2]until 31 August 2009.
[3]until 31 August 2009.
[4]until 31 December 2009.

10.1 Commissioning of CMS silicon pixel detector with first collision data

As the CMS pixel detector plays a key role for several physics analyses, our first priority was to measure its performance with LHC collisions and to compare with expectations. Last year we performed several important measurements and calibrations, ranging from a measurement of the detector occupancy and position resolution to that of the Lorentz angle in the 3.8 T magnetic field.

First, background events such as beam-halo or beam-gas interactions have to be carefully removed during the offline selection. We have developed several rejection algorithms that are now employed in CMS analyses and have studied the dependence of the background rate on LHC operating conditions. In the near future we will also test the effects of beam tuning on the background rate.

One of the most important benchmarks is the occupancy which provides estimates of the detector noise. The comparison with expectations from event generators is also very important to fine-tune phenomenological parameters such as parton showers and multiple partons interaction, which influence charged particle production at very low momenta, and can produce a large number of hits in the innermost layers of the pixel detector. The

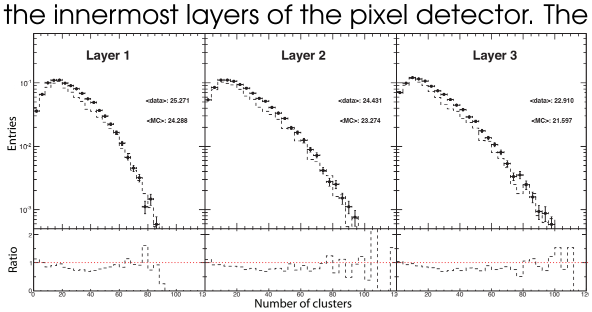

Figure 10.3: Measured (dots) and simulated pixel hit multiplicities in the three barrel layers at 900 GeV. The bottom plots show the ratios between measurements and simulations.

pixel detector occupancy was measured at 0.9 TeV and 2.36 TeV center-of-mass energies for the barrel section (see Fig. 10.3), and for single barrel modules (or blades in the end-cap sections). The average occupancy is in very good agreement with expectations, with discrepancies generally smaller than 5%. However, fine tuning of the Monte Carlo generators will be needed as no fitting to data was attempted so far for LHC energies.

Charge collection was also compared to Monte Carlo simulation (Fig. 10.4). The pixel cluster charges were normalized to the path lengths in the silicon sensors. We observed excellent agreement with simulation for the peak position, width and tails of the distribution, hence have a very good understanding of the analogue readout chain and charge calibration.

A measurement of the position resolution was performed using first collision data. We used pairs of consecutive hits along trajectories in the overlap regions between adjacent modules of a given layer, and calculated the differences in hit positions Δx_{hit} (Δy_{hit}) along the transverse (longitudinal) direction. We then

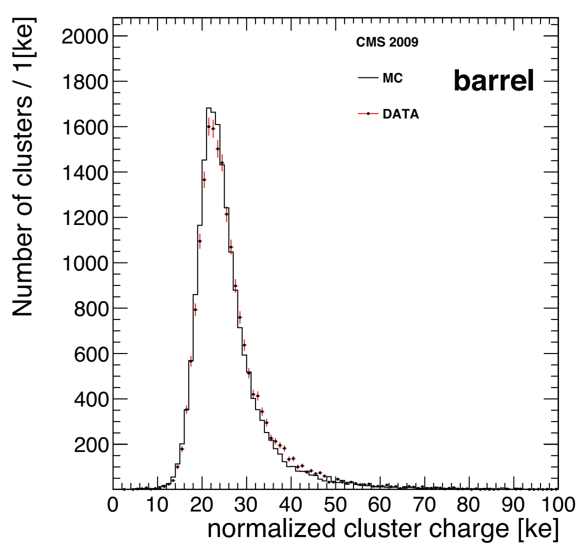

Figure 10.4: Measured (dots) and simulated cluster charge distribution in the barrel pixel detector.

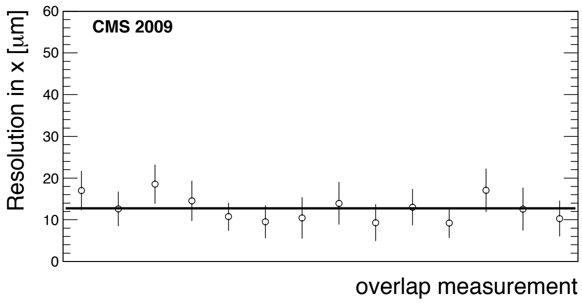

Figure 10.5: Position resolution for the barrel detector along the transverse coordinates. Each point corresponds to a pair of overlapping modules, calculated from more than 20 crossing tracks. The solid line shows the average resolution.

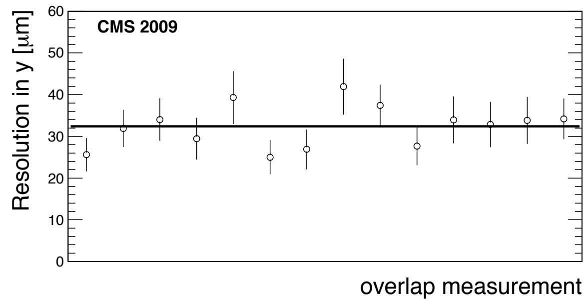

Figure 10.6: As in Fig. 10.5 but along the longitudinal coordinates.

computed the double difference, Δx (Δy) between Δx_{hit} (Δy_{hit}) and the differences Δx_{pred} (Δy_{pred}) between the expected positions from trajectory extrapolation. The double difference distribution was then fitted with a Gaussian and the uncertainty on the predicted position quadratically subtracted from the width, to recover the intrinsic hit resolution. The results are shown in Figs. 10.5 and 10.6. Each point represents the resolution measurement for a different pair of overlapping modules. The mean value is shown as a solid line in the plot. The r.m.s. resolutions are 12.9±3.0 μm along the transverse coordinate (x) and 32.4±4.9 μm along the longitudinal coordinate (y). The same technique on a Monte Carlo sample gives results in agreement with data.

Ionization charges produced by particles traversing the pixel sensors drift under the combined electric and magnetic fields. The ensuing Lorentz angle between drift direction and electric field leads to a systematic shift of the hit position that has to be corrected. The shift depends on various experimental conditions such as bias voltage, temperature and irradiation, and has therefore to be measured in-situ and monitored. Measurements of the Lorentz angle with the barrel pixel detector were performed with the 2009 cosmic ray run (CRAFT09 (6)). Since detector operating conditions (bias voltage, temperature, etc.) were different from the 2008 data (CRAFT08), a different Lorentz angle was expected (7; 8). The angle was measured by finding the minimum of the mean cluster size distribution, measured as a function of the track incidence angle (9). The result (first row in Table 10.1) is in good agreement with the prediction from the PIXELAV simulation (10). As expected, the measured value (Fig. 10.7) was about 2° lower than for CRAFT08.

The measurements were repeated with tracks from proton collisions using the "grazing angle" technique (11). The transverse cluster dis-

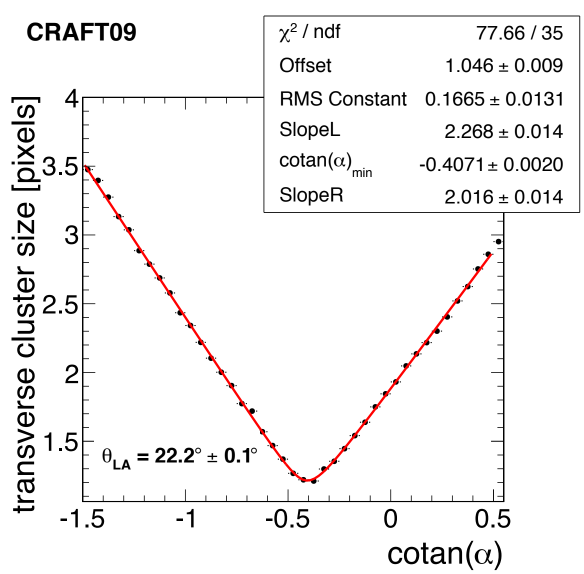

Figure 10.7: Measurements of the Lorentz angle in the 3.8 T magnetic field: pixel cluster size as a function of incidence angle from cosmic rays.

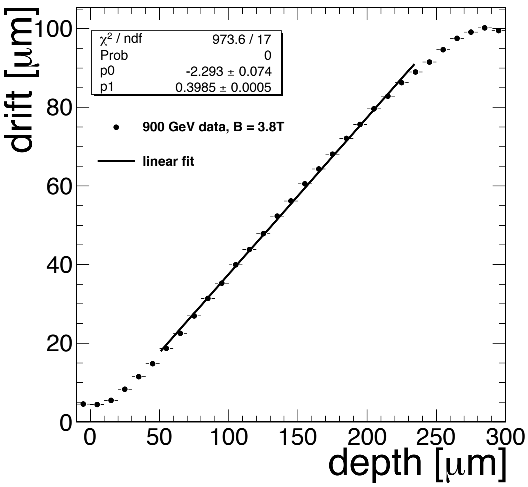

Figure 10.8: Transverse cluster displacement as a function of sensor depth for minimum bias events.

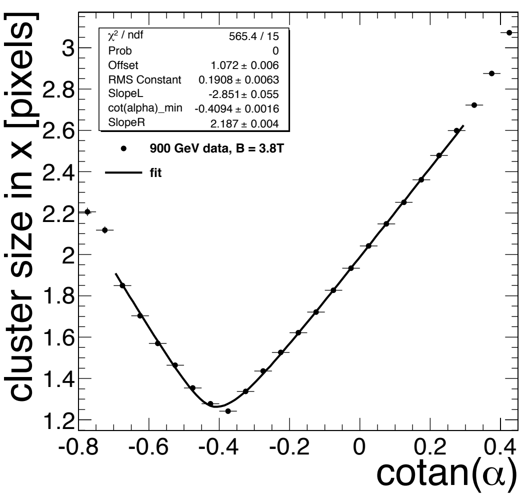

Figure 10.9: Cluster size as a function of incidence angle for minimum bias events. Solid lines represent fits to the data points.

placement was measured as a function of production depth from tracks with shallow impact angles (Fig. 10.8). The large number of low momentum tracks at 900 GeV also allowed a measurement using the cluster size technique (Fig. 10.9). In all cases excellent agreement was obtained with the results of a PIXELAV simulation (Table 10.1).

10.2 Spatial alignment of the silicon pixel and strip tracker

The alignment of the CMS tracker is a complex task in view of the very large number of silicon sensors (about 15′000) and their excellent position resolution. Two alignment algorithms are being used: the *Hit and Impact Point (HIP)* algorithms used by the Zurich groups, and the *Millepede* approach. While the latter is suitable to detect large movements, the former can lead to very precise positions for small distances. Hence the best alignment precision is obtained by applying the *HIP* algorithm starting on sensors positions previously obtained with the *Millepede* algorithm. We collected a large sample of cosmic ray tracks in summer 2009 before LHC operation. The data allowed a precise spatial alignment of the tracker after the hardware interventions of the previous year. The analysis of alignment data taken with pp-collisions is in progress. The alignment of the pixels can be achieved with a typical precision of 2 μm (4μm) in the transverse (longitudinal) directions.

Table 10.1: **Lorentz angle θ_L in the barrel pixel detector determined with two different techniques, using cosmic ray tracks and minimum bias events from LHC collisions.**

sample	method	$\tan\theta_L{}^a$	
		measurement	PIXELAV simulation
cosmic rays	cluster size	0.4071(20)	0.3972(30)
collisions	grazing angle	0.3985(5)	0.4006(5)
collisions	cluster size	0.4094(16)	0.4113(48)

[a] statistical error only

10.3 Improvements to the pixel hit reconstruction

Searches for the Higgs boson or new particles beyond the Standard Model (such as SUSY), depend heavily on the identification of τ-leptons and b-quark jets. For example, the τ-lepton decays into three charged pions (and an invisible neutrino) with a branching ratio of about 10%. Since the transverse momentum of the τ-jet is large compared to the τ mass, the decay pions emerge in a strongly collimated jet in which the charged tracks stay in close proximity. The larger the τ momentum, the more strongly collimated the three tracks, which makes them inseparable when the pixel hits merge into one large cluster. This occurs in the innermost pixel layer when the opening angle between the two trajectories is below 5 mr, which corresponds to a transverse momentum of 150 GeV/c for a typical 3-prong decay. This effect deteriorates the measurement of the particle trajectories and the reconstruction of the τ mass. Thus, an excellent spatial resolution is needed for τ reconstruction.

The measured cluster charge and track impact angles can be used to discriminate merged hits from isolated hits. Figure 10.10 shows a simulation of the pixel cluster charge distribution, corrected for the traversed path length, for merged and isolated clusters produced by τ decays. Merged clusters produce satellite peaks at twice or three times the minimum ionizing energy deposit and can therefore be recognized.

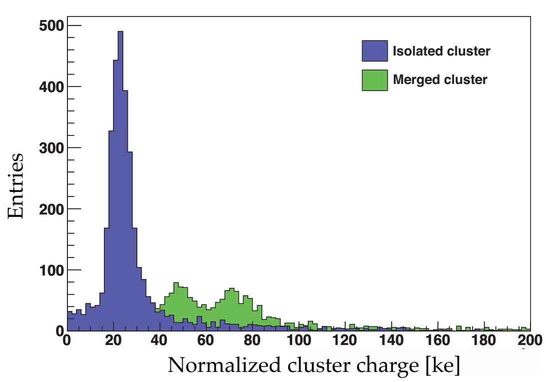

Figure 10.10: Pixel cluster charge distribution (corrected for impact angle) for hadronic τ decays. The blue histogram shows isolated clusters, while the green histogram shows the merged hits.

From simulations we have also shown that the splitting of merged clusters has an impact on the track parameter resolutions and on the b-jet selection efficiency. We are therefore implementing a cluster splitting technique in the pixel hit reconstruction software which we intend to use for Higgs searches in τ decays.

10.4 Improvements to b-quark tagging techniques

The b-tagging algorithms in the CMS fast Monte Carlo simulation (12) are under our responsibility. The fast b-tagging uses the same algorithms as the full detector simulation and reconstruction. The disadvantage is that the agreement between fast and full (GEANT4 based) detector simulations is not perfect in all regions of phase space. Various improvements have therefore been implemented:

- **pixel hit merging**
  Since the track reconstruction in the fast simulation does not include the step of pattern recognition, faked tracks are not reproduced. Thus, detector effects such as hit sharing between tracks or cluster merging (section 10.3), are not simulated. To estimate the contribution from these effects, a pixel hit merging algorithm was implemented in the fast simulation and tracks with shared hits were removed in the full detector reconstruction.

- **material effects**
  Particles traversing the tracking detectors are subject to multiple scattering, nuclear interactions and conversions (for photons).

The fast simulation uses a simplified detector geometry and the material budget is tuned according to the amount of photon conversions obtained from the full simulation. This simplified geometry potentially introduces biases which affect the tracking performance in the inner layers. These effects have been investigated by varying the thickness of materials.

- **pixel hit parameterization**
  The resolution of pixel hits was parameterized and tuned according to the full detector simulation.

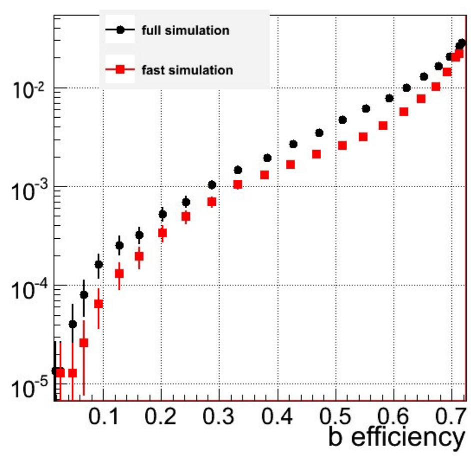

Figure 10.11:
Misidentification rate of the "secondary vertex" b-tagging algorithm vs. tagging efficiency, before the improvements described in the text.

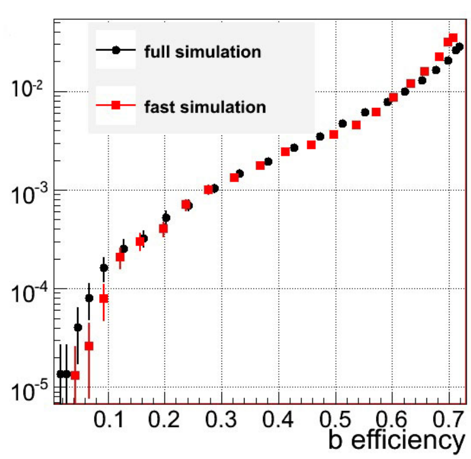

Figure 10.12:
As in Fig. 10.11 after the improvements.

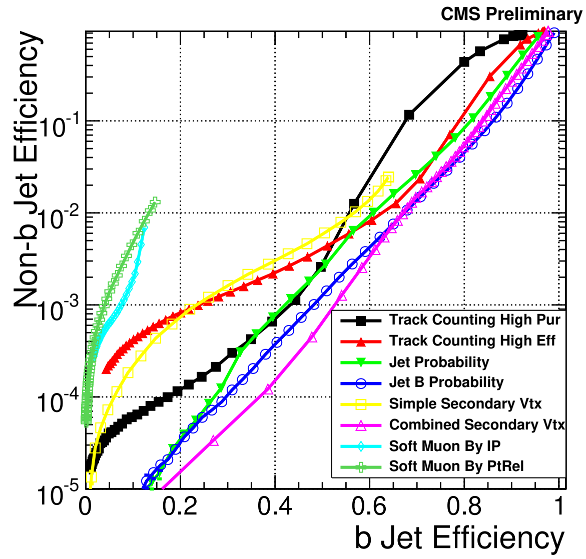

Figure 10.13: Mistagging efficiency of all CMS b-tagging techniques vs. b-tagging efficiency (from refs. [13; 14]).

Figures 10.11 and 10.12 display the performance of the secondary-vertex based b-tagging algorithm, without and with the new features, respectively. Depending on b-tagging efficiency, the misidentification rate increases by up to a factor of two, and agrees almost perfectly with the full simulation.

A comparison of the CMS b-tagging algorithms is shown in Fig. 10.13. During the 2010 runs we will monitor of the physics observables used in the b-tagging algorithms and determine the algorithm performances with data-driven methods.

10.5 Studies of $B_s \rightarrow (J/\psi)\phi$ and B_c-decays

The lifetime of the B-mesons is relatively long and the CMS pixel detector can determine B-decay vertices precisely. This reduces the background substantially and facilitates measurements of the B_s mass and mean life, and the measurement of B_s mixing parameters, such as the width

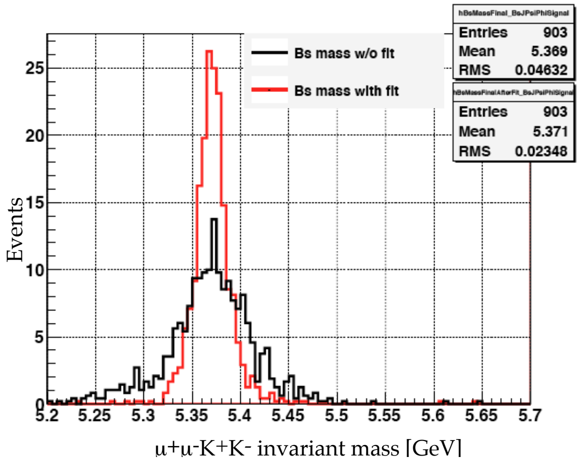

Figure 10.14: Mass distribution in the B_s region with and without kinematic fit (simulation).

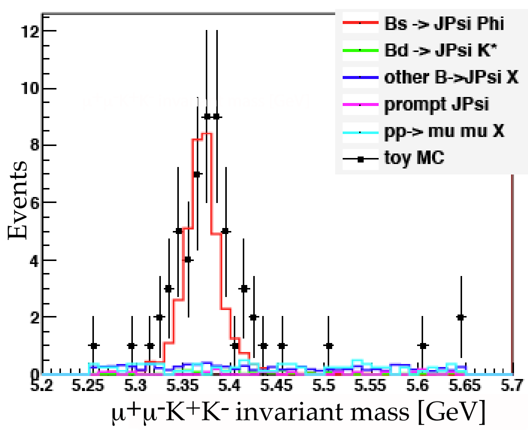

Figure 10.15: Reconstructed B_s-mass spectrum for 1pb^{-1} at 10 TeV.

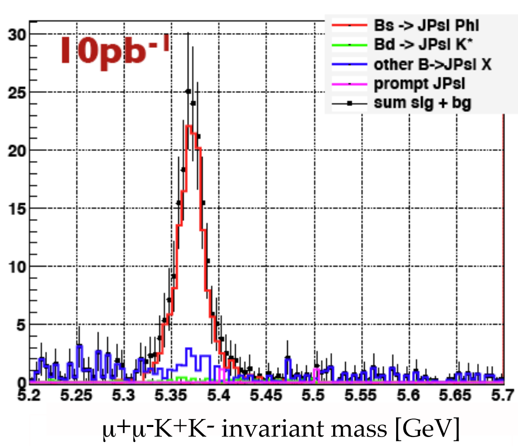

Figure 10.16:
Reconstructed B_s-mass spectrum for 10 pb^{-1}.

difference between the B_s^H andB_s^L mass eigenstates, together with the CP violating weak phase, which is sensitive to physics beyond the Standard Model.

Physics involving the b-quark will be among the first studies to be performed with LHC data. We have studied in detail the decay channel $B_s \to (J/\psi)\phi \to (\mu^+\mu^-)K^+K^-$ (9; 15). B_s-decays into J/ψ are selected during data taking using a di-muon trigger. Events are further selected offline by requiring two opposite sign muons from the J/ψ and a common vertex from the J/ψ and ϕ particles, and cutting on the transverse momentum of the kaons from ϕ decay. To reconstruct $B_s \to (J/\psi)\phi$ additional quality cuts are applied on the observables and a kinematic fit is applied. Figure 10.14 shows the factor of two improvement to the reconstructed B_s mass width obtained with the kinematic fit.

We will observe the $B_s \to (J/\psi)\phi$ decay already with an integrated luminosity of 1 pb^{-1}. We will then determine the B_s mass and mean life with 10 pb^{-1}, measure the CP-even and CP-odd components with more than 50 pb^{-1}, and extract the CP weak phase difference with more than 100 pb^{-1}. Figures 10.15 and 10.16 show the reconstructed B_s invariant mass for 1 pb^{-1} and 10 pb^{-1}, respectively (from two

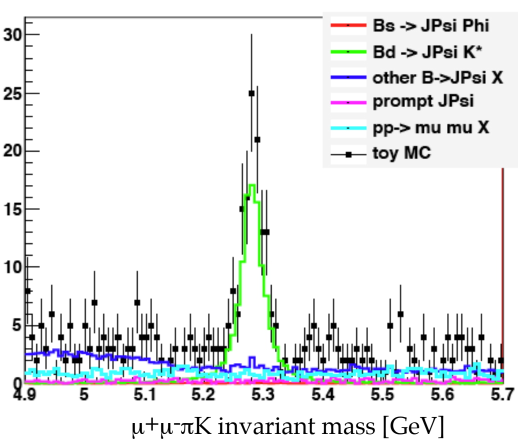

Figure 10.17:
Reconstructed B_d-mass spectrum for 1pb^{-1}.

analyses with slightly different cuts). The well measured channel $B_d \to (J/\psi)K^*$ was selected as calibration channel. Figure 10.17 shows the reconstructed B_d-mass using the same analysis code as for the B_s case shown in Fig. 10.16.

The B_c-meson is unique in that it is made of two different heavy quarks (b and c). We have started analyses to measure its mass and lifetime in two promising decay channels: $B_c^\pm \to J/\psi\ \rho^0\ \pi^\pm$ and $B_c^\pm \to J/\psi\ \rho^\pm$. The cleaner J/ψ-decay is into $\mu^+\mu^-$, but decays into e^+e^- pairs are also under investigation. In the first case, the ρ^0 decays into two charged pions, hence five tracks are associated to the same secondary vertex. In the latter case, the ρ^+ decays into a neutral and a charged pion, so three tracks and one electromagnetic cluster are produced.

10.6 Modeling of Higgs and jet production at the LHC

One of the main motivations for the LHC physics program is the study of the electroweak symmetry breaking mechanism and the Higgs boson discovery. The direct production of the Higgs boson via a top loop coupling to the incoming gluons has the largest cross-section, and hence is the most promising discovery channel, in particular via decays into two vector bosons. The survey of the different Higgs boson signatures above the Standard Model background will rely on data-driven studies, but also on comparison with Monte Carlo expectations.

For years, efforts have been made to develop Monte Carlo programs capable to model the collisions as accurately as possible, using both fixed order perturbative calculations and by merging matrix-element and parton-shower algorithms. Using the generators Herwig, HNNLO, Madgraph/Madevent, MC@NLO, POWHEG and Sherpa (16), one of us participated in the study of Higgs boson production via gluon-gluon fusion We have provided results using a jet merging technique (K_t-MLM) implemented in $Madgraph\ /\ MadEvent$. While a minimal set of parameters was chosen to be fixed for all simulations (parton densities, t-mass, center-of-mass energy), no detailed tuning was performed. The predictions from event generators for rapidity and transverse momentum of the Higgs boson are shown in Figs. 10.18 and 10.19, respectively (16).

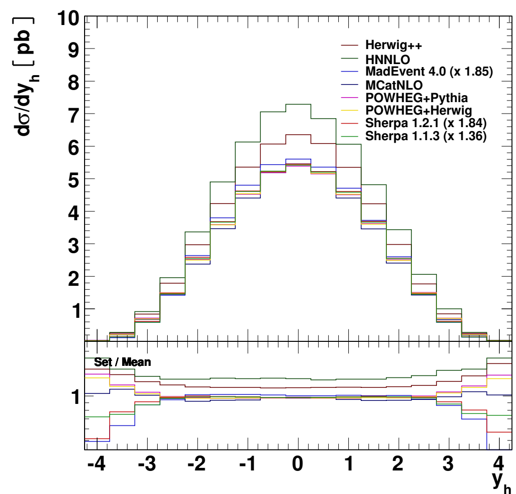

Figure 10.18: Rapidity distributions of the Higgs boson for LHC collisions predicted by different Monte Carlo simulations (from [16]).

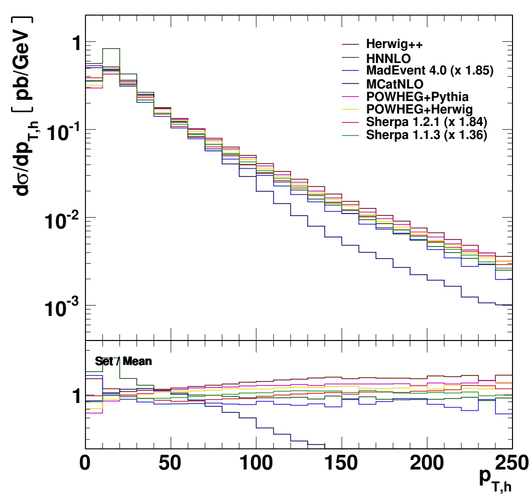

Figure 10.19: The corresponding transverse momentum distributions

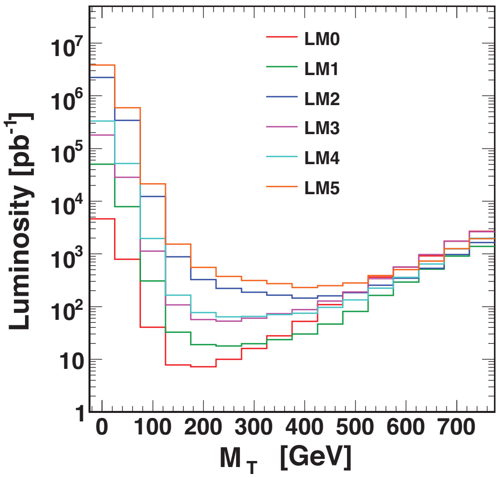

Figure 10.20: Integrated luminosity required for SUSY discovery as a function of cuts on M_T for various points of the mSUGRA parameter space[21].

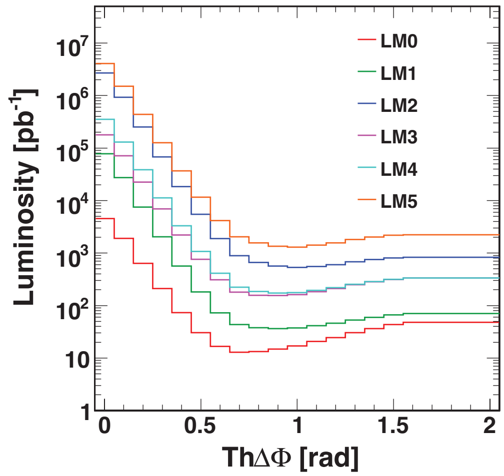

Figure 10.21: As for Fig. 10.20 but with cuts on $Th\Delta\Phi$.

10.7 Search for Supersymmetry (SUSY) in multi-jet final states

In previous annual reports we reported on SUSY decays into 2 jets, no missing lepton and large missing energy. In 2009 the Monte Carlo study of Supersymmetry in di-jet events (17) was refined and extended to higher jet multiplicities (18). Other approaches to reduce background have been studied and compared in terms of signal significance and robustness against systematic uncertainties. The basic selection for SUSY searches in hadronic final states relies on missing transverse energy. The corresponding cut is very effective in rejecting a large part of the QCD multi-jet background. Apart from the missing transverse energy M_T, another variable based on the global transverse thrust is useful, $Th\Delta\Phi$ (19): The direction of the thrust axis is used to combine all jets in an event into two pseudo-jets emitted into two hemispheres. The variable $Th\Delta\Phi$ is then the angle between the two pseudo-jets in the transverse plane.

Ignoring in a first step systematic uncertainties, the required minimum luminosity for a 5σ discovery of SUSY beyond Tevatron reach (20) is about 10 pb^{-1} (Figs. 10.20 and 10.21). Systematic errors are due to uncertainties in the jet energy scale and the azimuthal angle. They were studied in detail and found to lead to an increase of the required minimum luminosity by about a factor two to three, depending on whether the $Th\Delta\Phi$ or the M_T cut is used.

10.8 Upgrades of the computing infrastructure

We have assembled a computing cluster (TIER4) for our group at CERN, which is regularly upgraded. The computing cluster proved to be essential to achieve prompt physics results, a clear asset in the early phases of data analysis, when the data load will not be too heavy. In 2009 five additional blades were installed for a total of 20 (3.3 GHz) CPU cores. The storage capacity was expanded to 50 TB by adding a new 14 TB disk array. The network was submitted to a major revision and the GB Ethernet switches were replaced with a 10 GB device. One additional 4 GB FiberChannel switch was installed. For the CMS data taking during 2010, new software releases based on Scientific Linux 5 (SLC5) will benefit from improved C++ compilers. The current SLC4 will be deprecated. All of our machines are in the proces of being updated to SLC5.

10.9 Preparation for future upgrades of the CMS pixel detector

As a consequence of the latest LHC schedule review, the replacement of the current pixel system was postponed to the years 2016/17. Major upgrades are foreseen for the detector layout with the addition of a fourth barrel layer and a third disk in both endcap sections. The material thickness will be reduced by up to a factor of two in the central tracking region, thanks to new readout electronics and the evaporative cooling technique. The 0.13 μm CMOS technology for the front-end chip in the innermost layers is currently under evaluation. This technology allows a reduction of the pixel cell size, with corresponding improvements to the position and track resolutions in dense jets.

We performed a preliminary Monte Carlo study of the expected detector performances. The resolution on the hit position was studied as a function of pseudorapidity and cluster size with a sample of simulated muons. The resolution of the four track parameters that are measured by the pixel detector, namely the angles θ and ϕ, and the transverse and longitudinal impact parameters d_0 and d_z was also studied. As expected, the precision of track reconstruction is dominated by multiple scattering at low momenta, reaching an asymptotic value of $\sim$10 μm, respectively $\sim$30 μm, on the two impact parameters at high momenta. Estimates of the detector occupancy and b-tagging performance will be performed on a sample of simulated collisions events, and various pixel cell sizes will be compared.

[1] S. Chatrchyan *et al.* (CMS Collaboration), Journal of Instrumentation **3** (2008) S08004

[2] Y. Allkofer *et al.*, Nucl. Instr. Meth. in Phys. Res. **A584** (2008) 25

[3] V. Chiochia *et al.*, Nucl. Instr. Meth. in Phys. Res. **A568** (2006) 51

[4] A. Schmidt *et al.*, Journal of Instrumentation **4** (2009) P05003

[5] S. Chatrchyan *et al.*, (CMS Collaboration), Journal of High Energy Physics **02** (2010) 041

[6] S. Chatrchyan *et al.* (CMS Collaboration) Journal of Instrumentation **5** (2010) T03007

[7] A. Dorokhov *et al.*, Nucl. Instrum. Meth. in Phys. Research **A530** (2004) 71

[8] A. Dorokhov *et al.*, Nucl. Instrum. Meth. in Phys. Research **A560** (2006) 112

[9] L. Wilke, PhD Thesis, University of Zurich (2009)

[10] M. Swartz, Nucl. Instrum. Meth. **A511** (2003) 88

[11] L. Wilke, V. Chiochia, T. Speer, CMS Note 2008/012

[12] A. Schmidt, IEEE Nuclear Science Symposium Conference Record **N37-4** (2008) 2795

[13] W. Adam *et al.*, CMS Analysis Note 2009/085 and CMS PAS BTV-09-001.

[14] A. Schmidt, Proc. of Science (EPS-HEP 2009) 439

[15] K. Prokofiev, PhD Thesis, University of Zurich (2005)

[16] J. M. Butterworth *et al.*, Summary Report from the Les Houches 2009 Workshop on TeV Colliders, prep. arXiv:1003.1643 (2010)

[17] T. Rommerskirchen *et al.*, CMS Note PAS SUS-08-005

[18] T. Rommerskirchen *et al.*, CMS Note PAS SUS-09-001

[19] M. Weber *et al.*, CMS Note PAS QCD-08-003 (2008)

[20] G.L. Bayatian *et al.* (CMS Collaboration), J. Phys. G: Nucl. Part. Phys. **34** (2007) 995

[21] T. Rommerskirchen, PhD Thesis (in preparation)

11 Superconductivity and Magnetism

M. Bendele, S. Bosma (since November 2009), Z. Guguchia (since September 2009), A. Ichsanov (since October 2009), H. Keller, F. Murányi, P. Prem, J. Roos, S. Strässle, S. Weyeneth, B. M. Wojek

Visiting scientists: M. V. Eremin, B. Graneli, B. I. Kochelaev, R. Puzniak, A. Shengelaya
Emeritus members: K. A. Müller (Honorarprofessor), T. Schneider (Titularprofessor), M. Mali

in collaboration with:
ETH Zürich (J. Karpinski), Paul Scherrer Institute (K. Conder, R. Khasanov, E. Morenzoni), Max-Planck-Institute for Solid State Research Stuttgart (A. Bussmann-Holder), IBM Rüschlikon Research Laboratory (J. G. Bednorz, S. F. Alvarado), University of Geneva (Ø. Fischer, J. M. Triscone), University of Rome (D. Di Castro), Kazan State University (A. Dooglav, M. V. Eremin, B. I. Kochelaev), Polish Academy of Sciences (R. Puzniak), Tbilisi State University (A. Shengelaya), University of Tokyo (T. Sasagawa, H. Takagi), University of British Columbia (R. F. Kiefl).

In the following we report on selected projects in the research field of high-temperature superconductors (HTS) and materials with novel electronic properties. Our recent activities include studies by means of a variety of techniques, such as of muon-spin rotation (μSR), electron paramagnetic resonance (EPR), nuclear magnetic resonance (NMR), nuclear quadrupole resonance (NQR), and SQUID and torque magnetometry. Besides focusing on the cuprates and other, more conventional superconductors, the investigations have been further extended to the recently discovered iron-based superconductors.

11.1 Field dependent superfluid density in optimally doped SmFeAsO$_{1-x}$F$_y$

After the discovery of superconductivity in LaFeAsO$_{1-x}$F$_x$ with a transition temperature $T_{\mathrm{c}} \simeq 26$ K, a whole new family of iron pnictide superconductors was found (1) with a maximum $T_{\mathrm{c}} \simeq 55$ K for SmFeAsO$_{1-x}$F$_y$ (2). Various experiments indicate multi-gap superconductivity within the family REFeAsO$_{1-x}$F$_y$ (RE = rare-earth element) (3). Furthermore, the magnetic penetration depth anisotropy, $\gamma_\lambda = \lambda_c/\lambda_{ab}$, increases with decreasing temperature, in contrast to the upper critical field anisotropy, $\gamma_H = H_{\mathrm{c2}}^{||ab}/H_{\mathrm{c2}}^{||c}$, which decreases with decreasing temperature (3; 4), similar to that of the two-gap superconductor MgB$_2$ (5; 6), although with reversed slopes. Here λ_i and $H_{\mathrm{c2}}^{||i}$ denote the magnetic penetration depth and the upper critical field components, respectively, along the crystallographic direction i (ab-plane or c-axis).

Besides of the influence of the magnetic field H and temperature T on the anisotropy, the direct influence of H and T on λ is essential in probing multi-gap superconductivity (7). Importantly, the superfluid density $\rho_{\mathrm{s}} = n_{\mathrm{s}}/m^*$, with n_{s} being the superfluid carrier density and m^* the effective carrier mass, can be probed directly by measuring $\lambda^{-2} \propto \rho_{\mathrm{s}}$.

A single crystal sample of nominal composition SmFeAsO$_{0.8}$F$_{0.2}$ was investigated by torque magnetometry in order to determine $\lambda_{ab}(H)$. The magnetic torque $\vec{\tau} = \mu_0(\vec{m} \times \vec{H})$, related to the magnetic moment $\vec{m}$, was recorded in dependence of the angle θ between the magnetic field $\vec{H}$ and the c-axis of the crystal. During the measurement, H was rotated clockwise and counterclockwise around the sample at constant temperature T. The clockwise (θ^+) and counterclockwise

(θ^-) torque scans were averaged according to $\tau_{\rm rev}(\theta) = [\tau(\theta^+) + \tau(\theta^-)]/2$. A theoretical expression for the angular dependence of the torque, involving the two anisotropy parameters γ_λ and γ_H independently (8), was used to analyze the data. Representative experimental torque data collected for various magnetic fields together with the calculated curves are presented in Fig. 11.1. Obviously λ_{ab} increases substantially with increasing magnetic field (see insert to Fig. 11.1) (8).

In accordance with the result in Fig. 11.1, the data plotted in terms of the superfluid density λ_{ab}^{-2} imply a suppression of the superfluid density as the field is increased. The field dependence of λ_{ab}^{-2}, derived from the torque experiment together with μSR data taken on a larger powder sample of the same compound, are presented in Fig. 11.2. Evidently, λ_{ab}^{-2} gets substantially suppressed with increasing magnetic field at all temperatures studied and falls, when normalized to $\lambda_{ab}^{-2}(1.4\,\mathrm{T}/\mu_0)$, on a universal curve (see Fig. 11.2). We estimate a suppression of the superfluid density by 20% as the field increases from 0 to 1.4 T (8).

The observed magnetic field dependence of λ_{ab}^{-2} is absent in single-gap superconductors but has been observed in various multi-band superconductors, where the cases of MgB_2 (7; 9) and $La_{1.83}Sr_{0.17}CuO_4$ (10) have been analyzed in detail. The analogy to these systems suggests that related physics applies here. Assuming that $SmFeAsO_{1-x}F_y$ is a fully-gapped superconductor, a two-gap model (8; 11) is used to calculate the superfluid density $\rho_{\rm s} = \rho_{\rm s1} + \rho_{\rm s2}$, stemming from the two coupled gaps (Δ_1, Δ_2). Within this approach the calculated zero-temperature gaps are $\Delta_1(0) = 13.83$ meV and $\Delta_2(0) = 5.26$ meV. With increasing magnetic field the superfluid density is only suppressed in the band with the small gap $(\rho_{\rm s2}, \Delta_2)$ where the corresponding intra-band interaction approaches zero with increasing field. The total superfluid density $\rho_{\rm s}(H)$ is expressed as a sum of a contribution from the band with the large gap, $\rho_{\rm s1}$, which

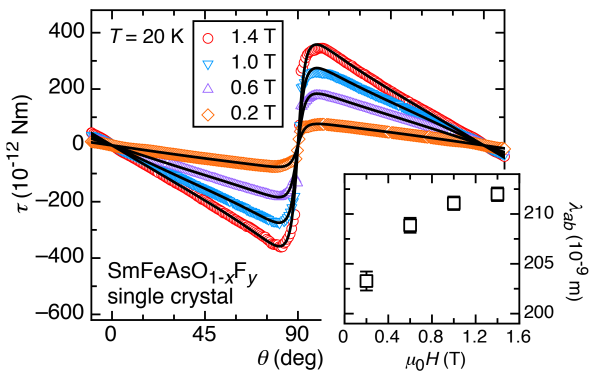

Figure 11.1: Angular dependent, reversible torque for single crystal $SmFeAsO_{1-x}F_y$ in various magnetic fields. Solid lines are fits to the data, from which λ_{ab} was extracted. The insert shows the field dependence of λ_{ab}.

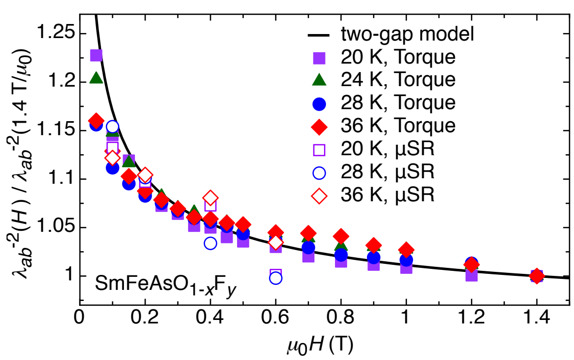

Figure 11.2: Universal behavior of ρ_s of single crystal $SmFeAsO_{1-x}F_y$ observed for all investigated temperatures, determined by magnetic torque and μSR experiments, normalized to 1.4 T. The black line is calculated using a two-gap model.

is independent of the field, and a field dependent contribution from the band with the small gap, $\rho_{\rm s2} \propto 1/\sqrt{H}$. A fit to the normalized superfluid density data (see Fig. 11.2) gives good agreement. It is important to emphasize that although $\rho_{\rm s}$ is suppressed by 20% in small fields, $T_{\rm c}$ is almost not changing on the same field scale, consistent with high values of $H_{\rm c2}$. This can be understood in terms of a suppression of the intra-band coupling within the band of the small gap, having a pronounced influence on the corresponding $\rho_{\rm s}$, but almost no effect on $T_{\rm c}$ (9).

[1] Y. Kamihara *et al.*, J. Am. Chem. Soc. **130**, 3296 (2008).
[2] Z.-A. Ren *et al.*, Chin. Phys. Lett. **25**, 2215 (2008).
[3] S. Weyeneth *et al.*, J. Supercond. Nov. Magn. **22**, 347 (2009).
[4] S. Weyeneth *et al.*, J. Supercond. Nov. Magn. **22**, 325 (2009).
[5] M. Angst *et al.*, Phys. Rev. Lett. **88**, 167004 (2002).
[6] J. D. Fletcher *et al.*, Phys. Rev. Lett. **95**, 097005 (2005).
[7] M. Angst *et al.*, Phys. Rev. B **70**, 224513 (2004).
[8] S. Weyeneth *et al.*, arXiv:cond-mat/0911.5420v1 (2009).
[9] M. Eisterer *et al.*, Phys. Rev. B **72**, 134525, (2005).
[10] R. Khasanov *et al.*, Phys. Rev. Lett. **98**, 057007 (2007).
[11] A. Bussmann-Holder *et al.*, J. Supercond. Nov. Magn. **23**, 365 (2010).

11.2 Pressure induced static magnetic order in superconducting $FeSe_{1-x}$

Besides materials containing iron-arsenic layers (*e.g.* FeAs-layers), superconductivity was observed as well in other iron-based compounds as in the $FeSe_{1-x}$ system (1). The transition temperature T_c of $FeSe_{1-x}$ reaches values up to 37 K by applying hydrostatic pressure (2). It has the simplest crystallographic structure among the Fe-based superconductors consisting of layers with a square Fe sheet tetrahedrally coordinated by Se (1). We report on a detailed investigation of the electronic phase diagram of the $FeSe_{1-x}$ system as a function of pressure up to 1.4 GPa by means of AC magnetization and muon-spin rotation measurements. These techniques are direct and bulk sensitive. At a pressure $p \simeq 0.8$ GPa the non-magnetic and superconducting $FeSe_{1-x}$ enters a region where static magnetic order is realized above T_c, and bulk superconductivity coexists and competes on short length scales with the magnetic order below T_c. For even higher pressures an enhancement of both the magnetic and the superconducting transition temperatures, as well as of the corresponding order parameters is observed. These exceptional properties make $FeSe_{1-x}$ to be one of the most interesting superconducting systems investigated extensively at present.

The phase diagram of the recently discovered Fe-based high-temperature superconductors (HTS) shares a common feature with cuprates and heavy fermion systems: The parent compounds of the Fe-based HTS, such as REOFeAs, AFe$_2$As$_2$ (A = alkaline earth metal) and FeCh (Ch = chalcogen) (3; 4; 5) exhibit long-range static magnetic order. Upon doping or application of pressure (chemical or external), magnetism is suppressed and superconductivity emerges.

It is possible to determine T_c as well as the Néel temperature T_N in a region where both magnetism and superconductivity coexist.

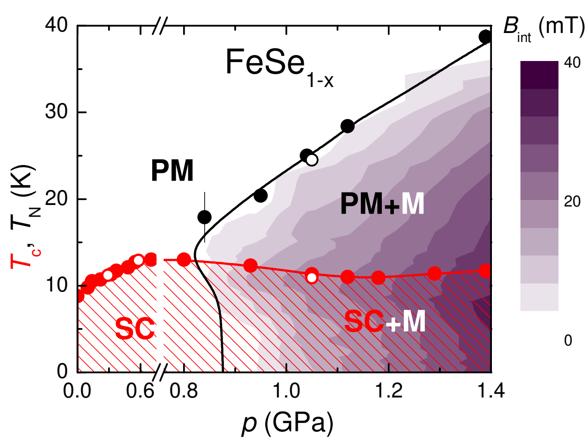

Figure 11.3:
Pressure dependence of the superconducting transition temperature T_c, the magnetic ordering temperature T_N, and the internal field B_{int} (magnetic order parameter) obtained from AC susceptibility and muon-spin rotation experiments of $FeSe_{1-x}$. The $T_c(p)$ and $T_N(p)$ lines are guides to the eye. The closed and the open symbols refer to the samples $FeSe_{0.94}$ and $FeSe_{0.98}$, respectively. SC, M, and PM denote the superconducting, magnetic, and non-magnetic (paramagnetic) states of the sample.

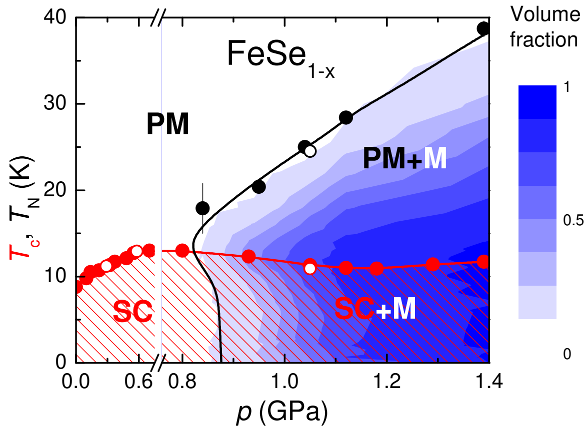

Figure 11.4: Pressure dependence of T_N, T_c, and the magnetic volume fraction of FeSe$_{1-x}$. The meaning of the symbols are the same as in Fig. 11.3.

The here obtained phase diagram is presented in Figs. 11.3 and 11.4. The transition temperature T_c shows a monotonic increase with pressure up to $p \simeq 0.8$ GPa. Static magnetic order is established for $T_c < T < T_N$, and bulk superconductivity sets in below T_c. The competition of the two ground states in this pressure range is evident from the following two observations: First, T_c decreases as a function of pressure as soon as magnetic order appears, leading to the local maximum at $p \simeq 0.8$ GPa in $T_c(p)$ (Fig. 11.5a). Second, the internal field $B_{\rm int}$ (magnetic order parameter), as well as the magnetic volume fraction, decrease as a function of temperature below T_c showing that magnetism, which develops at higher temperatures, becomes partially (or even fully) suppressed by superconductivity (Fig. 11.5b). The superconducting volume fraction is close to 100% for all pressures, while the magnetic fraction increases with increasing pressure and reaches $\simeq$ 90% at the highest pressure $p \simeq 1.39$ GPa. In other words, both ground states coexist in the full sample volume at 1.39 GPa. The data do not provide any indication for macroscopic phase separation into superconducting and magnetic clusters (larger than a few nm in size). Actually, the data rather point to a coexistence of both order parameters on an atomic scale and seem to be stabilized by pressure, since T_c as well as T_N and the magnetic order parameter simultaneously increase with increasing pressure. This observation provides a new challenge for theories describing the mechanism of high-temperature superconductivity (6).

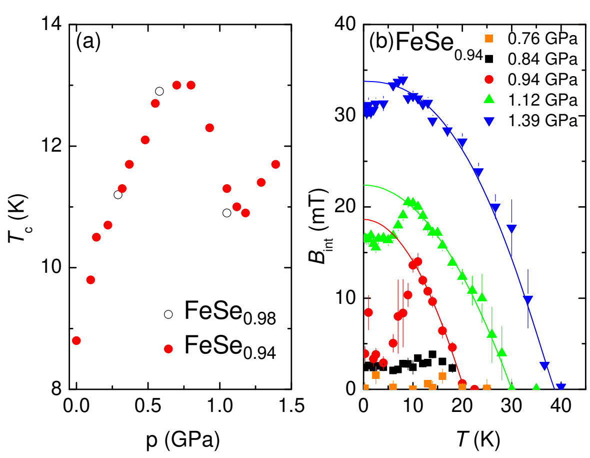

Figure 11.5: (a) Dependence of T_c on pressure p of FeSe$_{0.94}$ and FeSe$_{0.98}$. (b) Dependence of the internal field at the muon stopping site $B_{\rm int}$ which is proportional to the magnetic order parameter. The solid lines represent calculated $B_{\rm int}(T)$ using $B_{\rm int}(T) = B_{\rm int}(0)[1-(T/T_N)^\alpha]^\beta$ in the region $T_c(p) \le T \le T_N$ (α and β are the power exponents).

[1] F.-C. Hsu et al., Proc. Nat. Acad. Sci. USA **105**, 14262 (2008).
[2] S. Margadonna et al., Phys. Rev. B **80**, 064506 (2009).
[3] H. Luetkens *et al.*, Nature Mater. **8**, 305 (2009).
[4] A. Jesche *et al.*, Phys. Rev. B **78**, 180504(R) (2008).
[5] R. Khasanov *et al.*, Phys. Rev. B **80**, 140511(R) (2009).
[6] M. Bendele *et al.*, Phys. Rev. Lett. **104**, 087003 (2010).

11.3 NMR investigations of orbital currents in YBCO compounds

The concept of broken symmetry is a possible key element for a comprehensive theory of high-temperature superconductivity. In particular, states with broken time-reversal symmetry have been put forward to explain observations for cuprate high-temperature superconductors (1; 2). The t-J Hamiltonian defines states that break time-reversal symmetry, predicting so-called orbital currents (OCs) that are confined to the CuO_2 planes of the cuprates. Among the most prominent OC patterns are the d-density wave (1) and the circulating current (2) schemes.

The body of experimental evidence is not large but nevertheless contradictory. On the one hand, results from neutron spectroscopy (3) and angle resolved photoemission (4) indicate signatures of OCs, whereas measurements of muon-spin rotation and nuclear magnetic resonance (NMR) fail to provide any trace of the currents (5).

NMR is a suitable method to search for OCs (6), since the magnetic fields inevitably produced by OCs may be directly observed. Selected atoms of the sample serve as local magnetic probes, allowing static fields to be detected by the resonance linewidth broadening, and fluctuating fields from the nuclear spin-lattice relaxation measurements.

No evidence for OCs was found in our previous ^{89}Y-NMR study of the cuprate high-temperature superconductor $Y_2Ba_4Cu_7O_{15-\delta}$ (5). Reported here is the subsequent study of a c-axis oriented powder sample of intrinsically underdoped stoichiometric $YBa_2Cu_4O_8$, where we investigated additional local magnetic fields at the Y-site in the pseudogap regime. The ^{89}Y ($\mathrm{I} = 1/2$) isotope is 100% naturally abundant, and insensitive to electric field gradients because of the absence of a quadrupole moment. The well-defined oxygen stoichiometry of $YBa_2Cu_4O_8$ causes the ^{89}Y-NMR line to become exceedingly narrow, thus offering enhanced precision. In addition, compared to (5), more pronounced OC signatures are expected here because of the larger currents following from the lower doping level.

The temperature dependence of the ^{89}Y resonance linewidth were studied at 100 K for two orientations of an external 9 T field: B_0 perpendicular ($B_0 \parallel c$) and parallel ($B_0 \perp c$) to the CuO_2 planes. The line broadening observed corresponds to an additional magnetic field smaller than 0.05 mT, which we take as the upper bound for static OC fields at the Y-site. Since the line broadening was observed for both field directions, it is unlikely to be caused by OCs, making this a rather conservative estimate.

Any dynamic OCs confined to the CuO_2 planes produce magnetic fields, fluctuating either parallel or perpendicular to the crystallographic c-axis. For the spin-lattice relaxation, only magnetic fields that fluctuate perpendicular to the external field are relevant. The field direction depends on the actual OC pattern and is assumed to be independent of the orientation of the applied field. Consequently the ratio of the relaxation times measured for $B_0 \| c$ and $B_0 \perp c$ must change if non-static OCs appear. The investigation of the temperature dependence of the spin-lattice relaxation ratio did not reveal any significant change. Evaluation of the detection limits determined an upper bound of approximately 0.3 mT for any additional fluctuating field amplitude at the Y-site in the temperature range from 300 K to 100 K.

In conclusion, our ^{89}Y-NMR measurements in the pseudogap phase in $YBa_2Cu_4O_8$ show that any additional static magnetic field at the Y-site must be $\lesssim 0.05$ mT. For fluctuating fields an upper bound for the amplitude of approximately 0.3 mT was determined. These new results significantly tighten the previously established constraints for theories of OCs.

[1] S. Chakravarty *et al.*, Phys. Rev. B **63**, 094503 (2001).

[2] C.M. Varma, Phys. Rev. B **73**, 155113 (2006).

[3] Y. Li *et al.*, Nature **455**, 372 (2008).

[4] A. Kaminski *et al.*, Nature **416**, 610 (2002).

[5] S. Strässle *et al.*, Phys. Rev. Lett. **101**, 237001 (2008).

[6] J. E. Sonier*et al.*, Phys. Rev. Lett. **103**, 167002 (2009).

11.4 Oxygen isotope effects within the phase diagram of cuprates

The role of lattice effects in cuprate HTS still is a heavily debated issue. Over past years, a systematic isotope-effect (OIE) study on T_c and other quantities in cuprate HTS has tried to clarify, which role lattice effects play in cuprate systems (see Ref. (1) and references therein). The observed unusual OIEs are beyond the scheme of conventional BCS theory and strongly suggest that lattice effects are essential in the basic physics of cuprate HTS.

Cuprate HTSs exhibit a rich phase diagram consisting of various phases: long range 3D antiferromagnetic (AFM) order, spin-glass (SG) plus coexisting SG+SC state, superconducting (SC) phase and the so-called pseudogap phase. Recently, we performed a detailed OIE study of the various phases observed in all cuprate superconductors, using $Y_{1-x}Pr_xBa_2Cu_3O_{7-\delta}$ as a prototype system of cuprates (2). The various OIE's observed clearly show that lattice effects are effective in all phases of HTS, imposing serious constraints on theoretical models. So far, only a few OIE studies of the pseudogap state were performed for cuprate HTS close to optimal doping. For example, NMR/NQR studies of $YBa_2Cu_4O_8$ revealed a small OIE on the pseudogap temperature, comparable to the one on T_c (3). This is in contrast to results of inelastic neutron scattering experiments on slightly underdoped $HoBa_2Cu_4O_8$ (4), which revealed a large OIE that is sign reversed with respect to the small OIE on T_c.

In order to complete the OIE study of the various phases in the cuprate system $Y_{1-x}Pr_xBa_2Cu_3O_{7-\delta}$, we investigated the OIE on the pseudogap value in this system as a function of Pr doping by means of NMR experiments. The goal of this study was to get better insight in the nature of the pseudogap phase and in the role of lattice effects to form this phase.

A prominent feature of the pseudogap phenomenon is the characteristic temperature dependence of the relative magnetic shift tensor K in the normal conducting phase of underdoped cuprate superconductors. It is best observed in NMR experiments performed on the Cu nuclei in the CuO-$_2$ plane with the external magnetic field applied parallel to the plane, i.e. the component K_{ab} is determined. For this purpose the two investigated partially (90%) $^{16}O/^{18}O$ exchanged powder samples, $Y_{0.7}Pr_{0.3}Ba_2Cu_3O_{7-\delta}$ and $Y_{0.6}Pr_{0.4}Ba_2Cu_3O_{7-\delta}$, were c-axis aligned.

A fit of the well accepted empirical expression $^{16/18}K = C + b \cdot [1 - \tanh^2(\frac{^{16/18}\Delta}{2T})]$ to the observed temperature dependences of $^{16,18}K_{ab}$ (see Fig. 11.6) yields the values for the pseu-

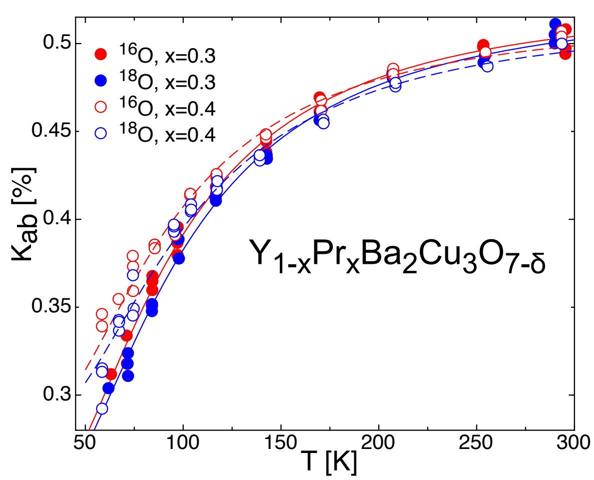

Figure 11.6: Temperature dependence of the magnetic shift K_{ab} of plane ^{63}Cu in $Y_{1-x}Pr_xBa_2Cu_3O_{7-\delta}$ with Pr substitution $x = 0.3$ and $x = 0.4$. Solid and dashed lines are fits to the empirical expression mentioned in the text.

dogap: $^{16}\Delta = 166(6)$ K, $^{18}\Delta = 175(7)$ K for $x = 0.3$ and $^{16}\Delta = 168(7)$ K, $^{18}\Delta = 182(8)$ K for $x = 0.4$, respectively. Using the usual definition we obtain for the OIE coefficient of the pseudo-energy gap value: $\alpha_{0.3}^{\rm PG} = -0.48(50)$ and $\alpha_{0.4}^{\rm PG} = -0.74(60)$.

Due to a strongly inhomogeneous distribution of Pr substitution in our samples the observed ^{63}Cu NMR lines are excessively broadened. This leads to insufficient accuracy in determining the lines' frequency positions and the deduced magnetic shifts. Hence, the errors of our results are large and do not allow for a conclusive comparison with other experiments.

[1] H. Keller, in *Superconductivity in Complex Systems*, eds. K.A. Müller and A. Bussmann-Holder, Structure and Bonding **114**, (Springer-Verlag, Berlin, Heidelberg, New York 2005) pp. 114-143.

[2] R. Khasanov *et al.*, Phys. Rev. Lett. **101**, 077001 (2008).

[3] F. Raffa *et al.*, Phys. Rev. Lett. **81**, 5912 (1998).

[4] D. Rubio Temprano *et al.*, Phys. Rev. Lett. **84**, 1990 (2000).

12 Phase transitions and superconducting photon detectors

H. Grundmann, O. Bossen, K. Inderbitzin, M. Reibelt, H. Bartolf, S. Siegrist, L. Gómez (visiting scientist), A. Engel and A. Schilling

in collaboration with:
Paul Scherrer Institute, University of Bern (K. Krämer), EPF Lausanne (H. Berger), Bhaba Atomic Research Center (G. Ravikumar), Tohoku University (N. Toyota), Universität Karlsruhe (K. Il'in), Deutsches Zentrum für Luft- und Raumfahrt (H.-W. Hübers, A. Semenov), FIRST Lab ETH Zürich.

12.1 Physics of superconducting thin-film nanostructures and fast single-photon detectors

In recent years we have developed a nanostructuring process that allows us to produce superconducting planar structures in the sub-100 nm range (1). Using this process we have fabricated state-of-the-art superconducting nanowire single-photon detectors (SNPD) with quantum-efficiencies in the percent range and pulse widths of only a few nanoseconds with rise times of ~ 200 ps, see Fig. 12.1. These kinds of detectors receive growing interest in the field of quantum information applications (2) and other areas of research and technology, where speed and fast response times are crucial. The working principle of the detector can be sketched in the following way: A superconducting wire of small cross-section—typical dimensions are 100 nm width and 5 nm thickness—is held at a temperature, T, well below its superconducting transition temperature ($T \approx 0.5T_c$). It is operated by applying a bias current, I_b, very close to the critical current (typically I_b between 90% and 95% of I_c). Then, the absorption of a photon constitutes a sufficient disturbance to temporarily drive a section of the wire into its resistive state, which can be registered as a voltage pulse.

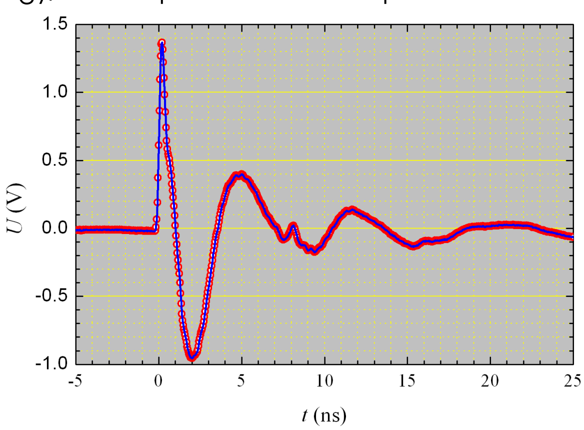

Figure 12.1: Photon-absorption event, indicated by a voltage pulse. The signal was recorded with a digital oscilloscope after amplification of the original pulse. The oscillations after the primary peak at t=0 are due to circuit resonances and reflections.

One important figure of merit is the noise-equivalent power (NEP) of a detector, which is a measure for the probability to detect a "false" photon, when in reality no photon has been absorbed. SNPD have a very low NEP, outperforming most other detector technologies. The NEP of a single-photon detector is proportional to $\sqrt{\Gamma_{\rm DC}}$, where $\Gamma_{\rm DC}$ is the dark-count rate of the detector, *i.e.* the number of events per second without the absorption of a real photon. We have measured the dark counts for three detectors with different strip widths as a function of the reduced bias current, as shown in Fig. 12.2. In an attempt to describe the nearly exponential dependence on the bias current we have developed three models based on three different fluctuation mechanisms (3).

One possible fluctuation mechanism is based on so called thermally-activated phase slips (TAPS) as they appear in one-dimensional superconducting wires (4), resulting in a non-

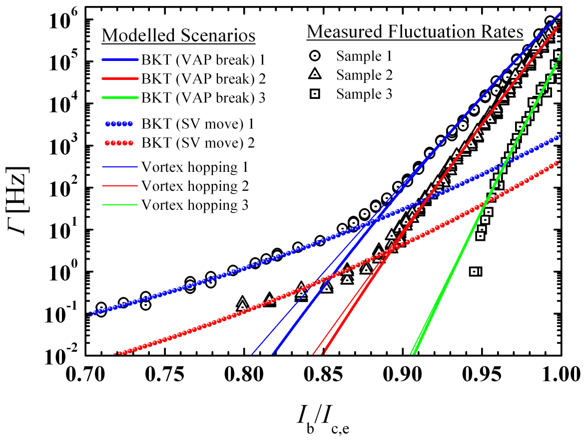

Figure 12.2: Dark count rates as a function of reduced bias current I_b/I_c with widths w=53, 83 and 171 nm for samples 1, 2 and 3, respectively. The symbols mark the experimental dark-count rates. The colored lines represent the calculated rates based on the BKT model (bold and dotted lines), and the vortex hopping model (thin lines). For the 170 nm wide meander the SV BKT mechanism may be below our detection limit.

vanishing resistance even below T_c. However, taking into account the effective cross-sectional area of our meander strips, we were not able to consistently describe the dark-count rates based on TAPS events. This is most likely due to the fact that the cross-sectional area of even the narrowest strip is still about 12 times the coherence length squared, which is usually taken as a criterion for one-dimensionality.

Supported by independent analyses of resistance *versus* temperature measurements near T_c we therefore assume the meanders to be still in the two-dimensional limit (5). Analogous to TAPS in one dimensions, magnetic vortices in two dimensions can be elementary, thermally-activated excitations. We considered two different vortex excitations. First, vortex-antivortex pairs (VAP) of a Berezinskii-Kosterlitz-Thouless (BKT) type (6) that become thermally unbound due to the applied bias current and lead to dark-count events. The other mechanism is based on single vortices hopping over edge barriers that are always present in finite-size superconducting films (7). Both vortex models are able to consistently describe the experimentally measured dark-count rates. The vortex-antivortex model may even allow to describe a "tail" observed for low bias currents (see Fig. 12.2), taking into account that in narrow superconducting strips, single unbound vortices will always be present. However, at the current stage we can also not exclude experimental artifacts (*e.g.* electro-magnetic interferences, ripples in the bias-current, etc.) as the cause for the observed "tail" for low bias currents.

12.2 Unveiling the peak effect in resistivity data of Nb_3Sn using vortex shaking

One of the important goals of our investigations in the field of vortex physics in type-II superconductors is to clarify the influence of transverse or longitudinal "vortex shaking" by the application of an oscillating magnetic field on the physical quantities. To obtain a complete physical picture we have studied possible related effects on the electrical resistivity, a quantity that is known to crucially depend on the details of the vortex physics, in particular of vortex pinning. We have observed (to the best of our knowledge for the first time) that the so-called peak effect in the resistivity data near the upper-critical field of a type-II superconductor can be "switched on and off" by the application of such an external oscillating magnetic field h_{ac} parallel to the main magnetic field H (8).

These experiments have been done on a Nb_3Sn single crystal (in collaboration with N. Toyota, Tohoku University, Sendai, Japan) using a home-built resistivity probe equipped with an ac "shaking" coil that can be used in a commercial PPMS (Physical Property Measurement System, Quantum Design, see Fig. 12.3). In Fig. 12.4 we show the manifes-

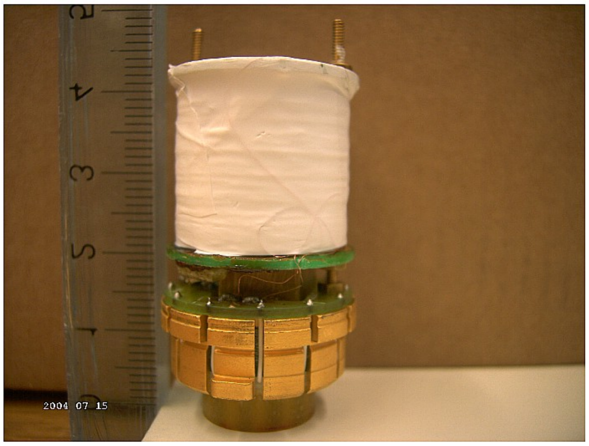

Figure 12.3: Resistivity "puck" with a coil mounted to apply an ac "shaking" magnetic field.

tation of the peak effect as we have measured it conventionally by dc magnetization-hysteresis loop measurements. In Fig. 12.5 we show the temperature dependence of the resistance of the same sample for different magnetic fields H. While the data in the upper part of Fig. 12.5 were taken without any oscillating magnetic field h_{ac}, the data displayed in the lower part were measured with $\mu_0 h_{ac} = 0.58$ mT$\,\|\, H$ at a frequency $f = 1$ kHz. With $h_{ac} = 0$, no feature other than the sharp transition to superconductivity is discernible. With an additional small oscillating magnetic field, however, a clear signature due to the peak effect appears for $\mu_0 H \leq 3$ T. This signature consists

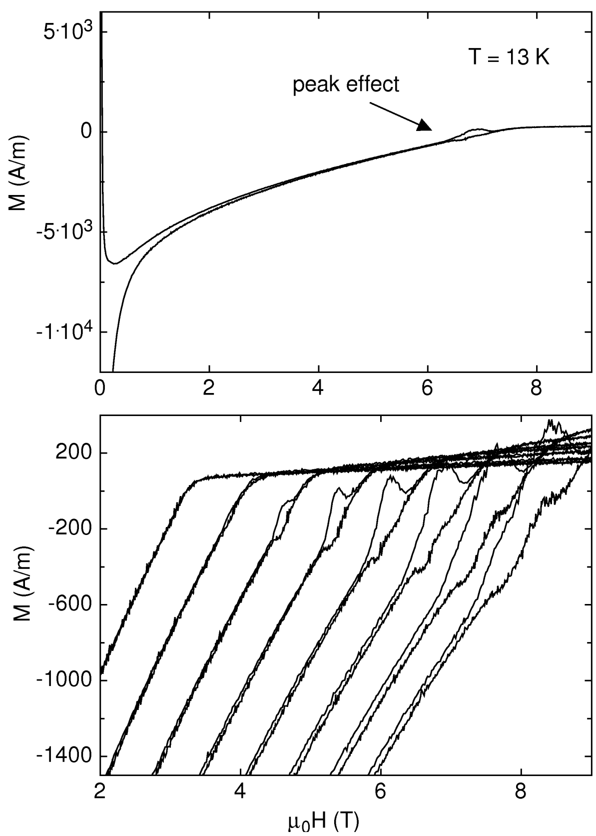

Figure 12.4: Upper panel: dc magnetization-hysteresis curve of a Nb_3Sn single crystal for T = 13 K. Lower panel: parts of the dc magnetization hysteresis curves for different temperatures (from left to right): 15.5 K, 15 K, 14.5 K, 14 K, 13.5 K, 13 K, 12.5 K, 12 K.

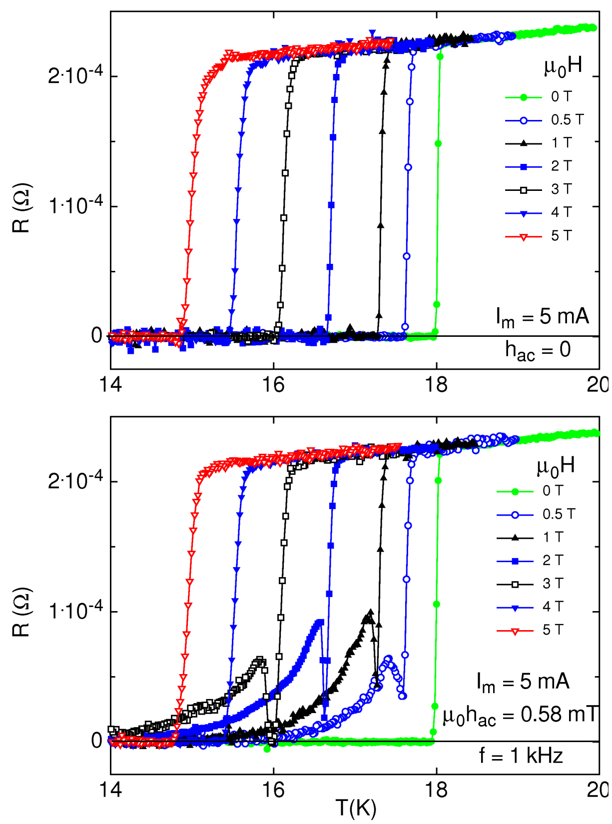

Figure 12.5: Resistance R(T) for magnetic fields $H \parallel c$ without (upper panel) and with (lower panel) an oscillating "shaking" magnetic field (f = 1 kHz, $\mu_0 h_{ac} = 0.58$ mT) superimposed.

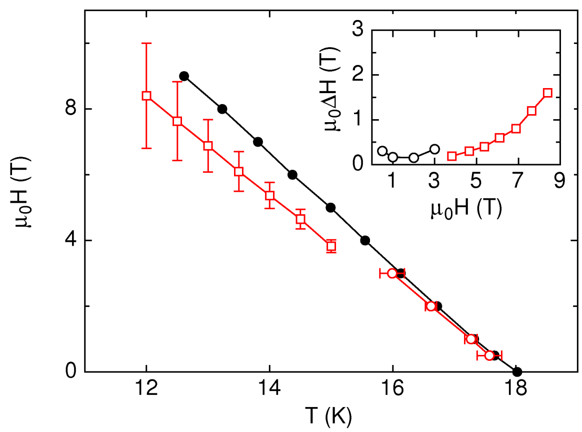

Figure 12.6:
Magnetic phase diagram of the investigated Nb_3Sn single crystal as derived from the data shown in Fig. 12.4 and 12.5. Filled circles: upper critical field. Open circles: peak-effect region from R(T) measurements with "vortex shaking". Open squares: peak-effect region from M(H) data. Inset: Magnetic-field dependence of the width of the peak-effect region $\mu_0 \Delta H$ (Circles: resistivity; squares: dc magnetization).

of a region with finite resistance for temperatures T well below T_c which we attribute to the dissipative motion of magnetic vortices, and a pronounced drop right below T_c that must indicate enhanced flux pinning in the peak-effect region.

We have systematically studied the dependence of this effect on the transport current, the "shaking" frequency f and the amplitude h_{ac} of the oscillating magnetic field. The resulting magnetic phase diagram shown in Fig. 12.6 clearly illustrates the 1:1 correspondence of the magnetically and the resistively determined peak-effect data.

We conclude that this technique of measuring $R(T)$ with an external, continuously oscillating magnetic field may be even more sensitive to explore the peak effect than inferring it from corresponding magnetization $M(H)$ measurements alone, at least in some parts of the magnetic phase diagram of a sample. While the peak-effect feature is not discernible at temperatures higher than 15 K in the $M(H)$ data shown in Figs. 12.4 and 12.5, the resistivity data (taken in combination with an ac magnetic field) reveal the peak-effect region also in this high-temperature region of the magnetic phase diagram. Therefore we believe that such resistivity measurements, in combination with an oscillating magnetic field, may turn out to be a versatile tool not only for the investigation of the peak effect, but also for studying other effects where the pinning of magnetic flux lines plays a certain role.

12.3 Construction of an ac-calorimetry experiment for vortex-shaking experiments

In the past we have done numerous experiments using differential-thermoanalysis (DTA) techniques to study phase transitions of various superconductors. Our recent calorimetric experiments on the above mentioned Nb_3Sn single crystal using an external oscillating magnetic field (not shown here) demonstrated, however, that self-heating effects due to eddy currents in combination with a finite resistance near T_c (or as a result of a sudden dissipative motion of vortices) are in some cases limiting the applicability of this technique. To overcome this obstacle and to obtain an even higher resolution in the vicinity of a possible sharp phase transition, we decided to build a specific-heat experiment based on ac calorimetry techniques that uses a periodic heating of the sample and allows for the use of lock-in amplifier electronics. As the base temperature of a sample can be fixed even with self-heating effects present, this technique should allow for much more accurate investigations of possible vortex phase transitions near the upper-critical field of type-II superconductors and in combination with an external ac "shaking" magnetic field.

Figure 12.7: Ac calorimeter puck that fits into a commercial PPMS (Quantum Design Inc.) system.

Two prototypes of such an experiment have been constructed. In both cases a thin sapphire disc suspended on nylon fibers acts as a sample platform, and the sample heater consists of a miniature thick-film resistor. In one version, the temperature difference to the thermal bath is measured with a thermopile of 30 gold-iron *vs.* chromel thermocouples connected in series. In a second version, this difference is measured with resistive thermometers in a Wheatstone-like differential configuration (see Fig. 12.7). Both setups are designed to fit into a commercial PPMS system that also provides the main magnetic field and the base temperature of the thermal bath. This will allow for a fast data acquisition and a reliable operation from $T = 1.8$ K up to room temperature.

12.4 Structural phase transition in magnetic insulators

There has been considerable interest in the unique properties of quantum-spin systems over the last decade. Much effort has been taken, experimentally as well as theoretically, to understand their behaviour in a magnetic field. A certain class of phase transitions, occurring at a critical field H_c and at low temperatures, has been interpreted in terms of a Bose-Einstein condensation (BEC) of magnetic quasi-particles (9; 10).

Previous work in our group focused on the three-dimensional spin system $TlCuCl_3$, mainly because its critical field ($\mu_0 H_c \approx 5.5$ T (12)) is well within reach of our existing cryo-system.

To prove whether a true BEC of the magnetic quasi-particles is formed or not, we earlier attempted to excite collective modes of the spin system via ac susceptometry, but no sign of a long-lived collective mode could be found (13).

We have then proposed that the symmetry of the spin in dimerized quantum magnets spontaneously changes as soon as the BEC sets in (14). The distortion of axial symmetry fixes the phase of the condensate to a constant value and therefore prevents the system from becoming a true superfluid. Signs for such a lattice distortion have been previously reported (15), but the corresponding changes in the crystal lattice could not be assigned to specific atoms in the unit cell of $TlCuCl_3$.

To investigate if a distortion of the axial symmetry takes place at the BEC, we decided to carry out diffraction experiments on a $TlCuCl_3$ single-crystal using both neutron- (at PSI Villigen) and synchrotron x-ray scattering (at the ESRF in Grenoble) techniques. The experiments will be carried out in high magnetic fields ($\mu_0 H = 10$ T) and at low temperature ($T = 1.9$ K).

The single crystals needed for these experiments are grown by Dr. Karl Krämer, University of Bern.

[1] H. Bartolf, A. Engel, L. Gómez, and A. Schilling, Raith application note, Physics Institute of the University of Zurich, Switzerland (2008).

[2] R. H. Hadfield, Nature Photonics, **3**, (2009) 696.

[3] H. Bartolf, A. Engel, A. Schilling, K. Il'in, M. Siegel, H.-W. Hübers, and A. Semenov, Phys. Rev. B, **81**, (2010) 024502.

[4] K. Y. Arutyunov, D. S. Golubev, and A. D. Zaikin, Phys. Rep., **464**, (2008) 1.

[5] A. Engel, H. Bartolf, A. Schilling, A. Semenov, H.-W. Hübers, K. Il'in, and M. Siegel, J. Mod. Optics, **56**, (2009) 352.

[6] J. M. Kosterlitz and D. J. Thouless, J. Phys. C, **6**, (1973) 1181.

[7] J. R. Clem, Bull. Am. Phys. Soc., volume 43 (1998), 411.

[8] M. Reibelt et al., Phys. Rev. B., **81** (2010) 094510.

[9] T. Giamarchi, A. M. Tsvelik, Phys. Rev. B, **59**, (1999) 11398.

[10] I. Affleck, Phys. Rev. B, **43**, (1991) 3215.

[11] H. Tanaka et al., J. Phys. Soc. Jap., **70**, (2001) 939.

[12] T. Nikuni et al., Phys. Rev. Lett., **84**, (2000) 5868.

[13] R. Dell'Amore, doctoral thesis, University of Zurich, 2008.

[14] R. Dell'Amore, A. Schilling and K. Krämer, Phys. Rev. B, **79**, (2009) 014438.

[15] O. Vyaselev et al., Phys. Rev. Lett., **92**, (2004) 207202.

13 Surface Physics

T. Greber, M. Hengsberger, J. H. Dil, H. Yanagisawa, H. Ma, M. Morscher, T. Brugger, F. Meier, D. Leuenberger, B. Slomski, M. Aksak, S. Roth, H. Cun, M. Thomann, D. Böni, C. Janssen, G. Landolt, M. Hausherr, P. Donà, M. Klöckner, J. Osterwalder

With the growing impact of nanoscience and -technology, surface and interface phenomena have to be understood more and more at the atomic level. The surface physics laboratory is well equipped for the preparation and characterization of clean surfaces, metal and molecular monolayer films, as well as covalently bonded single layers, using a wide variety of experimental techniques. Moreover, we operate two photoemission spectrometers at the nearby Swiss Light Source (SLS), one for spin- and angle-resolved photoemission spectroscopy (SARPES) and one for photoelectron diffraction.

The research carried out during the report period can be grouped into four topics:

- **Monolayer films of hexagonal boron nitride (*h*-BN) and graphene on metal surfaces**
  Due to their strong intra-layer sp^2 bonds, these two materials form robust and chemically rather inert single layers that couple relatively weakly in the third dimension. The mechanical stiffness of these bonds leads to the formation of regular superstructures when grown on top of metal surfaces with different lattice constants, that can be either flat moiré-type structures, or strongly corrugated layers with interesting functionalities (1; 2; 3). A prominent example is the boron nitride nanomesh that forms upon high-temperature chemical vapor deposition of borazine on Rh(111) (4). Graphene forms corresponding structures on Rh(111) and Ru(0001) but with inverted corrugations (5). Very accurate structural studies of these systems have been carried out in the last year by means of surface x-ray diffraction, in collaboration with a group from PSI (6; 7). These systems are studied in our group within two different contexts. The first one is the synthesis of heteroepitaxial layers of graphene and *h*-BN with a view on future electronic devices based on graphene. Due to its in sulating properties and similar crystal structure and lattice constant, *h*-BN might be the ideal "gate oxide". The second context is the exploitation of these corrugated functional layers as templates for the growth of molecular adlayers with defined periodicities (see Sec. 13.1). This second activity is supported by a Sinergia project of the Swiss National Science Foundation, funding a consortium of four different groups. As an important step, the interaction of water molecules with the *h*-BN nanomesh was studied at low temperature, where the formation of regular nano-ice clusters was observed (8). Due to the inertness of these films, molecular layers can also be deposited directly and much cheaper from solutions. These studies require a large supply of samples. Therefore, a new growth chamber has been designed and built, in which *h*-BN or graphene films can be grown on entire four-inch Si(111) wafers. The chamber is placed in a new clean-room that has been installed for this project, which will enable us to process such samples further in a dust-free environment.

- **Molecular adsorbates and molecular monolayers**
  In this past year, important steps were taken towards the setting up of a unique infrastructure for the characterization of molecular layers. A consortium of groups from EMPA, UZH, PSI and the universities of Fribourg and Basel have secured the funding for a new beamline PEARL (PhotoEmission and Atomic Resolution Laboratory) at

the SLS. It is currently under construction and will provide new opportunities to combine careful STM studies of molecular layers with synchrotron radiation based studies of local structure and bonding. In parallel, the development of a new type of Mott detector for spin analysis in our photoemission chamber has continued. The device has been built and is currently being tested in a separate vacuum chamber. This device will be used to study spin degrees of freedom in molecular adlayers and their coupling to a ferromagnetic substrate.

- **Ultrafast processes at surfaces**
  Four years ago the group received a vacuum chamber equipped with an elliptical display analyzer (EDA) from PSI in order to study the temporal evolution of photoemission patterns with femtosecond resolution. The setup needed some refurbishing, including a new channelplate detector and a new sample manipulator, and has been successfully commissioned in the last year. First photoemission patterns from a Cu(111) surface, using ultraviolet radiation for excitation, could be recorded, and experiments with pulsed laser excitation are currently underway. In the meantime, the photo-induced field emission patterns resulting from tightly focusing a pulsed laser beam onto a sharp tungsten tip could be understood quantitatively (see Sec. 13.3 and Ref. (9)).

- **Spin-resolved photoemission and momentum mapping**
  Our spin-resolved photoemission chamber (COPHEE) at the SLS has been in high demand as a general user instrument due to its unique capabilities. The group's own activities were centered around the study of Bi, Pb and Sb surface alloys on Ag(111), where the band filling and the spin splitting can be readily tuned (see Sec. 13.2). Moreover, two older projects dating back several years could finally be completed: (i) the exchange splitting of three surface states on Ni(111) could be quantified (10), and (ii) the spin-split surface state on Au(111) could be studied on related vicinal surfaces. The spin polarization and the spin texture in these latter states was found to be surprisingly robust against scattering in periodic step lattices, even in the presence of disorder (11). Spectacular results were obtained in collaboration with a group from Princeton University on a novel class of materials, so-called *topological insulators*. For the first time, the spin polarization of their topologically protected surface states could be measured, and their spin helicity around the Fermi surface was established (12).

[1] T. Greber, http://arXiv.org/abs/0904.1520 (2009).
[2] S. Berner et al., Angew. Chem. Int. Ed. 46, 5115 (2007).
[3] J. H. Dil et al., Science 319, 1824 (2008).
[4] M. Corso et al., Science 303, 217 (2004).
[5] T. Brugger et al., Phys. Rev. B 79, 045407 (2009).
[6] D. Martoccia et al., Surf. Sci. 604, L9 (2010).
[7] D. Martoccia et al., Surf. Sci. 604, L16 (2010).
[8] H. Ma et al., Chem. Phys. Chem. 11, 399 (2010).
[9] H. Yanagisawa et al., Phys. Rev. Lett. **103**, 257603 (2009).
[10] T. Okuda et al., Phys. Rev. B, 80, 180404(R) (2009).
[11] J. Lobo-Checa et al., Phys. Rev. Lett., to appear (2010).
[12] D. Hsieh et al., Nature 460, 1101-1106 (2009).

In the following, three highlights of last year's research are presented in more detail.

13.1 Switching surface texture by hydrogen intercalation

In collaboration with: M. Iannuzzi and J. Hutter, Physikalisch-Chemisches Institut, Universität, Zürich; A. Winkler, Institut für Festkörperphysik, Technische Universität Graz, Austria.

Intercalation – that is the reversible embedding of atomic or molecular species into a layered material – is a key concept for materials functionalization. Graphite is the prototype intercalation material in which the relatively weak bonding between *sp*^{2}-hybridized carbon sheets allows the packing of molecular species between subsequent layers. We address the question whether intercalation is also possible between single sheets of carbon (graphene) or h-BN and the supporting metal surface, and what the effect will be on the corrugated superstructures that are characteristic of these systems (1). It is found that the surface texture of the h-BN nanomesh on Rh(111) may be reversibly switched from corrugated to flat by intercalation of atomic hydrogen, and back to corrugated by hydrogen desorption (2).

The topographic STM data in Fig. 13.1a show that after exposure to atomic hydrogen, a new phase of single layer h-BN without superstructure corrugation (phase II) can coexist with the unaltered nanomesh (phase I). Phase II is basically flat whereas the pristine nanomesh exhibits a corrugated hexagonal surface texture with a periodicity of 3.2 nm. In the textured phase I region (Fig. 13.1b) several nanomesh unit cells are seen with their distinctive topographic elements, the *holes* ('H', tight bonding) and the *wires* ('W', loose bonding). The zoom into the untextured region is

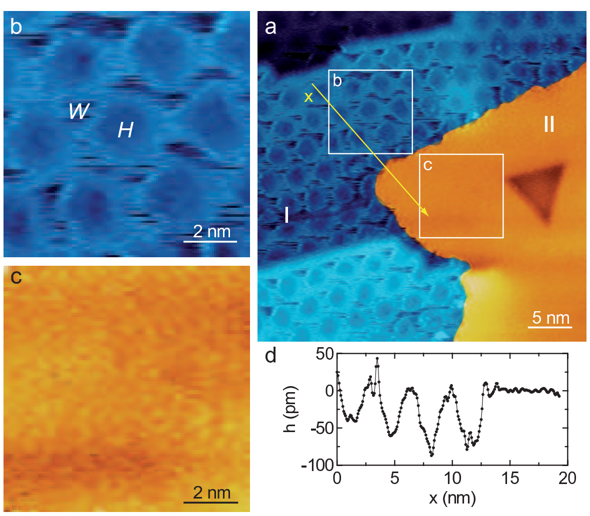

Figure 13.1: Topographic scanning tunneling microscopy (STM) data of h-BN/Rh(111) after exposure to atomic hydrogen. (a) Large scale image showing the coexistence of corrugated and flat h-BN/Rh(111) (regions I and II, respectively). (b) Zoom into the pristine h-BN/Rh(111) area showing the wire (W) and the hole (H) regions. (c) Zoom into the flat, hydrogen intercalated h-BN/H/Rh(111) area. (d) Line profile along the line in a) showing the transition from corrugated (I) to flat (II) h-BN/Rh(111).

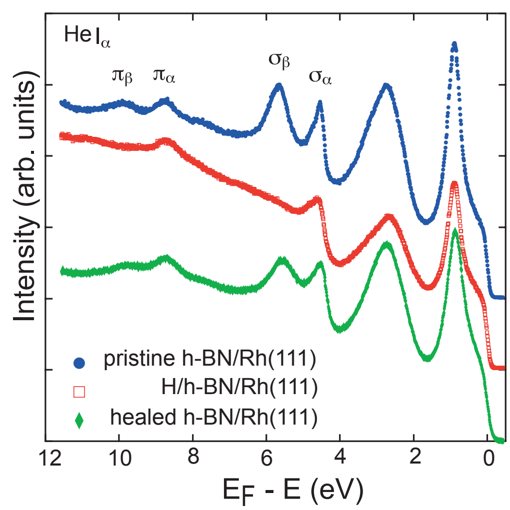

Figure 13.2: He I$_\alpha$ (21.21 eV photon energy) excited normal emission photoelectron spectra from a h-BN/Rh(111) nanomesh before (filled blue circles) and after (open red rectangles) exposure to atomic hydrogen, as well as after subsequent H desorption (filled green diamonds). They show the vanishing of the σ_β and π_β peaks which are attributed to the hole regions (H) of h-BN/Rh(111) after hydrogen intercalation, while the σ_α and π_α peaks corresponding to the wire regions (W) remain.

basically flat (Fig. 13.1c). The height profile in Fig. 13.1d shows the transition from the corrugated region into the flat region. The film surface in the flat region levels on the height of the wires, i.e. the loosely bonded regions in the nanomesh.

The photoemission spectra in Fig. 13.2 confirm the flattening of the h-BN layer and support the hydrogen intercalation picture: the bands related to the holes of the nanomesh (π_β and σ_β) vanish after extensive H exposure, indicating a complete lifting of the corrugation across the entire surface. Furthermore, annealing of the H exposed sample to about 600 K recovers the original band splitting as the pristine corrugation is restored. Calculated N p_x densities of states (DOS) in the hole and wire sites exhibit pronounced peaks at about 7 eV and 6 eV below E_F, respectively, explaining the experimentally observed σ band splitting of about 1 eV. On the other hand, the N p_x DOS with one monolayer of intercalated hydrogen shows only one pronounced peak roughly at the energy of the wire site, reproducing the experimentally observed disappearance of the hole derived band upon exposure to atomic hydrogen. These results thus confirm that hydrogen intercalates between the film and the metal surface.

The demonstration of reversible hydrogen intercalation in the h-BN/Rh(111) system, and the concomitant lifting and recovery of the surface corrugation, is expected to be a more general phenomenon in these sp^2-hybridized template systems on transition metal surfaces, including also graphene.

[1] T. Greber, http://arXiv.org/abs/0904.1520 (2009).
[2] T. Brugger et al., http://arXiv.org/abs/0911.1317v1.

13.2 Unconventional Fermi surface spin textures in surface alloys

In collaboration with: L. Patthey, Swiss Light Source, Paul Scherrer Institute; S. Guerrero and Ch. Mudry, Condensed Matter Theory Group, Paul Scherrer Institute; V. N. Petrov, St. Petersburg Polytechnical University, St. Petersburg, Russia.

At surfaces and interfaces, the space inversion symmetry is broken. The spin-orbit interaction can thus lift the degeneracy of the electronic states via the so-called Rashba effect (1). For a two-dimensional free-electron gas, this effect leads to two fully spin-polarized parabolae shifted away from the $\bar{\Gamma}$-point ($k_\parallel = 0$) in opposite directions by the wave vector k_0. The spin polarization vectors lie in-plane and perpendicular to the momentum k, rotating tangentially around the constant energy contours. This Rashba-type spin-splitting forms the basis of the spin field-effect transistor proposed by Datta and Das (2); it allows for a controlled precession of the electron spin.

The Bi/Ag(111) and Pb/Ag(111) surface alloys form a new class of materials, in which the Rashba-type spin-splitting is dramatically enhanced due to a combination of strong atomic spin-orbit interaction of the heavy metals with structural effects enhancing the local potential gradients at the surface (3; 4; 5). The surface state band structure in Bi/Ag(111) features four spin-split "upside-down" parabolae, forming two Kramers pairs, some of which can be seen in the ARPES data of Fig. 13.3a (x=1). By preparing mixed Bi_xPb_{1-x}/Ag(111) surface alloys, both the Fermi energy and the spin splitting can be tuned, as is shown in the same figure. In particular, there are concentrations x where the Fermi level lies between the apex and the crossing point of the inner Kramers pair (x=0.6). In this region, the Fermi surface topology is changed and the density of states features a Van Hove singularity (see Fig. 13.3h). As a

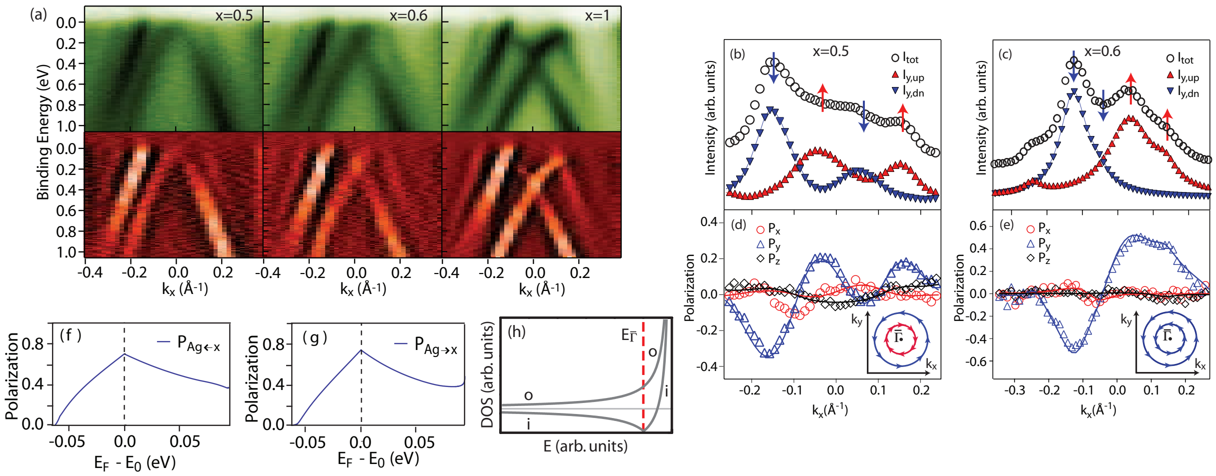

Figure 13.3: (a) Upper graphs: experimental band dispersion of Bi$_x$Pb$_{1-x}$/Ag(111) surface alloys for varying compositions x (from left to right) along the $\bar{\Gamma}\bar{K}$ direction. Lower graphs: second derivative data. (b) and (c) Total spin integrated intensity (circles) and spin-resolved intensity curves (P_y-projection) measured near the Fermi energy. (d) and (e) are the corresponding measured (symbols) and fitted (solid lines) spin-polarization data. (Insets) Schematically drawn Fermi surface spin textures. (f) Spin polarization of the electron current from the Rashba system to the Ag(111) surface state, calculated within the Drude limit, as a function of $E_F - E_{\bar{\Gamma}}$ and (g) spin polarization of a current flowing in the opposite direction. (h) Density of states for the inner (i) and the outer (o) constant energy textures. (from Ref. [8]).

consequence, intriguing physical effects can be expected, among them changes in the Fermi liquid parameters (6), superconductivity transition temperatures (7) and real-space spin accumulation(9).

We have performed spin and angle resolved photoemission measurements of the mixed Bi$_x$Pb$_{1-x}$/Ag(111) surface alloys with the focus on the inner Kramers pair. The data analysis employed our two-step fitting routine, which allows for a precise determination of the individual spin polarization vectors of the measured states (5). The main results are shown in Fig. 13.3b-e. For x=0.5, we find similar Fermi surface spin textures as observed for Pb/Ag(111), and for Bi/Ag(111) at higher binding energies, i.e. the spins on the two Fermi surface contours are mainly in-plane and point in opposite directions for the inner and outer contours at a given k direction as shown in Fig. 13.3b (and inset) (5). In contrast, for x=0.6 the Fermi surface spin textures are unconventional (see Fig. 13.3c and inset). Each two states crossed on the same side of $\bar{\Gamma}$ now belong to one and the same Kramers pair and thus have parallel spin polarization vectors and are reversed according to time reversal symmetry when $k \rightarrow -k$.

These findings demonstrate that such Rashba systems can be tuned, while still preserving their high degree of spin polarization. In this context, new prospects for potential applications for spintronics emerge. In Fig. 13.3f and g we show calculated values of the spin polarization for a surface electron current from the Bi$_x$Pb$_{1-x}$/Ag(111) Rashba system to the Ag(111) surface state (f) and vice versa (g) as a function of the Fermi level position relative to the crossing point $E_{\bar{\Gamma}}$ of the parabolae. Due to the difference of the densities of states deriving from the inner and the outer constant energy contours (see Fig. 13.3h) the current is highly spin polarized, reaching values of almost 80% when the Fermi energy lies at $E_{\bar{\Gamma}}$. Spin-polarized currents can thus be obtained from Rashba type spin-orbit interaction without the use of any magnetic materials.

[1] Y.A. Bychkov and E.I. Rashba, JETP Lett. 39, 78 (1984).
[2] S. Datta and B. Das, Appl. Phys. Lett. 56, 665 (1990).
[3] C. R. Ast et al., Phys. Rev. Lett. 98, 186807 (2007).
[4] D. Pacile et al., Phys. Rev. B 73, 245429 (2006).
[5] F. Meier et al., Phys. Rev. B 77, 165431 (2008).
[6] E. Cappelluti et al., Phys. Rev. Lett. 76, 085334 (2007).
[7] E. Cappelluti et al., Phys. Rev. Lett. 98, 167002 (2007).
[8] F. Meier et al., Phys. Rev. B 79, 241408(R) (2009).
[9] J. Sinova et al., Phys. Rev. Lett. 92, 126603 (2004).

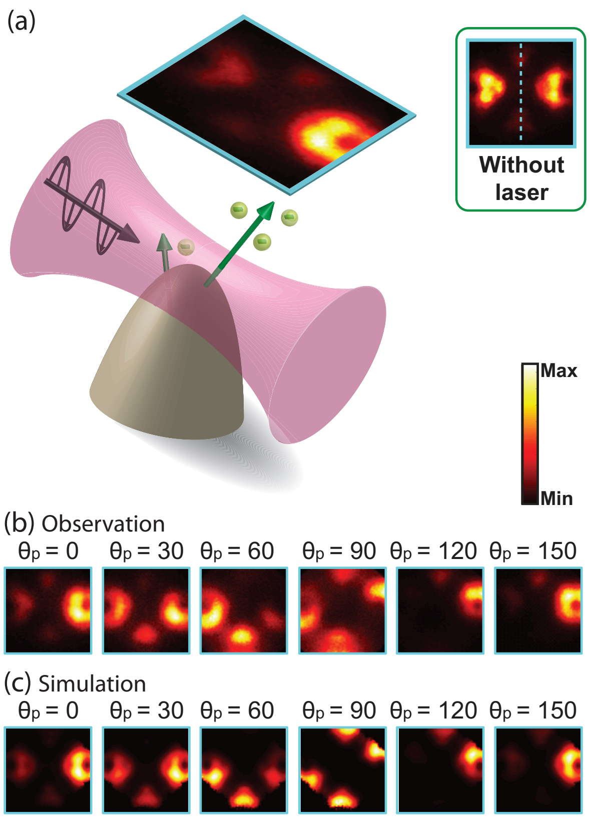

Figure 13.4:
(a) Schematic diagram of the laser-induced field emission. The emission pattern is observed by a two-dimensional detector. The inset shows the field emission pattern without laser excitation. (b) Observed and (c) simulated laser-induced field emission images for different light polarization angles θ_P, where θ_P is defined by the angle between the tip axis and the polarization vector; $\theta_P = 0$ is when the tip axis is parallel to the polarization vector.

13.3 Optical control of field-emission sites by femtosecond laser pulses

In collaboration with: Christian Hafner, Laboratory for Electromagnetic Fields and Microwave Electronics, ETH Zürich.

Applying strong electric fields to a metal enables field emission due to electron tunneling through the surface potential barrier into the vacuum. Field emission from metallic tips with nanometer sharpness is particularly interesting due to the high brightness and coherence of the resulting electron beams. When a focused pulsed laser beam illuminates the tip, the electric fields of the light wave are enhanced at the tip apex due to the excitation of surface electromagnetic (EM) waves like, e.g., surface plasmon polaritons. Only recently, it was found that the enhanced fields induce pulsed field emission in combination with a moderate DC voltage applied to the tip (1).

We have investigated electron emission patterns induced by femtosecond laser pulses from a clean tungsten tip apex which is oriented along the (011) direction, and compared them with those of field-emitted electrons without laser excitation. The laser light was focused to 4 μm onto the tip apex, and emitted electrons were detected by a two-dimensional detector as schematically depicted in Fig. 13.4a. We observed a striking difference in symmetry of the two patterns (2; 3). Without laser, we observed the typical field emission pattern of a clean tungsten tip as shown in the inset of Fig. 13.4a. With laser, emission sites were the same as those without laser, but the emission intensities become strongly asymmetric between the shadow and exposed sides with respect to the laser pulse, as shown in Fig. 13.4a. Varying the laser polarization angle changes these distributions substantially as shown in Fig. 13.4b, an effect that had not been observed in earlier experiments (1). In effect, we have realized an ultrafast pulsed electron source with emission site selectivity of a few ten nanometers.

To reveal the origin of the asymmetric emission patterns, simulations of local fields on the tip apex were performed by using the software package MaX-1 (4), and the resulting local fields were used for simulating electron emission patterns where the field emission from photo-excited nonequilibrium electron distributions were considered. The simulated emission patterns in Fig. 13.4c are in excellent agreement with the experimental data shown in (b). This comparison clearly demonstrates that the observed strongly asymmetric features originate from the modulation of the local photo-fields at the tip apex (2; 3).

[1] P. Hommelhoff et al., Phys. Rev. Lett. **96**, 077401 (2006).

[2] H. Yanagisawa et al., Phys. Rev. Lett. **103**, 257603 (2009).

[3] H. Yanagisawa et al., Phys. Rev. B **81**, 115429 (2010).

[4] http://MaX-1.ethz.ch

14 Physics of Biological Systems

Conrad Escher, Hans-Werner Fink, Heinz Gross (until December 2009), Dominik Grögler, Patrick Helfenstein (since May 2009), Tatiana Latychevskaia, Jean-Nicolas Longchamp, Elvira Steinwand.

in collaboration with:
Eugen Ermantraut, Clondiag Chip Technologies (Germany), Prof. John Miao, University of California at Los Angeles (USA), Prof. Andre Geim, Manchester Centre for Mesoscience and Nanotechnology, University of Manchester (Great Britain), Dr. Ilona Müllerová, Institute of Scientific Instruments (Czech Republic), Dr. Petr Formanek, University of Dresden (Germany), Dr. Soichiro Tsujino, PSI (Switzerland).

The structural investigation of individual biological objects by employing coherent low energy electrons is the primary goal of our research. It involves holography with low energy electrons as well as coherent diffraction and is assisted by micro-structuring techniques using a focused gallium ion beam device. Our current activities are divided in the following interconnected individual projects listed below.

- **SIBMAR**
  SIBMAR stands for Structural Information of Biological Molecules at Atomic Resolution and is part of the EU "New Emerging Science and Technology" Programme. SIBMAR aims at high resolution structural information of individual biological molecules by employing coherent low energy electron waves. Partners from the Institute of Scientific Instruments Academy of Sciences of the Czech Republic in Brno, the Physics Department of the University of Manchester and the Physics-Institute of the University of Zurich are involved in SIBMAR. The overall idea is to apply holography with low energy electrons to investigate the structure of individual biological molecules. Major experimental challenges are to improve the interference resolution in electron holograms, establish methods for creating free standing thin films of Graphene transparent for low energy electrons as well as appropriate techniques to present a single protein to the coherent electron wave front. Next to these experimental issues, a second, equally important aspect for achieving high resolution structural information is the reconstruction of the electron holograms. This is achieved by back-propagating the object wave information, recorded in the hologram plane, by employing a numerical algorithm to solve the integrals governing this coherent optics problem. An international workshop entitled "Current Trends in Structural Biology at the Single Molecule Level", held in Lucerne has critically reviewed the achievements of SIBMAR and compared it to state of the art research in the high energy electron and X-ray community.

- **Electron and Ion Point Sources**
  Field Ion Microscopy and related techniques are employed for fabricating and applying novel electron and ion point sources. In collaboration with the PSI, field emitter arrays are characterized and specified for their use as bright electron sources for the XFEL (X-Ray Free Electron Laser) project.

- **Fluorescent Microscopy**
  The aim of this project is to directly observe the dynamics of single DNA molecules in liquids by video fluorescent microscopy. In combination with molecular anchoring techniques, adopted from Clondiag, we

address the energetics of a single DNA molecule. Appropriate DNA modifications for attaching fluorescent proteins to are designed by Clondiag Chip Technologies in Jena and shall serve us in our efforts to obtain structural information about proteins by electron holography.

- **Coherent Low-Energy Electron Diffraction Microscopy**
  This is a second approach, next to electron holography, of using coherent electron wave fronts for structural biology at the single molecule level. It is based on an iterative phase retrieval scheme pioneered by John Miao from the University of California at Los Angeles with whom we collaborate in this project. Both, the principle setup for holography and coherent diffraction microscopy are depicted in Fig. 14.1. In the following two selected sub-projects shall be discussed in some more detail. The first addresses the vital question of radiation damage in imaging biological molecules. The second subject is related to the coherent diffraction microscopy project which requires a coherent parallel electron beam. The latter has been realized by employing a low aberration electron lens of micrometer dimension.

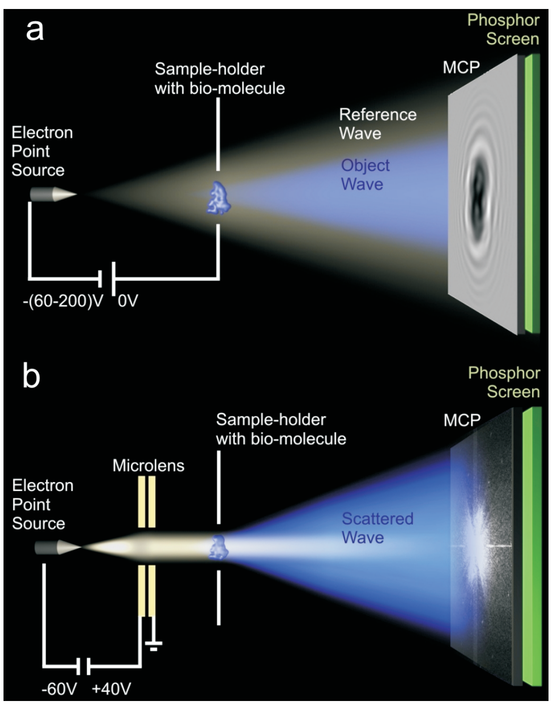

Figure 14.1: Schematic representation of the coherent electron diffraction microscope.

14.1 Non-destructive imaging of individual bio-molecules [1]

14.1.1 State of the art

Exploring the three-dimensional structure of individual biomolecules, in particular those of proteins, is the foundation for a basic understanding of bio-chemistry, molecular biology and bio-physics. Most of the protein structural information data available today have been obtained from crystallography experiments by averaging over many molecules assembled into a crystal. Despite this vast amount of available data, a strong desire for acquiring structural data from just one individual molecule is emerging for good reasons. Most of the relevant biological molecules exhibit different conformations; thus averaging does not reveal detailed structural information. Moreover, there is large quantity of proteins, in particular the important class of membrane proteins, featuring a pronounced reluctance to readily crystallize.

Due to the strong inelastic scattering of X-rays and high energy electrons there is little hope for obtaining structural information from just one single molecule by conventional X-ray or high energy electron microscopy tools. Despite recent advances in cryo-electron microscopy, especially in image processing and reconstruction, averaging over typically 10 000 images is still necessary to build up a high signal to noise ratio image with structural features finally emerging. This in turn smears out most of the details related to conformational flexibility. The necessity for averaging is given by radiation damage inherent to the interaction with high energy electrons and limits the obtainable resolution in conventional electron microscopy to 1nanometer. In order to obtain structures of individual biological molecules at atomic resolution, new concepts and technologies are envisioned. A major effort currently underway involves the development and implementation of the X-ray Free Electron Laser (XFEL), as a source of ultra short but extremely intense X-ray pulses. The overall idea is to take advantage of the principle of inertia: by keeping the interaction time of the intense X-ray burst with the molecule of interest extremely short, the site information of the atoms is carried to the detector before the molecule has been given time to finally decompose. Unfortunately, in X-ray diffraction, inelastic scattering outweighs elastic scattering but only the latter carries information about the structure of molecules. Hence, a very large number, of the order of 10^6, diffraction patterns of identical molecules must be recorded in order to obtain structural detail at a resolution of 3 Å, even with a 10 fs X-ray pulse containing $2{\cdot}10^{12}$ photons at 1.5 Å wave length.

14.1.2 Radiation damage in imaging DNA

In the following we show that a molecule as fragile as DNA withstands irradiation by coherent low energy electrons and remains unperturbed even after a total dose of at least 5 orders of magnitude larger than the permissible dose in X-ray or high energy electron imaging. The experimental set-up for testing radiation damage is illustrated in Fig. 14.2. DNA molecules are stretched over holes by using freeze drying technology known from cryo-microscopy. First, an array of 1 μm diameter holes in a thin carbon film is cleaned and rendered hydrophilic by UV-ozone treatment. Next, a droplet of λ-DNA solution of

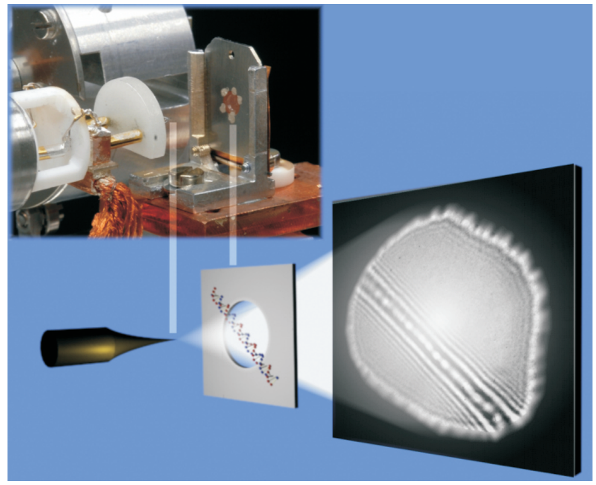

Figure 14.2: Schematic of the set-up. For exploring radiation damage effects on DNA, the molecules are exposed to coherent low energy electrons. A spherical wave emitted from a coherent electron source is scattered at DNA molecules stretched over holes in a thin film and positioned at about 1 μm beyond the source. At a 10 cm distant micro-channel-plate screen detector the interference between the elastic scattered wave (object wave) and the un-scattered wave (reference wave) produces the hologram captured by a 14 bit dynamic range CCD camera. Magnification is provided by the geometry of the set-up alone and can be adjusted by the source-sample distance. The smallest interference fringe spacing in the hologram amounts to 0.7 nm and is a measure for the achievable resolution.

2 μg/ml concentration is applied onto the carbon film. Following an incubation time of typically 10 minutes, blotting paper is used to remove excess water. The remaining thin water film is transformed into amorphous ice by rapid quenching in liquid ethane. Next, the sample is freeze-dried at -80 °C under vacuum conditions within typically 20 minutes and monitored by a mass-spectrometer above the sample. Finally, the sample is transferred into the Low Energy Electron Point Source (LEEPS)-microscope chamber for obtaining DNA electron holograms at various energies ranging from a few 10 eV up to about 300 eV.

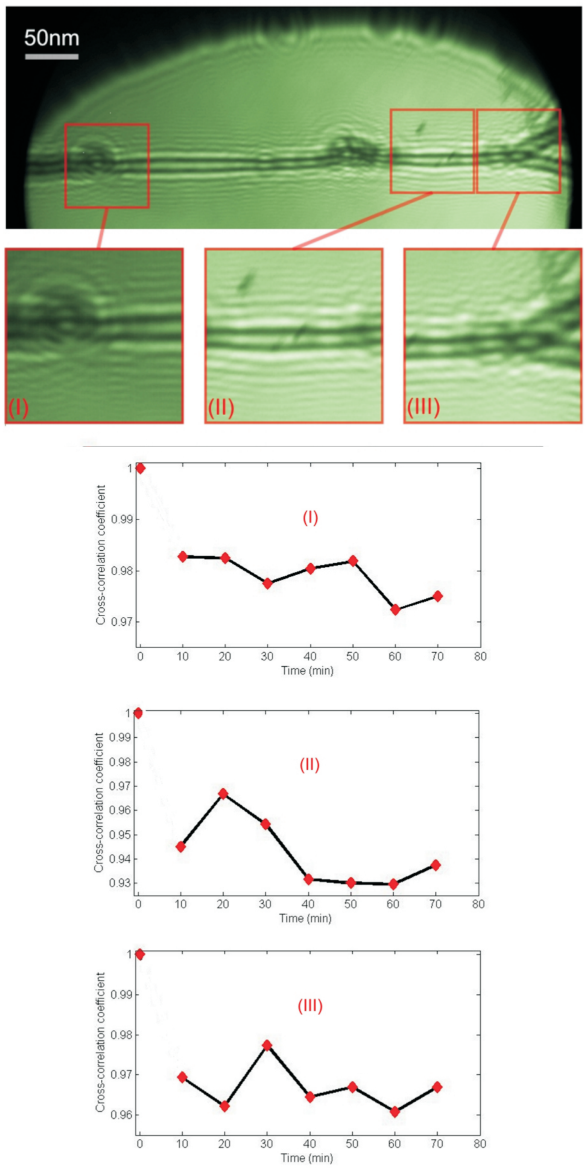

Figure 14.3: Non-destructive imaging of DNA. The low energy electron hologram of DNA molecules stretched over a hole in a thin film imaged continuously for 70 minutes using electrons of 60 eV kinetic energy and a total current of 200 nA is shown on top. Part of the rim of the 1μm diameter hole, spanning the free standing molecules, is visible at the very top of the image. Three regions of the hologram, marked in red, have been chosen to evaluate the cross-correlation function of subsequent holograms. The evolution of the cross-correlation coefficient is shown in the diagrams corresponding to the three regions.

For the holographic imaging solely the elastic scattered electrons contribute to the hologram, while the inelastic scattered electrons lead to an incoherent diffuse background at the detector level. The fraction of inelastically scattered electrons by an object can be estimated by negatively biasing the front of the detector. While there is a significant amount of inelastic scattering in imaging metals with low energy electrons, measurable inelastic scattering in imaging DNA has not been observed. This could be a first, albeit just qualitative, hint for little or no radiation damage caused by low energy electrons. To actually measure the electron dose leaving DNA molecules unperturbed, we have carried out quantitative experiments. Evidence for damage-free imaging is provided in Fig. 14.3 showing a hologram of DNA molecules subject to 60 eV electron radiation. In this experiment DNA has continuously been exposed to a 200 nA electron current for 70 minutes. A set of DNA holograms has been recorded every 10 minutes. Next, three regions in the DNA holograms have been selected, marked by red squares in Fig. 14.3. Thereafter, the cross-correlation function between the first holographic record and subsequent holograms taken at 10 min intervals have been computed for these very regions.

As is evident from Fig. 14.3, the cross-correlation coefficient varies between 0.93 and 1.0 indicating a high degree of similarity between the first and all subsequent holograms. While the fluctuation of the cross-correlation coefficient is apparent, its time dependence differs in all three DNA hologram regions. These fluctuations are due to statistical noise which varies from hologram to hologram and is attributed to the intrinsic stochastic process of field emission and to detector noise. As a consequence, the cross-correlation coefficient reaches values just below unity at best. However, there is no tendency of the cross-correlation coefficient to decay in time. In fact, the coefficient persists above 0.93 even after 70 minutes of continuous exposure. Thus, the molecule's structure remained intact during 70 minutes of exposure to 60 eV electrons. The total accumulated dose during that time amounts to 10^8 electrons/nm^2. This remarkably high electron dose certainly provides enough scattering events in a single molecule to be able to extract structural information at Ångstrom resolution. Moreover, there is nothing to be said against increasing the imaging current from 200 nA into the μA range or prolonging the exposure time. The kinetic energy of 60 eV has been chosen here because the corresponding deBroglie wave length is close to the 1.5 Å X-ray wave length used in XFEL simulations setting the boundaries for single molecule imaging. However, similar experiments as described above have also been carried out at 110 eV electron energies and quantitatively analyzed revealing the same result of no observable damage to DNA. To demonstrate that our findings depend only on electron energy but not on any particularities of our set-up, we would now like to present a control experiment, done in the same manner but at higher electron energies of 260 eV where DNA actually decomposes rapidly within a few seconds.

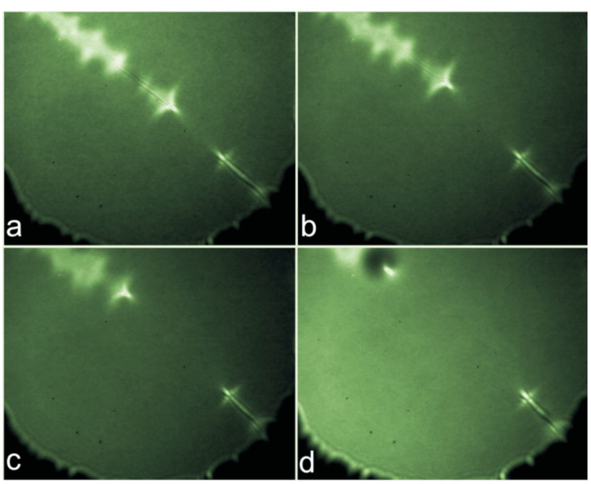

Figure 14.4: Decomposition of DNA. Control experiment showing the rapid decomposition of DNA stretched over a 1 μm diameter hole in a carbon film during imaging with 260 eV electrons.

In fact, a detailed analysis as in the non-damaging situation described above has not been possible here because of a too rapid decomposition of the molecules within the first 10 seconds of the observation process. The situation is illustrated in Figs. 14.4 and 14.5 . Again, DNA is stretched over a 1 μm diameter hole in a carbon film but now imaged with 260 eV energy electrons. Even before completing the data acquisition for the first image by the slow-scan CCD camera, the molecule had already been partly damaged as apparent in Fig. 14.4(a). Evidently the 260 eV electrons cause bond-braking in DNA. Since the DNA does not rest on a support but is free-standing, small molecular fragments created while DNA is decomposing sublimate into the vacuum. As a consequence, the remaining DNA gets shorter and shorter within a few seconds of observation.

For comparison to the non-damaging case, the evolution of the cross-correlation coefficient has also been computed and is shown in Fig. 14.5. As expected, the process of DNA decomposition is accompanied by a rapid decrease of the cross correlation coefficient between subsequent DNA images. The red bar displayed at the top of Fig. 14.5 illustrates the range of fluctuations of the cross-correlation coefficient in the non-damaging experiment.

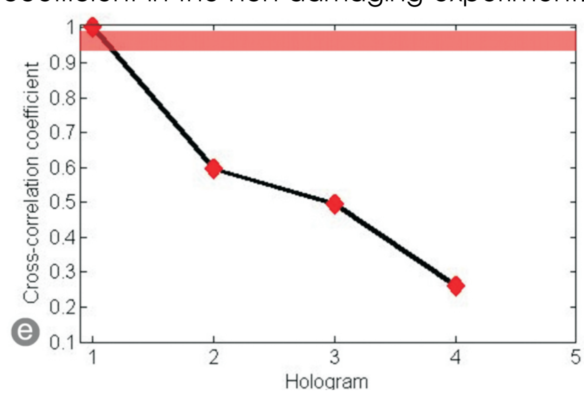

Figure 14.5: The associated change of the cross-correlation coefficient: the red bar at the top indicates the range in which this coefficient fluctuated in the non-damaging experiment with 60 eV electrons.

While 60 eV electrons apparently cause no detectable damage to DNA at all, a rapid decomposition on a 4000 times shorter time scale is observed when DNA is subject to the interaction with 260 eV electrons. We would like to point out that 60 eV kinetic energy of the imaging electron wave is not a unique value or condition for gently imaging DNA molecules. Equally non-destructive imaging conditions have empirically been found also at 115, 140, 215 and 230 eV kinetic electron energy for example. While high energy electrons in all keV kinetic energy ranges cause unavoidable damage to biological molecules, it has also been shown that very low kinetic energy electrons between 3 and 20 eV initiate strand breaks in DNA molecules. However, it is important to note that these studies suggest that there is not a simple threshold for damage, but a rather pronounced energy dependence pointing at distinct energies between 3 and 20 eV where resonance effects lead to damage.

14.1.3 Conclusion

Apparently, there are very low electron energy ranges around 10 eV, where DNA experiences rapid damage as well as higher energy resonances leading to damage at 260 eV as we have observed it and described above. But, fortunately there are also regimes in between where DNA can readily be imaged using an extremely high dose without any damage at all. The permissible dose leaving a molecule unperturbed is at least 5 orders of magnitude greater than in conventional X-rays or high energy electrons imaging, demonstrating that coherent low energy electrons are the only non-damaging $\AA$ngstrom wave lengths radiation. With coherent low energy electrons it shall thus be possible to look at truly just one entity if it comes to high resolution diffraction microscopy of individual bio molecules.

14.2 Fabrication and characterization of low-aberration micrometer-sized electron lenses [2]

14.2.1 Electron Lens Aberrations and the Scaling Concept

Back in 1936 already, Scherzer recognized that rotational symmetric static electron lenses suffer from intrinsic aberrations which have limited the resolution of conventional electron microscopes for over 50 years. These intrinsic limitations can only be overcome by using elaborate electron optical elements, like multi-pole correctors and mirrors, into the electron beam. Actually building and implementing such correctors has only recently been achieved and revolutionized modern electron microscopy design and performance. An alternative approach towards minimal aberrations relies on the concept of scaling down both electron source and lens dimensions. In scaling down the size of an electrostatic lens, the potential distribution created by the lens and with this the overall shape of the electron trajectories is conserved. Only the space in which the electron paths are shaped is changed. Thus the spherical aberration coefficient is directly proportional to the lens size. With a lens diameter of just one micrometer one assure thats the electron paths within an electron optical column deviate no more than a micrometer from the optical axes which guarantees paraxial conditions associated with minimal aberrations in all subsequent electron optical devices. While several attempts have already been undertaken in this direction, routine operation of low aberration micron-scale lenses and their application in scientific instruments are still lacking. While we routinely employ electron sources exhibiting an ultimate emission area of atomic dimension it is now a matter of scaling down a lens by about four orders of magnitude and positioning it with nanometer precision in front of the source.

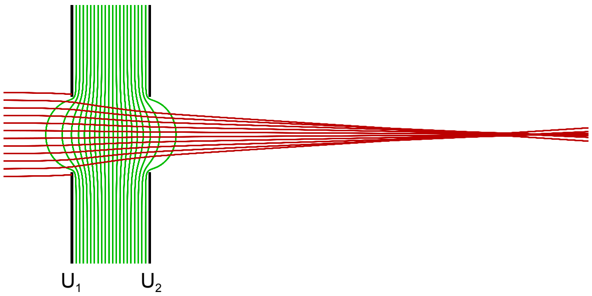

Figure 14.6: Operating principle of a two electrode aperture lens for an accelerating electrical field between the electrodes. Equipotential lines and electron trajectories have been calculated for $U_1 = 100$ V and $U_2 = 350$ V for an initial electron energy of 100 eV using a ray tracing software package.

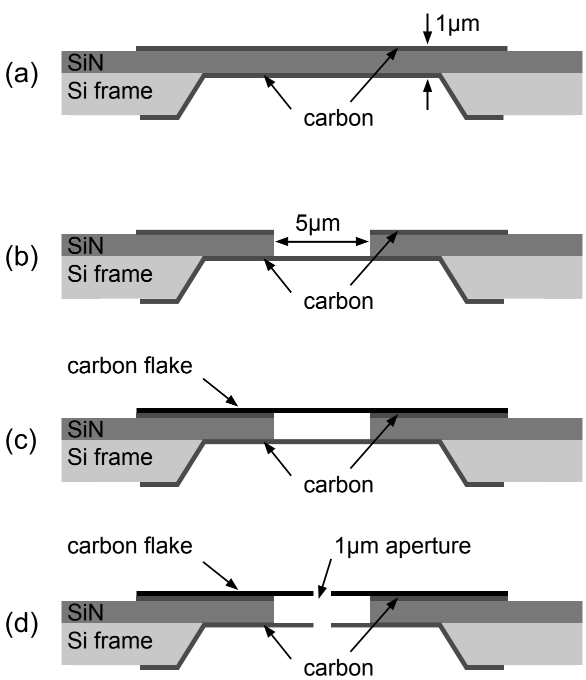

Figure 14.7: Schematic drawings of the various steps for lens fabrication.
(a) Carbon deposition on either side of a SiN membrane.
(b) Removing the upper carbon and the SiN layer in a circular 5 μm diameter region using a FIB.
(c) Covering of the structure with a carbon flake.
(d) Milling a 1 μm diameter aperture through the freestanding carbon layers using the FIB.

The simplest type of electrostatic lens consists of two parallel planar electrodes with two concentric apertures of not necessarily the same size. The electrodes must be separated by an insulating material to maintain a voltage between them, resulting in a focusing electrostatic field distribution at the apertures as illustrated in Fig. 14.6. Simulations and experiments show that the lens generates a focusing effect independent of the polarity of the applied voltage. A lens size as small as possible appears preferable in order to minimize spherical aberrations. Considering established micro-fabrication techniques and available materials, lens dimensions in the range of one micrometer appear sensible. Micrometer lens dimensions shall also ensure easy positioning of the lens in an electron-optical system using conventional nano-positioning devices based on piezo electric manipulators.

14.2.2 Lens fabrication and testing

We have developed several lens fabrication methods comprising various micro-fabrication steps, evaporation methods and materials for the insulating layers and lens electrodes. The result of all methods is a lens structure similar to the one depicted in Fig. 14.7(d) featuring a 1 μm thick insulating layer, two electrodes of several tens of nanometer thickness with one micrometer diameter apertures in them. The electrodes must be freestanding around the apertures to avoid charging effects of the insulating walls while the electron beam impinges on the lens. The fabrication of one particular type of microlens, showing good performance in terms of stability and cleanliness, will be described here in some detail. As a starting material for the fabrication we use commercially available silicon nitride (SiN) membranes of one micrometer thickness. They serve as insulating layers between the two lens electrodes and exhibit a measured breakdown voltage around 320 V, high enough to focus a beam of electrons with kinetic energies in the range of 100 eV. The initial fabrication step consists in electron-beam evaporation of a roughly 30 nm thick layer of amorphous carbon on either side of the SiN membrane (Fig. 14.7(a)). Next, a focused gallium ion beam (FIB) is used to remove the top carbon as well as the SiN layer within a circular region of 5 μm in diameter, whereas the carbon layer at the bottom side of the structure remains unchanged (Fig. 14.7(b)). For the following process step, carbon is first evaporated onto a mica sheet. Subsequently, the carbon film is floated off onto a clean water surface and can thus be deposited onto the upper side of the structure (Fig. 14.7(c)). As the final step, a hole of 1 μm diameter is ion-milled through the freestanding parts of both carbon films (Fig. 14.7(d)). A SEM image of such final lens structure is shown in Fig. 14.8.

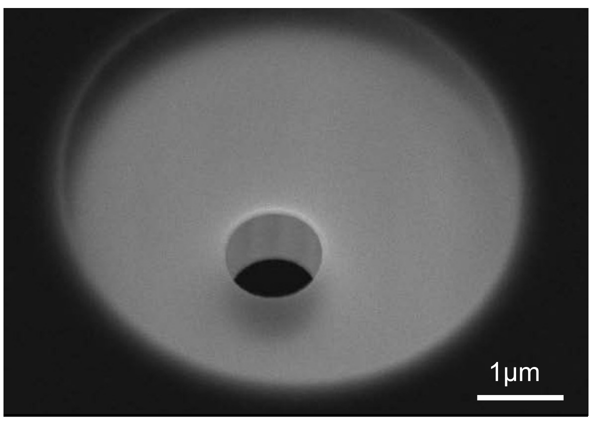

Figure 14.8: SEM image of the fabricated microlens, recorded at a tilt angle of 30 degrees. The penetration of the 12 keV electrons used in the SEM, allows recognizing the 5 μm diameter circular region where the carbon electrodes are freestanding. In this case, the lens aperture of 1 μm in diameter, is not concentric with the 5 μm region but the distance to the SiN walls is large enough to prevent charging effects when implemented as a lens.

14.2.3 Microlens operation

Lenses manufactured as described above have been tested in an ultra-high vacuum system designed for experiments with coherent low-energy electrons. A W(111) field emission tip is used as a source for a divergent electron beam of high spatial and temporal coherence. Typical emitter currents are in the 10 to 200 nA range and the kinetic energy of the electrons at the lens entrance is well below 200 eV. The electron detector consists of a microchannel plate (MCP) followed by an electroluminescent layer on the vacuum side of a fibre optic plate (FOP). At the ambient pressure side of the FOP a CCD camera collects the emitted light. The detector resolution has been measured to be around 120 μm. A dedicated holder allowing for rapid vacuum transfer of microlenses fixes the position of the lens (Figs. 14.9 and 14.10). The distance between lens and detector amounts to 75 mm. The electron source is mounted onto an x-y-z piezo stage for precise alignment with the lens aperture. For the experiments described here, the source to lens distance varied between 5 and 30 μm, leading to kinetic energies of the electrons at the lens entrance between 60 and 150 eV.

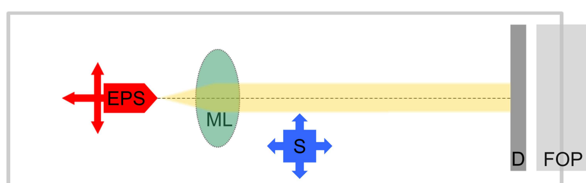

Figure 14.9: Schematic of the experimental UHV setup. The electron point source (EPS) is mounted onto an x-y-z piezo stage for nanometer precision alignment with the centre of the 1 micrometer diameter aperture of the microlens (ML). Beyond the microlens, a second x-y-z piezo stage carries the sample holder (S) to be moved into the beam. The beam profile is measured at a detector (D) placed at 75 mm beyond the lens. A fiber optic plate (FOP) transfers the image from the UHV to the ambient pressure side where it is captured by a CCD camera.

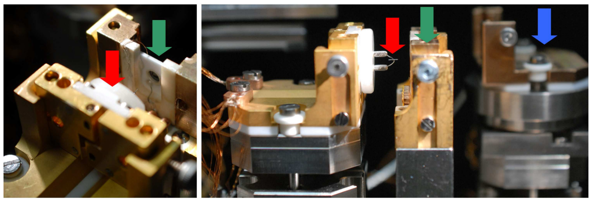

Figure 14.10: Two views into the experimental chamber showing the electron point source (red arrow), the microlens holder (green arrow) and the sample holder (blue arrow).

If the lens electrodes are at ground potential and a negative voltage is applied to the emitter tip, a projection image of the second lens aperture is visible at the screen. Its magnification can be varied by changing the source-lens distance. Examples of such electron projection images are shown in Fig. 14.11(a) and (e). Once a voltage is applied between the two lens electrodes, a focusing effect is observed. To ensure a field-free region beyond the lens, the second electrode is kept at ground potential. The voltage applied at the first lens electrode is varied together with the voltage at the emitter tip to keep the kinetic energy of the electrons at the lens entrance and the emission current constant. The voltage polarity at the first electrode can be chosen to either decelerate or accelerate the electrons when passing the lens. The effect of the lens is illustrated in Fig. 14.11 for both modes of operation. While increasing the voltage between the two lens electrodes, one first observes that the projection image of the lens aperture at the screen decreases (Fig. 14.11(b) and (f)). A further increase of the lens voltage reduces the divergence angle more and more until the electrons form a minimal spot at the detector (Fig. 14.11(c) and (g)). With still higher lens voltage, a crossover located between lens and detector is achieved (Fig. 14.11(d) and (h)). The distance between lens and crossover can even get smaller than the source-lens distance, resulting in an enlarged divergence angle of the beam as it is the case in illustrated in Fig. 14.11(d).

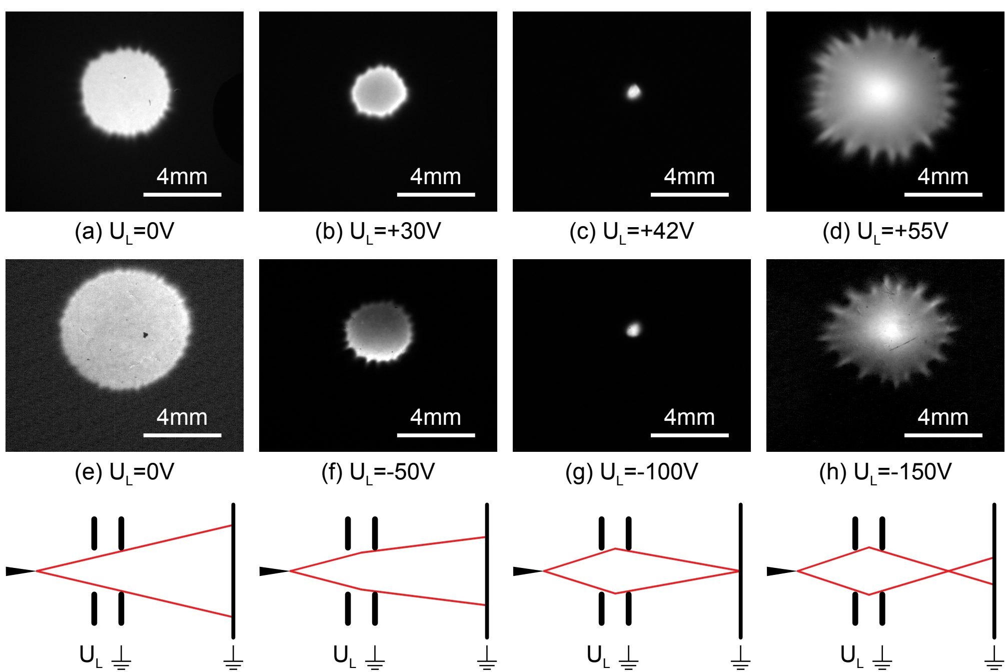

Figure 14.11: Focusing series of decelerating (top) and accelerating (middle) mode of the lens with corresponding focusing situations (bottom). The distance between virtual electron source and the first lens electrode amounts to 16 μm for the mode with a kinetic energy of 93 eV respectively 95 eV at the lens entrance.

14.2.4 Microlens performance and its aberration coefficients

To evaluate whether down-scaling of spherical aberrations by scaling down the size of the lens could actually be realized, the magnitude of spherical aberrations must be determined. Two quantities which are directly related to spherical aberrations are measured. In a second step they are compared to values obtained from ray tracing simulations assuming an idealized lens deteriorated only by intrinsic spherical aberrations. The order of magnitude of the spherical aberration coefficients de facto realized in the experiments can thus be deduced.

An experimentally easily accessible quantity is the image size of the electron source in the plane of the electron detector which is the smallest achievable spot size at the detector. As the distance from the lens to the detector plane is large compared to the diameter of the lens aperture, a minimal spot size at the detector is achieved when the beam leaves the lens almost parallel. Instead of determining spherical aberrations from the size of the spot obtained when a parallel incoming beam is focused, we do it the other way round. We instead measure the minimal achievable divergence when collimating a beam emitted by an almost perfect point source. Thus, the minimal spot size at the detector is directly related to the spherical aberrations of the lens. The minimal achievable spot size was measured for the decelerating mode of the lens. Each measurement started with recording a projection image of the lens aperture. This allowed determining the distance between the virtual electron source and the first lens aperture. Next, the lens voltage was adjusted for obtaining a minimal spot at the distant detector. The mean diameter of the minimal spot and the projection image was determined by fitting an ellipse to the contour of the half maximum of the images. It turns out, that the average spot size at the detector varies from 0.5 to 1.1 mm, measured with a detector resolution of 120 μm. Thus, assuming a Gaussian spot profile the broadening of the spot imposed by the finite detector resolution amounts to less than 3% and will not be accounted for in the following analysis. In addition to spherical aberrations there are several other intrinsic effects contributing to the size of the spot visible at the detector, namely chromatic aberrations, diffraction of the beam at the lens aperture and finite source size. For an estimation of chromatic aberrations the energy spread of 0.1 % of the electrons must be taken into account as well as the stability of the lens voltage. Ray tracing simulations showed that this leads to an enlargement of the spot size at the detector by about 15 μm. We estimated the influence of diffraction for the decelerating mode of the lens, by assuming a parallel beam being diffracted by the second aperture of the lens. This leads to a width of the central maximum of the diffraction pattern of 15 μm for 50 eV electrons. The magnified image of the virtual electron source contributes with less than 8 μm to the spot size, as the size of the virtual electron source is well below 1 nm; in fact it has been measured to be of atomic dimension. We can thus conclude that chromatic aberrations, diffraction at the lens aperture and finite source size are negligible contributions to the minimal spot size at the detector.

A more direct way to determine aberrations is to measure the beam diameter in a plane much closer to the lens than the 75 mm distant detector plane. This has been done by scanning a sharp edge perpendicular to the optical axis through the beam. The beam diameter in the plane of the edge is given by the displacement of the edge from the position where all electrons are blocked to the position where all electrons pass the edge. We fabricated such sharp edge by ion-milling a rectangular window into a 20 nm thick carbon foil, opaque for low-energy electrons. The sample was mounted onto a movable piezo-stage (see also Figs. 14.9 and 14.10) and the window was positioned into the electron beam 200 μm beyond the lens. Precise motion of the edge perpendicular to the optical axis is realized with a piezo-scanner exhibiting a scan-range of 4 μm. While moving the sample with a scan speed of typically 800 nm/s, the total intensity at the detector is recorded. The lens voltage is then adjusted for the steepest slope in the intensity versus edge position profile while repeatedly scanning through the beam.

Calculation of electrostatic fields and electron trajectories are done with the SIMION 8.0 software package to solve the Laplace equation using the finite element method. The lens is modeled as two planar electrodes separated by 1 μm and exhibiting concentric apertures of 1 μm in diameter with field-free regions on either side of the lens. Cylindrical symmetry reduces the computational effort since the Laplace equation must only be solved in two dimensions. The electrical field distributions are calculated on a 15000x1000 array with a grid size of 5 nm. Ray tracing was done with a fourth order Runge-Kutta algorithm implemented in SIMION.

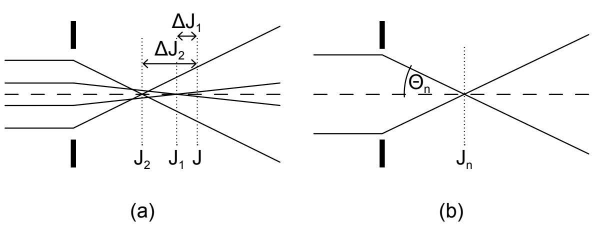

Figure 14.12: (a) Schematic drawing showing two rays with different initial distances from the optical axis which are focused at different positions J_1 and J_2. The paraxial focus is denoted as J. ΔJ_1 and ΔJ_2 are called the longitudinal spherical aberrations of the two rays. (b) The position of the focus J_n depends on the semi angular aperture Θ_n of the ray.

Spherical aberrations cause paraxial and marginal rays to be focused at different po sitions, as illustrated in Fig. 14.12. The distance between the paraxial focus J and the focus J_n of a ray passing the lens at a larger distance from the optical axis is called the longitudinal spherical aberration ΔJ_n of the ray, see Fig. 14.12(a) for denotation. In the case of a parallel incoming beam, the longitudinal spherical aberration of a ray ΔJ_n can be expressed as a power series of the ray's semi angular aperture Θ_n (see also Fig. 14.12(b)). As ΔJ_n is a symmetric function of Θ_n, the odd power terms vanish which leads to:

$$\Delta J_n = C_s \Theta_n^2 + c_4 \Theta_n^4 + c_6 \Theta_n^6 + ...,$$

Calculations were carried out for a parallel incident ray, both for the accelerating as well as for the decelerating mode of the lens. For this, a parallel beam of about 100 electrons has been generated, such that the lens aperture is completely filled. For each particle, the focus position J_n and the elevation angle Θ_n are computed. The position of the paraxial focus J is approximated by the focus of the ray with an initial distance to the optical axis of 5 nm. In this way, the longitudinal aberration $\Delta J_n = J - J_n$ is determined for each particle. A polynomial of sixth order is then fitted to the values $\Delta J_n(\Theta_n)$, yielding the primary aberration coefficient C_s. The described procedure has been applied to a series of lens voltages for the decelerating and accelerating mode respectively. In the following, voltages are always taken relative to the potential where the kinetic energy of the electrons is zero. Thus, the lens is completely described by its geometry and the voltages ratio between the two electrodes. The dependence of C_s on the voltage ratio for the accelerating and decelerating mode are shown in Fig. 14.13 for voltage ratios related to realistic experimentally accessible values. Aberration coefficients C_s are in the range of millimeters per square radian for both modes and decrease with increasing focusing strength of the lens. An ap-

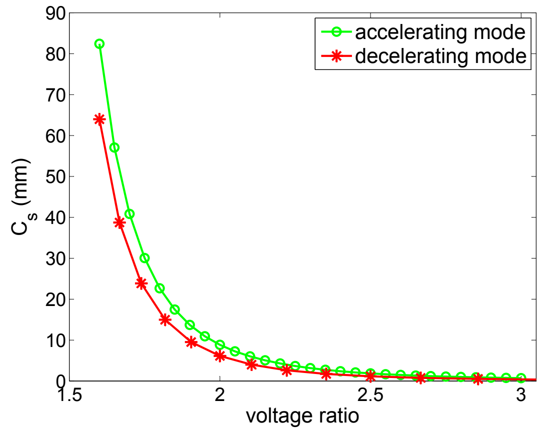

Figure 14.13: Primary aberration coefficient C_s as a function of the voltage ratio for the decelerating and accelerating mode of the lens.

proximate value for the lateral size of the focal spot d_s could be calculated using the relation $d_s = 0.5C_s\Theta^3$. For a crossover some tens of micrometers away from the lens, this yields a spot size of several tens of nanometers.

For comparison with experimental values the size of the image of the electron source was calculated in the detector plane 75 mm beyond the lens and in the plane located 200 μm beyond the lens. As the main contribution to the finite spot size in a plane distant to the lens is due to spherical aberrations, other factors influencing the spot size, as there are chromatic aberrations, finite source size and diffraction effects, were neglected. A monochromatic point source was thus assumed for the simulations. Since typical experimental tip to lens distances are larger than 5 μm, the electrostatic field near the first lens-aperture and the strong field close to the field emission tip the apex do not influence each other, so that they can be treated as two separated electron-optical components. The electron trajectories in the immediate vicinity of the field emission tip are slightly curved as most of the potential drops in front of the tip. However, further away from the tip, at the position of the lens, the trajectories are straight lines. At the lens entrance they seem to emanate from a virtual source located a short distance behind the physical tip apex. There is thus no need to include the field emission tip in the electrode array. Instead, the region at the entrance side of the lens can be assumed as field-free. Electrons originate at a point corresponding to the position of the virtual source and propagate straight with given kinetic energy and divergence angle towards the lens. As the region behind the lens is field-free, the beam radius in the planes of interest up to the 75 mm distant detector is calculated by extrapolating the trajectories. In accordance with experimental conditions, a sufficiently large divergence angle was selected to ensure that the electrons completely fill the lens aperture. The distance between subsequent electrons in the plane of the lens aperture was set as close as possible, that is to one grid unit corresponding to 5 nm. For several distances between electron source and first lens-aperture the spot radius in the plane under consideration was calculated for a set of various lens voltages. In this way, the minimal possible spot radius was computed as a function of source-lens distance for both planes evaluated in the experiments, which is at 75 mm and 200 μm beyond the microlens.

Measured spot sizes at the detector as a function of source-lens distance are depicted in Fig. 14.14, together with the corresponding simulated values. Simulations predict a minimal spot size at the detector between 0.2 and 1.1 mm in diameter for source-lens distances ranging from 5 to 30 μm. As expected, the increase of the divergence angle with decreasing source-lens distance leads to a larger spot size. The simulated values exhibit some fluctuations which are due to the limited precision in the determination of the lens-voltage required to form a minimal spot. Together with the simulations, two series of experimental measurements of the spot size at the detector are also plotted in Fig. 14.14. For series 1 several measurements were carried out with one and the same lens, fabricated in the manner described above. In contrast to

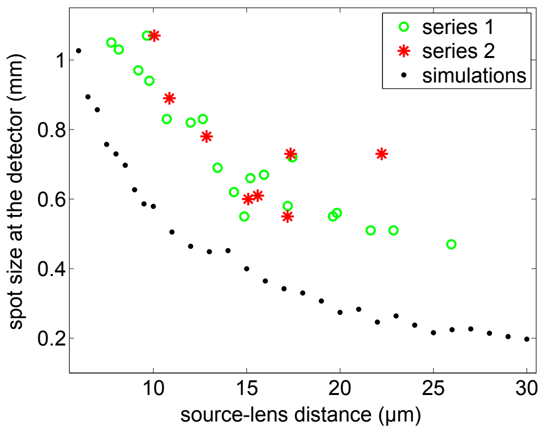

Figure 14.14: Simulated and experimental values for the minimal spot size at the detector. Series 1 was obtained with a sinle lens. Series 2 correspond to measurements with eight different lenses.

this, the eight data points of series 2 were obtained from measurements with eight different microlenses. Some of those lenses have been produced by methods different from the one described here; however all of them exhibit the same geometry. The measured values for the minimal spot size at the detector show the predicted dependency. The experimental data points however are shifted by 0.3 mm towards higher values compared to the simulated ones. The measured spot sizes assume values between 0.5 and 1 mm corresponding to a divergence angle of the collimated beam between just 6 and 14 mrad. The experimental values of series 2 obtained with different lenses exhibit similar characteristics. This implies that microlenses with comparable quality can now routinely be fabricated in a reproducible way. Moreover, as different lens fabrication methods result in similar lens performances, they appear to be equivalent with respect to the focusing properties of the lenses.

The simulated spot-sizes in the plane 200 μm beyond the lens vary from 3 μm diameter for a source-lens distance of 6 μm down to 0.6 μm diameter for a source-lens distance of 30 μm. Experimental values were obtained

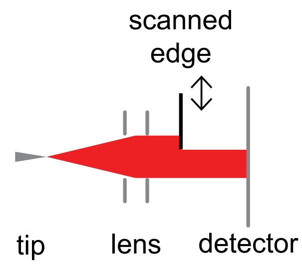

Figure 14.15: To measure the beam diameter 200 μm beyond the lens, a micro-machined edge is scanned through the beam while the total intensity at the screen is recorded.

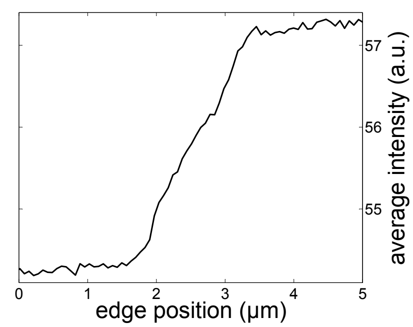

Figure 14.16: Intensity versus the edge position for a source-lens distance of 14 μm. A beam diameter of 1.8 μm is deduced.

as described above (see Fig. 14.15). For a source-lens distance of 14 μm and 92 eV electrons at the lens entrance, a lens-voltage of 48 V was found to generate a minimal spot. In Fig. 14.16, the total intensity at the screen, averaged over all pixels of the CCD chip, is plotted versus the position of the edge while moved perpendicular to the beam with a scan speed of 800 nm/s. From the intensity profile, a beam diameter of 1.8 μm has been derived. Corresponding simulations assuming identical conditions reveal a value of 1.2 μm. As the distance of 200 μm is still large compared to the 1 μm diameter of the lens apertures, focusing of the beam towards this plane is impossible. Instead, the beam diameter is minimal, when the beam leaves the lens as parallel as possible. Thus, the focusing conditions for a minimal beam diameter are just as in the case of a 75 mm distant detector as described and discussed above. In fact, the values for the beam divergence angle obtained by the two methods are in very good agreement; they amount to 9 mrad for a source-lens distance of 14 μm.

14.2.5 Conclusions

We could show that electrostatic lenses of micrometer dimensions can readily be fabricated and exhibit reproducible performance. Comparisons with ray tracing simulations show that the concept of scaling down spherical aberrations by decreasing lens dimensions can in fact be realized. Effects like misalignment of tip and lens, residual vibrations and ac-magnetic fields, deviations from perfect lens-symmetry and contaminations of the apertures have not been considered at all in our simulations. Therefore, the experimental values for the spot size are somewhat larger than the values predicted by simulations. Although these effects do reduce lens performance slightly, their magnitude turns out to be small compared to the achieved reduction of spherical aberrations by down-scaling lens dimensions. As a result, a simple micrometer-sized lens exhibits aberration coefficients comparable to those of high performance objective lenses found in modern electron microscopes. While the bare number of the aberration coefficient is just one aspect, an even more important feature of the scaling concept is the fact that the electron beam is always kept close to the optical axes. The coherent divergent beam originating from the electron point source is modified early on by the lens and thus never spreads out to macroscopic dimensions. The nearly parallel beam beyond the microlens deviates less than one micrometer from the optical axes at a distance of 200 micrometer beyond the lens. This implies that all following electron optical devices, as an objective lens for example, perceive a micron dimension paraxial electron beam with a broadening of just 10 mrad. No beam limiting aperture to improve resolution but decrease brightness at the same time would consequently be needed for an objective lens positioned beyond the microlens. Furthermore, since a coherent electron point source is combined with the microlens, imaging technologies relying on the wave character of electrons, like holography or coherent diffraction, appear feasible. The atomic dimension emission area of the source in combination with the microlens appears to also be favourable when it comes to creating a focus by means of an objective lens. Since the focus is nothing but the image of the primary source, there would be no need to obtain a demagnified image of the primary source. A sharp focused beam could thus be obtained and directed towards a sample placed at a convenient large working distance. In having shown the performance of such microlenses, we now expect and hope for a number of exciting applications in imaging with coherent low-energy electrons.

[1] M. Germann, T. Latychevskaia, C. Escher, H.-W. Fink, Phys. Rev. Lett. 104 (2010) 095501, and references therein.

[2] E. Steinwand, J.-N. Longchamp, H.-W. Fink, Ultramicroscopy (2010), in press.

15 Physical Systems Biology and non-equilibrium Soft Matter

C.M. Aegerter, D. Assmann (since September 2009), G. Ghielmetti (since October 2009), U. Nienhaus (since April 2009), T. Schluck, I.M. Vellekoop (till November 2009)

in collaboration with: Institute of Molecular Life Sciences (K. Basler, T. Aegerter-Wilmsen, C. Lehner, S. Luschnig), ETH Zürich (E. Hafen, I. Sbalzarini, P. Koumoutsakos), EPF Lausanne (P. Renaud, D. Floreano), University of Lausanne (S. Bergmann), Biozentrum Basel (M. Affolter), University of Strasbourg (N. Rivier), University of Konstanz (G. Maret, W. Bührer, S. Fiebig, N. Isert, C.C. Maass), Deutsches Luft- und Raumfahrtzentrum (M. Sperl), University of Twente (A. Mosk), Université Joseph Fourier Grenoble (S. Skipetrov, F. Graner), Technion Haifa (E. Akkermans), University of Exeter (P. Vukusic), Yale University (A. Monteiro).

Work in the group of physical systems biology and non-equilibrium soft-matter is concerned with the study of developmental biology using physical techniques. In this, we are developing novel imaging techniques for in-vivo imaging in turbid environments, as well as studying the influence of mechanical stresses on developmental processes. In the last year, we have made considerable progress in the development of imaging tools for turbid samples as well as the implication of mechanical forces in growth control in the wing imaginal disc of Drosophila.

In the imaging project, we are using wavefront shaping and the optical memory effect to create a scannable focus behind a turbid screen. Raster-scanning this focus we have then implemented into a form of fluorescence microscopy based on the use of scattered light rather than ballistic light. The long term goal of this project is to use this method in turbid situations, such as in an egg or fly pupa, where developmental processes happen hidden from view.

On the problem of the influence of mechanical forces on growth control, we have extended our modeling and experimental approach. In order to check for the possibility of mechanical stress dependent growth rates, we have simulated the tissue topology in a cellular model. This would be necessary to create a growth control via mechanical feedback. From these simulations, we determine the neighbour distributions of the cells, as well as of the cells, which are dividing. These are then compared to experimental data, where the tissue topology is obtained from a fluorescently marked protein in the cell boundaries. While simulations without a mechanical growth stimulation contradict the data, those including mechanical feedback give excellent agreement.

15.1 Imaging through turbid media

Turbid media abound in nature. This is a major limitation in biological investigations, since direct access to the system of interest is rendered unavailable. Thus much effort has been put into increasing the depth resolution of current microscopes, with the most notable examples of confocal microscopy and two-photon fluorescence microscopy (1). However, in the case of turbid samples, even these techniques are no longer able to produce useful images, since they rely on filtering the ballistic light from a multiply scattered background. In our investigations, we use the opposite approach and control the scattered light in such a way as to produce a scannable focus. This forms the basis of a fluorescence microscope. When coherent light is multiply

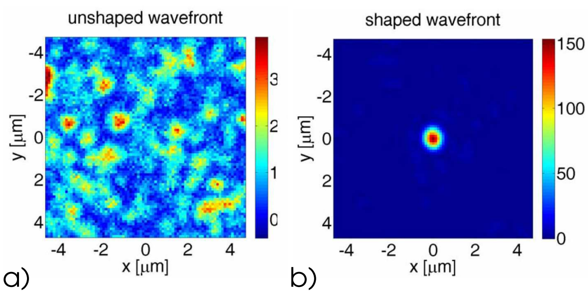

Figure 15.1: A speckle pattern (a) after illumination with coherent light onto a turbid layer. After wave-front shaping (b), the interference pattern changes to produce a narrow focus of the intensity. Note the different intensity scales on the figures. Wave-front shaping has increased the intensity of the focus more than onehundredfold.

scattered, interference on the random paths through the sample, leads to a random speckle pattern of high and low intensities. An example of this is shown in Fig. 15.1a, where the intensity behind a multiple scattering layer is shown. This pattern corresponds to a finger-print of the sample as it corresponds to the distribution of photon-paths inside the sample. Adjusting the phase of the illuminating light in a spatially varying manner, it is possible to induce constructive interference at only one point, thus creating a focus behind a turbid sample. Several ways have been employed to achieve this, e.g. time-reversal (2), optical phase conjugation (3) and wave-front shaping (4). In Fig. 15.1b, such a focus is shown obtained using wave-front shaping.

The fact that such a focus can be formed has great implications for the possibility of imaging behind such turbid structures. If this focus can be scanned, a fluorescence based scanning microscopy can be envisaged, where the focus is scanned across a fluorescent structure. However, it would seem that this is impossible due to the delicate nature of the interference from path length differences in the random medium. A translation of the incoming light of more than a wave-length would for instance destroy the interferometric focus. For turbid samples it has however been shown that a

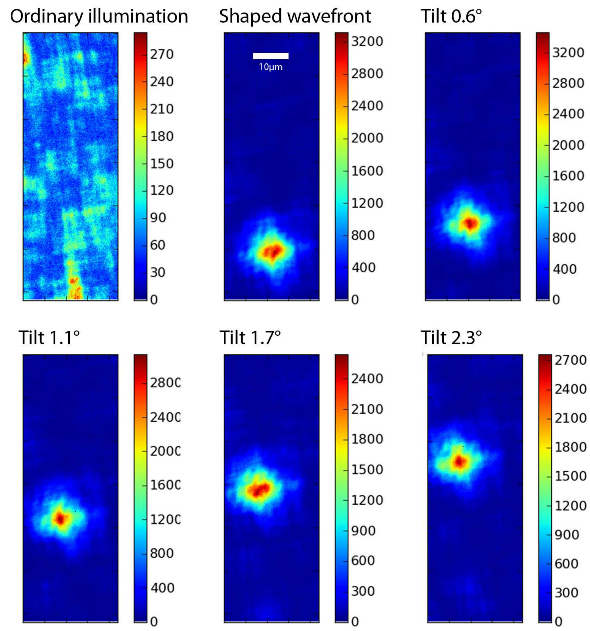

Figure 15.2: An interferometric focus behind a turbid layer is formed and then scanned over an angular range of a few degrees. This shows that it is possible to construct a scanning microscope based on interferometric focusing for samples where fluorescent structures are hidden behind turbid layers.

tilting of the wave-front leads to correlations behind the samples, which survive for small enough angles of tilt (5). The critical angle is determined by the inverse thickness of the layer and scanning over a few degrees is possible. This is shown in Fig. 15.2, where we show the position of the focus formed through a turbid layer at several stages of tilt.

Given that the interferometric focus can be scanned, we have then constructed a prototype setup, with which to demonstrate its microscope capabilities. We have used 200 nm diameter fluorescent beads, which have been added onto a cover-slip, which had a ZnO coating on the opposite side. Due to the highly scattering nature of ZnO, even a thin layer completely hides the fluorescent beads. In fact the scattering layer was such that its thickness corresponded to more than 10 mean free paths of the light. Using wave-front shaping, we have then created a focus in the plane of the fluorescent beads and scanned it over a field of view of 20x20 μm^2 (see Fig. 15.3 for a schematic of the setup).

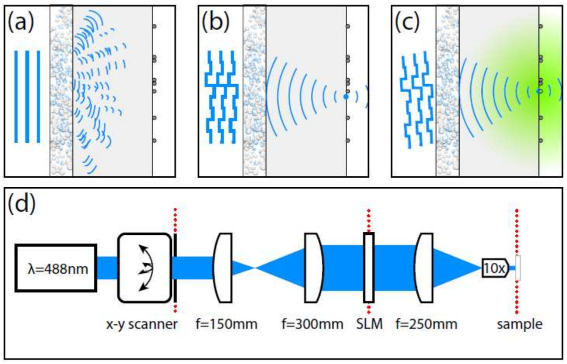

Figure 15.3: Schematic setup for the construction of a turbid microscope. A highly scattering layer of ZnO masks a collection of green fluorescent beads 200 nm in size. The thickness of the layer is more than 10 mean free paths, such that no ballistic light passes the sample. With this geometry, first an interferometric focus is formed via wave-front shaping in the plane of the fluorescent beads. This focus is then scanned using the optical memory effect and the emitted fluorescent light is collected by a photomultiplier. The scanning dependence of the intensity in the photomultiplier then corresponds to the microscopic image of the hidden structure.

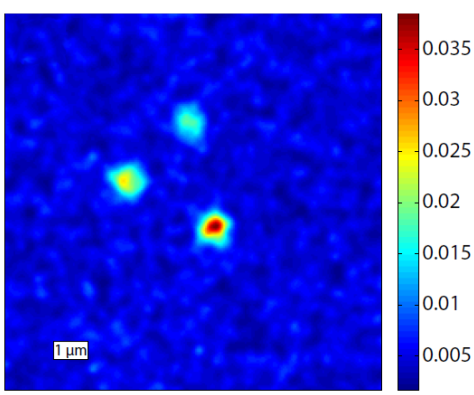

Figure 15.4: Microscopic image of three fluorescent beads behind a turbid layer more than 10 mean free paths thick. This image is obtained using the setup described in Fig. 15.3 and shows the feasibility of a scattering based microscope.

The fluorescence emitted by the beads when illuminated by the focus was collected with a photomultiplier. The dependence of this intensity in the photomultiplier on the scanning angle directly gives an scanning microscope picture of the fluorescent beads behind the turbid layer. The result of this is shown in Fig. 15.4, where a collection of three isolated beads is imaged. A cross-section of this image across a single bead, shown in Fig. 15.5, directly shows the resolution of the microscope (6). The half-width at half-maximum of the curve is at 300 nm, corresponding to the resolution. This is smaller than the wave-length of the illuminating laser used, which was 488 nm and thus can compete with high quality objectives.

Given the long term goal of applying these methods in the study of the development of Drosophila, we have also studied the inherent time scales in the fluctuations of the scattering medium of interest. Here, we are mainly interested in the stage of metamorphosis, where the changes to the organs occur creating them from the larval pre-cursors. This is important because the interferometric focusing relies on the stability of the turbid medium while the focus is formed (and scanned). A determination of the time scale of the fluctuations in the Drosophila pupa thus sets the speed needed for the imaging method. Determining the auto-correlation of a speckle behind a pupa, we found that the pattern is stable on a time scale around 10 seconds (7). This is in the range of what future developments can achieve. In fact, we have already shown that a poor focus is already possible with the current setup in a real biological specimen (7).

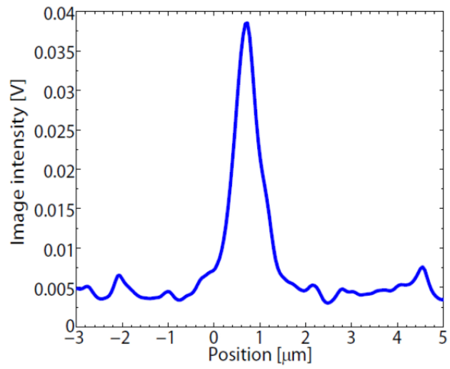

Figure 15.5: A cross-section through one of the beads in Fig. 15.4 , indicating the resolution of the microscope. With a half-width at half-maximum of 300 nm, distances well below the wave-length can be resolved, competing with high quality objectives in the absence of a turbid layer.

[1] A. Diaspro, ed., Confocal and Two-Photon Microscopy: Foundations, Applications and Advances (Wiley-Liss, New York, 2002).

[2] G. Lerosey, J. de Rosny, A. Tourin, and M. Fink, Science **315**, 1120–1122 (2007).

[3] Z. Yaqoob, D. Psaltis, M. S. Feld, and C. Yang, Nat. Photonics **2**, 110–115 (2008).

[4] I.M. Vellekoop and A.P. Mosk, Opt. Lett. **32**, 2309 (2007).

[5] S. Feng, C. Kane, P. A. Lee, and A. D. Stone, Phys. Rev. Lett. **61**, 834–837 (1988); I. Freund, M. Rosenbluh, and S. Feng, Phys. Rev. Lett. **61**, 2328–2331 (1988).

[6] I.M. Vellekoop and C.M. Aegerter, Opt. Lett. **35**, 1245 (2010).

[7] I.M. Vellekoop and C.M. Aegerter, SPIE proceedings **7554**, 75420 (2010).

15.2 The influence of mechanical stress on growth in the wing imaginal disc of Drosophila

The regulation of growth, and finally size in organs represents an interesting problem in developmental biology. One of the main subjects of study for this purpose is the wing imaginal disc of Drosophila. While much is known about the genetic players and growth factors, some fundamental puzzles remain. One concerns the fact that while the growth factors form spatial gradients, cell proliferation does not. We and others have recently proposed a model based on mechanical feedback that can explain this as well as the control of final size (1; 2; 3). In order to test this, we have previously studied the distribution of mechanical stresses in the tissue using photoelasticity (4). As a second step, we have now studied the possibility of feedback and a regulatory role of mechanical forces.

For this purpose, we have studied the topology of the tissue's cell shapes, which can be compared with experiments (5). Instead of describing the tissue as a fully elastic medium, our current model uses the vertices of a cellular network to describe the tissue. The mechanical properties of the tissue are then quantified by the energetics of the adhesion, surface tension and target area of the cells, which means that the positions of the vertices are obtained by minimizing an energy function first described by (6) and given by

$$\begin{aligned} \boldsymbol{E(R_i)} &= \boldsymbol{\Sigma_\alpha K_\alpha (A_\alpha - A_\alpha^0)^2 +} \\ & \boldsymbol{\Sigma_{\langle i,j\rangle} \Lambda_{i,j} l_{i,j} +} \\ & \boldsymbol{\Sigma_\alpha \Gamma_\alpha L_\alpha^2 .} \end{aligned} \tag{15.3}$$

Here, the index α runs over the different cells, whereas i, j describe the segments between different vertices. Moreover, K_α describes the area elasticity of a cell, with a preferred area A_α^0, $\Lambda_{i,j}$ describes a line tension of an individual segment of length $l_{i,j}$ and Γ_α is a measure of the cell's contractility, leading to a min-

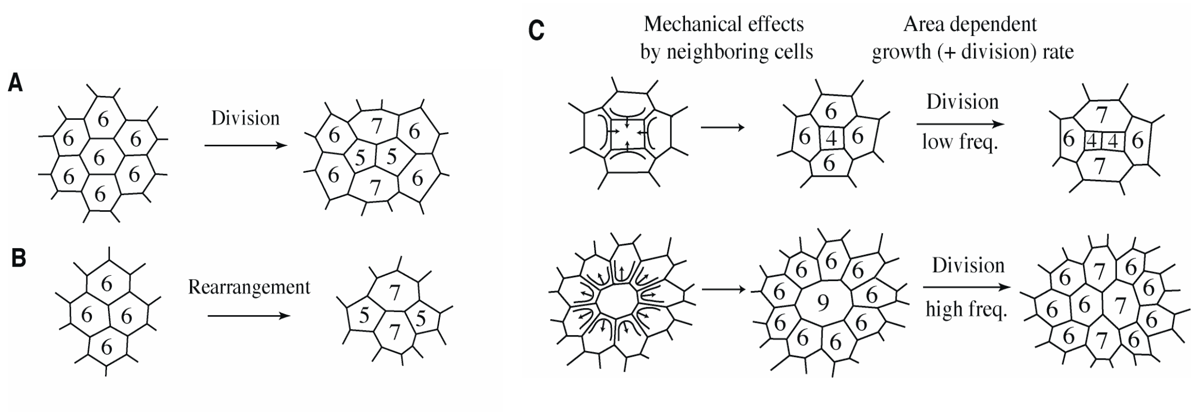

Figure 15.6: Different topological effects on a two dimensional epithelial tissue that affect the distribution of neighbour numbers. When a cell divides, the number of neighbours in the immediate surrounding of the division changes (A). This change also depends on the direction of the cell division boundary. Moreover, according to the energy function (Eq. 15.3), rearrangements of nearest neighbours are possible (T1-events, B). Finally, (C), a dependence of the division rate on the neighbour number and therefore mechanical stress will lead to an enhancement of 6 and 7-fold neighbours.

imisation of the cell's circumference L_α. This will describe the possible rearrangements depicted in Fig. 15.6B. In the simulations, all cells were treated as identical and the relative parameter values used were (6): Γ/KA^0 = 0.12 and $\Lambda/K(A^0)^{3/2}$ = 0.04.

To incorporate mechanical feedback of the growth model into the topology, we have added a growth rate dependence on the number of neighbours (see Fig. 15.6C). Subsequently letting cells grow, divide and rearrange according to the Hamiltonian then yields a tissue topology which is compared to the one found experimentally in Fig. 15.7. The two patterns look similar, but to quantify this, we have determined the neighbour statistics, both for all cells and for dividing (mitotic) cells only. This is shown in Fig. 15.8, where excellent agreement between the model and the experiments can be seen (7).

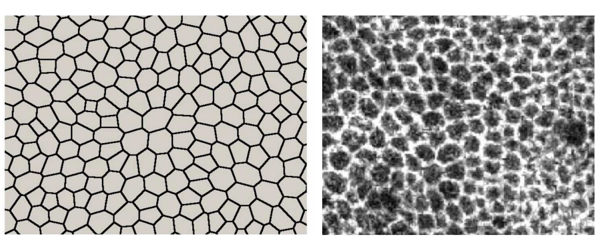

Figure 15.7: Cell shapes of a tissue both from simulation (left) and experiment (right). In the experiments, a protein present in cell membranes was fluorescently marked and imaged using confocal microscopy. From a general perspective, the two topologies look similar, which is quantitatively tested in Fig. 15.8, where the neighbour number distribution is determined.

When neglecting the possibility of rearrangements (5), both of these distributions cannot be reproduced. Not taking into account the mechanical feedback in determining the growth rates (6) does not reproduce the data for mitotic cells. This shows that mechanical stresses can play an important role in determining the tissue topology (7). Taking this together with the data on the presence of mechanical stresses (4) and the growth model (1), indicates that there is a strong role for mechanical forces in the development of the wing imaginal disc.

For future investigations, it would be ideal to have the energy terms motivated experimen-

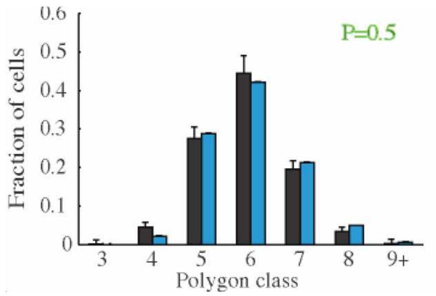

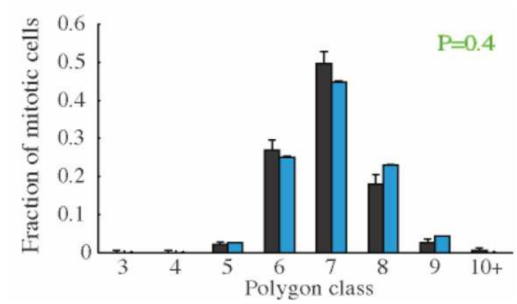

Figure 15.8: Neighbour distributions for all cells in the tissue as well as for dividing (mitotic) cells. In both cases, the simulated and experimentally determined distributions agree perfectly. When neglecting the possibility of rearrangements, the results do not agree with the experiments in both cases. Not taking into account the influence of mechanical feedback fails to reproduce the mitotic cells.

tally, which we intend to using direct mechanical stimulation of the wing disc while studying the cells. In addition, the model can also be compared directly to studies of a growing foam, since the adhesion and surface energies are known theoretically in that case.

[1] T. Aegerter-Wilmsen, C.M. Aegerter, E. Hafen, and K. Basler, Mech. Develop. **124**, 318 (2007).

[2] B.I. Shraiman, "Mechanical feedback as a possible regulator of tissue growth", Proc. Natl. Acad. Sci. USA. **102**, 3318 (2005).

[3] L. Hufnagel, A.A. Teleman, H. Rouault, S.M. Cohen, and B.I. Shraiman, Proc. Natl. Acad. Sci. USA. **104**, 3835 (2007).

[4] U. Nienhaus, T. Aegerter-Wilmsen, and C.M. Aegerter, Mech. Dev. **127**, 943 (2009).

[5] M.C. Gibson, A.B. Patel, R. Nagpal, and N. Perrimon, Nature **442**, 1038 (2006).

[6] R. Farhadifar, J.-C. Röper, B. Aigouy, S. Eaton, and F. Jülicher, Curr. Biology **17**, 2095 (2007).

[7] T. Aegerter-Wilmsen, A. Christen, E. Hafen, C.M. Aegerter, and K. Basler, Development **137**, 499 (2010).

16 Mechanical Workshop

K. Bösiger, B. Lussi, R. Maier, M. Schaffner, S. Scherr, D. Dürst (apprentice since August 2009), O. Fardin (until October 2009) and T. Naterop (apprentice)

Besides equipment for the research groups at the institute, an increasing number of parts for other departments of the University were produced with the modern tools of the mechanical workshop during the reporting period. The central metal and technical material store maintained by us [5] supplied again more than 30 institutes with materials and technical support. In November 2009 we organized again an information meeting for the central store customers. The large number of attendants shows that our services are highly appreciated. For outside companies construction and modification work was done and we built prototypes and produced limited-lot series. Ss in previous years, the resulting income was used to supplement and extend the central store. Also new tooling and the continuing education of the workshop staff and the apprentices could be financed this way. Various equipment was refurbished including a lathe of the type "Schaublin 125" used in the training workshop. We replenished the equipment of the material store with a laser engraving and cutting system (see Fig. 16.1). The power of the CO_2 laser is 65 Watt, sufficient to cut almost any kind of synthetic material, paper, wood, etc. and to engrave a large variety of materials. We also bought a bending machine for acrylic glass shown in Fig. 16.2.

For our 5-axes milling machine we purchased a new CAM software package. Using hyperMill a range of special cycles such as 5-axes top milling, 5-axes swarf cutting or cutting edge machining is available now which helps to produce parts faster and with higher quality. We also installed a network license of the SolidWorks 3D design software. With this tool the parts can be designed faster. It can be used by everybody of the technical and research staff at the institute.

Figure 16.1:
The new laser engraving and cutting system with a working area 965 mm x 610 mm and parts out of POM produced with it.

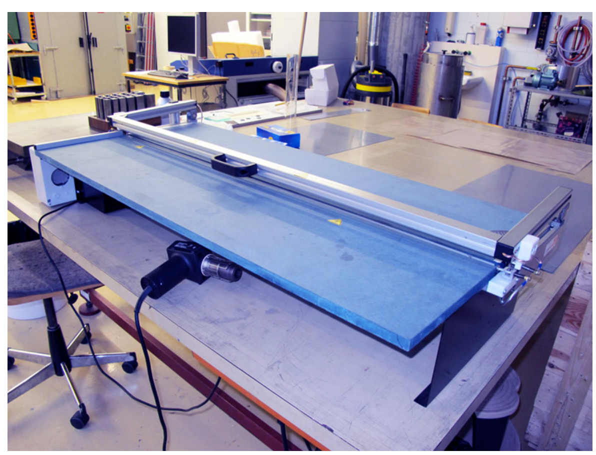

Figure 16.2: Acrylic-glass bending machine.

[5]For a catalogue see http://www.physik.uzh.ch/groups/werkstatt/dienstleistung.html

Below we list some of our projects and activities during the reporting period.

- **Basic mechanical workshop courses**
  We accomplished eight 35-hour basic mechanical workshop courses for bachelor students. During April and August 2009 1-week introductory mechanical workshop courses were provided for the research staff of the institute. These courses may also be attended by members of the other institutes of the University.

- **LHCb silicon tracking detector (Sec. 9)**
  Repair work was carried out and spare parts for the silicon detector modules were produced, to be installed during the next maintenance period.

- **CTA Cherenkov Telescope Array (Sec. 5)**
  We produced additional Winston Cone light concentrators with improved geometries. Modified mounting brackets for the mirror actuators were developed and produced. We made parts and assembled a test setup for these actuators.

  To measure the transparency and light collection efficiency of the new light concentrators we developed and built a goniometer (Fig. 16.3).

- **Surface Physics (Sec. 13)**
  The main workload during this reporting period went into the Synergia project. Only with the help of our 5-axes milling machine we could fabricate the very complex flanges (Fig. 16.4). Besides producing parts for several Bachelor- and Master-thesis projects maintenance and repair work was performed.

- **XENON Experiment (Sec. 4)**
  A transport trolley for nitrogen containers was developed and manufactured. Different parts made out of tantalum and Teflon were produced and the existing laboratory equipment was upgraded.

- **Fusion Neutron source**
  For the Neutron source which is being installed at the institute we produced different parts. The neutron generator replaces the old plutonium source.

- **Solid State Physics (Sec. 11)**
  The production of the demonstration experiment of a magnetic levitation train

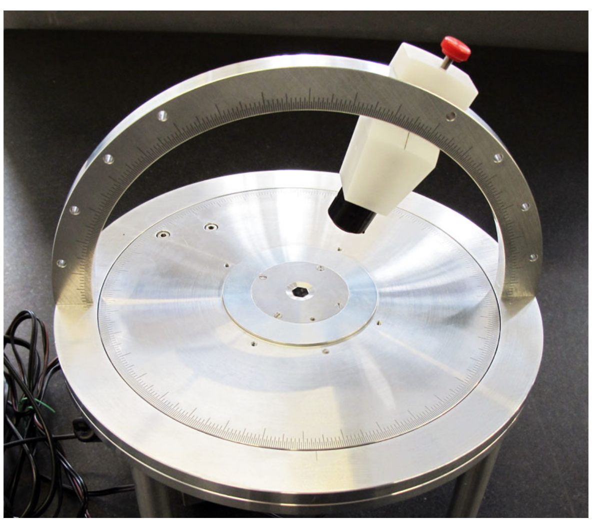

Figure 16.3: Goniometer to evaluate the different optical components.

Figure 16.4: The Synergia apparatus.

Figure 16.5: The institute director watching the model of a magnetic levitation train.

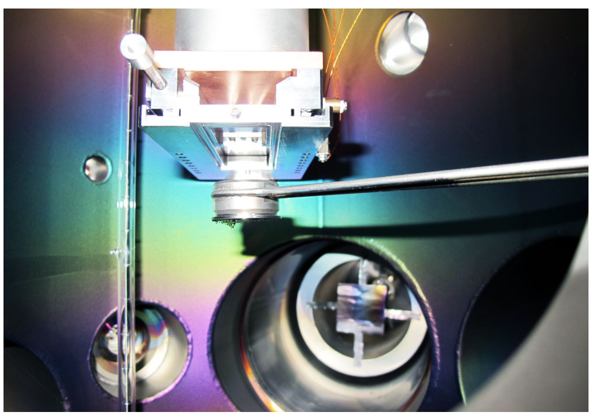

Figure 16.6: Inside view of the vapour deposition apparatus.

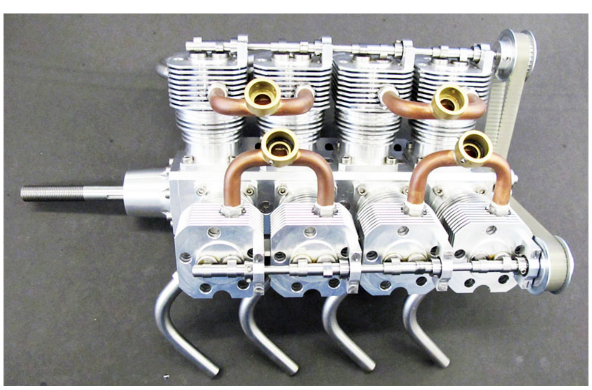

Figure 16.7: The V8 combustion engine.

(Fig. 16.5) using high-temperature superconductor was an interesting, complex but also time consuming task. We also produced motor-driven probe holders, evaporation masks and high-pressure containers made out of high-tensile materials. We had to repair a complete cryomagnetic system and installed experimental test setups.

- **Physics of Biological Systems (Sec. 14)**
  We completed the dedicated vapour deposition device with six coating stations (Fig. 16.6). Also maintenance and repair work was performed.

- **Demonstration and laboratory experiments**
  We designed and built components for a new student experiment which allows the measurement of the gravitational constant. Different instruments and devices were improved and refurbished.

- **Continuing education of the workshop staff**
  The main focus of the continuing education of the workshop staff was put on welding seminars and software courses. In-house introductory tutorials for the new "hyperMill" CAM software were organized.

- **Education of the apprentices**
  In April and September 2009 we again organized trial apprenticeships for candidates interested in getting a grade as polytechnician. In the period of May and June 2009 the final examination of an apprentice was successfully carried out in the workshop. In 72 hours of work the candidate had to manufacture all the required parts for a demonstration experiment. Besides the mandatory Swissmechanic courses the apprentices attended again advanced courses in computer controlled machine (CNC) programming, pneumatics and electronics. Also seminars introducing the use of different graphical and office software were attended. The project of constructing a V8 combustion

engine already presented in the previous report was finished successfully (Fig. 16.7).

- **Activities for other departments and outside companies**
  For other departments of the University we produced an increasing number of parts and devices. For an exhibition in the Museum of Zoology we built control desks (Fig. 16.8) and a dedicated microscope sample support. For the Institute of Forensic Medicine we constructed an improved probe holder (Fig. 16.9) which speeds up standard blood tests. Micro drives with sensor holders (Fig. 16.10) and custom designed camera packages were manufactured for the Institute of Neuro-informatics. For the Institute of Physiology a respiration demonstration experiment was renewed and special needles were produced used for the biopsy of the muscles of athletes (Fig. 16.11). Also for outside companies construction and modification work was done and we produced prototypes and limited-lot series. As an example we developed and manufactured holders for energy saving LED lamps for a company which sells illuminating systems.

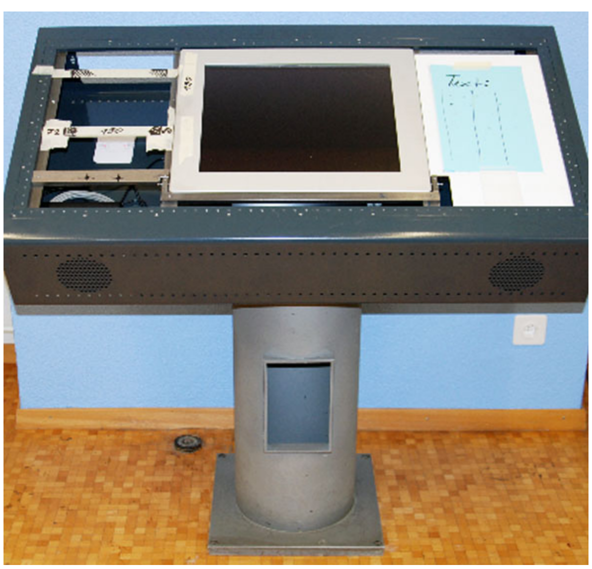

Figure 16.8: Control desk.

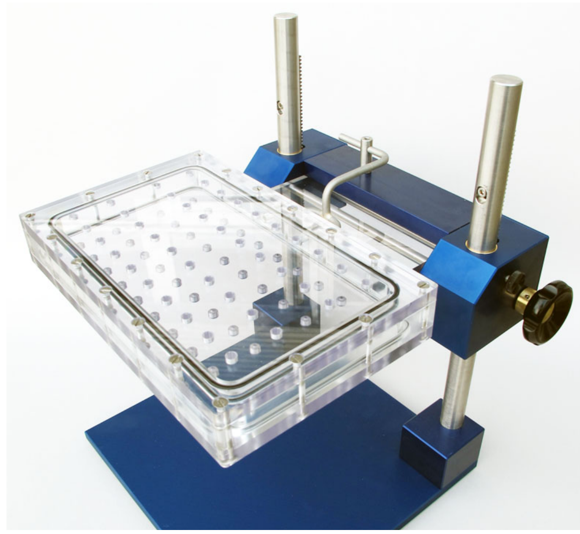

Figure 16.9:
Probe holder for the institute of forensic medicine

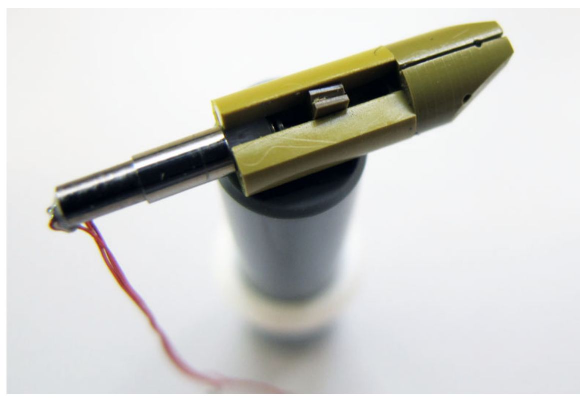

Figure 16.10:
Micro drive for the institute of neuro-informatics.

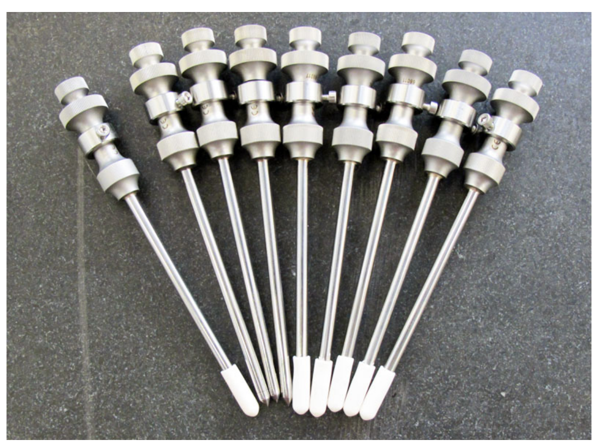

Figure 16.11: Biopsy needles.

17 Electronics Workshop

W. Fässler (retired June 2009), D. Florin (since March 2010), Hp. Meyer (until July 2009), P. Soland, and A. Vollhardt

During the reporting period the electronic workshop contributed to many projects of our institute and supported all research groups in maintaining and repairing existing equipment. Below we list some activities.

- **Remote controlled test setup for the CTA experiment (Sec. 5)**
  The Cherenkov Telescope Array (CTA) project is a planned network of optical gamma-ray telescopes. Mechanical instabilities in the support structure of the telescopes require a continuous alignment of the facets. This is done with two precise actuators installed on every segment. The electronic workshop developed and built the control electronics for a prototype system. To test the actuators under realistic long-term conditions with constant exposure to the environment we installed in spring 2009 a remote controlled test setup with a dummy mirror facet on the roof of the institute's building. Whereas the actuators are permanently moving we record the actual positions and weather conditions simultaneous. Meanwhile the system has gone through a number of moving cycles which correspond to a running time of 30 years, demonstrating that the requirements have been met.

- **CTA photomultiplier frontend-amplifier and frontend clock generator (Sec. 5)**
  A prototype camera will use photomultiplier tubes as photon detectors. The electronics workshop is involved in the development of associated amplifiers (Fig. 17.1). Requirements are low power consumption while having enough amplification for driving the following analogue-digital converters (ADC). To cover the large dynamic range of possible photon signals (up to 4000 photoelectrons), two parallel stages with different gains and shaping times are used for each PMT.

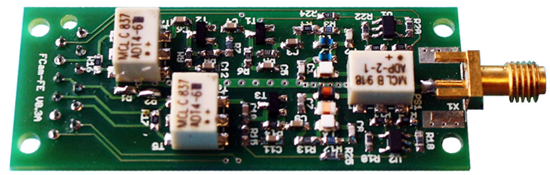

Figure 17.1: CTA frontend-amplifier.

  In addition, we are constructing a prototype for a stable clock, able to provide low-jitter clock signals to the ADCs at different frequencies. These clocks will be tied via a timing GPS receiver to the GPS time standard and will therefore provide an absolute time reference at the nanosecond level.

- **CTA trigger processor board (Sec. 5)**
  For studying different trigger algorithms, an FPGA based trigger processor is being designed. It is planned to be interfaced to ADC boards designed by the Max-Planck Institute for Nuclear Physics (Heidelberg).

- **Special ultra-clean PMT bases (Sec. 4)**
  For the Xenon experiment additional special ultra-clean PMT bases made out of a Teflon substrate were built.

- **PPMS-heater and kHz-amplifier (Sec. 12)**
  For a PPMS (Physical Property Measurement System) device a heater interface was built (Fig. 17.2). The output voltage signal of the lock-in amplifier is converted to a power signal which is used to drive a heater in the cryostat. In return, the thermocouple signal is amplified and connected to the input of the lock-in amplifier. Another frontend amplifier for the

PPMS (shown in Fig. 17.3) consists of two stages with integrated active low-pass filter for noise rejection.

- **Prototype infrared detector (Sec. 12)**
  In the beginning of 2010 we finished the assembly of an infrared detector for the single photon counter test setup (Fig. 17.4). A final unit consisting of the IR detector, the preamplifier, a 400 Hz filter and a rectifier was realized on a compact printed circuit board and installed in a shielding enclosure. The device allows the intensity measurement of the infrared radiation clocked with 400 Hz.

- **Solid State Physics (Sec. 11)**
  We renewed a motor control unit for the NMR laboratory because the faulty drive controller chip was no longer available on the market. In a second device we implemented in addition an electronic drive brake circuit.

- **Demonstration and laboratory experiments**
  For a laboratory experiment used to measure the gravitational constant we integrated a converter which steers the drive with the needed control electronics to connect the system to a computer. For a demonstration experiment based on high-temperature superconductors (magnetic levitation train, Maglev), an automatic acceleration system has been developed. Controlled by a photo-sensor, once per lap pressurized air is released to accelerate the train and thus compensate losses caused by air friction.

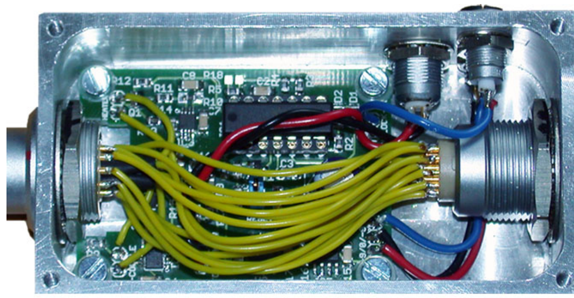

Figure 17.2: PPMS heater.

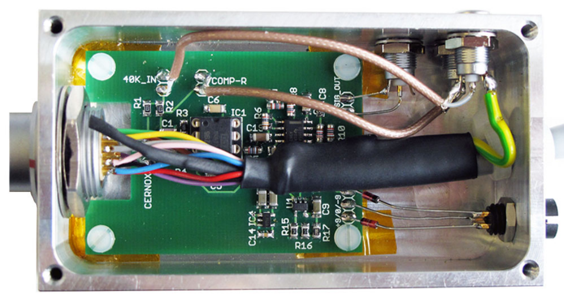

Figure 17.3: kHz amplifier.

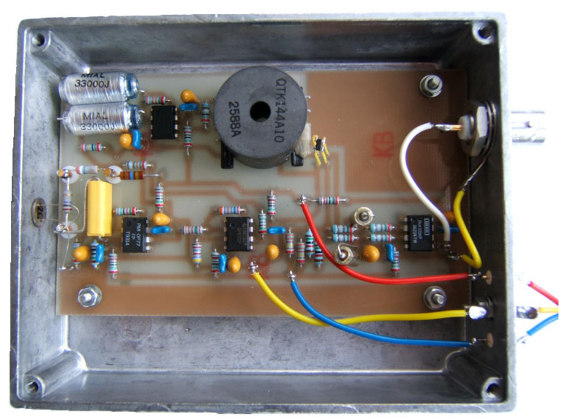

Figure 17.4: Final device with the electronics for the infrared detector.

18 Publications

18.1 Elementary particles and their interactions

18.1.1 ArDM

Articles

- **Development of wavelength shifter coated reflectors for the ArDM argon dark matter detector**
  V. Boccone *et al.*, Journal of Instrumentation **4** (2009) P06001.

- **ArDM, a 1t liquid argon detector for dark matter searches**
  C. Amsler, Proc. of Science PoS (EPS-HEP 2009) 110.

- **The ArDM project: A Liquid Argon TPC for Dark Matter Detection**
  V. Boccone, J. Phys.: Conference Series **160** (2009) 012032.

- **Test in Liquid Argon of the Light Readout System for the ArDM Experiment**
  V. Boccone, IEEE Nucl. Science Symp. Conf. Rec., Orlando N25-153 (2009).

Articles in press

- **Development and test in liquid argon of the light readout system for the ArDM experiment**
  V. Boccone, Proc. of the Tenth Conf. on the Intersections of Part. and Nucl. Phys. (CIPANP 2009), San Diego.

- **The ArDM, a ton-scale liquid argon experiment for direct Dark Matter detection**
  P. Otyugova, Proc. of the 5th Patras Workshop on Axions, WIMPs and WISPs, Durham (2009).

- **The ArDM - a ton-scale liquid argon experiment for direct Dark Matter detection**
  P. Otyugova, Proc. of the Invisible Universe Int. Conf., Paris (2009).

- **The Argon Dark Matter Experiment (ArDM)**
  C. Regenfus, Proc. of the Conf. on Topics in Astroparticle and Underground Physics (TAUP 09), Rome, Prep. arXiv:0912.2962v1 (physics.ins-det).

Lectures

- C. Amsler: **ArDM, a large liquid argon detector for dark matter searches**
  Seminar, Tata Institute of Fundamental Research (TIFR), Mumbai, 9 November 2009.

- C. Amsler: **From antihydrogen production to dark matter searches, some experimental aspects**
  Colloquium, Tata Institute of Fundamental Research (TIFR), Mumbai, 11 November 2009.

- V. Boccone: **Development and test in liquid argon of the light readout system for the ArDM experiment**
  Tenth Conference on the Intersections of Part. and Nucl. Phys. (CIPANP 2009), San Diego, 27 May 2009.

- P. Otyugova: **The ArDM (CERN RE 18) – a ton-scale liquid argon experiment for direct Dark Matter detection**
  Invisible Universe International Conference 2009, Paris, 1 July 2009.

- P. Otyugova: **The ArDM, a ton-scale liquid argon experiment for direct Dark Matter detection**
  5th Patras Workshop on Axions, WIMPs and WISPs, 16 July 2009.

- C. Regenfus: **The Argon Dark Matter Experiment (ArDM)**
  Conf. on Topics in Astroparticle and Underground Physics (TAUP 09), Rome, 1 July 2009.

- C. Regenfus: **1 ton liquid argon TPC/calorimeter for direct detection of DM**
  Presentation at the Scientific Commitee meeting, Laboratorio Subterráneo de Canfranc, 22 October 2009.

18.1.2 ATHENA

Lecture

- C. Regenfus: **The AEgIS experiment at CERN: Dropping antihydrogen atoms**
  SPS/ ÖPG meeting, Innsbruck, 2 September 2009.

18.1.3 CDMS

Articles

- **Search for Axions with the CDMS Experiment**
  CDMS Collaboration, Phys. Rev. Lett. 103, 141802 (2009).

- **Analysis of the low-energy electron-recoil spectrum of the CDMS experiment**
  CDMS Collaboration, Phys. Rev. D 81, 042002 (2010).

- **Results from the Final Exposure of the CDMS II Experiment**
  CDMS Collaboration, Science, 1186112 (2010).

Lectures

- S. Arrenberg: **Search for Dark Matter with the CDMS Experiment**
  WIN09, Perugia, Italy, Sep. 16 2009.

- S. Arrenberg: **Search for Dark Matter with the CDMS Experiment**
  SPS meeting 2009, Innsbruck, Sep. 4 2009.

- T. Bruch: **CDMS-II to SuperCDMS: WIMP search at a zeptobarn**
  PATRAS 09, Durham, UK, July 13 2009.

18.1.4 CMS

Articles

- **Mechanical design and material budget of the CMS barrel pixel detector**
  C. Amsler *et al.*,Journal of Instrumentation **4** (2009) P05003.

- **Stand-alone cosmic muon reconstruction before installation of the CMS silicon strip tracker**
  CMS Tracker Collaboration, Journal of Instrumentation **4** (2009) P05004.

- **Commissioning of the CMS experiment and the cosmic run at four tesla**
  CMS Collaboration, Journal of Instrumentation **5** (2010) T03001.

- **Performance of the CMS Level-1 trigger during commissioning with cosmic ray muons and LHC beams**
  CMS Collaboration, Journal of Instrumentation **5** (2010) T03002.

- **Performance of the CMS drift-tube chamber local trigger with cosmic rays**
  CMS Collaboration, Journal of Instrumentation **5** (2010) T03003.

- **Fine synchronization of the CMS muon drift-tube local trigger using cosmic rays**
  CMS Collaboration, Journal of Instrumentation **5** (2010) T03004.

- **Commissioning of the CMS High-Level Trigger with cosmic rays**
  CMS Collaboration, Journal of Instrumentation **5** (2010) T03005.

- **CMS data processing workflows during an extended cosmic ray run**
  CMS Collaboration, Journal of Instrumentation **5** (2010) T03006.

- **Commissioning and performance of the CMS pixel tracker with cosmic ray muons**
  CMS Collaboration, Journal of Instrumentation **5** (2010) T03007.

- **Commissioning and performance of the CMS silicon strip tracker with cosmic ray muons**
  CMS Collaboration, Journal of Instrumentation **5** (2010) T03008.

- **Alignment of the CMS silicon tracker during commissioning with cosmic rays**
  CMS Collaboration, Journal of Instrumentation **5** (2010) T03009.

- **Performance and operation of the CMS electromagnetic calorimeter**
  CMS Collaboration, Journal of Instrumentation **5** (2010) T03010.

- **Time reconstruction and performance of the CMS electromagnetic calorimeter**
  CMS Collaboration, Journal of Instrumentation **5** (2010) T03011.

- **Performance of the CMS hadron calorimeter with cosmic ray muons and LHC beam data**
  CMS Collaboration, Journal of Instrumentation **5** (2010) T03012.

- **Performance of CMS hadron calorimeter timing and synchronization using test beam, cosmic ray, and LHC beam data**
  CMS Collaboration, Journal of Instrumentation **5** (2010) T03013.

- **Identification and filtering of uncharacteristic noise in the CMS hadron calorimeter**
  CMS Collaboration, Journal of Instrumentation **5** (2010) T03014.

- **Performance of the CMS drift tube chambers with cosmic rays**
  CMS Collaboration, Journal of Instrumentation **5** (2010) T03015.

- **Calibration of the CMS drift tube chambers and measurement of the drift velocity with cosmic rays**
  CMS Collaboration, Journal of Instrumentation **5** (2010) T03016.

- **Performance study of the CMS barrel resistive plate chambers with cosmic rays**
  CMS Collaboration, Journal of Instrumentation **5** (2010) T03017.

- **Performance of the CMS cathode strip chambers with cosmic rays**
  CMS Collaboration, Journal of Instrumentation **5** (2010) T03018.

- **Aligning the CMS muon chambers with the muon alignment system during an extended cosmic ray run**
  CMS Collaboration, Journal of Instrumentation **5** (2010) T03019.

- **Alignment of the CMS muon system with cosmic-ray and beam-halo muons**
  CMS Collaboration, Journal of Instrumentation **5** (2010) T03020.

- **Precise mapping of the magnetic field in the CMS barrel yoke using cosmic rays**
  CMS Collaboration, Journal of Instrumentation **5** (2010) T03021.

- **Performance of CMS muon reconstruction in cosmic-ray events**
  CMS Collaboration, Journal of Instrumentation **5** (2010) T03022.

- **Measurement of the muon stopping power in lead tungstate**
  CMS Collaboration, Journal of Instrumentation **5** (2010) P03007.

- **Transverse-momentum and pseudorapidity distributions of charged hadrons in pp collisions at $\sqrt{s}$ = 0.9 and 2.36 TeV**
  CMS Collaboration, Journal of High Energy Physics **02** (2010) 041.

- **Algorithms for b-Jet Identication at CMS**
  A. Schmidt, Proc. of Science PoS (EPS-HEP 2009) 439.

- **Experience with CMS pixel software commissioning**
  V. Chiochia, Proc. of Science PoS (VERTEX 2008) 010.

- **Heavy Flavor Physics at CMS and ATLAS**
  L. Wilke, Proc. of Moriond Conf. on QCD and High Energy Interactions, Ed. THE GIOI (Vietnam), 2009, p. 147.

- **Searches for New Phenomena at CMS and ATLAS**
  T. Rommerskirchen, Proc. of Moriond Conf. on QCD and High Energy Interactions, Ed. THE GIOI (Vietnam), 2009, p. 171.

Article in press

- **Study of the B_s meson with forthcoming LHC data at CMS**
  B. Millán Mejías, Proc. of the VIII Latin Am. Symp. on Nucl. Phys. and Appl., Santiago de Chile.

CMS notes and reports

- **Algorithms for b-Jet identification in CMS**
  A. Schmidt *et al.*, CMS Note PAS BTV-09-001.

- **Search strategy for exclusive muti-jet events from supersymmetry at CMS**
  T. Rommerskirchen *et al.*, CMS PAS SUS-09-001.

- **Algorithms for Identification of jets containing b-quarks**
  C. Saout and A. Schmidt, CMS Times, 7 September 2009.

PhD theses

- **Simulation and beam test measurements of the CMS pixel detector**
  E. Alagöz, Inaugural Dissertation, Universität Zürich, 2009.

- **Early observation of t-Quark in Single-Leptonic $t\bar{t}$ Decays at CMS**
  D. Tsirigkas, Inaugural Dissertation, Universität Zürich, 2009.

- **Study of the B_s-Meson with the first LHC Data**
  L. Wilke, Inaugural Dissertation, Universität Zürich, 2009.

Invited Lectures

- V. Chiochia: **Study of the CMS experiment at the Large Hadron Collider**
  SPS/ ÖPG meeting, Innsbruck, 3 September 2009.

- C. Favaro: **The phase 1 upgrade of the CMS silicon pixel detector**
  Contributed talk, CHIPP PhD Winter School 2010, Monte Verità, Ascona, 24 January 2010.

- M. Ivova Rikova: **Measurements of the Lorentz angle in the CMS barrel pixel detector with collision and cosmic data**
  Contributed talk, CHIPP PhD Winter School 2010, Monte Verità, Ascona, 24 January 2010.

- A. Jaeger: **Commissioning of the CMS pixel detector using first data**
  Contributed talk, CHIPP PhD Winter School 2010, Monte Verità, Ascona, 24 January 2010.

- B. Millán Mejías: **Study of the Bs meson with first LHC data at CMS**
  Invited talk, Proc. of the VIII Latin Am. Symp. on Nucl. Phys. and Appl., Santiago de Chile, 18 December 2009.

- S. de Visscher: **Overview of the pixel performance results from 900 GeV run and program for 7 TeV**
  CMS Plenary talk, 16 March 2010.

- S. de Visscher: **Unconventional phenomenology of a minimal two-Higgs-doublet model**
  Spring plenary meeting of the GDR Terascale meeting, Saclay, 30 March 2010.

18.1.5 CTA

Bachelor thesis

- **Wireless Short Range Network for the Active Mirror Control of the CTA Experiment**
  Roman Gredig, Bachelor thesis, August 2009.

Conference contributions

- **Two design studies in the framework of the Cherenkov Telescope Array (CTA)**
  Arno Gadola, Joint annual meeting of the SPS, ÖPG, ÖGAA, 3 September 2009.
- **Solid Light Concentrators for Cherenkov Astronomy**
  Isabel Braun *et al.*, Proceedings of the 31st International Cosmic Ray Conference, Lodz, 7 - 15 July 2009.

18.1.6 D0

Article (based on the Master thesis of Christophe Salzmann)

- **Relative rates of B meson decays into psi(2S) and J/psi mesons**
  V. M. Abazov *et al.*, D0 Collaboration, Phys. Rev. **D**79, 111102 (2009).

18.1.7 DARWIN

Invited Lectures

- L. Baudis: **DARWIN: DARk matter WImp search with Noble liquids**
  WONDER Workshop on next dark matter experimental researches at LNGS, Gran Sasso Laboratory, March 23 2010.
- L. Baudis: **DARWIN: DARk matter WImp search with Noble liquids**
  Ninths UCLA Symposium on Sources and Detection of Dark Matter and Dark Energy, Marina del Rey, February 26 2010.

18.1.8 DIRAC

Articles

- **Observation of πK-atoms with DIRAC-II**
  Y. Allkofer, Hyperfine Interactions **193** (2009) 39.

- **Experimental evidence for πK-atoms**
  C. Amsler, Proc. of Science PoS (EPS-HEP 2009) 078.

- **Evidence for $K\pi$ atoms with DIRAC**
  A. Benelli, Proc. of Science PoS (CD09) 008.

Note

- **Kaon/proton separation with the aerogel**
  A. Benelli and V. Yazkov, DIRAC note 09-07.

Lecture

- A. Benelli: **Evidence for $K\pi$ atoms with DIRAC**
  6th Int. Workshop on Chiral Dynamics, Bern, 6 July 2009.

18.1.9 GERDA

Lectures

- F. Froborg: **The Calibration System for the GERDA Experiment**
  DPG, Bonn, Germany, Mar. 19 2010.

- R. Santorelli: **The GERDA experiment: A search for neutrinoless double beta decay**
  SPS meeting 2009, Innsbruck, Sep 4 2009.

Posters

- **Development of a low neutron emission source for the GERDA experiment**
  M. Tarka, SLAC Summer Institute 2009, CA, USA, Aug 3-14 2009.

- **Calibration System for GERDA**
  F. Froborg, SLAC Summer Institute 2009, Menlo Park, CA, USA, Aug 3-14 2009.

18.1.10 H1

Articles

- **Strangeness Production at Low Q^2 in Deep Inelastic ep Scattering at HERA**
  H1-Collaboration, F.D. Aaron *et al.*, Eur.Phys.J. **C61** (2009) 185.

- **Events with Isolated Leptons and Missing Transverse Momentum and Measurement of W Production at HERA**
  H1-Collaboration, F.D. Aaron *et al.*, Eur.Phys.J. **C64** (2009) 251.

- **Inclusive Photoproduction of $\rho^0,\ K^{*0}$ and ϕ Mesons at HERA**
  H1-Collaboration, F.D. Aaron *et al.*, Phys.Lett. **B673** (2009) 119.

- **General Search for New Phenomena at HERA**
  H1-Collaboration, F.D. Aaron *et al.*, Phys.Lett. **B674** (2009) 257.

- **Measurement of the Inclusive ep Scattering Cross Section at Low Q^2 and x at HERA**
  H1-Collaboration, F.D. Aaron *et al.*, Eur.Phys.J. **C63** (2009) 625.

- **Search for Excited Quarks in ep Collisions at HERA**
  H1-Collaboration, F.D. Aaron *et al.*, Phys.Lett. **B678** (2009) 335.

- **A Precision Measurement of the Inclusive ep Scattering Cross Section at HERA**
  H1-Collaboration, F.D. Aaron *et al.*, Eur.Phys.J. **C64** (2009) 561.

- **Jet Production in ep Collisions at High Q^2 and Determination of α_S Using Full HERA Data**
  H1-Collaboration, F.D. Aaron *et al.*, Eur.Phys.J. **C65** (2010) 363.

- **Search for Single Top Quark Production at HERA**
  H1-Collaboration, F.D. Aaron *et al.*, Phys.Lett. **B678** (2009) 450.

- **Measurement of the Charm and Beauty Structure Function using the H1 Vertex Detector at HERA**
  H1-Collaboration, F.D. Aaron *et al.*, Eur.Phys.J. **C65** (2010) 89.

- **Observation of Hadronic Final State Charge Asymmetry in High Q^2 Deep-Inelastic Scattering at HERA**
  H1-Collaboration, F.D. Aaron *et al.*, Phys.Lett. **B681** (2009) 125.

- **Multi-Leptons with High Transverse Momentum at HERA**
  H1- and ZEUS-Collaboration***, F.D. Aaron *et al.*, JHEP **10** (2009) 013.

- **Deeply Virtual Compton Scattering and its Beam Charge Asymmetry in $e^{\pm}p$ Collisions at HERA**
  H1-Collaboration, F.D. Aaron *et al.*, Phys.Lett. **B681** (2009) 391.

- **Prompt Photons in Photoproduction at HERA**
  H1-Collaboration, F.D. Aaron *et al.*, Eur.Phys.J. **C66** (2010) 17.

- **Diffractive Electroproduction of ρ and ϕ Mesons at HERA**
  H1-Collaboration, F.D. Aaron *et al.*, JHEP **05** (2010) 032.

- **Events with Isolated Leptons and Missing Transverse Momentum and Measurement of W-Production at HERA**
  H1- and ZEUS-Collaboration, F.D. Aaron *et al.*, JHEP **03** (2010) 035.

- **Combined Measurement and QCD Analysis of the Inclusive $e^{\pm}p$ Neutral Scattering Cross-Sections at HERA**
  H1- and ZEUS-Collaboration, F.D. Aaron *et al.*, JHEP **01** (2010) 109.
- **Measurement of $D^{*\pm}$ Meson Production Cross Section and $F_2^{c\bar{c}}$ at High Q^2 in Electron-Proton Scattering at HERA**
  H1-Collaboration, F.D. Aaron *et al.*, Phys.Lett. **B686** (2010) 91.
- **Jet Production in ep Collisions at Low Q^2 and Determination of α_S**
  H1-Collaboration, F.D. Aaron *et al.*, Eur.Phys.J. **C67** (2010) 1.

Article in print

- **Measurement of Leading Neutron Production in Deep-Inelastic Scattering at HERA**
  H1-Collaboration, F.D. Aaron *et al.*, DESY 09 – 185, arXiv:1001.0532 (hep-ex), Eur.Phys.J. **C** (2010).

PhD thesis

- **Prompt Photon Production in Photoproduction at HERA**
  Krysztof Nowak, PhD thesis, Universität Zürich, October 2009.

Lectures

- Kryzsztof Nowak: **Prompt Photons in Photoproduction**
  XVII Int. Workshop on Deep Inelastic Scattering and Related Subjects, Madrid, Spain, 26-30 April 2009.
- Katharina Müller: **Photon Structure in Photoproduction**
  Int. Conf. on the Structure and Interactions of the Photon, Hamburg, Germany, 11-15 May 2009.
- Krzystof Nowak: **Prompt photons in DIS and γp**
  2009 Europhysics Conf. on High Energy Physics, Krakow, Poland, 16-22 July 2009.

18.1.11 LHCb

Bachelor and Master theses

- **Noise Investigations for the Tracker Turicensis of the LHCb Experiment**
  Viktor Hangartner, Master thesis, Universität Zürich, August 2009.
- **Setting up an LHCb TT-Detector Test Stand**
  Gabriel Landolt, Bachelor thesis, August 2009.
- **Wireless Short Range Network for the Active Mirror Control of the CTA Experiment**
  Roman Gredig, Bachelor Thesis, August 2009.

- **Online Monitoring for the Silicon Tracker of the LHCb Experiment**
  Nicola Chiapolini, Master Thesis, Juli 2009.

Invited Lectures

- **First Collisions in LHC**
  Jeroen van Tilburg, Workshop on the New, the Rare and the Beautiful, University of Zurich, 6 - 8 January 2010.
- **LHCb: Preparation for LHC beam**
  Jeroen van Tilburg, CHIPP annual meeting 2009, Appenberg, August 2009.

Conference contributions

- **Commissioning and performance of the LHCb Silicon Tracker**
  Jeroen van Tilburg, Proceedings of the the Vienna Conference on Instrumentation, March 2010.
- **You are so beautiful: Rare b decays at LHCb**
  Michel De Cian and Angela Büchler, Joint Annual Meeting OePG/SPS, Innsbruck, 2 - 4 September 2009.
- **Alignment of the LHCb Silicon Tracker using LHC beam injection data**
  Christophe Salzmann, Joint Annual meeting OePG/SPS, Innsbruck, 2 - 4 September 2009.
- **LHCb silicon detector alignment with first LHC beam induced tracks**
  Christophe Salzmann, 3rd LHC Detector Alignment Workshop, CERN, 15 - 16 June 2009.
- **Probing low-x with Drell-Yan events at LHCb**
  J. Anderson, XVII International Workshop on Deep-Inelastic Scattering and Related Subjects, Madrid, Spain, 26 - 30 April 2009.
- **The LHCb Silicon Tracker Commissioning and First Data**
  Angela Büchler, IEEE Nuclear Science Symposium, Orlando, Florida, USA, 25 - 31 October 2009.

18.1.12 PEN

Article

- **New Precise Measurement of the Pion Weak Form Factors in $\pi^+ \rightarrow e^+\nu\gamma$ Decay**
  M. Bychkov *et al.*, Phys. Rev. Lett. **103**, 051802 (2009).

Conference Proceedings

- **PEN: a sensitive search for non-(V-A) weak processes**
  D. Pocanic *et al.*, PEN Collaboration, Proc. of PANIC08, Eilat, 928-933 (2009).
- **PEN experiment: A Precise measurement of the $\pi^+ \to e^+\nu$ decay branching fraction**
  D. Pocanic *et al.*, PEN Collaboration, AIP Conf.Proc. 1182, 698-701 (2009).

18.1.13 UCN

PhD thesis

- **Towards a new measurement of the neutron electric dipole moment**
  Andreas Knecht, PhD Thesis, Universität Zürich, November 2009.

18.1.14 XENON

Article in press

- **Spatially uniform calibration of a liquid xenon detector at low energies using 83m-Kr**
  A. Manalaysay, T. Marrodan Undagoitia, A. Askin, L. Baudis, A. Behrens, A. Kish, O. Lebeda, D. Venos, Review of Scientific Instruments.

PhD thesis

- **Response of liquid xenon to low-energy ionizing radiation and its use in the XENON10 Dark Matter search**
  A. Manalaysay, PhD thesis, Universität Zürich, December 2009.

Invited Lecture

- L. Baudis: **The Physics of the Universe**
  SpaceX and Caltech, Los Angeles, January 9, 2010.

18.1.15 Miscellaneous

Reports

- **Physics at a future Neutrino Factory and super-beam facility**
  ISS Physics Working Group, A. Bandyopadhyay *et al.* (A. van der Schaaf), Rept. Prog. Phys. **72** 106201 (2009).

Invited Lectures

- F. Froborg: **Neutrinoless Double Beta Decay**
  "The New, the Rare and the Beautiful" Workshop in Zurich, Jan. 07 2010.

- T. Marrodan Undagoitia: **Future detectors for low energy neutrino astronomy: LAGUNA, LENA and Hano-hano**
  Neutrino Champagne, Rheims, France, Oct. 21 2009.

- T. Marrodan Undagoitia: **Search for dark matter with liquid xenon**
  E15 Seminar, München, July 21 2009.

- A. Manalaysay: **Improved understanding of liquid xenon's response in dark matter searches**
  TAUP 2009, Rome, July 1 2009.

- L. Baudis: **Dark matter: overview of terrestrial, non-accelerator experiments; DARWIN**
  LAUNCH 2009, Heidelberg, November 10 2009.

- L. Baudis: **Direct searches for dark matter**
  Physics Colloquium, IFAE UA Barcelona, October 5 2009.

- L. Baudis: **Direct Dark Matter Searches: an Overview**
  CHIPP Plenary meeting, Appenberg, August 25 2009.

- L. Baudis: **WIMPs**
  Summary Talk, 5th Patras Workshop on Axions, WIMPs and WISPs, Durham University, July 17 2009.

- L. Baudis: **Direct Searches for Cold Dark Matter in the Milky Way**
  XXIemes Rencontres de Blois, Blois, June 23 2009.

- L. Baudis: **Direct Dark Matter Searches**
  rapporteur talk, New Opportunities in the Physics Landscape at CERN, CERN, May 11-13 2009.

- T. Bruch: **The dark connection to the LHC**
  International Conference on Neutrino Physics in the LHC Era, Luxor, Egypt, Nov. 18 2009.

18.1.16 Outreach

Lectures

- L. Baudis: **The Unbearable Lightness of Neutrinos**
  zurich.minds, Zurich, December 16 2009.

- L. Baudis: **Die dunkle Seite des Universums**
  Weizmann Symposium, University of Zurich, November 25 2009.

- L. Baudis: **Das Universum in 50 Minuten**
  Montagsforum, Dornbirn, May 18 2009.

18.2 Condensed matter

18.2.1 Superconductivity and Magnetism

Articles

- **Evidence for Kosterlitz-Thouless and three-dimensional XY critical behavior in $Bi_2Sr_2CaCu_2O_{8+\delta}$**
  S. Weyeneth, T. Schneider, and E. Giannini, Phys. Rev. B **79**, 214504-1-8 (2009).

- **Single crystals of $LnFeAsO_{1-x}F_x$ (Ln=La, Pr, Nd, Sm, Gd) and $Ba_{1-x}Rb_xFe_2As_2$: Growth, structure and superconducting properties**
  J. Karpinski, N.D. Zhigadlo, S. Katrych, Z. Bukowski, P. Moll, S. Weyeneth, H. Keller, R. Puzniak, M. Tortello, D. Daghero, R. Gonnelli, I. Maggio-Aprile, Y. Fasano, Ø. Fischer, K. Rogacki, and B. Batlogg, Physica C **469**, 370-380 (2009).

- **Zero-field superfluid density in a d-wave superconductor evaluated from muon-spin-rotation experiments in the vortex state**
  R. Khasanov, Takeshi Kondo, S. Strässle, D.O.G. Heron, A. Kaminski, H. Keller, S.L. Lee, and Tsunehiro Takeuchi, Phys. Rev. B **79**, 180507(R)-1-4 (2009).

- **Anomalous asymmetry in the Fermi surface of the high-temperature superconductor $YBa_2Cu_4O_8$ revealed by angle-resolved photoemission spectroscopy**
  Takeshi Kondo, R. Khasanov, Y. Sassa, A. Bendounan, S. Pailhes, J. Chang, J. Mesot, H. Keller, N.D. Zhigadlo, M. Shi, Z. Bukowski, J. Karpinski, and A. Kaminski, Phys. Rev. B **80**, 100505(R)-1-4 (2009)

- **Controlled oxygen vacancies and space correlation with Cr^{3+} in $SrTiO_3$**
  F. La Mattina, J.G. Bednorz, S.F. Alvarado, A. Shengelaya, K. A. Müller, and H. Keller, Phys. Rev. B **80**, 075122-1-8 (2009).

- **Synthesis, crystal structure, and chemical stability of the superconductor $FeSe_{1-x}$**
  E. Pomjakushina, K. Conder, V. Pomjakushin, M. Bendele, and R. Khasanov, Phys. Rev. B **80**, 024517-1-7 (2009).

- **Coexistence of incommensurate magnetism and superconductivity in $Fe_{1+y}Se_xTe_{1-x}$**
  R. Khasanov, M. Bendele, A. Amato, P. Babkevich, A.T. Boothroyd, A. Cervellino, K. Conder, S.N. Gvasaliya, H. Keller, H.-H. Klauss, H. Luetkens, V. Pomjakushin, E. Pomjakushina, and B. Roessli, Phys. Rev. B **80**, 140511-1-4 (2009).

- **Local Electron-Lattice Interactions in High-Temperature Cuprate Superconductors**
  Hugo Keller and Annette Bussmann-Holder, Advances in Condensed Matter Physics **2010**, 1-17 (2009).

- **Comparative study of the pressure effects on the magnetic penetration depth in electron- and hole-doped cuprate superconductors**
  D. Di Castro, R. Khasanov, A. Shengelaya, K. Conder, D.-J. Jang, M.-S. Park, S.-I. Lee, and H. Keller, J. Phys.: Condens. Matter **21**, 275701 (5pp) (2009).

- **Superconductivity in Fe and As Based Compounds: A Bridge Between MgB_2 and Cuprates**
  A. Bussmann-Holder, A. Simon, H. Keller, and A.R. Bishop, J. Supercond. Nov. Magn. **23**, 365-369 (2010).

- **Pressure Induced Static Magnetic Order in Superconducting $FeSe_{1-x}$**
  M. Bendele, A. Amato, K. Conder, M. Elender, H. Keller, H.-H. Klauss, H. Luetkens, E. Pomjakushina, A. Raselli, and R. Khasanov, Phys. Rev. Lett. **1**04, 087003-1-4 (2010).

- **Evolution of Two-Gap Behavior of the Superconductor $FeSe_{1-x}$**
  R. Khasanov, M. Bendele, A. Amato, K. Conder, H. Keller, H.-H. Klauss, H. Luetkens, and E. Pomjakushina, Phys. Rev. Lett. **104**, 087004-1-4 (2010).

- **Magnetic excitations of $Fe_{1+y}Se_xTe_{1-x}$ in magnetic and superconductive phases**
  P. Babkevich, M. Bendele, A. T. Boothroyd, K. Conder, S. N. Gvasaliya, R. Khasanov, E. Pomjakushina, and B. Roessli, J. Phys.: Condens. Matter **22**, 142202-1-6 (2010).

- **Novel carboxymethyl chitin nanoparticles for cancer drug delivery applications**
  A. Dev, J. C. Mohan, V. Sreeja, H. Tamura, G. R. Patzke, F. Hussain, S. Weyeneth, S. V. Nair, and R. Jayakumar, Carbohydrate Polymers **79**, 1073-1079 (2010).

- **Testing polaron coherence and the pairing symmetry in cuprate superconductors by local probe methods**
  A. Bussmann-Holder, H. Keller, J. Mustre de Leon, A. Simon, A.R. Bishop, K.A. Müller, J. Supercond. Nov. Magn. **23**, 295-299 (2010).

Article in press

- **Bulk superconductivity at 2.6 K in undoped $RbFe_2As_2$**
  Z. Bukowski, S. Weyeneth, R. Puzniak, J. Karpinski, and B. Batlogg, Physica C.

PhD thesis

- **Anisotropic Properties and Critical Behavior of High-Temperature Superconductors**
  S. Weyeneth, PhD thesis of the University of Zurich, 2009.

Conference reports

- **Temperature Dependent Anisotropy of Novel Iron-Based Superconductors**
  S. Weyeneth, R. Puzniak, N.D. Zhigadlo, Z. Bukowski, S. Katrych, J. Karpinski, and H. Keller, Swiss Workshop on Materials with Novel Electronic Properties, Les Diablerets, Switzerland, 26-28 August, 2009.

- **Temperature Dependent Anisotropy of Novel Iron-Pnictide Superconductors**
  S. Weyeneth, R. Puzniak, N.D. Zhigadlo, Z. Bukowski, S. Katrych, J. Karpinski, and H. Keller, 9th International Conference on Materials and Mechanisms of Superconductivity, Tokyo, Japan, 7-12 September, 2009.

- **Superconductivity and Magnetism in Cuprate Heterostructures Studied by Low Energy μSR**
  B.M. Wojek, E. Morenzoni, D.G. Eshchenko, T. Prokscha, A. Suter, E. Koller, E. Treboux, Ø. Fischer, and H. Keller, DPG Frühjahrstagung der Sektion Kondensierte Materie (SKM), Dresden, Germany, March 22-27, 2009.

- **Magnetism and Interface Superconductivity in Metal-Insulator $La_{2-x}Sr_xCuO_4$ superlattices**
  A. Suter, E. Morenzoni, T. Prokscha, B.M. Wojek, H. Luetkens, G. Nieuwenhuys, A. Gozar, G. Logvenov, and I. Bozovic, Swiss Workshop on Materials with Novel Electronic Properties, Les Diablerets, August 26-28, 2009.

- **Diamagnetic Response in LSCO Heterostructures**
  E. Morenzoni, B.M. Wojek, A. Suter, I. Bozovic, G. Logvenov, T. Prokscha, H. Keller, and Ø. Fischer, Swiss Workshop on Materials with Novel Electronic Properties, Les Diablerets, August 26-28, 2009.

- **Magnetism and Interface Superconductivity in Metal-Insulator $La_{2-x}Sr_xCuO_4$ superlattices**
  A. Suter, E. Morenzoni, T. Prokscha, B.M. Wojek, H. Luetkens, G. Nieuwenhuys, A. Gozar, G. Logvenov, and I. Bozovic, Joint Users' Meeting at PSI 2009, Villigen, October 12-13, 2009.

- **Diamagnetic Response in LSCO Heterostructures**
  E. Morenzoni, B.M. Wojek, A. Suter, I. Bozovic, G. Logvenov, T. Prokscha, H. Keller, and Ø. Fischer, Joint Users' Meeting at PSI 2009, Villigen, October 12-13, 2009.

- **Low energy μSR as a new local probe technique to study photo-induced phenomena in thin films and heterostructures**
  T. Prokscha, K.H. Chow, D.G. Eshchenko, H. Luetkens, E. Morenzoni, G. Nieuwenhuys, Z. Salman, R. Scheuermann, A. Suter, and B.M. Wojek, Joint Users' Meeting at PSI 2009, Villigen, October 12-13, 2009.

- **Local proximity studies of normal-superconductor bilayers by LE-μSR and β-NMR**
  E. Morenzoni, A. Suter, B.M. Wojek, E. Kirk, R.F. Kiefl, W.A. MacFarlane, G.D. Morris, W. Dong, D.G. Eshchenko, T. Prokscha, K.H. Chow, M.D. Hossain, T.J. Parolin, H. Saadaoui, M. Smadella, and Q. Song, Advanced Science Research Symposium 2009, Tokai, Japan, November 10-12, 2009.

- **Superconductivity and magnetism in the oxypnictides: ESR and μSR studies of (La,Gd)$FeAsO_{1-x}F_x$ compounds**
  F. Murányi, A. Alfonsov, V. Kataev, A. Köhler, J. Werner, G. Behr, N. Leps, R. Klingeler, A. Kondrat, C. Hess, B. Büchner, A. Amato, R. Khasanov, H. Luetkens, H.-H. Klauss, N.D. Zhigadlo,

S. Katrych, Z. Bukowski, J. Karpinski, DPG Spring Meeting Dresden, Germany, March 22-27, 2009.

- **High field ESR spectroscopy on $GdO_{1-x}F_x$FeAs**
  A. Alfonsov, F. Murányi, V. Kataev, N. Leps, R. Klingeler, A. Kondrat, C. Hess, J. Werner, G. Behr, B. Büchner, 9th International Conference on Research in High Magnetic Fields Dresden, Germany, July 22-25, 2009.

- **EPR of the doped and undoped $GdFeAsO_xF_{1-x}$**
  F. Murányi, A. Alfonsov, V. Kataev, A. Köhler, J. Werner, G. Behr, H. Keller, B. Büchner, Swiss Workshop on Materials with Novel Electronic Properties, Les Diablerets, Switzerland, 26-28 August, 2009.

- **Pressure Induced Static Magnetic Order in Superconducting $FeSe_{1-x}$**
  M. Bendele, R. Khasanov, K. Conder, E. Pomjakushina, and H. Keller; Joint Users' Meeting at PSI 2009, Villigen, October 12-13, 2009.

- **Superconductivity and Magnetism in $FeSe_{1-x}$: μSR pressure study**
  M. Bendele, R. Khasanov, K. Conder, E. Pomjakushina, E. Morenzoni, MaNEP Workshop, Neuchatel, 27. Januar 2010.

Invited lectures

- H. Keller: **Isotope effects and multi-band superconductivity in high-temperature superconductors**
  SMEC 2009 Conference, Study of Matter at Extreme Conditions, Miami - Western Caribbean, U.S.A., March 28 - April 2, 2009.

- H. Keller: **Isotope effects and multi-band superconductivity in high-temperature superconductors**
  Workshop on Routes to Superconductivity at Ambient Conditions, ICCMP, Brasilia, Brasilia, April 13 - 24, 2009.

- H. Keller: **Experimental and theoretical evidence for subtle lattice effects in layered high T_c systems**
  The Institute of Physics, Chinese Academy of Sciences Beijing, Beijing, China, May 12, 2009.

- H. Keller: **Isotope effects and multi-band superconductivity in layered high-temperature superconductors**
  Seventh International Conference on New Theories, Discoveries and Applications of Superconductors and Related Materials (New3SC-7), Beijing, China, May 13-16, 2009.

- H. Keller: **Isotope effects and multi-band superconductivity in layered high-temperature superconductors**
  Mini-Workshop on High-T_c Superconductivity and Related Topics, University of Miami, Coral Cables, USA, November 14, 2009.

- S. Strässle: **NMR Search for Orbital-Current Effects in YBCO Compounds**
  Swiss Workshop on Materials with Novel Electronic Properties, Les Diablerets, 26-28 August, 2009.

- S. Weyeneth: **Anisotropy and Critical Behavior of High-Temperature Superconductors**
  Lecture at Material Science Division, Argonne National Laboratory, Argonne, USA, 8. October, 2009.

18.2.2 Phase transitions and superconducting photon detectors

Articles

- **Optical and transport properties of ultrathin NbN films and nanostructures**
  A. Semenov, B. Günther, U. Böttger, H.-W. Hübers, H. Bartolf, A. Engel, A. Schilling, K. Il'in, M. Siegel, R. Schneider, D. Gerthsen and N. A. Gippius, Phys. Rev. B, **80** (2009) 054510.

- **NbN superconducting nanowire photon counters: magnetoconductivity and other detector properties**
  A. Engel, H. Bartolf, L. Gómez, A. Semenov, K. Il'in, A. Schilling, H.-W. Hübers and M. Siegel, AIP Conference Proceedings, **1185** (2009) 76-79.

- **Current-assisted thermally activated flux liberation in ultrathin nanopatterned NbN superconducting meander structures**
  H. Bartolf, A. Engel, A. Schilling, K.Il'in, M. Siegel, H.-W. Hübers and A. Semenov, Phys. Rev. B, **81** (2010) 024502.

- **Application of a small oscillating magnetic field to reveal the peak effect in the resistivity of Nb_3Sn**
  M. Reibelt, A. Schilling and N. Toyota, Phys. Rev. B, **81** (2010) 094510.

- **Comment on 'Superconducting transition in Nb nanowires fabricated using a focused-ion beam'**
  A. Engel, Nanotechnology, **21** (2010) 168001.

PhD thesis

- **Fabrication and Characterization of Superconducting Nanowire Highspeed Single-Photon Detectors**
  Holger Bartolf, PhD Thesis, Physik-Institut Universität Zürich, 2009.

Bachelor thesis

- **Aufbau eines ^{3}He-Kryostaten zur Charakterisierung supraleitender, extrem schneller Einphotonen-Zähler**
  Simon Gross, Bachelor Thesis, Physik-Institut Universität Zürich, 2009.

Contributed Conference Presentations

- **NbN nanowire photon counters: optical, electronic and detector properties**
  A. Engel, 13$^{\mathrm{th}}$ International Workshop on Low Temperature Detectors, Stanford, USA, 20.-24.7.2009.

- **Fluctuation Effects near the 1D-2D Cross-Over in Superconducting Nanostrips**
  A. Engel, 2009 Swiss Workshop on Materials with Novel Electronic Properties, Les Diablerets, Switzerland, 26.-28.8.2009.

Invited Lectures

- H. Bartolf: **Detection of Electromagnetic Quanta and Thermal Vortex-Excitations within a Nanowire High-speed Single-Photon Detector**

Seminar Talk at IBM, IBM Research GmbH, Zurich Research Laboratory, Rüschlikon, Switzerland, 19.1.2010.

18.2.3 Surface Physics

Articles

- **Fermi surfaces of single-layer dielectrics on transition metals**
  T. Greber, M. Corso, J. Osterwalder, Surf. Sci. 603, 1373-1377 (2009).
- **Advanced photoelectric effect experiment beamline at ELETTRA: a surface science laboratory coupled with synchrotron radiation**
  G. Panaccione, I. Vobornik, J. Fujii, D. Krizmancic, E. Annese, L. Giovanelli, F. Maccherozzi, F. Salvador, A. De Luisa, D. Benedetti, A. Gruden, P. Bertoch, F. Polack, D. Cocco, G. Sostero, B. Diviacco, M. Hochstrasser, U. Maier, D. Pescia, C. H. Back, T. Greber, J. Osterwalder, M. Galaktionov, M. Sancrotti, and G. Rossi, Rev. Sci. Instrum. 80, 043105:1-12 (2009).
- **Unconventional Fermi surface spin textures in the BixPb1-x/Ag(111) surface alloy**
  F. Meier, V. Petrov, S. Guerrero, C. Mudry, L. Patthey, J. Osterwalder, and J. Hugo Dil, Phys. Rev. B 79, 241408(R):1-4 (2009).
- **Multimorphism in molecular monolayers: pentacene on Cu(110)**
  K. Müller, A. Kara, T. K. Kim, R. Bertschinger, A. Scheybal, J. Osterwalder, and T. A. Jung, Phys. Rev. B 79, 245421:1-7 (2009).
- **Looking inside an endohedral fullerene: inter- and intramolecular ordering of Dy3N@C80 (Ih) on Cu(111)**
  M. Treier, P. Ruffieux, R. Fasel, F. Nolting, S. Yang, L. Dunsch, and T. Greber, Phys. Rev. B 80, 081403(R):1-4 (2009).
- **A tunable topological insulator in the spin helical Dirac transport regime**
  D. Hsieh, Y. Xia, D. Qian, L. Wray, J. H. Dil, F. Meier, J. Osterwalder, L. Patthey, J. G. Checkelsky, N. P. Ong, A. V. Fedorov, H. Lin, A. Bansil, D. Grauer, Y. S. Hor, R. J. Cava, and M. Z. Hasan, Nature 460, 1101-1106 (2009).
- **Band formation from coupled quantum dots formed by a nanoporous network on a copper surface**
  J. Lobo-Checa, M. Matena, K. Müller, J. H. Dil, F. Meier, L. H. Gade, T. A. Jung, and M. Stöhr, Science 325, 300-303 (2009).
- **Spin and angle resolved photoemission on non-magnetic low-dimensional systems**
  J. H. Dil, J. Phys.: Condens. Matter 21, 403001:1-22 (2009).
- **Exchange splitting of the three Gamma bar surface states of Ni(111) from three-dimensional spin- and angle-resolved photoemission spectroscopy**
  T. Okuda, J. Lobo-Checa, W. Auwärter, M. Morscher, M. Hoesch, V. N. Petrov, M. Hengsberger, A. Tamai, A. Dolocan, C. Cirelli, M. Corso, M. Muntwiler, M. Klöckner, M. Roos, J. Osterwalder, and T. Greber, Phys. Rev. B, 80, 180404(R):1-4 (2009).
- **Measuring spin-polarization vectors in angle-resolved photoemission spectroscopy**
  F. Meier, J. H. Dil, and J. Osterwalder, New J. Phys., 11, 125008:1-21 (2009).

- **Observation of time-reversal-protected single-Dirac-cone topological-insulator states in Bi2 Te3 and Sb2 Te3**
  D. Hsieh, Y. Xia, D. Qian, L. Wray, F. Meier, J. H. Dil, J. Osterwalder, L. Patthey, A. V. Fedorov, H. Lin, A. Bansil, D. Grauer, Y. S. Hor, R. J. Cava, and M. Z. Hasan, Phys. Rev. Lett. 103, 146401:1-4 (2009).

- **Optical Control of Field-Emission Sites by Femtosecond Laser Pulses**
  H. Yanagisawa, C. Hafner, P. Dona, M. Klöckner, D. Leuenberger, T. Greber, M. Hengsberger, and J. Osterwalder, Phys. Rev. Lett. 103, 257603:1-4 (2009).

- **Spintronics without magnetism?**
  J. H. Dil, SPG Mitteilungen 30, 8-10 (2010).

- **LUMO photoemission lineshape in quasi-one-dimensional C60 chains**
  A. Tamai, F. Baumberger, M. Hengsberger, J. Lobo-Checa, M. Muntwiler, M. Corso, C. Cirelli, L. Patthey, Z.-X. Shen, T. Greber, and J. Osterwalder, Phys. Rev. B, 81, 045423:1-6 (2010).

- **Nano-ice on boron nitride nanomesh: accessing proton disorder**
  H. Ma, T. Brugger, S. Berner, Y. Ding, M. Iannuzzi, J. Hutter, J. Osterwalder, and T. Greber, Chem. Phys. Chem. 11, 399-403 (2010).

- **Graphene and Hexagonal Boron Nitride Layers: Nanostructures with 3 bond hierarchy levels**
  T. Greber, eJSSN 8, 62-64 (2010).

- **h-BN on Rh(111): persistence of a commensurate 13-on-12 superstructure up to high temperatures**
  D. Martoccia, S. A. Pauli, T. Brugger, T. Greber, B. D. Patterson, and P. R. Willmott, Surf. Sci. 604, L9-L11 (2010).

- **h-BN/Ru(0001) nanomesh: a 14-on-13 superstructure with 3.5 nm periodicity**
  D. Martoccia, S. A. Pauli, T. Brugger, T. Greber, B. D. Patterson, and P. R. Willmott, Surf. Sci. 604, L16-L19 (2010).

- **Supramolecular assemblies formed on an epitaxial graphene superstructure**
  A. J. Pollard, E. W. Perkins, N. A. Smith, A. Saywell, G. Goretzki, A. G. Phillips, S. P. Argent, H. Sachdev, F. Müller, S. Hüfner, S. Gsell, M. Fischer, M. Schreck, J. Osterwalder, T. Greber, S. Berner, N. R. Champness, P. H. Beton, Angew. Chem. Int. Ed. 49, 1794-1799 (2010).

- **Laser-induced field emission from tungsten tip: optical control of emission sites and emission process**
  H. Yanagisawa, C. Hafner, P. Dona, M. Klöckner, D. Leuenberger, T. Greber, J. Osterwalder, M. Hengsberger, Phys. Rev. B 81, 115429:1-10 (2010).

- **Influence of the substrate lattice structure on the formation of quantum well states in thin In and Pb films on silicon**
  J. H. Dil, B. Hülsen, T. U. Kampen, P. Kratzer and K. Horn, J. Phys.: Condens. Matter 22, 135008:1-9 (2010).

PhD theses

- **Systematic structure investigation of YBCO thin films with direct methods and surface x-ray diffraction**
  Christian Schlepütz, PhD Thesis, Physik-Institut, Universität Zürich, 2009.

- **Organic semiconductor interfaces with insulators and metals**
  Kathrin Müller, PhD Thesis, Physik-Institut, Universität Zürich, 2009, Cuvillier Verlag, Göttingen (2009).

- **Graphene and hexagonal boron nitride on transition metals and their application**
  Thomas Brugger, PhD Thesis, Physik-Institut, Universität Zürich, 2010.

Master theses

- **Photon emission during inelastic electron tunneling with nanometer resolution from the h-BN/Rh(111) nanomesh**
  Mario Thomann, Master Thesis, Physik-Institut, Universität Zürich, 2009.

- **Graphene on h-BN nanomesh**
  Dominic Böni, Master Thesis, Physik-Institut, Universität Zürich, 2009.

Contributed conference presentations

- **Asymmetric electron emission from a tungsten tip apex due to surface electromagnetic waves excited by laser pulses**
  H. Yanagisawa, 5th Workshop on Numerical Methods for Optical Nanostructures, ETH Zürich, 07.07.09.

- **Time-resolved photoemission on a ferromagnetic h-BN/Ni(111) surface and exciton excitation (Poster)**
  D. Leuenberger, Femto-9 Conference, Beijing University, Beijing, China, 10.08.09.

- **Nano-ice on the boron nitride nanomesh**
  H. Ma, Gemeinsame Jahrestagung der Schweizerischen und Österreichischen Physikalischen Gesellschaften, Innsbruck, Österreich, 04.09.09.

- **ARPES on epitaxial graphene on transition metals**
  T. Brugger, SLS Symposium on Graphene, PSI Villigen, 01.09.09.

- **Asymmetric electron emission from a tungsten tip apex due to a Zenneck wave excited by a laser pulse**
  H. Yanagisawa, 10th International Conference on Atomically Controlled Surfaces, Interfaces and Nanostructures (ACSIN-10), Granada, Spain, 22.09.09.

- **Determination of the surface magnetization direction with resonant x-ray photoelectron diffraction**
  M. Morscher, International Conference on Electron Spectroscopy and Structure (ICESS-11), Nara, Japan, 06.10.09.

- **COPHEE and SMOKE**
  G. Landolt, Spectroscopy on Novel Materials Workshop, Rigi, 13.01.10.

- **Half of what you always wanted to know about topological insulators**
  J. Osterwalder, Spectroscopy on Novel Materials Workshop, Rigi, 14.01.10.

- **Spin-state interference in photoemission from Sb/Ag(111)**
  F. Meier, Spectroscopy on Novel Materials Workshop, Rigi, 14.01.10.

- **Spin-exchange in quantum well states due to hybridization effects**
  B. Slomski, Spectroscopy on Novel Materials Workshop, Rigi, 14.01.10.

- **Spin- and angle-resolved photoemission on low-dimensional Rashba systems: a direct probe for spintronics**
  J. H. Dil, 26th Annual SAOG Meeting (Schweizerische Arbeitsgemeinschaft für Oberflächen und Grenzflächen), Fribourg, 22.01.10.

- **Switching the surface texture by hydrogen intercalation**
  T. Greber, Surface Science Symposium (3S10), St. Christoph, Austria, 08.03.10.

- **Topological insulators: a new surface science playground**
  J. H. Dil, Surface Science Symposium (3S10), St. Christoph, Austria, 09.03.10.

- **Spin state interference in photoemission from Sb/Ag(111)**
  F. Meier, Surface Science Symposium (3S10), St. Christoph, Austria, 09.03.10.

- **Reversible switching of surface texture by hydrogen intercalation**
  T. Greber, March Meeting of the Americal Physical Society, Portland, OR, USA, 15.03.10.

- **Nano-ice on the boron nitride nanomesh - accessing proton disorder**
  H. Ma, March Meeting of the Americal Physical Society, Portland, OR, USA, 17.03.10.

Invited lectures

- J. H. Dil: **Spin-resolved ARPES: from model Rashba systems to topological metals**
  Seminar, AG Wiesendanger, Institut für Angewandte Physik, Universität Hamburg, 18.05.09.

- T. Greber: **Graphene and boron nitride single layer templates for molecules**
  4th Annual ITSLEIF Meeting and 2nd Symposium on Ion Insulator Interactions, Girano, Spain, 20.05.09.

- J. Osterwalder: **Monolagen von hexagonalem Bornitrid und Graphene: zwei ungleiche Verwandte**
  Augsburger Physikalisches Kolloquium, Physikalisches Institut, Universität Augsburg, 15.06.09.

- J. Osterwalder: **Monolayers of hexagonal boron nitride and graphene: two unlike cousins**
  Seminar, Laboratory for Photochemistry and Spectroscopy, Katholieke Universiteit Leuven, Leuven, Belgium, 10.08.09.

- J. H. Dil: **Spin-resolved ARPES: from model systems to topological metals**
  International Workshop on Strong Correlations and Angle-Resolved Photoemission Spectroscopy - CORPES09, Zürich, 24.07.09.

- T. Greber: **Hosting molecules in a 3 nm grid on sp^2 single layers on transition metals**
  International Conference on Materials for Advanced Technologies - ICMAT09, Singapore, 30.06.09.

- T. Greber: **Functional nano-templates: sp^2 single layer superstructures**
  2009 International Workshop on Nanostructures and Nanodevices, Institute of Physics, Chinese Academy of Sciences, Beijing, China, 02.07.09.

- T. Greber: **Substrates for molecular spintronics - dedicated to H. C. Siegmann (1935-2009)**
  2009 International Workshop on Nanostructures and Nanodevices, Sichuan University, Chengdou, China, 06.07.09.

- T. Greber: **Towards substrates for molecular spintronics**
  Abteilungsseminar, EMPA Thun, 24.08.09.

- T. Greber: **sp^2-hybridized single layer templates: hexagonal boron nitride and graphene**
  Gemeinsame Jahrestagung der Schweizerischen und Österreichischen Physikalischen Gesellschaften, Innsbruck, Österreich, 03.09.09.

- J. Osterwalder: **Boron nitride monolayers on transition metal surfaces - and their relation to graphene**
  Sehlendorf-Seminar, Abteilung Festkörperphysik, Universität Kiel, 17.09.09.

- T. Greber: **Molecular trapping in sp^2 hybridized single layer superstructures**
  10th International Conference on Atomically Controlled Surfaces, Interfaces and Nanostructures (ACSIN-10), Granada, Spain, 25.09.09.

- J. Osterwalder: **Measuring spin polarization vectors of surface state electrons**
  International Workshop on Electron Spectroscopy for Gas-phase Molecules and Solid Surfaces, Matsushima, Japan, 15.10.09.

- J. H. Dil: **Spin-resolved ARPES on low-dimensional Rashba systems**
  International Conference on Electron Spectroscopy and Structure (ICESS-11), Nara, Japan, 10.10.09.

- T. Greber: **Corrugated and chiral graphene and boron nitride single layers on transition metals**
  CECAM Workshop, EPF Lausanne, 14.10.09.

- T. Greber: **sp^2-hybridized templates for molecules: from h-BN nanomesh to graphene nanodots**
  Condensed Matter Seminar, Physikalisches Institut, Universität Basel, 23.11.09.

- T. Greber: **Boron nitride single layers: the polar sister of graphene**
  Seminar, Physics Department, University of Hawaii at Manoa, Honolulu, HI, USA, 04.12.09.

- T. Greber: **Graphene and boron nitride single layers: nanostructures with three bond hierarchy levels**
  7th International Symposium on Atomic Level Characterizations for New Materials and Devices (ALC-09), Maui, Hawaii, USA, 09.12.09.

- J. Osterwalder: **The insulating cousin of graphene: monolayers of hexagonal boron nitride**
  Kolloquium, Physikalisches Institut, Universität Würzburg, 21.12.09.

- J. Osterwalder: **Topological insulators in the Bi systems**
  449. WE-Heraeus Seminar on "Rashba and related spin-orbit effects in metals", Bad Honnef, Germany, 01.01.10.

- T. Greber: **News from the photoemission world: looking inside endofullerenes**
  Surface and Interface Microscopy / SLS Beamline Workshop, Weggis, 15.01.10.

- J. Osterwalder: **White graphene: monolayers of hexagonal boron nitride**
  Ruoff Group Seminar, Department of Mechanical Engineering, University of Texas, Austin, TX, USA, 08.02.10.

- J. Osterwalder: **Of nanotemplates, spin state interference and laser-induced field emission**
  Shen Group Seminar, Department of Applied Physics, Stanford University, Palo Alto, CA, USA, 10.02.10.
- J. Osterwalder: **Spin-polarized photoemission from surface states**
  Workshop / Winter School on Photoemission, Dijon, France, 25.02.10.
- H. Yanagisawa: **Optical control of field emission sites by femtosecond laser pulses**
  Seminar, Laboratory for Electromagnetic Fields and Microwave Electronics, ETHZ, 10.03.10

18.2.4 Physics of Biological systems

Articles

- **Off-axis and inline electron holography: Experimental comparison**
  T. Latychevskaia, P. Formanek, C. T. Koch and A. Lubk, Ultramicroscopy 110(5) (2010) 472-482.
- **Nondestructive imaging of individual biomolecules**
  M. Germann, T. Latychevskaia, C. Escher and H.-W. Fink, Phys. Rev. Lett. 104 (9) (2010) 095501.
- **Simultaneous amplitude and phase reconstruction in holography**
  T. Latychevskaia and H.-W. Fink, Optics Express 17 (13) (2009) 10697-10705.

Article in press

- **Fabrication and characterization of low aberration micrometer-sized electron lenses**
  E. Steinwand, J.-N. Longchamp and H.-W. Fink, Ultramicroscopy, in press.

Invited lecture

- H.-W. Fink: **Structural Biology at the Single Molecule Level Using Coherent Low Energy Electrons**
  Talk at the "Swiss Soft Days", Zurich, 04.02.2010.

Posters

- **Low Energy Electron Holography**
  T. Latychevskaia, J.-N. Longchamp, M. Germann, C. Escher and H.-W. Fink at the "Swiss Soft Days", Zurich, 04.02.2010.
- **Coherent Diffraction Microscopy with Low Energy Electrons**
  E. Steinwand, J.-N. Longchamp and H.-W. Fink at the "Swiss Soft Days" 04.02.2010 Zurich.
- **Low-energy electron coherent diffraction microscopy**
  E. Steinwand, J.-N. Longchamp and H.-W. Fink at "Nanostructures at Surfaces", Monte Verita, Ascona, 20-25.09.2009.

18.2.5 Physical Systems Biology and non-equilibrium Soft Matter

Articles

- **Determination of Mechanical Stress Distribution in Drosophila Wing Discs Using Photoelasticity**
  U. Nienhaus, T. Aegerter-Wilmsen, and C.M. Aegerter, Mechanisms of Development **126**, 942 (2009).
- **Effects of growth regulation by mechanical stress on epithelial topology**
  T. Aegerter-Wilmsen, A. Smith, A. Christen, C.M. Aegerter, E. Hafen, and K. Basler, Development **137**, 499 (2010).
- **Focusing light through living tissue.**
  I.M. Vellekoop and C.M. Aegerter, SPIE **7554**, 75420 (2010).
- **Scattering based fluorescence microscopy: imaging through turbid media**
  I.M. Vellekoop and C.M. Aegerter, Optics Letters **35**, 1245 (2010).

Articles in press

- **Photo-elastic properties of the wing imaginal disc of Drosophila**
  T. Schluck and C.M. Aegerter, Europ. Phys. J. E **32** (2010).
- **Exploiting disorder for perfect focusing.**
  I.M. Vellekoop, A. Lagendijk, and A. P. Mosk, Nature Photonics **4** (2010).
- **Velocity distributions of uniformly heated three dimensional granular gases**
  C.C. Maass, G. Maret, and C.M. Aegerter.

Conference reports

- **Imaging techniques**
  C.M. Aegerter, U. Nienhaus, T. Schluck, and I.M. Vellekoop, WingX retreat, Olivone, Switzerland (June 8th - 10th 2009).
- **Mechanics of Drosophila wing discs (poster)**
  U. Nienhaus, T. Aegerter-Wilmsen, T. Schluck and C.M. Aegerter, Gordon conference on Soft condensed matter Physics, Colby Sawyer college, USA (August 9th - 13th 2009)
- **Dynamics of levitated foams**
  N. Isert, G.Maret, and C.M. Aegerter, Workshop of the European graduate college in soft condensed matter, Strasbourg, France (September 28th - October 1st 2009)
- **Non-linear effects in Anderson localization**
  W. Bührer, S. Kammerer S. Fiebig, G. Maret, and C.M. Aegerter, Workshop of the European graduate college in soft condensed matter, Strasbourg, France (September 28th - October 1st 2009)
- **Coherent backscattering from fluidized granular beds**
  S. Fiebig, W. Bührer, G. Maret, and C.M. Aegerter, Workshop of the European graduate college in soft condensed matter, Strasbourg, France (September 28th - October 1st 2009)

- **Focusing light through living tissue. (poster).**
  I.M. Vellekoop and C.M. Aegerter, Photonics West, San Francisco CA, USA (January 15th - 20th, 2010).
- **Birefringent properties of developing trachea. (poster)**
  D. Assmann, T. Schluck, and C.M. Aegerter, Systemsbiology retreat, Monte Verita, Switzerland (February 28th - March 3rd 2010).
- **Photo-elastic properties of the wing imaginal disc of Drosophila. (poster)**
  T. Schluck, D. Assmann, A. Smith, and C.M. Aegerter, Systemsbiology retreat, Monte Verita, Switzerland (February 28th - March 3rd 2010).
- **Determination of stresses in Drosophila wing imaginal discs**
  U. Nienhaus, T. Schluck and C.M. Aegerter, Systemsbiology retreat, Monte Verita, Switzerland (February 28th - March 3rd 2010).
- **Imaging through turbid media.**
  G. Ghielmetti, I.M. Vellekoop, and C.M. Aegerter, Systemsbiology retreat, Monte Verita, Switzerland (February 28th - March 3rd 2010).

Invited lectures

- I.M. Vellekoop: **Focusing light through non-transparent objects**
  UMCG, Groningen, The Netherlands (18.05.2009).
- C.M. Aegerter: **Allometric scaling laws in Biology.**
  Habilitationsvortrag, Zürich, Switzerland (01.10.2009).
- C.M. Aegerter: **Imaging through a turbid layer.**
  MesoImage GDR Conference, Paris, France (29.10.2009).
- C.M. Aegerter: **Mechanics of Drosophila wing discs.**
  International conference on Physics Biology interface, Kalkutta, India (14.12.2009).
- C.M. Aegerter: **Mechanical properties of Drosophila wing discs.**
  Swiss Soft Matter Day, Zürich, Switzerland (04.02.2010).
- C.M. Aegerter: **Physical Systems Biology of Drosophila.**
  Systemsbiology retreat, Monte Verita, Switzerland (02.03.2010).

18.2.6 Outreach

Invited lectures

- H. Keller: **Was ist Licht?**
  Kinderuniversität Waldshut, Universität Zürich, Zürich, Switzerland, June 17, 2009.
- J. Osterwalder: **Unser Leben ohne Elektrizität**
  Kinderuniversität der Universität Zürich, 18.11.09.